Measurements of the ϕ^*_η distribution of $Z \to \mu^+\mu^-$ events in $p\bar{p}$ collisions at $\sqrt{s} =$ 1.96 TeV and measurements of the isolated diphoton cross section in pp collisions at $\sqrt{s} =$ 8 TeV

A thesis submitted to the University of Manchester for the degree of Doctor of Philosophy in the Faculty of Engineering and Physical Sciences

Xingguo Li

School of Physics and Astronomy

2016

Contents

Word count: 33,737

Measurements of the ϕ^*_η distribution of $Z \to \mu^+\mu^-$ events in $p\bar{p}$ collisions at $\sqrt{s} =$ 1.96 TeV and measurements of the isolated diphoton cross section in pp collisions at $\sqrt{s} =$ 8 TeV

A thesis submitted to the University of Manchester for the degree of Doctor of Philosophy in the Faculty of Engineering and Physical Sciences

Xingguo Li

School of Physics and Astronomy

2016

Abstract

Two precision measurements have been performed using the large number of dilepton and diphoton events produced in $p\bar{p}$ and pp collisions. A measurement of the distribution of the kinematic variable ϕ^*_η in the Drell-Yan process is performed in bins of boson rapidity and invariant mass using 10.4 fb^{-1} data collected by the D0 experiment with a centre-of-mass energy of 1.96 TeV in $p\bar{p}$ collisions. ϕ^*_η, defined in terms of lepton track directions, is well-measured and is sensitive to higher order effects in Quantum chromodynamics (QCD). Data are compared to predictions from state-of-the-art QCD Monte Carlo programs and are in good agreement. Measurements of the production of prompt photon pairs are performed using 20.24 fb^{-1} data collected by the ATLAS experiment at 8 TeV in pp collisions. QCD Monte Carlo programs including higher order effects are found to describe the data. In addition, a luminosity algorithm that renders its susceptibility to noise and inefficiency of certain modules in the diamond beam monitor has been proposed and validated using ATLAS simulations.

Declaration

No portion of the work referred to in the thesis has been submitted in support of an application for another degree or qualification of this or any other university or other institute of learning.

Copyright statement

1. The author of this thesis (including any appendices and/or schedules to this thesis) owns certain copyright or related rights in it (the "Copyright") and he has given The University of Manchester certain rights to use such Copyright, including for administrative purposes.

2. Copies of this thesis, either in full or in extracts and whether in hard or electronic copy, may be made **only** in accordance with the Copyright, Designs and Patents Act 1988 (as amended) and regulations issued under it or, where appropriate, in accordance with licensing agreements which the University has from time to time. This page must form part of any such copies made.

3. The ownership of certain Copyright, patents, designs, trade marks and other intellectual property (the "Intellectual Property") and any reproductions of copyright works in the thesis, for example graphs and tables ("Reproductions"), which may be described in this thesis, may not be owned by the author and may be owned by third parties. Such Intellectual Property and Reproductions cannot and must not be made available for use without the prior written permission of the owner(s) of the relevant Intellectual Property and/or Reproductions.

4. Further information on the conditions under which disclosure, publication and commercialisation of this thesis, the Copyright and any Intellectual Property and/or Reproductions described in it may take place is available in the University IP Policy[1], in any relevant Thesis restriction declarations deposited in the University Library, The University Librarys regulations[2] and in The Universitys policy on Presentation of Theses.

[1]see http://documents.manchester.ac.uk/DocuInfo.aspx?DocID=487
[2]see http://www.manchester.ac.uk/library/aboutus/regulations

Acknowledgements

I would like to thank my Supervisor, Terry Wyatt, for supervising and guiding me through the past four years. I also thank Mika Vesterinen for his patience and useful discussions in the D0 analysis. In addition, I thank all members of the particle group and my friends who helped to make my past four years enjoyable.

Finally I would like to thank my parents, Xiuying Wang and Lianhe Li, and my elder brother Xingzhou Li, for their constant support and encouragement during the past seven years when I was studying in Manchester University.

Chapter 1

Introduction

This thesis describes two precision measurements using the large number of dilepton and diphoton events produced in the $p\bar{p}$ and pp collisions respectively. The first precision measurement is the study of the distribution of the dilepton transverse momentum in the Drell-Yan process with a novel approach in $p\bar{p}$ collisions, which is sensitive to higher order effects in Quantum chromodynamics. The second measurement is to measure both the inclusive and differential cross sections of prompt photon pairs in pp collisions.

Chapter 2 documents the theoretical background and the physics motivations for performing these two measurements. The introduction to the D0 experiment at the Tevatron and the ATLAS experiment at the Large Hadron Collider is described in Chapter 3. This is followed by Chapter 4 describing the experimental techniques to reconstruct the physics objects. A variable called ϕ^*_η is used to probe the dilepton transverse momentum in the Drell-Yan process and Chapter 5 details the measurement of the normalised differential cross-section of this variable at the D0 experiment. Chapter 6 studies the performance of a luminosity detector named diamond beam monitor and proposes an algorithm to measure the luminosity with this detector using simulations at the ATLAS experiment. Chapter 7 presents the measurements of the inclusive and differential cross sections of prompt photon pairs in pp collisions at the ATLAS experiment.

Chapter 2

Theoretical Background

2.1 The Standard Model of Particle Physics

The Standard Model (SM) of particle physics is a theory to describe the fundamental constituents of matter in the universe and the interactions between them. The Standard Model has demonstrated extraordinary successes in predicting the interactions of high-energy particles as probed by a variety of experiments up to the 13 TeV scale. Interactions between particles are assumed to be mediated by force-carrying spin-1 bosons, namely, the photon (γ) for the electromagnetic interaction, $W^{\pm}$ and Z bosons for the weak interaction and the gluon (g) for the strong interaction. Certain interactions among these force-carriers themselves such as triple gauge couplings are also possible. Gravitational forces as described by general relativity are not considered in the current Standard Model.

Matter is understood in terms of twelve point-like spin-half fermions as presented in Table 2.1, which can be divided into two sets, leptons and quarks, with each having an anti-matter counterpart except possibly neutrinos[1]. All of the fermions can interact via electromagnetic and weak interactions. Quarks, but not leptons, are also involved in the strong interaction. Each set contains three generations, with each generation consisting of a pair of leptons and a pair of quarks. All generations of leptons have the same properties such as charge and spin, where the only difference between generations is mass. The same is also true for the quark generations. Quarks may carry one of three colours, and colour serves as the source of strong interaction. Anti-quarks carry the equivalent anti-colour. Quarks and gluons are collectively referred to as partons. The weak bosons and fermions obtain masses via interaction with a spin-0 Higgs field, the excitation of which is manifested as the Higgs boson (H).

[1]The question of whether a neutrino is its own antiparticle or not is still under investigation [1].

Gauge Bosons			
Electromagnetic	Weak	Strong	Scalar
γ	$W^{\pm}$, Z	g	H
Fermions			
Quarks	$\begin{pmatrix} u \\ d \end{pmatrix}$	$\begin{pmatrix} c \\ s \end{pmatrix}$	$\begin{pmatrix} t \\ b \end{pmatrix}$
Leptons	$\begin{pmatrix} e \\ \nu_e \end{pmatrix}$	$\begin{pmatrix} \mu \\ \nu_\mu \end{pmatrix}$	$\begin{pmatrix} \tau \\ \nu_\tau \end{pmatrix}$

Table 2.1: A summary of elementary particles in the Standard Model.

The theoretical framework of the SM is based on quantum field theory (QFT), in which particles are regarded as excited states of an underlying physical field. The three fundamental interactions in the SM are made possible by introducing a set of symmetries onto the quantum field of particles. The SM Lagrangian, which controls the dynamics and kinematics of the theory, needs to be invariant under a *local* phase transformation, $\psi \rightarrow \psi' = e^{i\phi(x)}\psi$. The term *local* implies that the phase change ϕ varies as a function of the space-time coordinate of the field x. These transformations are often referred to as gauge transformations. In order to preserve the invariance of the theory under gauge transformations, it requires the presence of additional gauge fields that interact with fermions and the existence of gauge bosons that arise from these additional gauge fields. The fundamental interactions of SM particles can be described by a combination of local gauge symmetry groups $\mathrm{SU(3)}_C \otimes \mathrm{SU(2)}_L \otimes \mathrm{U(1)}_Y$, where $\mathrm{SU(3)}_C$, $\mathrm{SU(2)}_L$ and $\mathrm{U(1)}_Y$ denotes the gauge group of colour, weak isospin and weak hypercharge respectively. More details on each of these gauge symmetry groups will be provided in the later text.

Despite the triumph of the Standard Model in providing numerous predictions that have been established by the experiments, there are a few known problems with the current model which are listed and discussed as follows.

- The gravitational interactions as described by general relativity are not explained by the model in terms of QFT.

- The model is inconsistent with observations from cosmology over large length scales. Firstly, it is unable to give a natural candidate for dark matter. Secondly, the model cannot explain the predominance of matter over anti-matter in the universe.

- It is known that the quantum loop corrections to the Higgs mass diverge quadratically. At the Planck scale (10^{19} GeV) where quantum effects of gravity become significant, the Higgs mass would be forced to be around the Planck

scale. However, the current measurement of the Higgs mass is ∼125 GeV [2]. This is called the hierarchy problem [3].

New models beyond the Standard Model, such as Supersymmetry (SUSY), were proposed to resolve the hierarchy problem and to constitute natural candidates for dark matter. However, no direct experimental evidence for SUSY has been observed so far [4].

2.2 Electroweak interactions

A unified description of electromagnetism and weak interaction, known as the electroweak interaction, was proposed by Weinberg [5], Salam [6] and Glashow [7] in the 1960s. The group structure of the electroweak (EW) theory is composed of $\mathrm{SU}(2)_L$ representing weak isospin and $\mathrm{U}(1)_Y$ representing weak hyperchage. The subscript L on $\mathrm{SU}(2)_L$ implies that only left-handed[2] fermions couple to the weak isospin. The third component of weak isospin, denoted by I_3, is a conserved quantum number in the SM interactions. The electric charge, Q_f, is related to I_3 and the weak hypercharge Y_W, where $Q_f = Y_W/2 + I_3$. The values of I_3 and Q_f for the generation of fermions with the lightest masses are shown in Table 2.2.

The theory of electroweak forces is required to be invariant under $\mathrm{SU}(2)_L \otimes \mathrm{U}(1)_Y$ gauge transformations, generating three gauge bosons ($W^{\pm}$ and W^0) from $\mathrm{SU}(2)_L$ and one gauge boson (B) from $\mathrm{U}(1)_Y$. All these bosons are massless at this stage. $W^{\pm}$, Z bosons and the photons are then produced via a process known as spontaneous symmetry breaking. Spontaneous symmetry breaking is accomplished by introducing the Higgs scalar field into the theory, which can spontaneously break the $\mathrm{SU}(2)_L \otimes \mathrm{U}(1)_Y$ gauge symmetry at the electroweak scale. Spontaneous symmetry breaking is used to generate mass terms for $W^{\pm}$ and Z bosons and the fermions whilst keeping photons massless. This process is referred to as the Brout-Englert-Higgs (BEH) mechanism [8, 9]. A striking feature of the BEH mechanism is the prediction of a scalar boson, H, which was discovered in 2012 by the ATLAS [10] and CMS [11] experiments at the Large Hadron Collider (LHC).

[2]The helicity of a particle is the projection of the angular momentum onto the momentum direction, which can be positive or negative. Left- or right-handedness refers to chirality. A particle is left-handed (right-handed) given that the particle has its spin pointing along the opposite (same) direction with respect to its momentum. For massless particles, chirality equals helicity because a given massless particle travelling at the speed of light spins in the same direction along its axis of motion irrespective of the reference frame. However, they must be distinguished for massive particles where a change of the reference frame can lead to changing the momentum direction and thus reversing helicity.

	Fermions		Antifermions	
	I_3^f	Q_f	$I_3^{\bar{f}}$	$Q_{\bar{f}}$
$\begin{pmatrix} u \\ d \end{pmatrix}_{\mathrm{L}}$	$+\frac{1}{2}$	$+\frac{2}{3}$	0	$-\frac{2}{3}$
	$-\frac{1}{2}$	$-\frac{1}{3}$	0	$+\frac{1}{3}$
u_R	0	$+\frac{2}{3}$	$-\frac{1}{2}$	$-\frac{2}{3}$
d_R	0	$-\frac{1}{3}$	$\frac{1}{2}$	$+\frac{1}{3}$
$\begin{pmatrix} e \\ \nu_e \end{pmatrix}_{\mathrm{L}}$	0	-1	$-\frac{1}{2}$	$+1$
	$+\frac{1}{2}$	0	-	-
e_R	0	-1	$+\frac{1}{2}$	$+1$
v_R	-	-	$-\frac{1}{2}$	0

Table 2.2: The third component of weak isospin and the electric charge for the left-handed and right-handed fermions (anti-fermions) respectively. Only the generation of leptons or quarks with the lightest masses is shown and the other generations obey the same pattern. The subscripts L and R represents the left-handed and right-handed fermions. Only left-handed neutrino and right-handed anti-neutrino are physically observed.

Spontaneous symmetry breaking causes the mixing between B and W^0 in the (B,W^0) plane to form the physically observed γ and Z bosons:

$$\begin{pmatrix} \gamma \\ Z \end{pmatrix} = \begin{pmatrix} \cos\theta_W & \sin\theta_W \\ -\sin\theta_W & \cos\theta_W \end{pmatrix} \times \begin{pmatrix} B \\ W^0 \end{pmatrix}, \tag{2.1}$$

where θ_W denotes the weak mixing angle. Such a procedure also introduces the following relations:

$$\cos\theta_W = \frac{m_W}{m_Z} = \frac{g}{\sqrt{g^2 + g'^2}}, \tag{2.2}$$

where g and g' represent the coupling constant of the $\mathrm{SU}(2)_L$ and $\mathrm{U}(1)_Y$ gauge groups respectively. It suggests that the weak mixing angle also describes the relative strength between the electromagnetic and weak interactions.

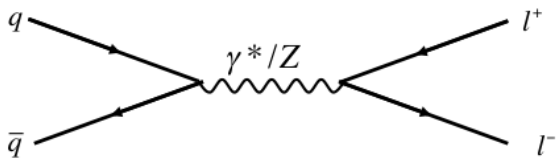

Figure 2.1: A tree level Feynman diagram at the lowest order for annihilation of quark and anti-quark to form a virtual photon or a Z boson which then decays into a pair of leptons.

In particle physics, a Feynman diagram is a graphical representation of quantum

field theory processes from some initial quantum state to some final quantum state. One can calculate perturbative[3] contributions to the quantum transition amplitude by assigning the proper mathematical expression to each line and vertex in the Feynman diagram. Figure 2.1 shows the lowest order Feynman diagram for the annihilation of a quark-antiquark pair to produce a lepton-antilepton pair via a Z boson or a virtual[4] photon γ^*. It belongs to a category of processes called neutral current interactions, in which the propagator of the interaction is a neutral boson Z/γ^*. The photon couples to fermions irrespective of the handedness and its coupling strength to fermions is directly proportional to the electric charge eQ_f. The coupling strengths of the Z boson to the left-handed and right-handed fermions, represented by g_L^f and g_R^f respectively, are characterized by the following functions:

$$g_L^f = I_3^f - Q_f \sin^2\theta_W, \quad g_R^f = -Q_f \sin^2\theta_W. \tag{2.3}$$

As the values of g are distinct for left-handed and right-handed fermions, they couple to the Z boson with different coupling strengths. Conventionally, the couplings of the Z boson to fermions were written in terms of the vector coupling constant $c_v = g_L^f - g_R^f$ and the axial vector coupling constant $c_A = g_L^f + g_R^f$.

The charged current interactions, mediated by $W^\pm$ gauge bosons, only couple to left-handed fermions and right-handed antifermions. For leptons, the conversion can only occur in the same generation. The decay of $W^\pm$ to muons can take place via the following processes: $W^+ \to \mu^+ v_\mu$ and $W^- \to \mu^- \bar{v}_\mu$. The conversion of an up-type quark to a down-type quark, not necessarily in the same generation, can take place in a charged current interaction given that it is kinematically allowed. An example is the c quark decay via the following processes: $c \to sW^+$ and $c \to dW^+$. The strength of the flavour-changing weak decay is determined by a 3×3 unitary matrix called the Cabibbo-Kobayashi-Maskawa (CKM) matrix [12, 13]. Similarly, neutrino oscillations have been observed experimentally and the probability for neutrino flavour oscillations is described by a 3×3 Pontecorvo-Maki-Nakagawa-Sakata (PMNS) matrix [14, 15].

Given the mathematical structure of the Standard Model, the couplings of all particles can be predicted by a limited number of free input parameters that must be determined by experiments. The consistency of the Standard Model can be examined by performing a global fit to the precision electroweak data. Figure 2.2 shows the overall result of such a fit [16]. The indirect determination of an observable is obtained from the fit without considering the corresponding direct measurement

[3]The perturbative regime requires the coupling constant to be small.

[4]For a virtual particle, the energy-momentum relation could break down: $E^2 \neq m^2 + p^2$.

of that observable. All indirect measurements are consistent with the corresponding direct precision measurement, providing a powerful self-consistency check of the SM.

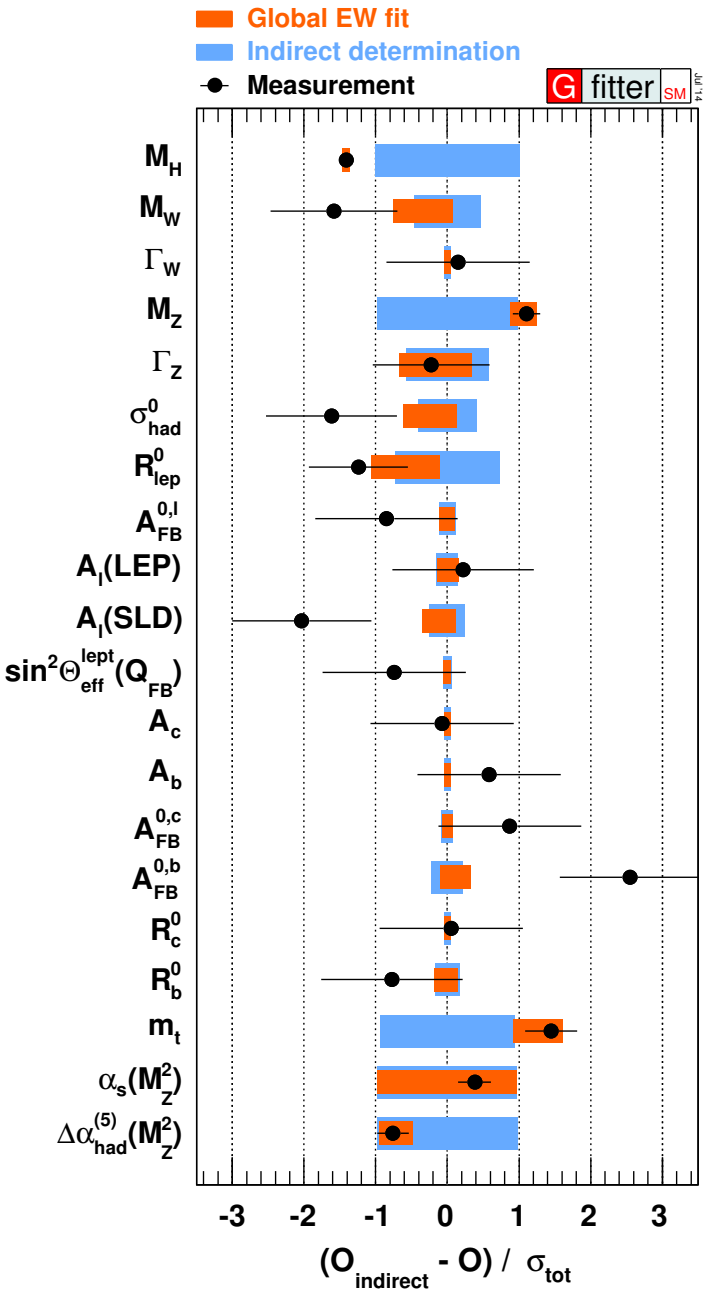

Figure 2.2: Overall result of the global fit to the precision electroweak data [16]. The indirect determination of an observable shown as the blue horizontal bar is obtained by repeating the electroweak fit without considering the corresponding direct measurement of that observable. The red horizontal bar shows the number of standard deviations for the global fit and the point with error bars shows the indirect determination.

2.3 Strong interactions

The strong interaction is described by the $SU(3)_C$ gauge group of quantum chromodynamics (QCD), where C represents the colour charge that is the source of the strong interaction. The strength of the strong interaction is determined by a single coupling constant, α_s, which varies as a function of the momentum transfer Q (at one-loop precision):

$$\alpha_S(Q^2) = \frac{\alpha_S(\mu_R^2)}{1 + \alpha_S(\mu_R^2)\beta_0 \ln \frac{Q^2}{\mu_R^2}}, \tag{2.4}$$

where μ_R is the renormalisation scale introduced as an approach of truncating calculations of α_S at a finite scale, $\beta_0 = \frac{33-2n_f}{12\pi}$ and n_f denotes the number of quark flavours that is allowed in the loop. Figure 2.3 presents the comparison of α_s over a broad range of energy scale between precision measurements and QCD predictions [4]. The predictions from QCD are consistent with various measurements for up to ~1000 GeV.

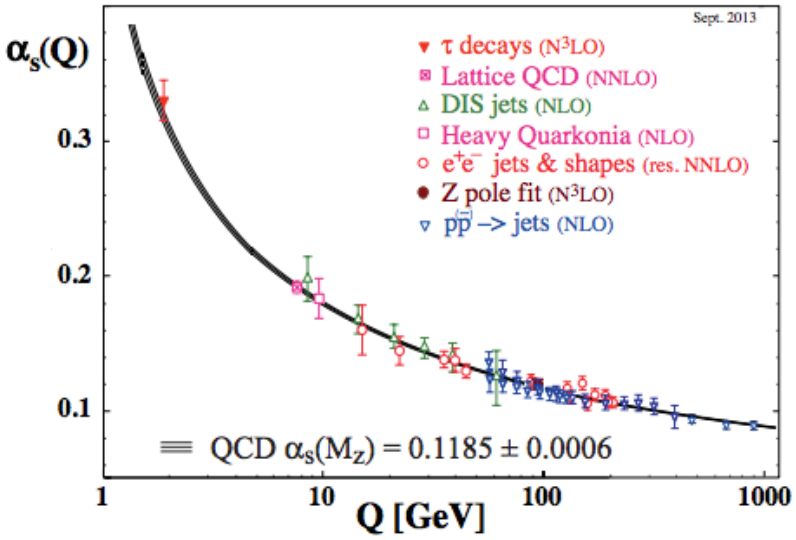

Figure 2.3: Comparison of α_s over a broad range of energy scale between theoretical predictions and a number of precision measurements [4]. The band represented by three bold lines is the theoretical prediction with the corresponding theoretical uncertainties.

Using Equation 2.4 and Figure 2.3, one can easily see α_S decreases at large energies, which correspond to short distances, giving rise to asymptotic freedom where quarks behave as if they were free particles. Also, α_S increases rapidly at small energies, which correspond to long distances, giving rise to the colour confinement

of quarks. This property explains the reason why individual quarks are never observed physically and what we observe in the detector is a collection of collimated hadrons called "jets". Hadrons are colourless and can be divided into baryons and mesons. Baryons are composed of three quarks and an arbitrary number of pairs of a quark and an antiquark and mesons consist of one or more pairs of a quark and an antiquark. High-energy quarks or gluons produced in hadron-hadron collisions will continue radiating partons until the energies reach the typical scale of QCD, $\Lambda_{QCD} \sim 100$ MeV, at which this "parton showering" stops and these partons are confined to form hadrons.

2.4 The Drell-Yan process

The Drell-Yan process is the production of a pair of leptons in hadron-hadron collisions via the exchange of a virtual photon γ^*, a Z boson or a W boson [17].

2.4.1 Overview

The partonic cross-section at high-collision energies can be calculated using perturbation theory, where the strong coupling constant becomes small ($\alpha_s \sim 0.1$ for $Q \sim$100 GeV) due to asymptotic freedom. However, partons are confined to the structure of the hadrons as a result of colour confinement, which cannot be treated perturbatively due to the presence of the relatively large coupling constant at the QCD scale ($\alpha_S \sim 1$ for $Q \sim$200 MeV). The factorization theorem allows us to calculate the cross-section of hadron-hadron collisions by separating the perturbative part and the non-perturbative part in a systematic fashion:

$$\sigma = \sum_{a,b=q,\bar{q},g} \underbrace{\int_0^1 dx_a \int_0^1 dx_b f_a(x_a, \mu_F^2) f_b(x_b, \mu_F^2)}_{\text{non-perturbative part}} \underbrace{\sigma_{hard}(\mu_R, \mu_F)}_{\text{perturbative part}}, \tag{2.5}$$

where

- The sum is over all possible combinations of the incoming parton species.
- x_a and x_b represent the fractions of the hadron parent momenta carried by the colliding partons.
- The factorization scale μ_F is an arbitrary scale to distinguish between the long-distance and the short-distance physics, which is usually set to the momentum transfer Q.

- The probability for a hadron to contain a parton of flavour a at factorization scale μ_F is given by the Parton Distribution Functions (PDFs) denoted by $f_a(x_a, \mu_F^2)$.
- The cross section of the hard process $\sigma_{hard}(\mu_R, \mu_F)$ can be calculated using perturbation theory.

It should be noted that the Drell-Yan process is the only hadron-hadron process in which the factorization theorem has been demonstrated analytically [18].

It is impossible to derive PDFs from first-principles in QCD because they are non-perturbative, and so PDFs must be determined experimentally. A number of collider experiments have provided constraints on the PDFs. The most recent PDFs including data from the Tevatron and the LHC are produced by the CTEQ collaboration [19] and the NNPDF collaboration [20]. The DGLAP equations [21–23] are employed to extrapolate PDFs determined at a certain Q^2 to other values of Q^2.

2.4.2 Z/γ^* transverse momentum distribution in Drell-Yan process

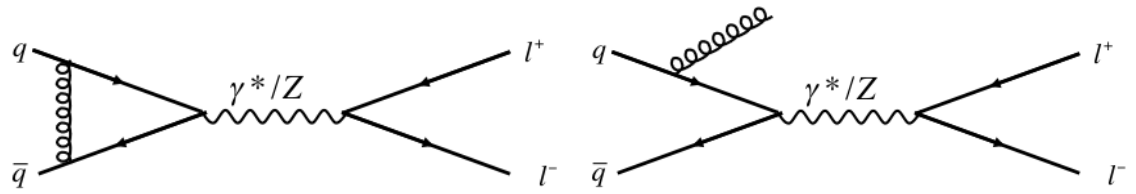

(a) (b)

Figure 2.4: Feynman diagrams of the Drell-Yan sub-process. Figure 2.4a shows an example of higher order virtual corrections with a gluon exchange between the incoming quark and anti-quark. Figure 2.4b shows a real gluon emission off the quark.

The dilepton transverse momentum in $Z/\gamma^* \rightarrow l^+l^-$ production is defined as $p_T^{ll} = |\vec{p_T}^1 + \vec{p_T}^2|$, where $\vec{p_T}^1$ and $\vec{p_T}^2$ refer to the vector of the momentum of the two leptons in the plane transverse to the beam direction. Assuming no intrinsic transverse motion of the colliding partons in the head-on hadron-hadron collisions, the dilepton should be produced with zero p_T^{ll} at the lowest order tree-level Feynman diagram (Figure 2.1) according to momentum conservation. This Feynman diagram is called a leading-order (LO) diagram. Figure 2.4a shows an example of a higher order virtual correction with a gluon exchange between the incoming quark and anti-quark, where the dilepton transverse momentum is zero. Figure 2.4b presents

the first non-zero contribution to the dilepton transverse momentum in which a real gluon is radiated off the quark. The diagrams shown in Figure 2.4 are included in the next-to-leading-order (NLO) calculations of the inclusive Drell-Yan process.

At finite order of α_S in the perturbative series, the leading logarithmic term takes the form $1/{p_T^{ll}}^2 \alpha_s^n ln^{2n-1}(Q^2/{p_T^{ll}}^2)$ [18] with n being an integer. When the gluon is soft (low energy) or radiated collinear to the parent parton direction ($p_T^{ll} \to 0$), the logarithmic terms in the perturbative calculations will become important due to incomplete cancellations between divergent virtual and real diagrams. These large logarithmic divergences can be "resummed" to all orders in α_S in perturbation theory using resummation schemes [18]. The obtained low p_T^{ll} spectrums are then matched to the fixed-order perturbative QCD (pQCD) predictions to remove the overlap that has been double counted between resummation and pQCD calculations. Resummation including only the leading logs is called leading-log (LL) accuracy. The state-of-art resummation is often at next-to-next-to LL (NNLL) accuracy which includes the sub-leading logs. The resummation technique introduces another theoretical uncertainty arising from the choice of the resummation scale, μ_Q, which is usually set to the momentum transfer Q.

For $0 \leq p_T^{ll} < \Lambda_{QCD}$, pQCD calculations are not valid any more and non-perturbative form factors have to be introduced to give a sensible cross section at low p_T^{ll}. The following GNW [24] non-perturbative parametrizations have been found to describe the experimental data:

$$\tilde{W}^{NP}(b,a) = \exp\ [-b^2 a(Q,\sqrt{s})] \tag{2.6}$$

with

$$a(Q,\sqrt{s}) = a_Z(1.96\ \text{TeV}) + a_2 \ln\ (\frac{Q}{M_Z}) + a_3\ \ln(\frac{Q^2}{M_Z^2}\frac{s}{(1.96\ \text{TeV})^2}), \tag{2.7}$$

where b corresponds to the impact parameter ($b \sim 1/p_T^{ll}$), a_Z is determined in [24] by fitting measurements sensitive to the small-p_T^{ll} region in the Drell-Yan process at around Z-mass region from the D0 experiment [25], a_2 and a_3 are determined in [26] by a global fit of Drell-Yan precision data at various values of Q and $\sqrt{s}$ denotes the centre of mass energy at hadron colliders.

At a fixed value of Q, the non-perturbative parameter dependence on the parton momentum fraction x at small p_T^{ll} can be probed by looking at different boson rapidity y regions, which is defined as:

$$y = \frac{1}{2}\ln\frac{E-p_z}{E+p_z}, \tag{2.8}$$

where E is the dilepton energy and p_z is the dilepton momentum along the beam axis. The parton momentum fraction $x_{a,b}$ is related to the boson rapidity:

$$x_{a,b} = \frac{Q}{\sqrt{s}} e^{\pm y}. \tag{2.9}$$

For Z/γ^* production at the Tevatron, the range of x probed by the experiment is typically between 0.001 and 0.1. In the region $|y| > 2$ at the D0 experiment, x corresponds to $\sim$0.001. Therefore, the x dependence of the non-perturbative functions can be verified by precise measurements of p_T^{ll} distribution of the Drell-Yan process, at various values of momentum transfer Q and a number of rapidity regions.

2.5 Monte-Carlo event generators

Monte-Carlo (MC) event generators are used extensively in particle physics experiments to predict production rates and kinematic distributions of physical processes. MC samples are produced via several stages.

At the first stage, the hard process in a single pp ($p\bar{p}$) collision is generated according to the probability distribution predicted by the SM, where the cross-section can be factorized into the non-perturbative part and the perturbative part as shown in Equation 2.5. Other processes including the hadron remnants or multiple parton scatterings in the single pp ($p\bar{p}$) collision produced at the same time as the hard process (underlying event) and additional pp ($p\bar{p}$) collisions (pile-up) are also produced.

The initial (final) state radiations from incoming (outgoing) partons are simulated using a technique called "parton showers" [27]. High-energy partons evolve down in scale by emitting additional partons until a point where α_S becomes large and the fixed-order pQCD calculations are invalid. The probability for no emission of partons in a parton shower is given by Sudakov form factors [28]. Matching between the fixed-order pQCD calculations (matrix elements) and parton showers has to be performed to avoid a double counting. The PYTHIA MC program [29] matches the LO matrix element to the LL parton shower. There are a few "free" parameters in the modeling of the parton shower that are sensitive to initial state parton emissions, which must be determined by experiments. The hadronization model needs to be incorporated within the parton shower model, which has additional free parameters that must be tuned using experimental data.

These events produced by event generators are then passed through a detector

simulation using the GEANT4 program [30] and reconstructed using the same algorithm implemented in the reconstruction of collision data. For some of the fixed order calculations like RESBOS [31] and DIPHOX [32], predictions are only available for hard processes without modelling of the underlying event or hadronization.

2.6 The ϕ^*_η distributions in the Drell-Yan process

2.6.1 Physics motivation

Precise study of the Drell-Yan p_T^{ll} spectrum provides an ideal ground for testing and improving initial state QCD radiation models because of the relatively low background and the absence of colour flow between the initial state and the final state. Understanding the performance of such models is important in the precision determination of the W-mass and Higgs properties as well as searching for new physics beyond the SM.

As already explained in Section 2.4.2, the low p_T^{ll} region is sensitive to non-perturbative effects due to initial state radiations from partons. The precision of the p_T^{ll} spectrum is limited by the lepton momentum resolution, which is around a few percent at the D0 experiment. An alternative observable, denoted as ϕ^*_η, has been developed in [33] to probe the low p_T^{ll} region. A schematic diagram of the relevant variables for the definition of ϕ^*_η is illustrated in Figure 2.5. ϕ^*_η is defined in terms of track directions (η, ϕ)[5]:

$$\phi^*_\eta = \tan\ (\phi_{acop}/2) \sin\ (\theta^*_\eta), \tag{2.10}$$

where the acoplanarity angle ϕ_{acop} can be expressed as a function of the opening angle of the final state dilepton $\phi_{acop} = \pi - \Delta\phi$. θ^*_η is the scattering angle of the lepton with respect to the beam axis in the rest frame of the dilepton system, which is given by

$$\cos\theta^*_\eta = \tanh\ (\frac{\eta^- - \eta^+}{2}). \tag{2.11}$$

η^- and η^+ represent pseudorapidities of the negatively charged and positively charged lepton respectively. The rest frame of the dilepton system refers to a frame where a Lorentz boost $\beta = \tanh\ ((\eta^- + \eta^+)/2)$ is applied along the beam axis. It is such that the two leptons have equal and opposite rapidity, i.e., the two leptons are back-to-back in the $r - \theta$ plane. Since ϕ^*_η is exclusively dependent on the track directions

[5]The pseudorapidity η is defined as $\eta = -\ln\ (\tan(\theta/2))$, where θ is the scattering angle of the outgoing particle relative to the beam direction

of the leptons, which are well measured with a precision of around miliradians, it can be determined more precisely than p_T^{ll}, which depends on the momenta of the two leptons. It is shown in [33] that ϕ_η^* is highly correlated with $a_T/M_{\ell\ell}$, where a_T is the transverse component of p_T^{ll} with respect to the thrust axis as illustrated in Figure 2.5. The thrust axis is defined as $\hat{t} = (\vec{p_T}^1 - \vec{p_T}^2)/|\vec{p_T}^1 - \vec{p_T}^2|$ and a_T can be written as $a_T = |\hat{t} \times p_T^{ll}|$.

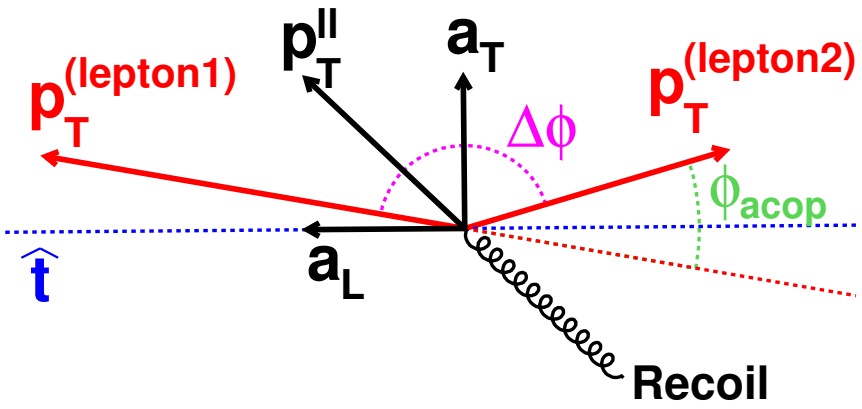

Figure 2.5: A schematic diagram of the relevant variables in the transverse plane relative to the beam direction [33]. p_T^{ll} can be decomposed into two orthogonal components, a_T and a_L with respect to the thrust axis $\hat{t}$.

2.6.2 Previous measurements

The normalised differential cross section of ϕ_η^*, $(1/d\sigma)(d\sigma/d\phi_\eta^*)$, was first measured by the D0 experiment [25], in which the measurement was performed close to the Z-mass peak region in the Drell-Yan process in bins of rapidity $|y|$ for the dimuon and dielectron channels separately. Figure 2.6 presents the ratio of D0 data distributions of $(1/d\sigma)(d\sigma/d\phi_\eta^*)$ to NNLL+NLO predictions from RESBOS. The RESBOS prediction is in reasonable agreement with data but cannot describe the detailed shape of ϕ_η^*. In particular, the "small-x" broadening model, which predicts a broadening of the p_T^{ll} shape at small parton momentum fraction, is strongly disfavoured by the D0 data. Perturbative QCD predictions [34, 35] including resummation calculations at NNLL accuracy matched to the NLO QCD calculations from MCFM [36] were found to describe the D0 data within the assigned theoretical uncertainties. The D0 measurement also made it possible to determine the non-perturbative parameter a_Z implemented in RESBOS [24] with unprecedented precision.

Experimental measurements of the ϕ_η^* distribution were subsequently followed by the ATLAS collaboration [37] at $\sqrt{s}$ =7 TeV. These measurements have been used to tune the free parameters in parton showers of MC programs such as PYTHIA

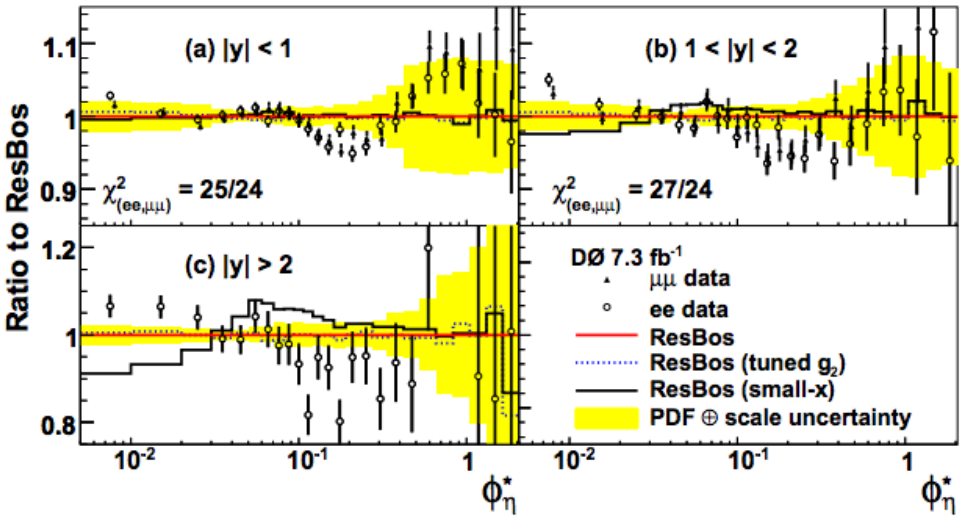

Figure 2.6: The ratio of the corrected data distributions of $(1/d\sigma)(d\sigma/d\phi^*_\eta)$ in the dimuon and dielectron channels to the RESBOS prediction for $70 < M_{ll} < 110$ GeV in bins of rapidity from the 2011 D0 publication [25]. The ratio to the nominal RESBOS prediction (red line) of alternative RESBOS predictions with tuned g_2 value (blue) and the small-x broadening effect (solid black line) are also shown. $\chi^2_{(ee,\mu\mu)}$ is calculated assuming the uncertainties are uncorrelated between the dimuon and dielectron channels. The yellow band represents the theoretical uncertainties. g_2 in the legend represents the non-perturbative parameter in the non-perturbative formalism of Brock, Landry, Nadolsky and Yuan (BLNY) in [26].

and POWHEG+PYTHIA [38]. The LHCb collaboration measured the absolute differential cross section of ϕ^*_η [39], with precision limited by the available statistics. As only bosons that are produced highly boosted relative to the beam direction can be detected at LHCb, the LHCb ϕ^*_η measurements allow stringent tests of QCD predictions at very small parton momentum fraction, thus are complementary to the D0 and ATLAS results. Chapter 5 will describe an update of the D0 ϕ^*_η measurements for $70 < M_{\ell\ell} < 110$ GeV in the dimuon channel and for $M_{\ell\ell}$ away from the Z-mass peak region, and these results have been published in [40].

2.7 Isolated diphoton production at LHC

The dominant processes that contribute to photon production in hadron-hadron collisions are: direct photons, photon Bremsstrahlung and fragmentation. A fragmentation photon corresponds to a photon that carries a large fraction of the energy of a jet arising from a fragmented quark. The bremsstrahlung or fragmentation emission of photons are collectively referred to as fragmentation photons in the later text.

Direct diphoton production is dominated by quark-antiquark annihilation. The

LO Feynman diagram of direct diphoton production at Born level is illustrated in Figure 2.7a. Figure 2.7b presents the NLO virtual correction with a virtual gluon exchange between the incoming quarks. Figure 2.7c shows the direct diphoton production via gluon-gluon scattering, which is known as the box diagram. Although the box diagram in Figure 2.7c is suppressed by $O(\alpha_s^2)$ compared to Figure 2.7a, these two contributions are comparable due to the large gluon densities in pp collisions.

Feynman diagrams of one-photon fragmentation, corresponding to the production of one direct photon and one photon from bremsstrahlung or fragmentation of a parton, are presented in Figure 2.8. Divergences appear in the collinear limit when the photon is emitted in the same direction to the parton. One way of resolving such divergences is to introduce the quark (gluon) fragmentation function $D_{\gamma/q}$ ($D_{\gamma/g}$), which describes the showering of a parton in the collinear limit. Experimentally, the fragmentation photon is usually less well isolated than the direct photon. Figure 2.9 shows Feynman diagrams of two-photon fragmentation process at LO (Figure 2.9a) and NLO (Figure 2.9b and Figure 2.9c), respectively.

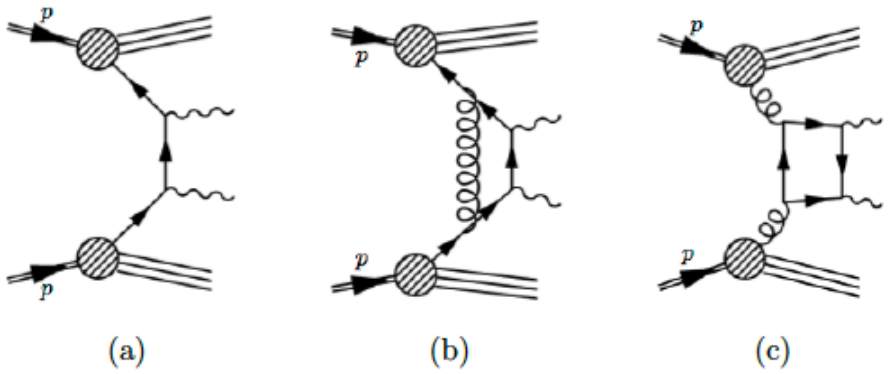

Figure 2.7: Feynman diagrams of direct diphoton production in [41] at (a) Born level, (b) NLO with a virtual gluon exchange between the incoming quarks, and (c) Box level with gluon-gluon scattering to produce two photons.

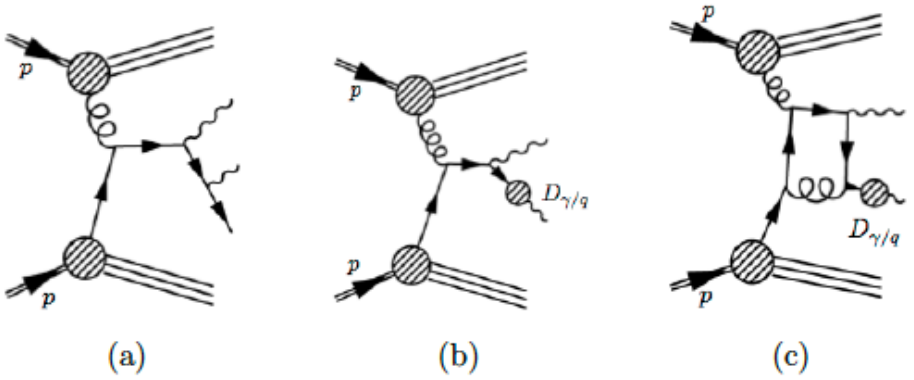

Figure 2.8: Feynman diagram of diphoton production in [41] with one photon produced via fragmentation including (a) one photon Bremsstrahlung, (b) one photon fragmentation, and (c) NLO diagram with a virtual gluon exchange.

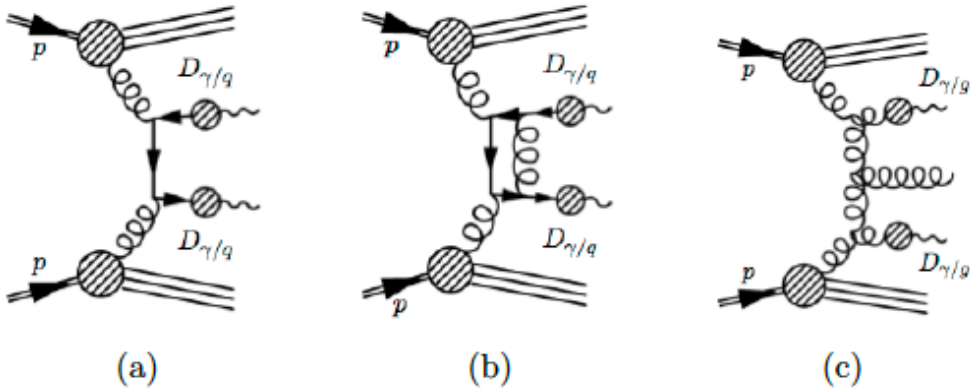

Figure 2.9: Feynman diagram of diphoton production in [41] with both photons produced via fragmentation at (a) LO, (b) NLO with a virtual gluon exchange between the outgoing quarks, and (c) NLO with a real gluon emission.

The production of isolated photon pairs, $pp \to \gamma\gamma + X$, can be used to verify the perturbative QCD calculations and resummation techniques of multiple soft gluons. Specific regions in kinematic distributions are sensitive to different aspects of QCD. An example is the difference in the azimuthal angle, which is susceptible to the fragmentation contributions, particularly when the two photons emitted are collinear ($\Delta\phi_{\gamma\gamma} \sim 0$). For two photons which are back-to-back in the transverse plane ($\Delta\phi_{\gamma\gamma} \sim \pi$ and $p_{\mathrm{T},\gamma\gamma} \sim 0$), the kinematic region is sensitive to emission of multiple soft gluons, where resummation schemes can be tested.

In addition, the isolated diphoton process is a major irreducible background for the Higgs searches and new physics searches beyond the SM. Precise measurement of the kinematic distributions of isolated photon pairs is critical for these searches and the study of Higgs properties. For instance, the distribution of the diphoton invariant mass ($m_{\gamma\gamma}$) is important for resonance searches and the extraction of the

$H \to \gamma\gamma$ signal. Another example is the cosine of the scattering angle calculated in the Collin-Soper frame ($\cos\theta^*_{CS}$) [42], which is sensitive to the spin of the diphoton system.

2.7.1 Previous measurements

Previous measurements of the diphoton cross section both inclusively and as a function of various observables have been conducted by the D0 [43] and CDF [44] experiments in $p\bar{p}$ collisions at $\sqrt{s} = 1.96$ TeV. These measurements were also performed by the ATLAS [45,46] and CMS [47,48] experiments in pp collisions at $\sqrt{s} = 7$ TeV. The large amount of data at the LHC allows precision tests of diphoton production. The ATLAS data have been compared to the following predictions: Pythia [29] and Sherpa [49] MC in which LL parton showers are matched to LO matrix elements, fixed order calculations at NLO from DIPHOX+2GammaMC [32,50] and with resummation of soft gluons from ResBos [51–53] at NLO+NNLL accuracy and 2γNNLO [54] calculations at NNLL+NNLO accuracy. For the inclusive diphoton cross section, Pythia and Sherpa predictions disagree with data due to a lack of higher-order contributions whereas the fixed order calculations were consistent with data within the assigned theoretical uncertainties. Concerning the differential cross section, none of the event generators can describe the detailed shape of the kinematic distributions accurately. Figure 2.10 shows the comparison of various kinematic distributions between ATLAS data and fixed order calculations. It can be observed that 2γNNLO predictions give a much better description of data than DIPHOX+2GammaMC. Chapter 7 will describe the diphoton cross section measurements using the full data set collected by the ATLAS experiment at $\sqrt{s} = 8$ TeV.

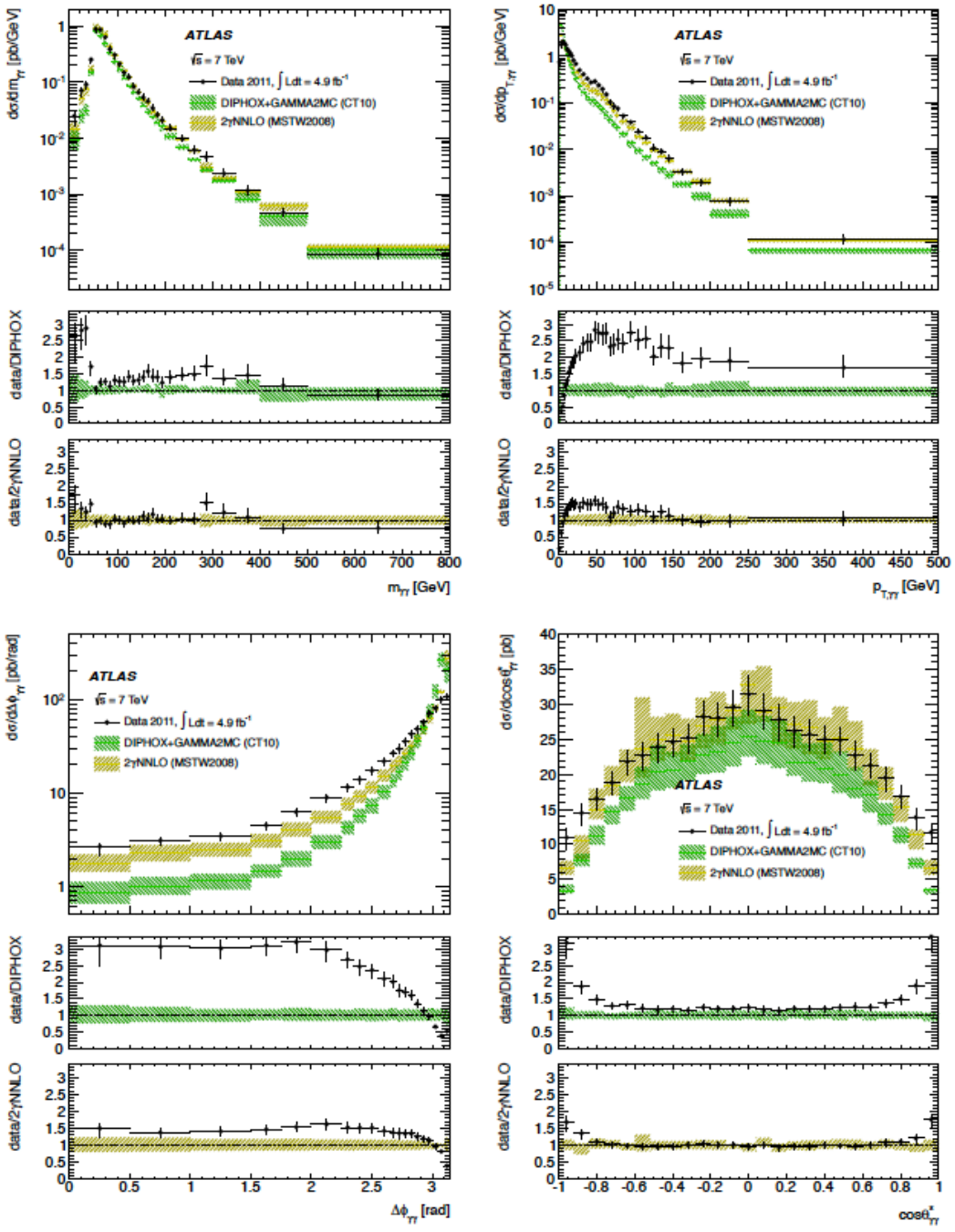

Figure 2.10: Comparison of the differential cross section between experimental data and theoretical predictions from DIPHOX+2GAMMAMC and 2γNNLO as a function of $m_{\gamma\gamma}$ (top left), $p_{\mathrm{T},\gamma\gamma}$ (top right), $\Delta\phi_{\gamma\gamma}$ (bottom left) and cos θ^*_{CS} (bottom right) from [46]. Black dots represent data with error bars denoting total uncertainties. Theoretical predictions with their uncertainties are shown as green bands for DIPHOX+2GAMMAMC and yellow bands for 2γNNLO.

Chapter 3

Experimental Apparatus

Over the last few decades, the high-energy frontier of particle physics has been dominated by collider experiments. The Tevatron, which was a circular collider with a circumference of 6 km, collided protons and anti-protons with a centre of mass energy $\sqrt{s}$ = 1.96 TeV. This $p\bar{p}$ collider was situated in the Fermi National Accelerator Laboratory and was shut down in 2011. The current largest and highest-energy collider, the LHC, is a pp circular collider with a circumference of 27 km at CERN. The LHC was operated at $\sqrt{s}$ =7 TeV from 2010 to 2011 and at $\sqrt{s}$ =8 TeV in 2012. After a long shutdown, the LHC is currently running at $\sqrt{s}$ =13 TeV. The design central mass energy for the LHC is 14 TeV.

A brief view of the accelerator complex at the Tevatron and the LHC is given in Section 3.1. Section 3.2 describes the coordinate system used in the detectors. This is followed by Section 3.3 explaining the different sub-systems of the D0 experiment at the Tevatron and the ATLAS experiment at the LHC.

3.1 Accelerator chain

3.1.1 Introduction to luminosity

In a particle collider, the interaction rate R for a given process $A + B \rightarrow X$, is related to the instantaneous luminosity $\mathscr{L}$ via the following equation:

$$R_{A+B\rightarrow X} = \sigma_{A+B\rightarrow X} \times \mathscr{L}, \tag{3.1}$$

where $\sigma_{A+B\rightarrow X}$ denotes the cross-section for $A+B \rightarrow X$. The cross section implies an intrinsic probability for an interaction to take place and includes no ingredients that can be controlled experimentally. However, the instantaneous luminosity involves ingredients that can be adjusted experimentally to enhance the interaction rate,

thus making observations and precision measurements possible. The instantaneous luminosity $\mathscr{L}$ can be written as:

$$\mathscr{L} = \frac{\mu_{vis} n_b f_r}{\sigma_{vis}}, \tag{3.2}$$

where μ_{vis} is the observed, or visible, average number of inelastic interactions per bunch crossing (BC), σ_{vis} is the visible inelastic cross section seen by a particular detector (set of detectors) with a given trigger condition, f_r represents the revolution frequency and n_b denotes the number of bunches.

3.1.2 The Tevatron

The high energies of protons and anti-protons at the Tevatron are achieved by accelerating the proton and anti-proton beams in electromagnetic fields through a series of accelerators and storage rings. Figure 3.1 shows the schematic layout of the Tevatron and the accelerator complex. The production of high-energy protons starts by ionizing hydrogen gases into H^- ions in the Cockroft-Walton pre-accelerator which subsequently accelerates these ions to 750 keV. The beam of H^- ions is then accelerated through a linear accelerator (Linac) to an energy of 400 MeV. These H^- ions are transformed to protons by passing them through a thin carbon foil that removes electrons from the H^- ions. The protons then proceed to a circular synchrotron called the booster ring and are accelerated up to 8 GeV before being transferred into the main injector. The main injector accelerates protons to 150 GeV, and the protons that are grouped into bunches are ready for injection into the Tevatron. The Tevatron ramps their energy up to 980 GeV.

The anti-protons are produced by smashing a beam of 120 GeV protons from the main injector into a nickel (Ni) target. Around 5×10^{12} protons hit the target every 1.47 seconds, and a range of particles is produced in the $p-$Ni collisions, among which approximately 5×10^7 anti-protons are collected using a mass-charge spectrometer. These collected anti-protons are cooled and accelerated to 8 GeV in the debuncher before moving to the accumulator to be ready for the next p-Ni collision. The accumulator stores anti-protons over a few hours in which the spread in energy of anti-protons and beam transverse size is decreased using the stochastic cooling method [55]. The anti-protons are periodically moved to the recycler, situated in the same tunnel of the main injector, which performs electron cooling and stochastic cooling of the anti-proton beam. They then enter the main injector and are accelerated to 150 GeV and grouped into bunches before they are injected into the Tevatron, which increases the energy of the anti-proton beam up

to 980 GeV.

There are 36 bunches in the proton (anti-proton) beam at the Tevatron, in which the time separation between each bunch in the proton (anti-proton) beam is 396 ns. The maximum instantaneous luminosity recorded at the Tevatron is over 4×10^{32} cm^{-2}s^{-1}. The proton and anti-proton beams are kept apart everywhere except at two interaction points, where they are brought into collisions at the CDF and the D0 interaction points.

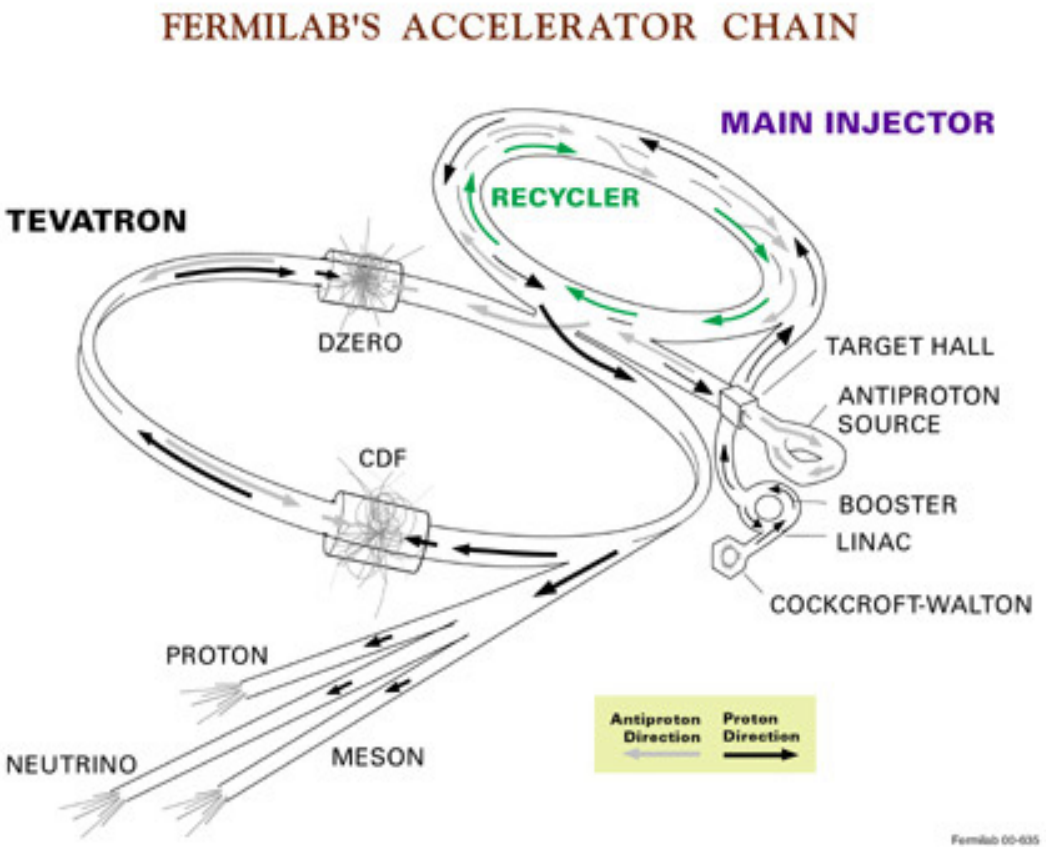

Figure 3.1: A schematic layout of the Tevatron and the accelerator complex [56].

3.1.3 The LHC

A schematic view of the LHC and the accelerator supply chain is presented in Figure 3.2. At the LHC, protons are produced by stripping electrons from hydrogen gases via acceleration through electric fields. These protons are accelerated to 500 MeV in the linear accelerator called Linac2. They are then injected into the Proton Synchrotron (PS) Booster, which ramps the energy of protons to 1.4 GeV before transfer to the PS to be accelerated to 26 GeV. These protons subsequently move to the Super Proton Synchrotron (SPS), which accelerates them to 450 GeV

ready for injection into the LHC. There were 1400 bunches in a proton beam in 2012 and each bunch was separated by 50 ns. In 2012, the LHC increased the energy of the proton beams to 4 TeV before collisions and the maximum instantaneous luminosity recorded was 7.7×10^{33} cm^{-2}s^{-1}. In comparison to the Tevatron, the LHC has already delivered 2.5 times of the integrated luminosity of the entire Tevatron lifespan within the first three years of its running at unprecedented collision energies in 2012. In 2015, the LHC was operating at $\sqrt{s} = 13$ TeV with a target instantaneous luminosity of 10^{34} cm^{-2}s^{-1}. The maximum instantaneous luminosity in 2016 has increased to 1.2×10^{34} cm^{-2}s^{-1}.

The collider tunnel consists of two parallel beam pipes that intersect at four interaction points, and each interaction point is surrounded by a particle detector. Two of these interaction points are surrounded by two general purpose particle detectors, ATLAS and CMS. The LHCb experiment is designed to study heavy flavour physics and to measure the parameters related to the asymmetry between matter and antimatter. The ALICE experiment primarily focuses on the measurements of heavy-ion collisions, in which the quark-gluon plasma produced at extreme energy densities is of great interest.

3.2 Coordinate system

Both the ATLAS and the D0 detectors employ a right-handed cylindrical coordinate system with the z-axis aligned along the beam direction[1], the y axis pointing upward[2] and the x axis pointing away from (towards) the centre of the synchrotron accelerator at the Tevatron (LHC). The geometrical centre of the detector is defined as the origin of the coordinate. Most of the components in these detectors are geometrically symmetric relative to the azimuthal angle ϕ in the transverse plane and the polar angle θ. ϕ is measured around the beam axis and defined to be zero along the x axis. The pseudorapidity, η, is defined as $\eta = -\ln\ (\tan(\theta/2))$. η is favoured over θ because differences in pseudorapidity are invariant under a Lorentz boost along the beam direction.

[1] At the Tevatron (LHC), the positive z direction is in the same direction as the protons travelling clockwise (anticlockwise) if one looks from above the ring.

[2] The positive y axis at the LHC is not exactly pointing upward with respect to the ground due to the inclination of the accelerator.

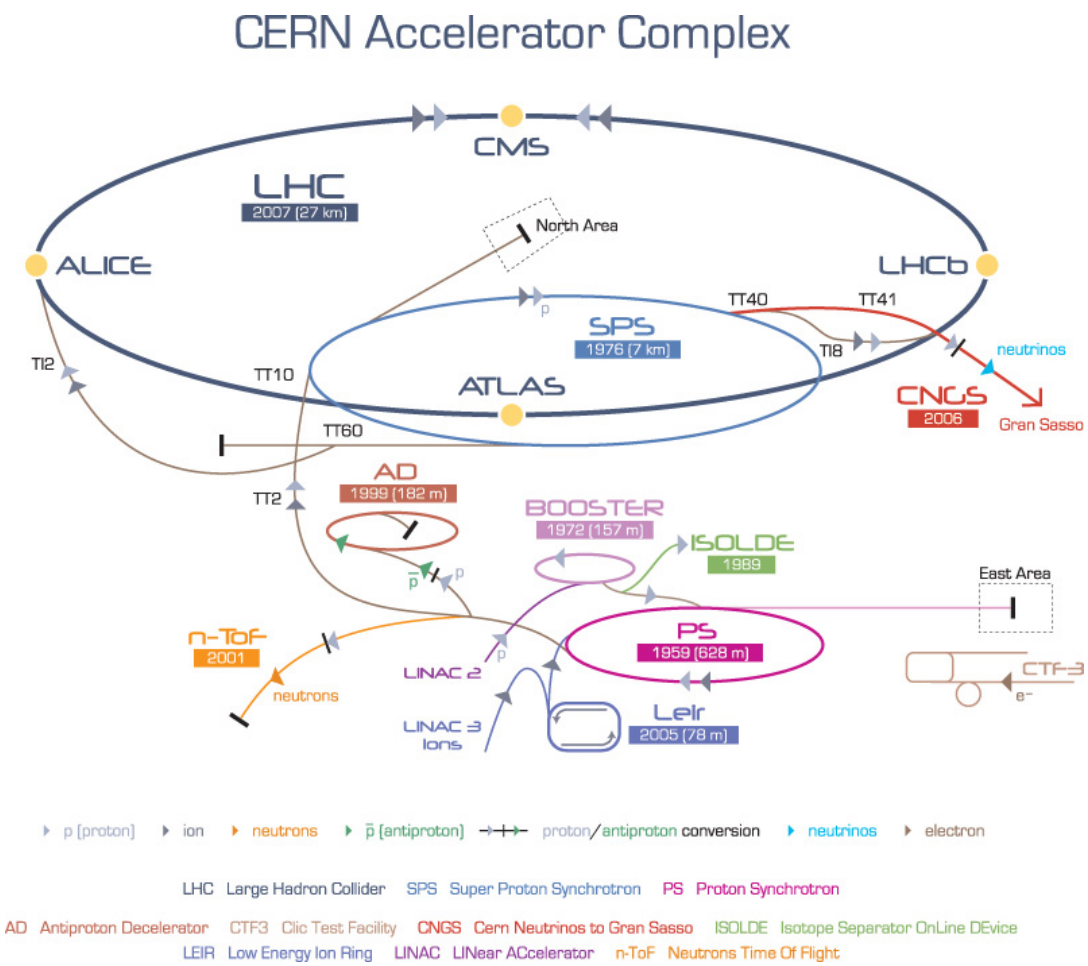

Figure 3.2: A schematic layout of the accelerator complex at the LHC [57].

3.3 The D0 and ATLAS detectors

General-purpose particle detectors such as the D0 detector (Figure 3.3) and the ATLAS detector (Figure 3.4), are typically composed of four major parts. The part closest to the interaction point is the central tracking system, which is used to measure the momentum of charged particles precisely and to reconstruct the vertices accurately in the pp ($p\bar{p}$) collisions. It is surrounded by the electromagnetic (EM) and the hadronic (HAD) calorimeters that enable measurements of the energy of both neutral and charged particles. The outermost part of the detector is the muon system, which identifies and determines the momentum of muons with high precision. The last main part is the trigger system, which selects events of interest in real time. Each part of the detector mentioned above will be discussed in the following sections. Since the work in the thesis involves both the D0 and the ATLAS detectors, only the detector parts that are relevant to the specific analysis are explained in more detail. A more complete description of the D0 and the ATLAS detectors

can be found in [58] and [59], respectively. The detector performance relevant to the analysis presented in the thesis is briefly discussed in Chapter 4.

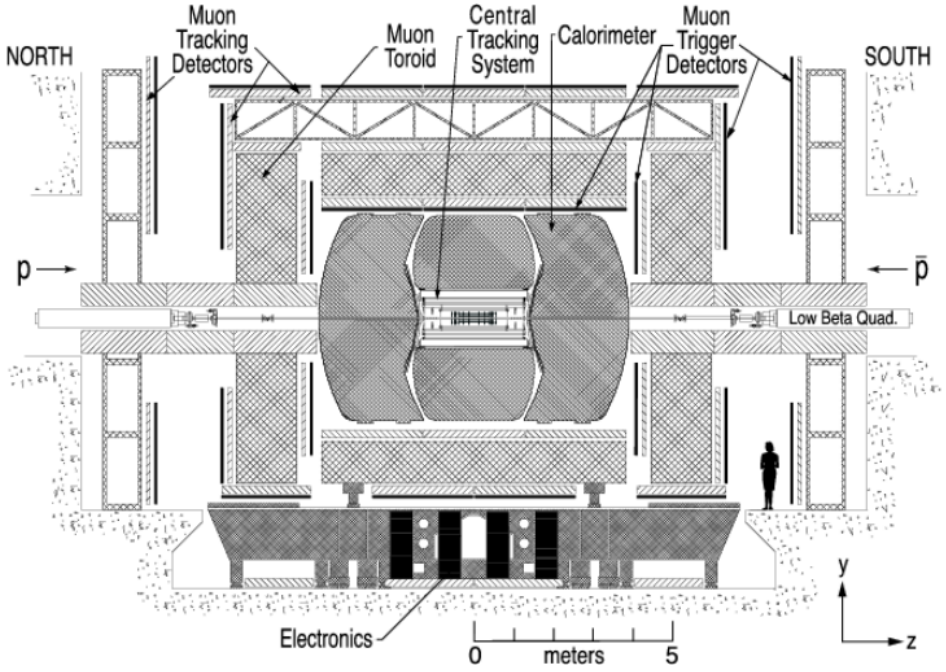

Figure 3.3: A diagram of the D0 Run II detector viewed from the centre of the collider. The main detector components are labeled [58].

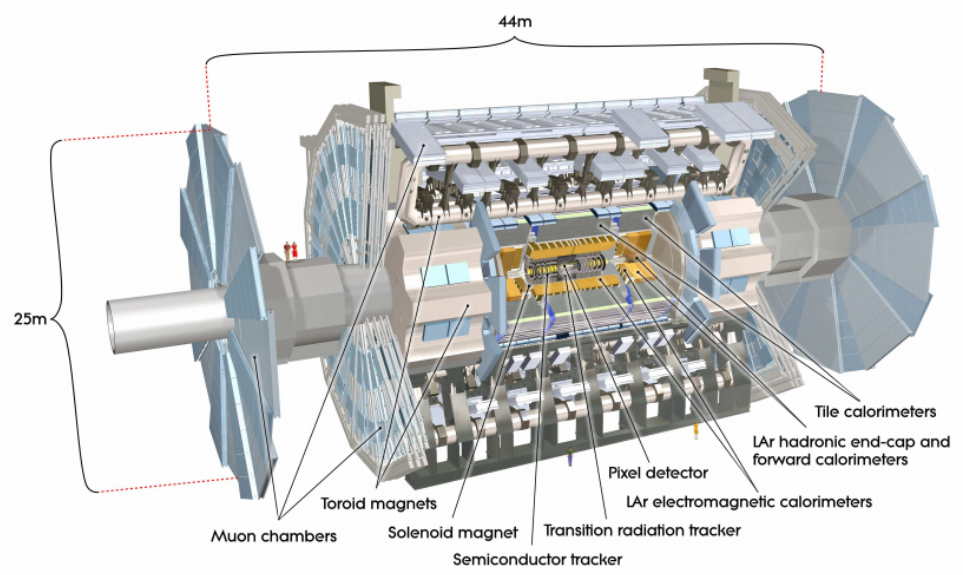

Figure 3.4: A diagram of the ATLAS experiment with major detector sub-systems labeled [59].

3.3.1 Central tracking system

Inside the D0 and the ATLAS detectors, the beam pipe is made of a thin layer of beryllium to reduce scatterings of particles produced in the collisions. The whole central tracking system is immersed in a 2 T solenoidal magnetic field, which is aligned along the beam direction. The magnetic field causes the trajectory of charged particles to bend in the ϕ direction. The momentum of these charged particles can be determined by measuring the curvature of the trajectory.

D0 experiment

The D0 central tracking detector shown in Figure 3.5 is made up of two key components. Closest to the beam pipe is the Silicon Microstrip Tracker (SMT), which is surrounded by the Central Fibre Tracker (CFT).

The SMT is composed of six barrel modules interspersed with six disks (F disks), covering the central region in z. There are three additional F disks followed by two large diameter disks (H disks) on each side of the end-cap. The outer radius of the F disks and H disks is approximately 10 cm and 26 cm. Such a layout of barrel modules and disks allows a wide coverage of measurement for tracks that can travel either perpendicular to or in the direction of the beam direction. An additional radiation-hard silicon layer, layer-0, was inserted close to the beam pipe to improve tracking and vertex reconstruction in 2006.

The CFT consists of scintillating fibres on eight cylinders. Each of the eight cylinders contains two doublet layers. One doublet layer is along the beam direction and the other doublet layer is at a stereo angle of either plus or minus three degrees with respect to the beam axis. The CFT can measure trajectories of charged particles up to $|\eta| \sim 1.7$. The passage of a charged particle in the CFT causes emission of photons which are transported by fibres and subsequently detected in the Visible Light Photon Counters (VLPCs).

The preshower detectors are split into two components, the Central Preshower Detector (CPS) covering the region $|\eta| < 1.3$ and the Forward Preshower Detector (FPS) covering the region $1.5 < |\eta| < 2.5$. The CPS and the FPS are located between the central tracking detector and the calorimeters.

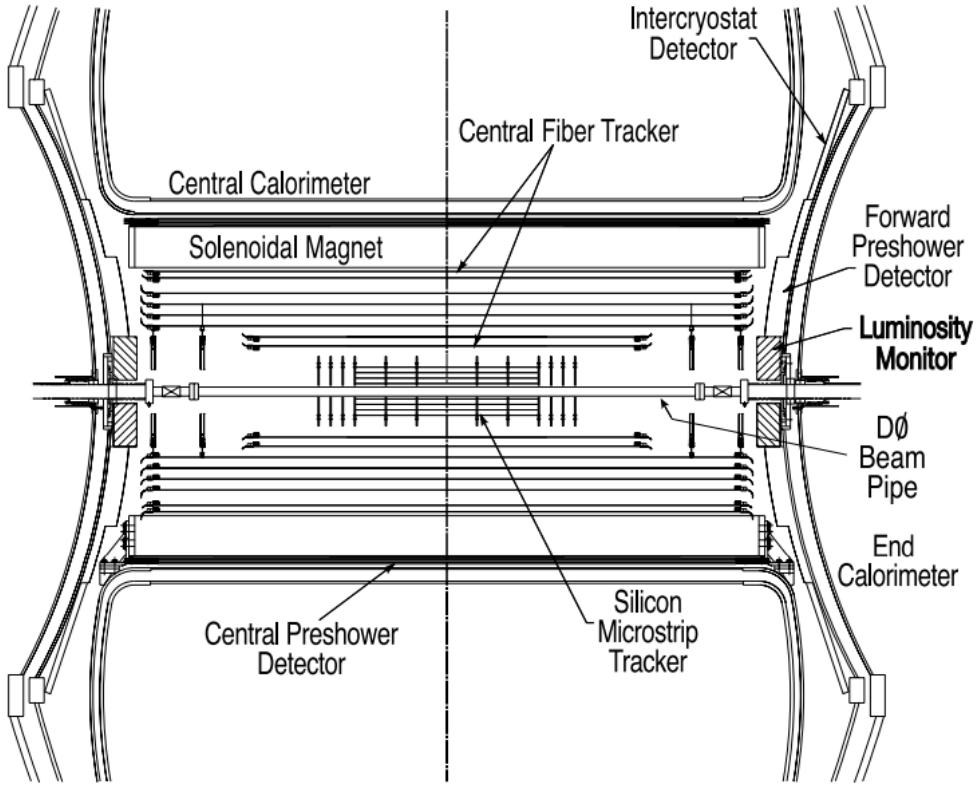

Figure 3.5: A diagram of the D0 central tracking system [58].

ATLAS experiment

The ATLAS Inner detector (ID) contains three main sub-detectors, as presented in Figure 3.6. The innermost sub-detector is the pixel detector, followed by the Semi-Conductor Tracker (SCT) and the Transition Radiation Tracker (TRT).

The pixel detector is comprised of three concentric barrel layers and two sets of three end-cap disks with 1744 silicon modules. Each module is made up of

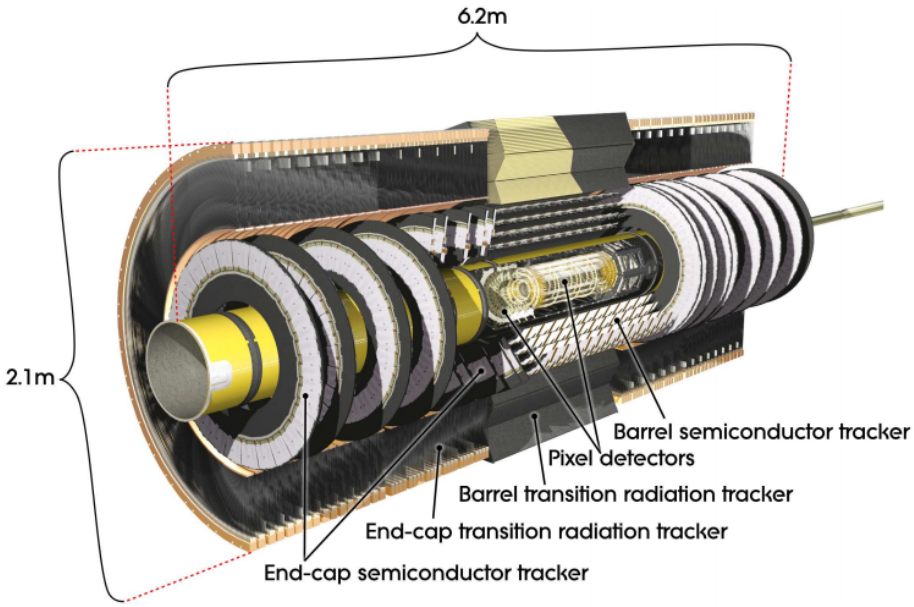

Figure 3.6: A diagram of the ATLAS inner tracker [59].

47232 pixels, each of which measures 50×400 μm^2. Such a high granularity ensures an excellent spatial resolution that is required to reconstruct the large number of vertices in pp collisions. The barrel layers cover the region up to $|\eta| \sim 1.7$ and provide full coverage in ϕ. The endcap disks cover the pseudorapidity range of $1.7 < |\eta| < 2.5$. The layer closest to the beam line in the pixel detector is the so-called b-layer, which provides important information on identification of long-lived particles such as b-hadrons (b-tagging). A fourth layer, the insertable b layer [60], was installed in 2015 to improve the reconstruction of vertices and b-tagging.

Surrounding the pixel detector is the SCT detector, with four layers of silicon microstrip modules in the barrel and nine disk layers in each of the endcaps. There are 2112 SCT modules in the barrel and 1976 SCT modules in the endcap, each of which contains two pairs of sensors arranged back-to-back with each sensor containing 768 strips. The strips in the barrel layer lie along the beam axis whereas the strips of endcap disks are aligned radially. This arrangement allows a precise determination of the ϕ coordinate of the produced charged particles.

The outermost part of the ID, the TRT, is made up of drift tubes of diameter 4 mm which are filled with a gas mixture containing mainly Xenon. There are approximately 52500 straws in the barrel, arranged in 73 layers, which are aligned parallel to the beam direction. The endcap contains 160 planes of straws, which are arranged radially. The drift tubes are interspersed with radiator materials. When a charged particle traverses the TRT, in addition to the ionization of the gas mixture,

which provides tracking information, ultra-relativistic particles passing through the boundary between radiator material and the drift tubes radiate photons that intensify the signal. The strength of the transition radiation is inversely proportional to the mass of the charged particle, thus a measurement of transition radiation can be used to distinguish electrons from pions.

3.3.2 Calorimeter system

Calorimeters are built to measure the energy of particles that interact with the calorimeter medium through absorption. The calorimeter system is comprised of the electromagnetic calorimeters (ECAL) and the hadronic calorimeters (HCAL), each of which is contained within its own cryostat that maintains the operating temperature at around 90 K. It should be noted the tile calorimeter is not housed inside its own cryostat at the ATLAS experiment. The calorimeter cells, arranged in modules, contain alternating layers of absorbing material and sampling material (e.g. liquid argon). Absorbing materials are used to induce showers into secondary particles, the energy of which can be collected and measured via ionisation of the sampling materials. The ECAL are used to measure the energy of particles (electrons and photons) that interact with the calorimeter material via electromagnetic interactions. When electrons or photons traverse the ECAL, which are made of heavy-nuclei (e.g. lead), electromagnetic showers of electrons and photons via photon Bremsstrahlung and pair production are induced. Similarly to the ECAL, the HCAL measure the energy of hadrons that interact with the calorimeter material via the strong interaction. Ultra-relativistic hadrons interact with the heavy nuclei material, which subsequently produces hadronic showers. These secondary particles produced in the EM or HAD showers ionize the active medium (e.g. liquid argon), in which the charge is collected using copper electrodes. The energy of the passing particles can be determined by integration over these collected charges. Both liquid argon (LAr) and scintillation tiles are used as sampling material in the calorimeters at the D0 and ATLAS experiments.

D0 experiment

The D0 calorimeter system as shown in Figure 3.7 is split into three sections, the Central Calorimeter (CC), which covers the region $|\eta| < 1$ and two Endcap Calorimeters (ECs), which extend the coverage up to $|\eta| \sim 4$. There is little or no EM coverage in the pseudorapidity region $1.1 < |\eta| < 1.5$. The region is further instrumented with the so-called Inter-Cryostat Detector (ICD) composed of scintillation tiles.

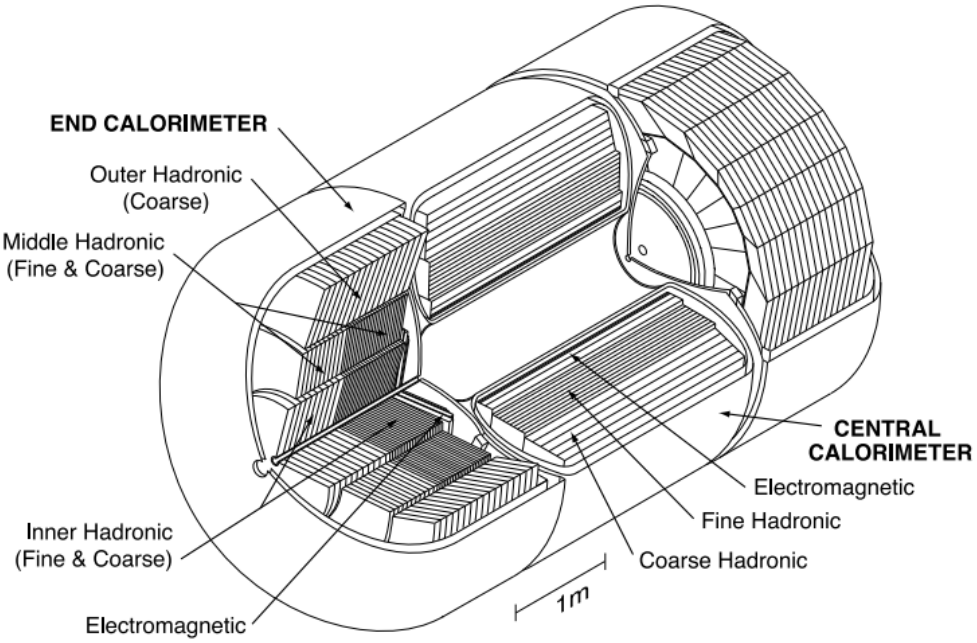

Figure 3.7: An isometric view of the D0 calorimeter system [58].

The ECAL is made up of four layers of calorimeter cells in which the absorbing material is depleted uranium. The total thickness of the absorber is 19.2 X_0 in the CC and 21.7 X_0 in the EC, where X_0 represents one radiation length. Each layer has a granularity of 0.1 $\times$ 0.1 in η and ϕ apart from the third layer, which has a finer granularity of $\eta \times \phi = 0.05 \times 0.05$. The third layer was designed to be at the maximum of the EM shower, an excellent granularity in this layer provides a high spatial resolution that allows precision measurements for electrons and photons. However, there are ϕ gaps in the calorimeters due to poorly instrumented CC module boundaries that can degrade the EM energy response.

Surrounding the ECAL are three layers that make up the Fine Hadronic Calorimeter (FH), where the absorber material in these layers is 6 mm thick uranium-niobium alloy. The FH is followed by the outermost layer of the calorimeter, the Coarse Hadronic Calorimeter (CH). The absorbers in the FH layers are 46.5 mm thick copper plates in the CC and brass plates in the EC. The calorimeter cells in the FH and CH have an angular size of 0.1 $\times$ 0.1 in η and ϕ, which is increased to 0.2 $\times$ 0.2 at high $|\eta|$.

ATLAS experiment

The ECAL consist of accordion-shaped electrodes and lead absorbers in the barrel and endcap regions that give full coverage in ϕ without any cracks or gaps. The barrel calorimeters cover the pseudorapidity region $|\eta| < 1.475$. Two wheels are arranged at each endcap, in which an inner wheel covers $1.375 < |\eta| < 2.5$ and

an outer wheel covers $2.5 < |\eta| < 3.2$. The barrel ECAL have a thickness between 22 X_0 and 33 X_0 whereas the endcap ECAL provide more than 24 X_0 thickness of material. The ECAL contain three active layers in the region $|\eta| < 2.5$ and two layers extending the coverage to $|\eta| \sim 3.2$, which are designed for precision measurements of electrons and photons. The granularity of the three layers is different as presented in Figure 3.8. The first layer is finely segmented such that it ensures the determination of the photon position. The second layer has a granularity of $\eta \times \phi = 0.025 \times 0.025$. The photon cluster in the first and second layers of the ECAL can be used to determine the η direction of photons. The region $1.37 < |\eta| < 1.56$ gives a poor momentum resolution due to additional interactions with cables in the transition region between the barrel and endcap cryostats, thus is excluded in the diphoton cross section measurement in Chapter 7.

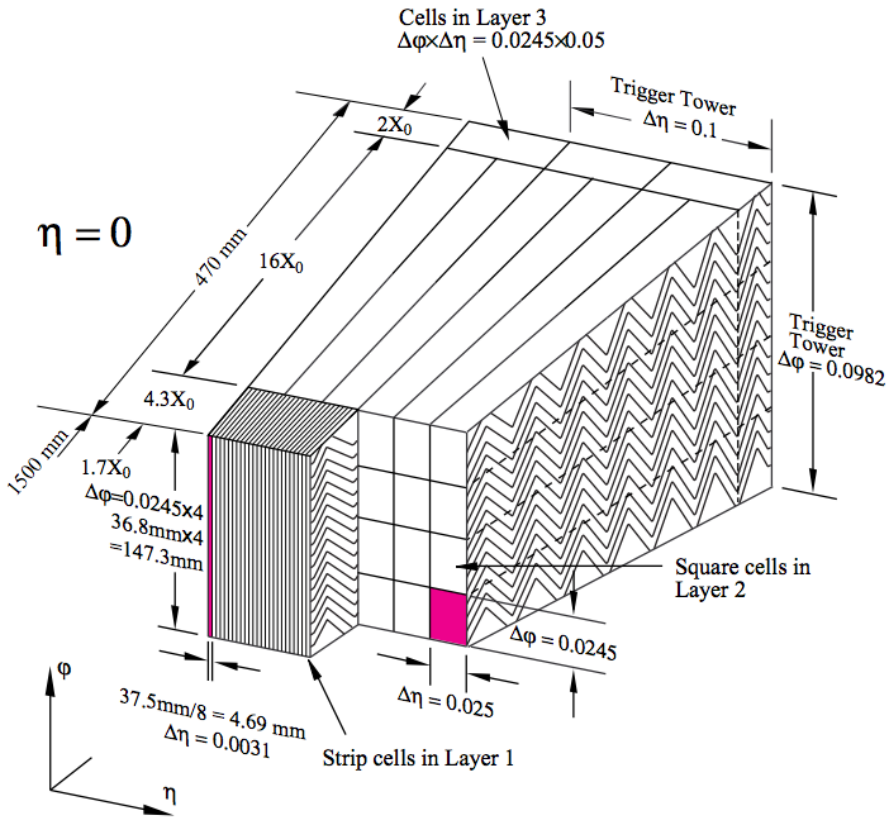

Figure 3.8: A sketch of an ECAL module in the barrel illustrating granularity in η and ϕ of the cells in each of the three layers [59].

Outside the ECAL sits the tile hadronic sampling calorimeter (TileCal), constructed in a central barrel of 5.8 m in length and two extended barrels of 2.6 m in length, providing a pseudorapidity coverage of $|\eta| < 1.7$. Each of these barrels

is comprised of 64 wedge-shaped modules, and each module is made up of alternate layers of stainless steel as the absorbing material and scintillating tiles as the sampling material. The energy of the charged particles produced by hadronic interactions in the absorber is first absorbed by the scintillators, and then ionization of scintillator produces scintillation light, which after having their wavelength shifted by optical fibres are converted to electric signals in the photomultiplier tubes. The TileCal cells have a size of $\Delta\eta \times \Delta\phi = 0.1 \times 0.1$ in the first layer and 0.2×0.1 in the second layer. The hadronic end-cap calorimeters (HEC) use copper as the absorber material and LAr as the sampling material, and cover the pseudorapidity range of $1.5 < |\eta| < 3.5$. The angular size of the cell varies with $|\eta|$, ranging from 0.1×0.1 to 0.2×0.2 at large $|\eta|$ in the HEC. The final layer of HCAL is the forward calorimeters (FCal), which covers the region $3.1 < |\eta| < 4.9$. Each of the FCal is composed of three modules: one module using copper rods as the absorber material for electromagnetic measurements and two modules employing tungsten rods for hadronic measurements. All three modules use LAr as the sampling material and share the same cryostat systems as the other endcap calorimeters.

3.3.3 Muon detectors

Muons are the only ionizing particles that can penetrate the calorimeter system. The muon system is the outermost component of the ATLAS and the D0 detectors, and it consists of three major parts: toroidal magnets providing a non-uniform magnetic field, muon chambers, which are used to measure tracks of outgoing muons with high spatial resolution, and muon triggering chambers with excellent time resolution. The toroidal magnets at the D0 experiment produce an approximate 1.8 T magnetic field whereas at the ATLAS experiment the average field strength provided by the barrel and the endcap toroids is 0.5 T and 1 T respectively. The toroidal magnets allow the measurement of the muon momentum independent of the central tracking system and bend the muons in the η direction. The muon hits in the η direction are typically measured by drift tubes filled with a gas mixture, in which the passage of charged particles through the tubes cause ionisation of the gas and the resultant charge can be collected.

D0 experiment

The D0 muon system can be divided into two sections: the central ($|\eta| < 1.0$) muon system made up of the Proportional Drift Tubes (PDTs) and scintillation counters and the forward ($1.0< |\eta| < 2.0$) muon system which contains Mini Drift Tubes (MDTs) and scintillation counters. The PDTs are filled with a gas mixture

dominated by argon. The drift tubes and scintillation counters are arranged into three layers, where the A layer sits inside the toroids and the B and C layers are outside. For the central muon system, the PDTs are instrumented with cosmic cap and cosmic bottom scintillation counters on the outer layer, as shown in Figure 3.9. The bottom scintillation counters have reduced coverage to allow for the detector support structures. The A layer PDTs are covered with $A\phi$ scintillation counters. These scintillation counters provide input for the trigger system. The trigger scintillation counters are mounted on all three layers in the forward muon system. The muon system in both the central and forward region is split into eight octants in ϕ, which are poorly instrumented in the boundaries between neighbouring octants. *ATLAS experiment*

The ATLAS Muon Spectrometer (MS) is composed of Monitored Drift Tubes (MDTs) in both the barrel and endcap regions, complemented by the Cathode Strip Chambers (CSCs) in the forward pseudorapidity region ($2.0< |\eta| < 2.7$). The MS is divided into eight octants in ϕ, each of which is further split into two sections with slightly different lateral extensions. Such a layout enables minimization of detector gaps in ϕ. The trigger chambers, which are located next to the muon tracking chambers, comprise of the Resistive Plate Chambers (RPCs) in the barrel region and the Thin Gap Chambers (TCGs) in the endcap regions.

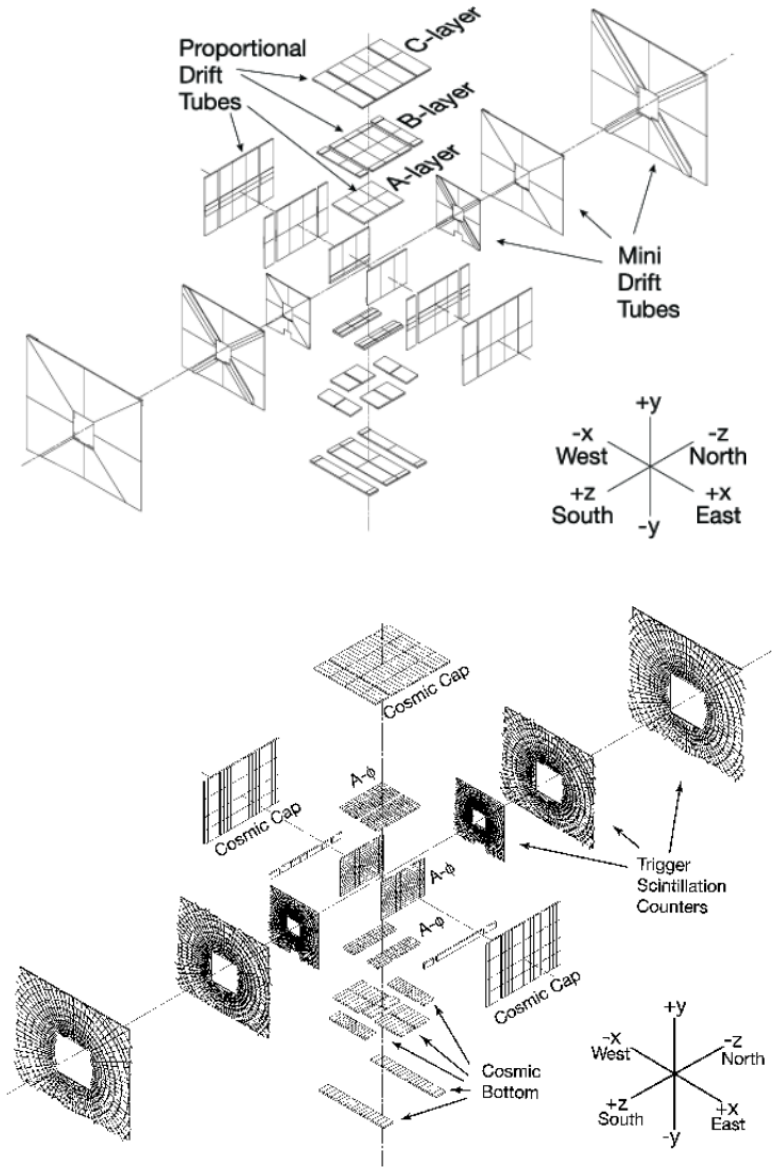

Figure 3.9: An exploded isometric view of the muon wire (top) and scintillator (bottom) systems [58].

3.3.4 Trigger system

With the beam crossing frequency at the Tevatron and the LHC reaching 1.7 MHz and 40 MHz separately, writing every event to the disk at this rate would not be possible. Therefore it is important to decide in real time which event is the most interesting one to keep. A three level-trigger system is employed by the D0 and the ATLAS experiments to reduce the event rate to around 100 Hz and 200 Hz respectively. The D0 analysis in the thesis relies on the muon trigger that requires the presence of two muons with high transverse momenta whereas the ATLAS analysis utilises the diphoton trigger that requires the presence of two loosely identified photons with certain transverse energy thresholds.

Level-1 trigger

The level-1 trigger (LVL1) is hardware based, which performs the primary selection of interesting events using the granularity information from a subset of detectors within a short time.

D0 experiment

The LVL1 at the D0 experiment reduces the event rate to around 2 kHz. A decision on whether the event is interesting enough is made within 4.2 μs. This is achieved via the Level-1 Central Track Trigger (L1CTT), the Level-1 Calorimeter Trigger (L1Cal) and the Level-1 Muon Trigger (L1Muon). The CTT takes input from the CFT and preshower detectors to look for predefined patterns consistent with the passage of a charged particle with transverse momentum above a specified threshold. The L1Cal, consisting of EM and HAD trigger towers, places requirements on the transverse energy in individual towers to select calorimeter objects such as electrons, photons, jets and hadronically decaying τ leptons. The L1Muon reconstructs muon objects using information from wire and scintillator muon chambers as well as inputs from the L1CTT.

ATLAS experiment

At the ATLAS experiment, the event rate is decreased to 75 kHz using the LVL1. The decision to retain an event is made within 2.5 μs. The LVL1 performs the event selection using a subset of the ATLAS detectors (e.g. calorimeters and muon chambers), based on certain requirements of the signatures of physics objects with a minimum transverse momentum. Further requirements can be made in terms of the combinations of these signatures of physics objects. Once a physics object is selected by the L1V1, a region of interest (RoI) around the object defined in η and

ϕ is taken as input for further processing.

Level-2 trigger

The Level-2 trigger (LVL2) refines the object reconstruction obtained from the LVL1 and combines L1V1 objects of all sub-detectors to make a global decision.

D0 experiment

The LVL2 is both hardware and software based at the D0 experiment, which has an accept rate of 1000 Hz that requires a decision time of 100 μs per event. The silicon track trigger (STT) is included in the LVL2 trigger decisions on physics objects. The Level-2 Muon Trigger (L2Muon) can classify muons into three qualities of *loose, medium,* and *tight* according to the number of wire chamber and scintillator hits in the muon system.

ATLAS experiment

Unlike the D0 LVL2, the LVL2 system at the ATLAS experiment is software-based. The accept rate at LVL2 is around 3500 Hz with an average processing time of 40 ms. The LVL2 algorithms make use of all the available information within the RoI to improve the reconstruction of physics objects. The Level-2 defines two operation points (*loose, tight*) for photon identification qualities based on requirements on the shower shape variables within the RoIs in the calorimeters.

Level-3 trigger

The Level-3 Trigger (LVL3) is the final tier of the trigger system, which utilises simplified offline algorithms and the complete detector information with full granularity to reconstruct the selected physics objects. At the D0 experiment, the event rate is further reduced to 100 Hz with an average event size of 150 KB. The LVL3 system at the ATLAS experiment, referred to as the Event Filter, records the events at a rate of 200 Hz with an average event size of 1.5 MB.

Chapter 4

The Reconstruction of physics objects

4.1 Charged particle tracks

Charged particle tracks in the ID are reconstructed using the hit information from the central tracking system. The track of a charged particle can be defined in terms of the following parameters: its curvature (proportional to q/p_T), the dip angle[1] ($\tan\lambda$) made with a plane perpendicular to the magnetic field and coordinates of the point of closest approach to the interaction point. The resolution of the curvature can be written as:

$$\sigma(\frac{q}{p_T}) = a \oplus \frac{b}{p_T}, \tag{4.1}$$

where the constant term a is related to the intrinsic resolution of the detector[2] and b indicates effects arising from multiple Coulomb scattering. The tracks of charged particles are used as input for the reconstruction of vertices for an event and the primary vertex is usually chosen as the vertex with the largest sum of p_T^2 of all tracks.

[1] The sum of the dip angle and θ is $\pi/2$.

[2] The intrinsic resolution of the detector is associated with the number of hits, the length of the central tracking system, the magnetic field strength and the spatial resolution of individual hits.

4.2 Muon reconstruction at the D0 experiment

4.2.1 Muon reconstruction

The reconstruction of muons uses a combination of information provided by the central tracking system and the muon system. It starts with track segments in the three layers of the muon system, which are combined to give a local muon. The local muon can be then matched to the tracks in the central tracking system. An alternative algorithm is to begin with a charged particle track in the ID and to require its energy deposits in the calorimeter to be consistent with the passage of a minimum ionizing particle.

4.2.2 Muon identification

At the D0 experiment, n_{seg} represents the type of the local muon track. $n_{seg} \geq 0$ represents a local muon matched to the central track while $n_{seg} < 0$ denotes a muon without a match to the central track. Different types of muon track qualities are associated with distinctive values of n_{seg} defined as follows:

- $n_{seg} = 0$ inner track that is matched to a muon like signature in the calorimeter, or a few muon hits.
- $n_{seg} = 1$ muon hits with A layer segment only.
- $n_{seg} = 2$ muon hits with BC layer segments only.
- $n_{seg} = 3$ muon hits throughout all three layer segments.

The local muon can be further categorized into *loose*, *medium* and *tight* according to the number of scintillator and wire chamber hits as well as n_{seg}.

The muons produced in the Drell-Yan process are required to be isolated to discriminate against background processes such as semi-leptonic decay of heavy flavour quarks and mesons. The relevant isolation variables used in the selection of the muons are calorimeter isolation $\mathscr{I}_{cal}$ and track isolation $\mathscr{I}_{trk}$. $\mathscr{I}_{cal}$ is defined as

$$\mathscr{I}_{cal} = \frac{\sum_i E_T^i}{p_T^\mu},\ 0.1 < \Delta R < 0.4, \tag{4.2}$$

where E_T^i is the transverse energy of the calorimeter cell i excluding the muon itself and $\Delta R = \sqrt{(\Delta\phi)^2 + (\Delta\eta)^2}$ is the separation between the calorimeter cell i and the muon direction in η and ϕ. $\mathscr{I}_{trk}$ is defined as

$$\mathscr{I}_{trk} = \frac{\sum_i p_T^i}{p_T^\mu},\ \Delta R < 0.5, \tag{4.3}$$

where p_T^i is the transverse momentum of track i excluding the muon itself.

4.3 Photon reconstruction at the ATLAS experiment

4.3.1 Photon reconstruction

Photons and electrons are reconstructed from clusters of energy deposits in the ECAL. In order to reconstruct clusters, the ECAL can be split into a grid of $N_\phi \times N_\eta$ towers, each of which has an angular size of 0.025×0.025 in η and ϕ. The reconstruction of clusters is performed using a sliding window algorithm with a fixed window size that corresponds to 3×5 towers in η and ϕ respectively. A pre-cluster is formed if the sum of the transverse energy within the 3×5 window is above 2.5 GeV, which together with the tracking information provided by the ID gives the final EM cluster. A seed EM cluster matched to at least one well-reconstructed ID track is identified as an electron, otherwise it is considered as a photon. Both converted and unconverted photons are retained in the analysis. A converted photon refers to a seed EM cluster matched with one or two ID tracks that originate from a conversion vertex. An unconverted photon is defined as a seed EM cluster with no matched ID tracks.

The electron cluster is subsequently rebuilt with 3×7 towers in the barrel region and 5×5 towers in the endcap region. For photon clusters in the barrel region, a 3×7 cluster size is associated with converted photons and a 3×5 cluster size is used for unconverted photons. As for the endcap region, EM clusters for converted and unconverted photons are reconstructed with 5×5 towers. The total energy of reconstructed electrons or photons is determined by the EM cluster energy, the energy deposited in the dead material in front of the ECAL and the energy leakage outside the cluster window and beyond the calorimeter.

The energy resolution of a sampling calorimeter can be approximated by

$$\frac{\sigma_E}{E} = C \oplus \frac{B}{\sqrt{E}} \oplus \frac{A}{E}, \tag{4.4}$$

where $\oplus$ corresponds to addition in quadrature and the three terms are dependent on η. The constant term, C ($\sim 0.7\%$), arises due to residual non-uniformities (e.g. dead material) in the energy response of the sampling calorimeter. B represents the sampling term, which takes account of the statistical fluctuations of the observed number of particles that produce the calorimeter signal used in the energy measure-

ment. B is around 10% at low $|\eta|$ but becomes large in the forward $|\eta|$ region due to the presence of additional material. A is the noise term to take into account of the electronic noise in the detector, which is around 0.35 GeV for $\eta \sim 0$. For low-energy EM clusters the energy resolution is determined by the noise term whereas the constant term dominates at high energies.

The energy response of electrons and photons is calibrated using a set of techniques described in [61]. A MC-based calibration associates the observed properties of EM clusters with the true electron or photon energy based on a Multi-Variate Analysis (MVA) [62]. It requires a reliable description of the detector geometry as well as interactions between particles and detector materials in the MC simulation. Prior to the MC-based calibration, corrections are determined and applied to take into account differences in energy response between data and simulation for specific regions of the detector [63]. The MC-based calibration is then applied to the reconstructed EM clusters from both the collision data and the MC, and afterwards the residual non-uniformities in energy response are corrected in data. The final step of the calibration procedure involves the absolute energy scale determination, which is achieved by comparison of the invariant mass distribution in $Z \to e^+e^-$ events between data and MC.

4.3.2 Photon identification

Two sets of identification criteria with increasing discrimination power against hadronic background, Loose and Tight (**T**), are developed based on the energy leakage into the HCAL and longitudinal and transverse shower profiles in the ECAL. The Loose requirement mainly uses the information in the middle layer of ECAL and the hadronic leakage into the HCAL. The Tight selection consists of nine discriminating variables defined as follows:

- Hadronic leakage:
  - R_{had}: the ratio of E_{T} in the first layer of the hadronic calorimeter to the E_{T} of the EM cluster. In the pseudorapidity range $0.8 < |\eta| < 1.37$, which is not covered by the first hadronic layer, the total hadronic E_{T} to the EM E_{T} ratio is used.
- The middle layer of ECAL:
  - R_{η}: the ratio of the energy in 3×7 cells to that in 7×7 cells.
  - w_2: the lateral width of the shower calculated in a window of 3×5 cells using the energy weighted sum over all cells.

- R_ϕ: the ratio of the energy deposit in 3×3 cells to the one included in 3×7 cells.

- The first layer of ECAL ("strips"):

  - $w_{s\,3}$: the shower width for three strips around the strip with the highest energy deposited, using the energy weighted sum over the total energy contained in the three strips.

  - $w_{s\,\mathrm{tot}}$: the total lateral shower width determined with the energy weighted sum over cells in a window corresponding to the cluster size.

  - F_{side}: the ratio of energy outside a core of 3 central strip cells, but within 7 strip cells, to the energy in the core of 3 central strip cells.

  - ΔE: the difference between the energy of the strip with the second largest energy deposited and the energy of the strip with the smallest energy deposited between the two leading strip cells.

  - E_{ratio}: the ratio of the energy difference between the largest and second largest energy deposit to the sum over these two.

The selection criteria on the shower-shape variables are developed in seven pseudorapidity bins to account for variations in the distribution of the material before the ECAL and in the calorimeter geometry. These are optimised separately for unconverted and converted photons to take into account the different evolutions of showers between them.

The hadronic background is further reduced by requirements on the following isolation variables. In addition, these isolation requirements suppress the contributions from fragmentation photons.

Calorimeter isolation

The topological calorimeter isolation energy $E_{\mathrm{T}}^{\mathrm{iso}}$ [64] is determined by summing over the transverse energy of uncalibrated positive-energy topological clusters within a cone of $\Delta R < 0.4$ around the candidate photon. The photon energy within a window size of 5×7 towers is excluded from the calculation of $E_{\mathrm{T}}^{\mathrm{iso}}$. The topological clustering algorithm serves as a noise suppression algorithm, which keeps only those cells with a considerable energy deposit and their neighbouring cells. A detailed description of the topological cluster algorithm is given in [65].

When the photon energy within a window size of 5×7 towers is excluded to calculate the calorimeter isolation energy, an amount of the photon energy, which

increases with E_{T}^{γ}, leaks outside the window. A leakage correction evaluated using the single photon MC is therefore applied to the calorimeter isolation energy. The calorimeter isolation energy is also corrected per event for the energy deposits from the underlying event and pile-up using the techniques developed in [66, 67].

Track isolation

The track isolation is defined as the scalar sum of the p_T of the tracks with $p_T > 1$ GeV within a cone of $\Delta R < 0.2$ around the photon candidate. Only tracks consistent with originating from the diphoton vertex are used and the conversion tracks associated with a converted photon are subtracted.

Chapter 5

Drell-Yan ϕ^*_η distribution measurement with the D0 detector

In this chapter, measurements of the shape of the ϕ^*_η distribution, $(1/\sigma)(d\sigma/d\phi^*_\eta)$, in bins of dimuon invariant mass $M_{\ell\ell}$ and boson rapidity $|y|$, are presented. An outline of the measurement is described as follows:

- Measure the normalised distribution of ϕ^*_η in four dimuon invariant mass regions: $30 < M_{\ell\ell} < 60$ GeV, $70 < M_{\ell\ell} < 110$ GeV, $130 < M_{\ell\ell} < 300$ GeV and $300 < M_{\ell\ell} < 500$ GeV, where the $30 < M_{\ell\ell} < 60$ GeV region is referred to as the low-mass region and the $70 < M_{\ell\ell} < 110$ GeV region as the peak region and the remaining as the high-mass region. These are the first measurements of the ϕ^*_η distribution away from the Z-mass peak region.

- For the low-mass and the peak region, the measurement is made in two dimuon rapidity bins: $|y| < 1$ and $1 < |y| < 2$. The high-mass region measurement is performed only in the inclusive rapidity region due to a lack of statistics. This chapter mainly focuses on the low-mass and the updated peak region measurement that I have performed.

- After the background subtraction, data are corrected back to the same kinematic measurement region at the particle level after final state radiation (FSR).

- The corrected data distributions of ϕ^*_η are compared to two NNLL+NLO predictions including resummation of multiple soft gluons, one from ResBos with the QED radiative corrections from PHOTOS [68] and the other using resummation at NNLL accuracy and the NLO calculation from MCFM [34,35].

- The updated peak region measurements of the normalised ϕ^*_η distributions using the complete D0 data in the dimuon channel are also compared to the

previously published D0 measurements [25] using both dielectron and dimuon channels detailed in Section 2.6.2.

As already mentioned in Section 2.6.2, ϕ^*_η is highly correlated with $a_T/M_{\ell\ell}$. The width of the p_T^{ll} distribution is directly proportional to the logarithm of $M_{\ell\ell}$ due to the harder radiations from the initial partons required to produce heavier dilepton states [18]. Thus the width of ϕ^*_η decreases with increasing $M_{\ell\ell}$ and these measurements of ϕ^*_η in various dimuon mass regions can be used to validate this particular feature of the predictions. In addition, measuring the ϕ^*_η shape in various mass and rapidity regions allows the x dependence of the non-perturbative functions implemented in RESBOS to be tested. Particularly, higher order EW corrections and QCD corrections might become important at large values of ϕ^*_η in the dimuon mass region away from the Z-mass peak. The low-mass region measurements are sensitive to the small-x effects. A significant systematic uncertainty in high-mass final states such as in the $t\bar{t}$ system arises due to modelling of initial state gluon radiations. A measurement of ϕ^*_η distributions in the high-mass region can be used to verify the modeling of gluon radiations in event generators.

There are two main motivations of measuring the shape of ϕ^*_η distributions rather than absolute differential cross-section measurements. Firstly, the overall scale uncertainties are cancelled because they are fully correlated between bins of $d\sigma/d\phi^*_\eta$ and total cross-section σ. For instance, the luminosity systematic uncertainty is cancelled when performing the shape measurement of ϕ^*_η distributions. Secondly, most of the information, which can be used to tune the free parameters in non-perturbative formulations or parton showers, remains in the normalised ϕ^*_η distribution.

The data are corrected to the particle level muon after FSR, known as a "bare" muon, to mimic the muon track reconstruction in the detector. Apart from the requirement on the invariant mass and dimuon rapidity, the following common kinematic requirements are applied at the particle level: $p_T > 15$ GeV and $|\eta| < 2$. In the low-mass region, the requirement on p_T of one of the muons is lowered to 10 GeV and the maximum allowed transverse energy of any radiated photon E_T^γ is 14 GeV.

The particle level electron in the previously published D0 ϕ^*_η analysis is defined as the four-vector sum of the EM particles, i.e., photons and electrons, within a cone of $\Delta R < 0.2$. This is referred to as the "dressed" electrons to mimic the way in which electrons are reconstructed in the D0 detector. The kinematic requirements in the previously published dielectron channel are $70 < M_{\ell\ell} < 110$ GeV, $p_T > 20$ GeV and $|\eta| < 3$ excluding the crack region $1.1 < |\eta| < 1.5$. Besides, the measurement was performed in three rapidity bins with an additional rapidity bin $|y| > 2$. In addition to the "bare" and "dressed" particle level definitions, the "Born" level refers to

leptons before any QED radiation.

5.1 Event selection

5.1.1 Data samples

The analysis includes data recorded throughout the complete Run II period. Events with their corresponding data-taking periods flagged as bad by the D0 data quality group are kept to maximise our event yields because the measurement is effectively a shape measurement, which is essentially insensitive to the operational problems that can change the absolute efficiency. Events firing calorimeter noise flags are removed. After these requirements, the data used in this analysis correspond to an integrated luminosity of 10.4 fb^{-1}.

5.1.2 Common selection criteria

Events must have at least one $n_{seg} = 3$ muon with scintillator and wire chamber hits in the A/BC layers (n_{seg} is defined in Section 4.2.2), which must pass the single muon trigger object at all three levels. The two muon tracks must originate from the same primary vertex and pass loose selection criteria on χ^2/dof. Cosmic ray muons are rejected by requiring that the muon candidates are produced from the interaction point using information based on time-of-flight and impact parameters, and are further excluded by the requirement $|\eta^0 + \eta^1| < 0.02$[1]. The two muon candidates must be oppositely charged and meet the requirement that $|\eta_{det}| < 2$[2].

5.1.2.1 Peak region selection

For the $70 < M_{\ell\ell} < 110$ GeV region, both muon candidates are required to be of $n_{seg} \geq 0$ quality with a central track of $p_T > 15$ GeV. Events must contain at most two of the four isolation variables ($\mathscr{I}_{cal}$ and $\mathscr{I}_{trk}$ described in Section 4.2.2) greater than 0.09 to reject misidentified muons originating from the multijets background.

5.1.2.2 Low-mass region selection

For the low-mass region, $30 < M_{\ell\ell} < 60$ GeV, events must contain one muon matched to a central track with $p_T > 10$ GeV and the other muon with $p_T > 15$ GeV. Each

[1] muon "0" and "1" superscripts are used to distinguish the two muon candidates.

[2] At the D0 experiment, the detector pseudorapidity, η_{det}, is defined by a line connecting the centre of the detector to the particle tracks in a particular sub-detector.

muon track must have at least one SMT and one CFT hit and both muon tracks are required to have χ^2/dof< 4.

Events are further classified according to n_{seg} quality of each muon and we use *lepnseg*(X,Y) to denote an event category containing a muon with $n^0_{seg} = X$ and the other muon with $n^1_{seg} = Y$ ($X, Y = 0, 1, 2, 3$). The two muon candidates are ordered such that $p^0_T > p^1_T$ in all categories apart from the *lepnseg*(3,0) category, in which $n^0_{seg} > n^1_{seg}$. The selected events can be split into five categories based on the n_{seg} variable of the two muons and wire chamber hits:

- *lepnseg*(3,0) with wire chamber hits: n^0_{seg}=3, n^1_{seg}=0
- *lepnseg*(3,0) without wire chamber hits: n^0_{seg}=3, n^1_{seg}=0
- *lepnseg*(3,1)(3,2): n^0_{seg}=3, n^1_{seg}=1 or 2
- *lepnseg*(1,3)(2,3): n^0_{seg}=1 or 2, n^1_{seg}=3
- *lepnseg*(3,3): n^0_{seg}=3, n^1_{seg}=3

Note that the wire chamber hits in the *lepnseg*(3,0) category refers specifically to the $n_{seg} = 0$ muon. Furthermore, the poor-quality muon in the *lepnseg*(3,0) category without wire chamber hits must be in the bottom hole region ($4.2 < \phi < 5.1$ and $|\eta_{det}| < 1.1$) in the detector where the muon coverage is compromised by the support structures for the experiment. This classification of events were designed for the optimisation of selection criteria. A set of selection requirements were developed specifically for the low-mass region, as described in Section 5.4.1.

5.2 Signal and background estimation

MC simulations are employed to estimate the signal and background contributions in the data sample. The signal $Z/\gamma^* \to \mu^+\mu^-$ MC in this analysis is generated using PYTHIA [69] at LL+LO accuracy. For cases in which simulations give unreliable predictions (QCD background), data-driven methods are used. MC predictions for both signal and background are first normalised relative to each other and then normalised to data after the multijet (QCD) background subtraction in the analysis.

Figure 5.1 displays the legend used to separate different contributions in the data-MC comparison plots in the peak region and Figure 5.2 shows the legend in the low-mass region.

5.2.1 Peak region backgrounds

The total number of the selected events is 645k, and the background contamination is almost negligible (∼0.16% mainly from multijet background) around the Z-mass peak region.

- **$Z/\gamma^* \to \tau^+\tau^-$ and WW background**

  PYTHIA [69] is used to generate the electroweak background including $Z/\gamma^* \to \tau^+\tau^-$ and $WW \to \mu\nu\mu\nu$.

- **$t\bar{t}$ backgrounds**

  For the $t\bar{t}$ events, ALPGEN [70] is used to generate the hard process with parton shower and hadronisation simulated by PYTHIA [69].

- **Multijets background**

  Muonic decays of hadrons in multijet events can mimic the signal events. A data-driven method is used to estimate this background. The multijets sample is obtained by inverting the requirement on isolation variables with at most two isolation variables greater than 0.09 and dropping requirement on the lepton charge.

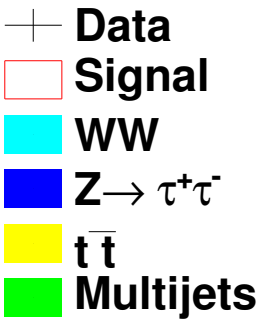

Figure 5.1: Legend for data versus MC comparisons in the peak region.

5.2.2 Low-mass region backgrounds

After the full event selection, a total of 74k events are retained. Backgrounds from mismeasurement and other physics processes in the low-mass region are as follows:

- **QCD background**

  Decay products of hadrons in QCD multi-jet events can be misidentified as dimuon signals. Since the opposite sign (OS) events are expected to be balanced by the same sign (SS) events to the first order approximation, the QCD

background can be evaluated by a data-driven method. A procedure to estimate QCD background is described in Section 5.6.

- **Migration background**

  The "migration" background originates from two sources: mismeasurement in the transverse momentum and FSR. For the purpose of justifying the event selection cuts we refer to the migration background in this analysis as events with dimuon invariant mass at generator level in MC satisfying $M_Z^{Gen} < 30$ GeV or $M_Z^{Gen} > 70$ GeV, where M_Z^{Gen} refers to the invariant mass at the Born level.

- **$Z/\gamma^* \to \tau^+\tau^-$ background**

  $Z/\gamma^* \to \tau^+\tau^-$ is the dominant background in the low mass dimuon sample and its contribution is around 5%.

- **$W+$ jet background**

  The misidentification of muons in jets in $W+$ jet events can fake the dimuon signature. The $W+$ jet background is simulated by PYTHIA [69]. The contribution is around 0.4%, which is small relative to the other backgrounds in the low-mass region.

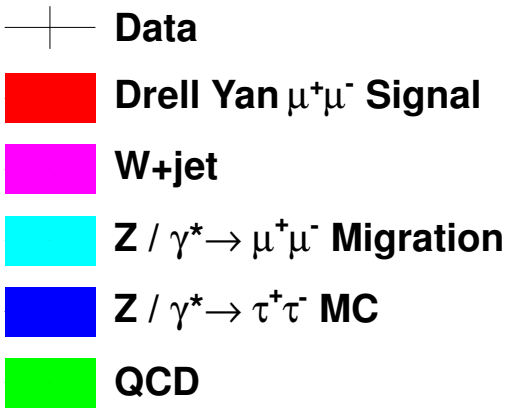

Figure 5.2: Legend for comparison between data and MC in the low-mass region.

5.3 Corrections to the Monte Carlo events

5.3.1 Generator level reweighting

Events are reweighted at the particle level to the predictions of RESBOS [24, 31] in the boson transverse momentum p_T^Z and boson rapidity $|y|$. A NLO $\to$ NNLO

K-factor[3] is implemented in the grid[4] files to generate the ResBos events for the Z boson exchange. Figure 5.3 shows the ratio of normalised ResBos distributions to PYTHIA in two dimensions (p_T^Z and $|y|$).

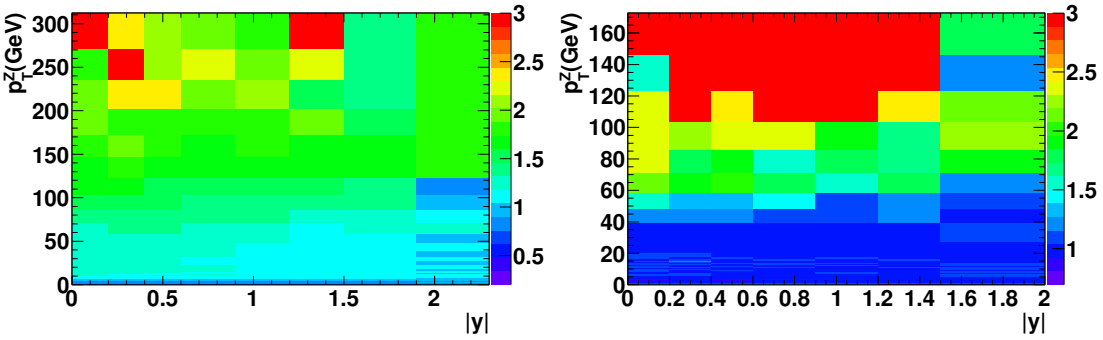

(a) $70 < M_{\mu\mu} < 110$ GeV (b) $30 < M_{\mu\mu} < 60$ GeV

Figure 5.3: Ratio of the normalised distribution of ResBos to that of PYTHIA in p_T^Z and $|y|$ at generator level.

5.3.2 Track smearing

The track ϕ and η resolutions in data are found to be worse than in simulations. Gaussian smearing parameters in ϕ and η are evaluated in terms of SMT hits by comparing the resolutions estimated using cosmic ray muon data to the resolutions in the simulation. Gaussian smearing parameters for z and the distance of closest approach to the tracks in the transverse plane with respect to the beam centroid r_{dca} in terms of SMT hits are adjusted by eye because the cut on these two variables is loose, and these corrections are applied to simulations to provide a better description of data. In order to perform the measurement of tracking efficiency in the simulation, a Gaussian smearing in the local muon transverse momentum $1/p_T^{local}$ and a scaling factor are applied to all local muons. A more complete description is given in [71].

5.3.3 Efficiency corrections

The tag and probe method

A "tag and probe" method is used to measure the muon trigger, identification and tracking efficiencies in data. The principle of the method is illustrated by the mea-

[3]The K factor is the ratio of NNLO to NLO cross section, which is particularly important at the large boson transverse momentum region arising from harder initial radiations.

[4] The grid refers to a phase space consisting of the boson invariant mass, boson transverse momentum and boson rapidity.

surement of the trigger efficiency. The process starts by the selection of a sample of $Z/\gamma^* \to \mu^+\mu^-$ events, and each event is required to pass the single muon trigger at all three levels. The dimuon invariant mass is required to be close to the Z-mass region to ensure the sample is predominantly composed of genuine dimuon events. Each of the two muons can act as a "tag" and a "probe". One of the muons must be matched to the trigger at all three levels, referred to as the "tag" muon. The other muon, known as the "probe" muon, is used to calculate the trigger efficiency by counting the fraction of events with the probe matched to the trigger at all three levels. The trigger efficiency is usually calculated in terms of p_T and η, which is applied to MC on an event-by-event basis.

The muon identification and tracking efficiency can also be measured from MC such that data-MC correction factors can be evaluated. The tag and probe method is likely to suffer from biases. For instance, when the tag muon is required to be matched to an inner detector track, the "tag and probe" sample selected is more likely to be originated from data-taking periods with higher tracking efficiency. Potential bias on the selection of the tag is partially cancelled when estimating the data-MC efficiency correction factors.

The trigger efficiency, tracking efficiency and muon reconstruction efficiency are measured in the full 10.4 fb^{-1} data set using the same tag and probe sample definitions employed in the previously published analysis [25] and a complete record of the selection criteria is documented in [71].

Figures 5.4–5.5 present the invariant mass distribution of the tag and probe samples between data and dimuon simulation samples for the measurement of the tracking efficiency and the muon reconstruction efficiency. An extended invariant mass range between 65 GeV and 115 GeV is shown whereas the requirement is $70 < M_{ll} < 110$ GeV. The disagreement between data and MC at the relatively low and high mass regions in Figures 5.4–5.5 arises due to the presence of background and the resolution difference of the invariant mass line shape between data and MC.

- **Single muon "OR" Trigger**

  Figure 5.6 shows the efficiency for the offline muons to fire any of the single muon triggers for $n_{seg} = 3$ muons.

- **Central track reconstruction**

  The tracking efficiency for muons is shown in Figure 5.7 in terms of η_{det}, ϕ, p_T^{local} and z_{dca} [5]. Figure 5.8 illustrates the data/MC scale factors in two dimensions.

[5] z_{dca} is the z position of distance of closest approach to the tracks in the transverse plane with respect to the beam centroid.

The tracking efficiency in MC is corrected in η_{det}, ϕ and z_{dca}. The scale factor is set to be 0.95 in regions where it cannot be determined due to insufficient numbers of probe muons. This scale factor (0.95) is roughly the tracking efficiency in the surrounding regions, where we have observed no significant variations of the electron tracking efficiency in the region of $|\eta| < 1.1$ and $4.2 < \phi < 5.1$ [71].

- **Local muon reconstruction efficiency**

  Figures 5.9, 5.10 and 5.11 show the relevant reconstruction efficiency for $n_{seg} = X$ $(X = 0, 1, 2, 3)$ muons and wire chamber hits determined with respect to isolated track muon candidates. $n_{seg} = 1$ and $n_{seg} = 2$ muons are not distinguished in terms of the muon reconstruction efficiency measurement. The corrections to MC for muon reconstruction efficiency are applied in bins of η_{det} and ϕ, as presented in Figure 5.12. The muon wire chamber hits efficiency corrections are not applied to MC in the peak region analysis, but have been used in the low-mass region analysis.

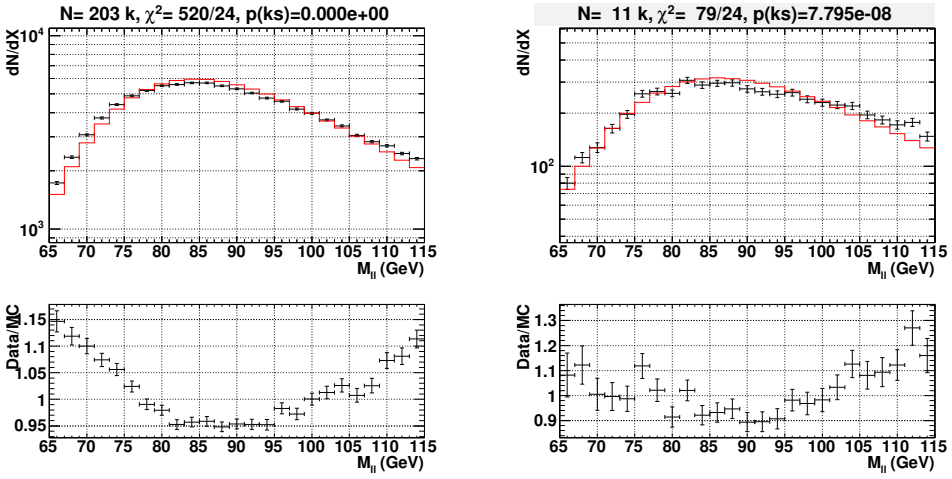

(a) tracking pass

(b) tracking fail

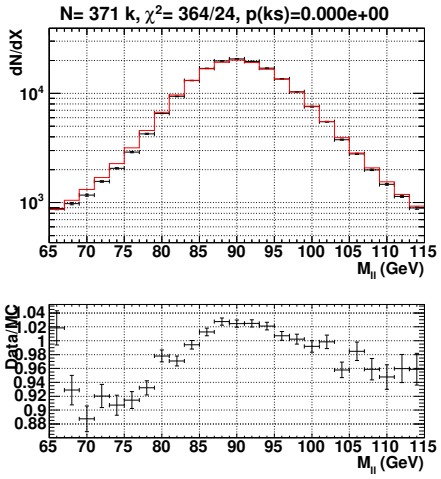

(c) $n_{seg} = 0$ (pass)

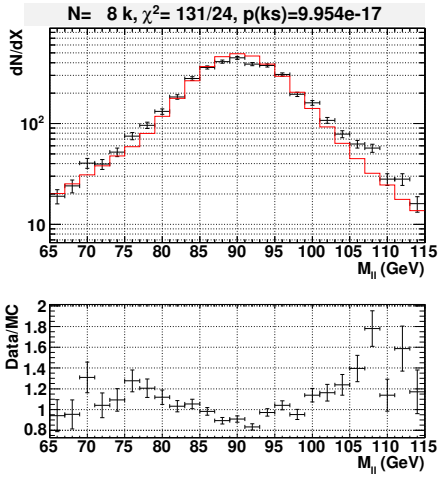

(d) $n_{seg} = 0$ (fail)

Figure 5.4: Comparison of invariant mass distribution of the tag and probe muons for events that pass or fail the requirement in the tracking efficiency measurement and $n_{seg} = 0$ muon reconstruction efficiency between data and MC. The red histograms represent the $Z/\gamma^* \rightarrow \mu^+\mu^-$ MC prediction and the data are indicated by black points with error bars. Also shown in the plot title are the total number of events in the tag and probe sample, the χ^2 per degree of freedom determined from the M_{ll} distribution between data and dimuon MC predictions and the corresponding p value.

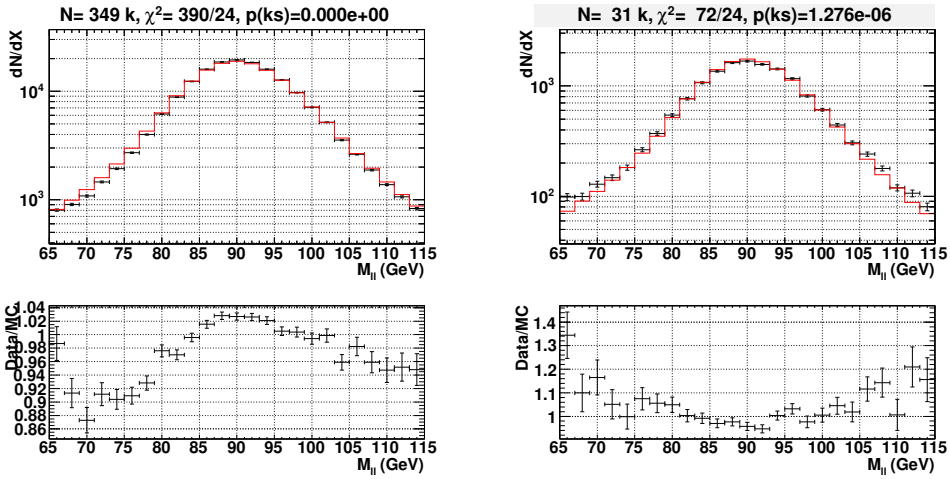

(a) $n_{seg} = 1$ pass

(b) $n_{seg} = 1$ fail

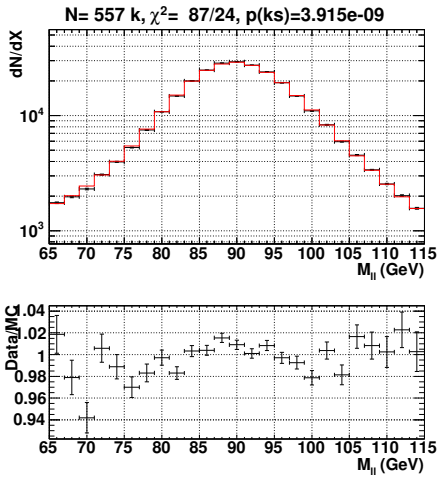

(c) $n_{seg} = 3$ pass

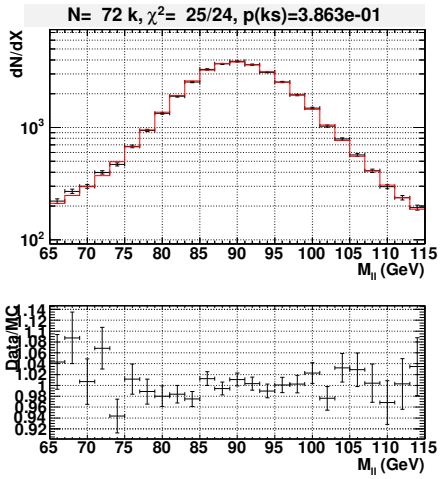

(d) $n_{seg} = 3$ fail

Figure 5.5: Comparison of invariant mass distribution of the tag and probe muons for events that pass or fail the requirement in the muon reconstruction efficiency measurement between data and MC. The red histograms represent the $Z/\gamma^* \rightarrow \mu^+\mu^-$ MC prediction and the data are indicated by black points with error bars. Also shown in the plot title are the total number of events in the tag and probe sample, the χ^2 per degree of freedom determined from the M_{ll} distribution between data and dimuon MC predictions and the corresponding p value.

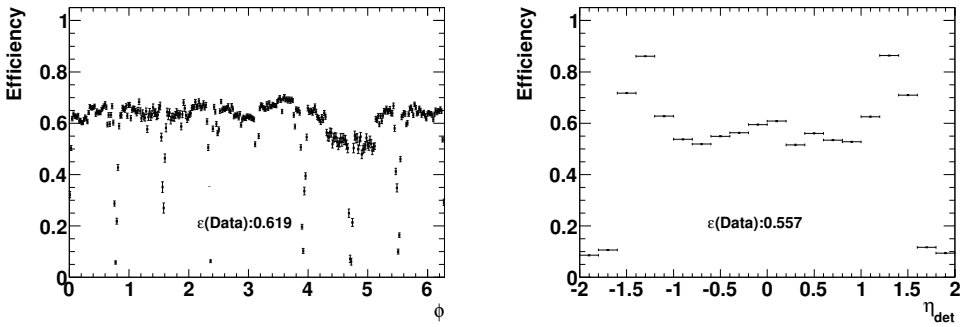

(a)

(b)

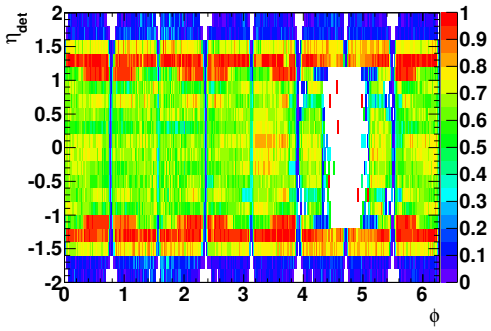

(c)

Figure 5.6: Trigger efficiency for $n_{seg} = 3$ muons determined from data in terms of ϕ , η_{det} and in 2D. The white space in the plot represents the bottom hole region ($4.2 < \phi < 5.1$ and $|\eta_{det}| < 1.1$) in the detector where the muon coverage is compromised by the support structures for the experiment. The trigger efficiency in ϕ around the eight octant gap regions is much lower than the surrounding regions because the octant gap regions are poorly instrumented.

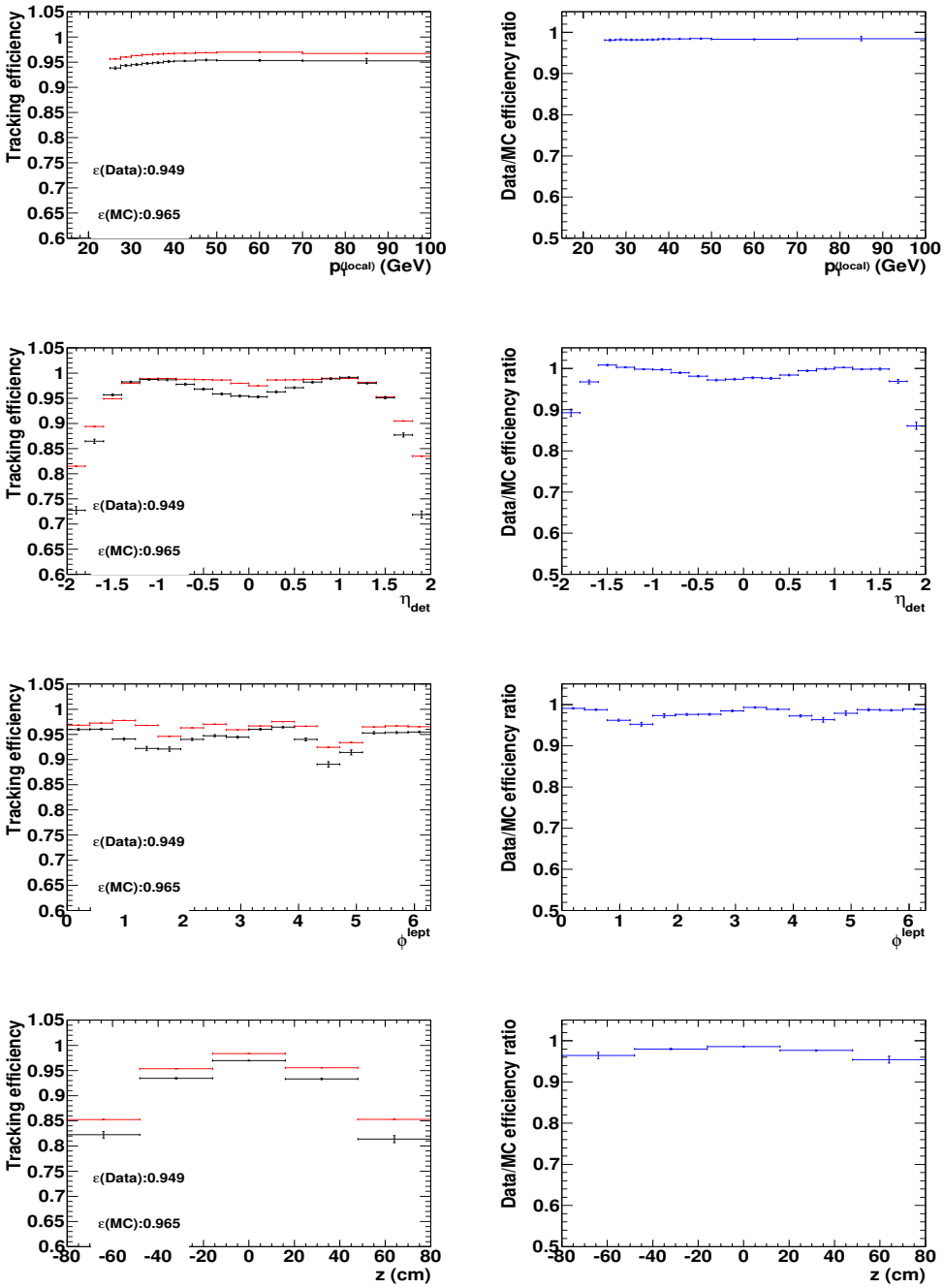

Figure 5.7: Muon central track reconstruction efficiency (left) and data/MC scale factor (right) as a function of p_T^{local}, η_{det}, ϕ^{lept} and z. The red points represent the MC prediction and the data are indicated by black points with error bars.

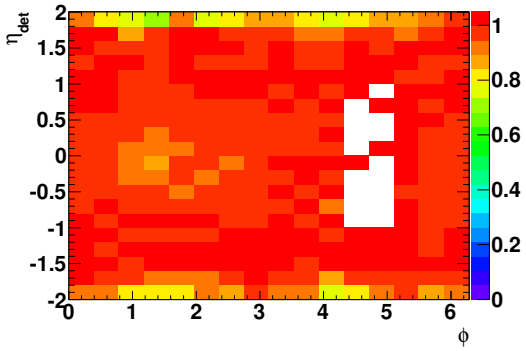

(a)

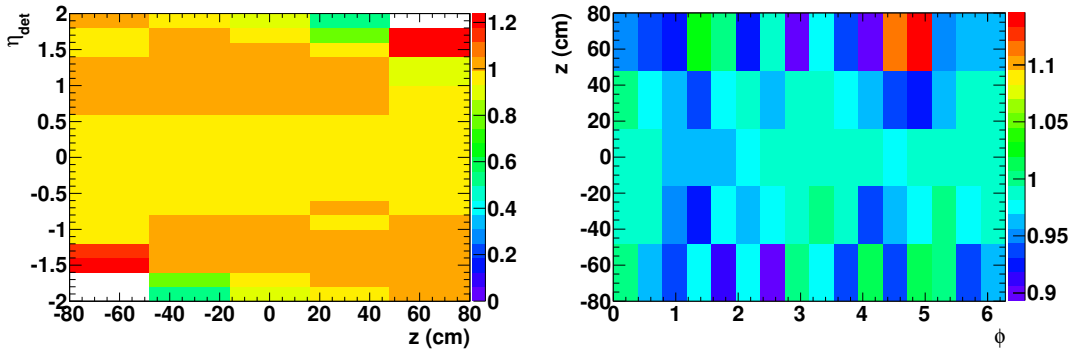

(b) (c)

Figure 5.8: Data/MC scale factors in 2D projections of η_{det}, ϕ and z for the tracking efficiency measurement.

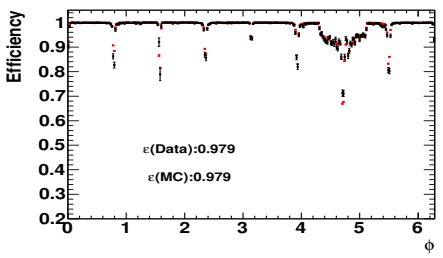

(a) $n_{seg} \geq 0$

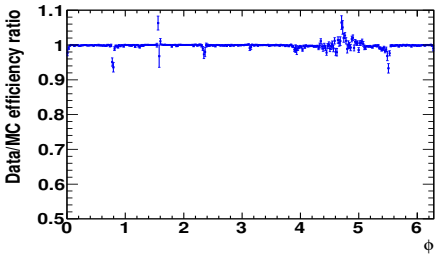

(b) $n_{seg} \geq 0$

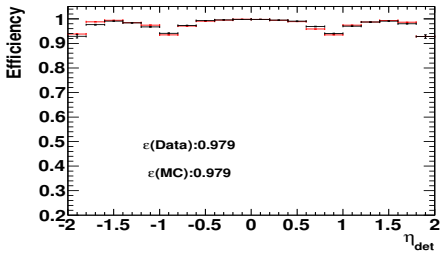

(c) $n_{seg} \geq 0$

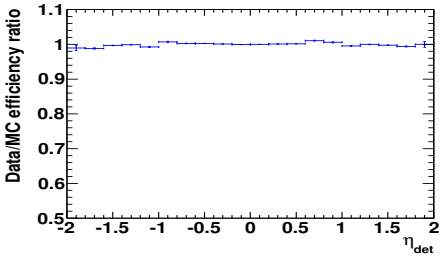

(d) $n_{seg} \geq 0$

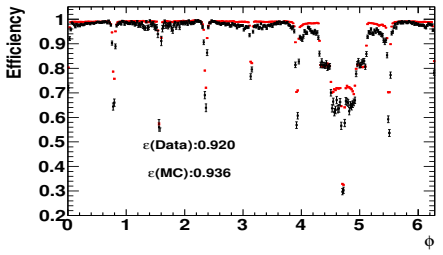

(e) $n_{seg} \geq 1$

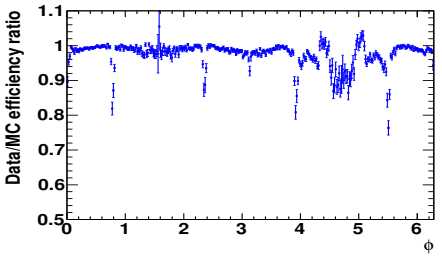

(f) $n_{seg} \geq 1$

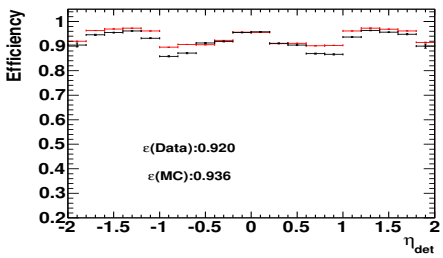

(g) $n_{seg} \geq 1$

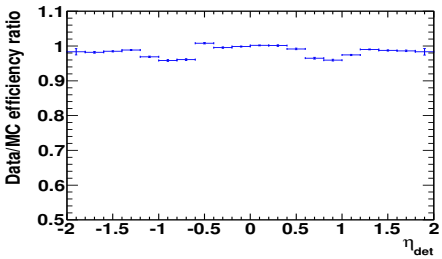

(h) $n_{seg} \geq 1$

Figure 5.9: Muon identification reconstruction efficiency (left) and data/MC scale factors (right) for $n_{seg} \geq 0$ and $n_{seg} \geq 1$ muons determined with respect to the isolated track muon candidates. The red points with error bars represent the MC prediction and the data are indicated by black points with error bars.

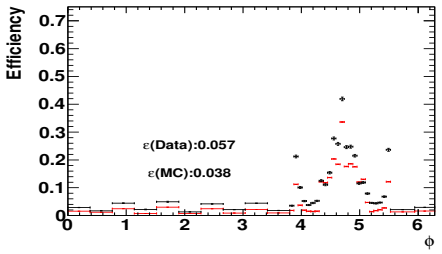

(a) $n_{seg} = 0$

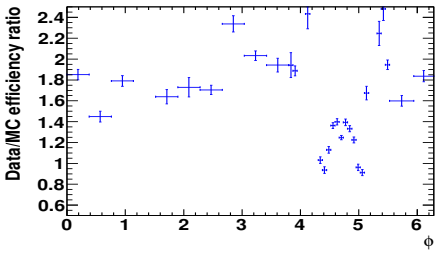

(b) $n_{seg} = 0$

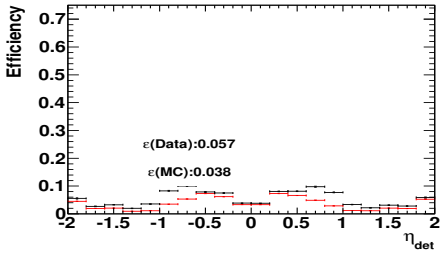

(c) $n_{seg} = 0$

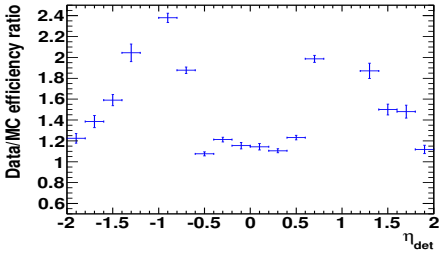

(d) $n_{seg} = 0$

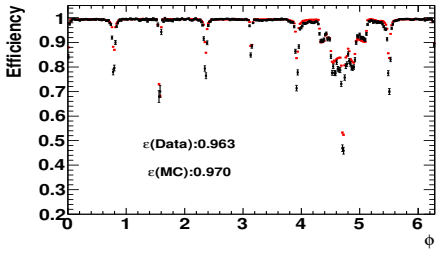

(e) wire chamber hits

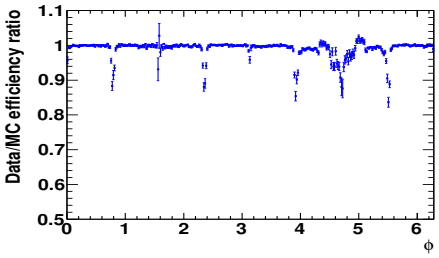

(f) wire chamber hits

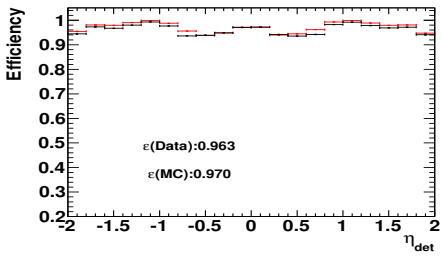

(g) wire chamber hits

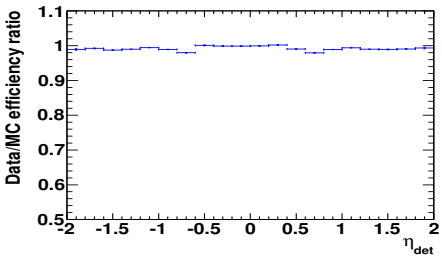

(h) wire chamber hits

Figure 5.10: Muon reconstruction efficiency (left) and data/MC scale factors (right) as a function of ϕ and η_{det} for $n_{seg} = 0$ muons and wire chamber hits with respect to $n_{seg} \geq 0$ muons. The red points with error bars represent the MC prediction and the data are indicated by black points with error bars. In Figure (e), the scale factor has a rather large statistical uncertainty for regions outside the bottom hole region ($|\eta| < 1.1$ and $4.2 < \phi < 5.1$) because of a lack of probe muons in these regions. However, only 3% of the total selected events are from *lepnseg*(3,0) category so such has a negligible effect on the ϕ^*_η shape combining all the *lepnseg* categories.

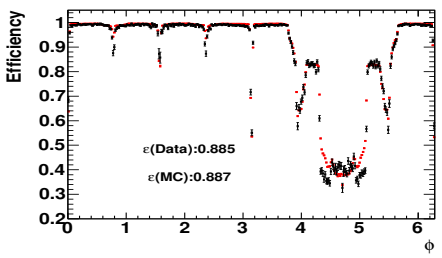

(a) $n_{seg} = 3$

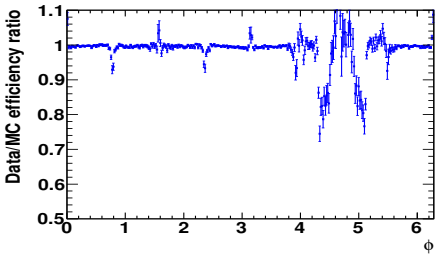

(b) $n_{seg} = 3$

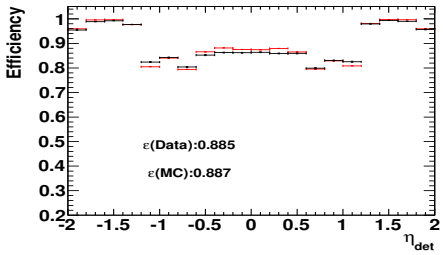

(c) $n_{seg} = 3$

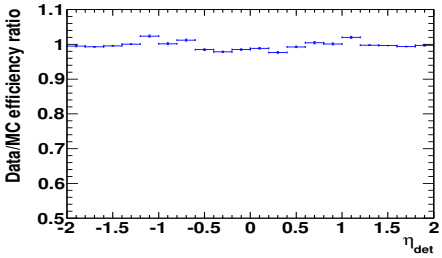

(d) $n_{seg} = 3$

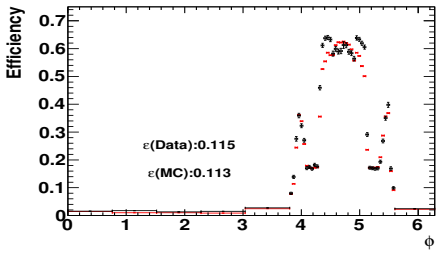

(e) $n_{seg} = 1$ and $n_{seg} = 2$

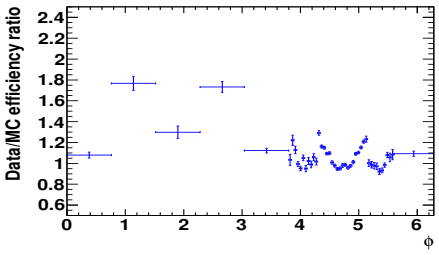

(f) $n_{seg} = 1$ and $n_{seg} = 2$

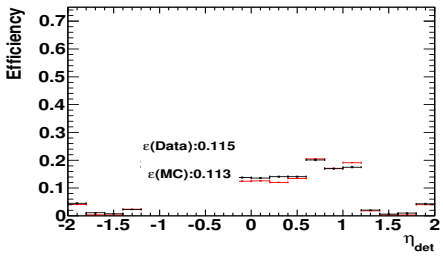

(g) $n_{seg} = 1$ and $n_{seg} = 2$

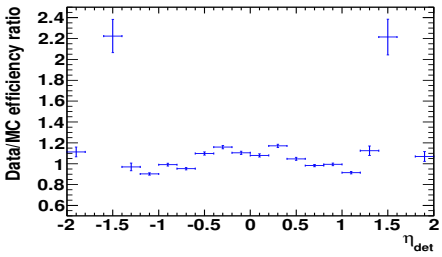

(h) $n_{seg} = 1$ and $n_{seg} = 2$

Figure 5.11: Muon reconstruction efficiency (left) and data/MC scale factor (right) as a function of ϕ and η_{det} for $n_{seg} = 3$, $n_{seg} = 1$ and $n_{seg} = 2$ muons with respect to $n_{seg} \geq 1$ muons. The red points with error bars represent the MC prediction and the data are indicated by black points with error bars.

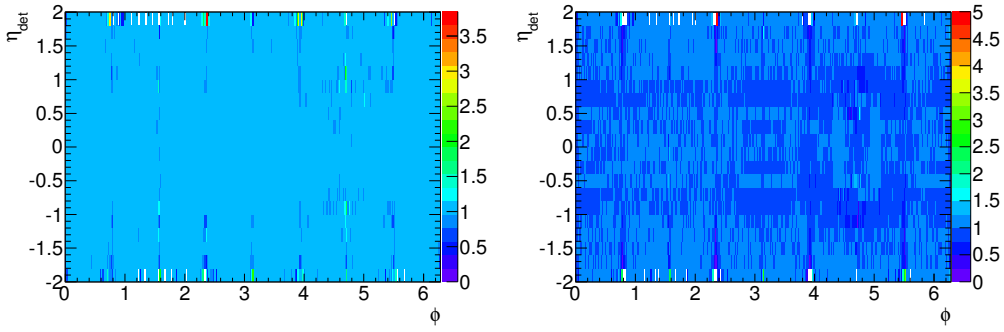

(a) $n_{seg} \geq 0$ muon

(b) $n_{seg} \geq 1$ muon

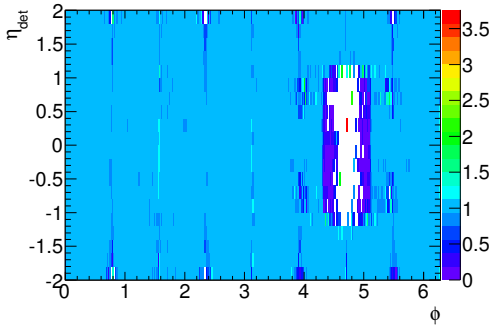

(c) $n_{seg} = 3$ muon w.r.t.$n_{seg} \geq 1$ muon

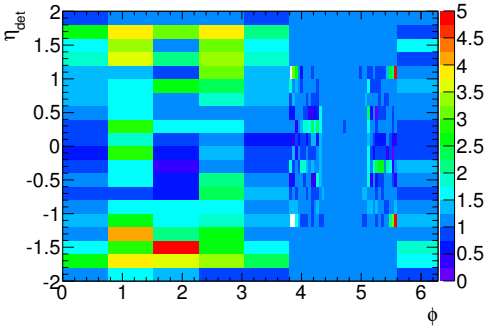

(d) $n_{seg} < 3$ muon w.r.t. $n_{seg} \geq 1$ muon

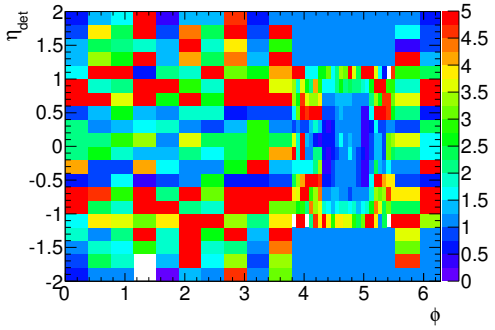

(e) $n_{seg} = 0$ muon w.r.t. $n_{seg} \geq 0$ muon

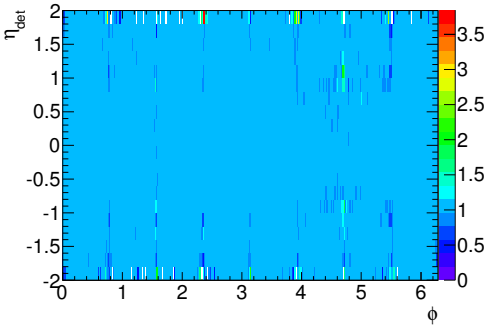

(f) wire chamber hits w.r.t. $n_{seg} \geq 0$ muon

Figure 5.12: Data/MC scale factors for muon identification efficiency corrections in two dimensions of ϕ and η_{det}. "w.r.t." stands for "with respect to". The scatter in Figure (e) arises from a lack of probe muons in these regions, but it is not important as lepnseg (3,0) without wire chamber hits are a small data sample and required to be in the bottom hole region ($4.2 < \phi < 5.1$ and $|\eta_{det}| < 1.1$).

5.3.4 Ad hoc corrections

The following ad hoc scale factors have been applied to the tracking efficiency in the MC in order to improve agreement with data in the η_{det} or ϕ_{mod} distribution. As there are 8 octant gap regions in the muon chamber, the variable ϕ_{mod} is defined as $\phi_{mod} = |mod(8\phi/2\pi, 1) - 0.5|$, where the region $\phi_{mod} > 0.45$ represents the octant gap region, which is poorly instrumented between boundaries. These scale factors were adjusted by eye and their associated systematic uncertainties are evaluated by switching off the ad hoc scale factors and symmetrised, as described in Section 5.9.

- Scale by a factor of 1.08 for $1.1 < |\eta_{det}| < 1.5$
- Scale by a factor of 0.96 for $|\eta_{det}| < 0.5$
- Scale by a factor of 1.04 for $\phi_{mod} > 0.475$ (only for $30 < M_{\mu\mu} < 60$ GeV region)

5.3.5 Further trigger efficiency corrections in the low-mass region

In the on-peak ϕ^*_η analysis the trigger efficiency is evaluated as a function of η and ϕ (but not p_T) using events in which both muons satisfy $p_T > 15$ GeV. In the low mass ϕ^*_η analysis a large fraction of muons have p_T in the region of 15 GeV, in which the trigger efficiency shows a strong variation with p_T. In addition, for the low mass analysis we have loosened the cut on the p_T of the second muon to be p^1_T >10 GeV. Therefore, a careful treatment of the efficiency dependence on p_T should be considered in the low mass analysis. In order to get the additional data/MC scale factors to correct the trigger efficiency dependence on p_T in the low mass region, a tag and probe method was used in the peak region in both data and MC but with the cut on the p_T of the second muon to be p^1_T >10 GeV. The motivation for performing the study in the peak region is that it is of low background and of high statistics. The trigger efficiency evaluated as a function of η and ϕ using the tag and probe method in the peak region, in which both muons satisfy $p_T > 15$ GeV, is used as MC input. The additional scale factor is the ratio of the data trigger efficiency to the MC trigger efficiency in bins of p_T. As shown in Figure 5.13a, the resulting MC overestimates the trigger efficiency at low p_T. An error function with $\epsilon(p_T) = 0.9813 \times erf(1.0 + (p_T - 13.89)/5.989\sqrt{2})$ is applied to the $n_{seg} = 3$ muon with $p_T < 30$ GeV as shown in Figure 5.13b.

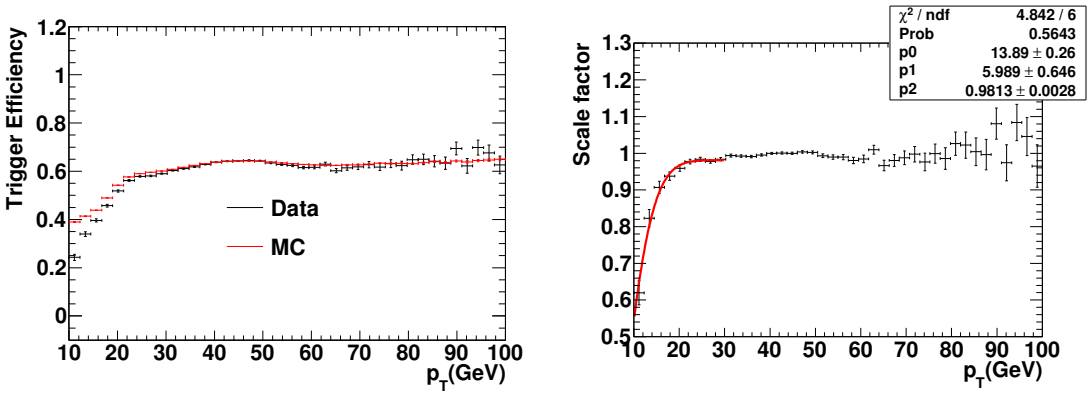

(a) (b)

Figure 5.13: Trigger efficiency (left) and its scale factor (right) as a function of p_T in *lepnseg*(3,3) category in the peak region. The efficiency corrections from the peak region analysis are used as input in the tag and probe method in MC in the peak region ($70 < M_{\mu\mu} < 110$ GeV).

5.3.6 Data versus MC comparison with all corrections implemented in the low-mass region

ϕ_{mod}, p_T and η_{det} distributions are presented in Figure 5.14 and Figure 5.15 with all corrections applied. A significant improvement has been observed for p_T distribution and η_{det} distribution after applying the additional corrections. The ϕ^*_η distribution can be distorted by ϕ_{mod} dependence on the efficiency corrections and so it is important that the ϕ_{mod} distribution is well described. The disagreement in the η_{det} distribution gives additional systematic uncertainty evaluated in Section 5.9.

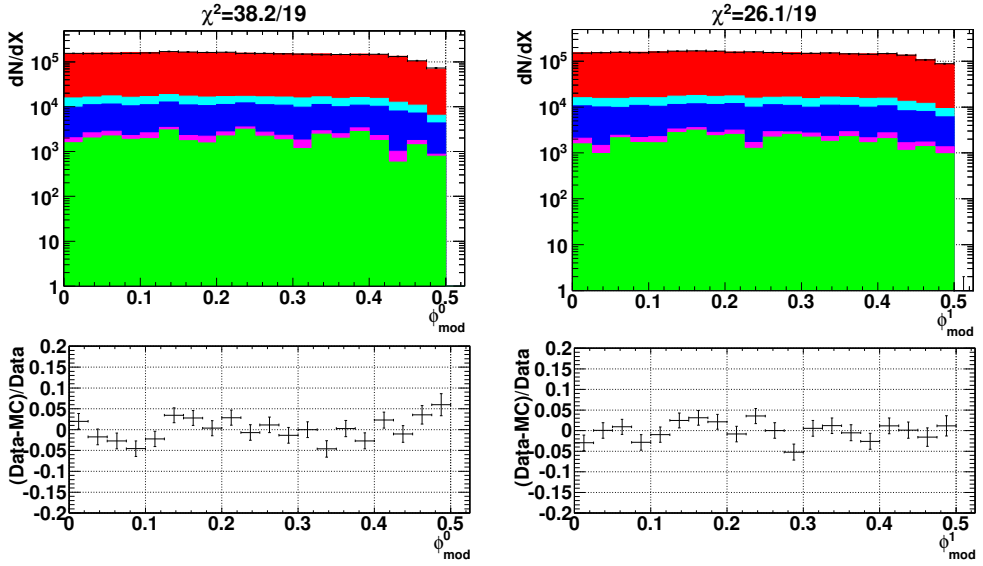

(a)

(b)

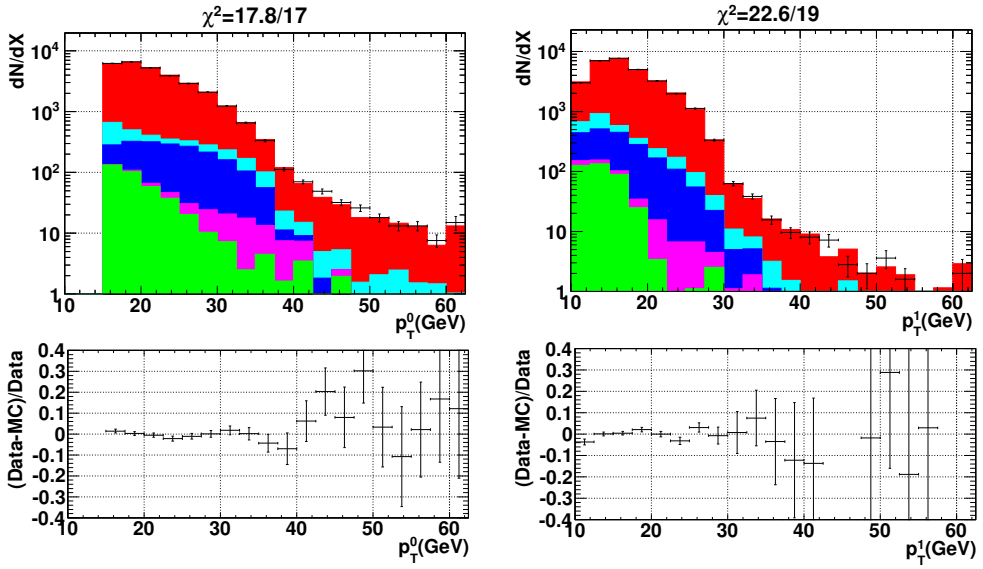

(c)

(d)

Figure 5.14: ϕ_{mod} (top) and p_T (bottom) distribution for muon 0 (left) and muon 1 (right) with all efficiency corrections applied in the $30 < M_{\mu\mu} < 60$ region. χ^2 per degree of freedom calculated using all bins of the spectrum between data and simululations is also presented.

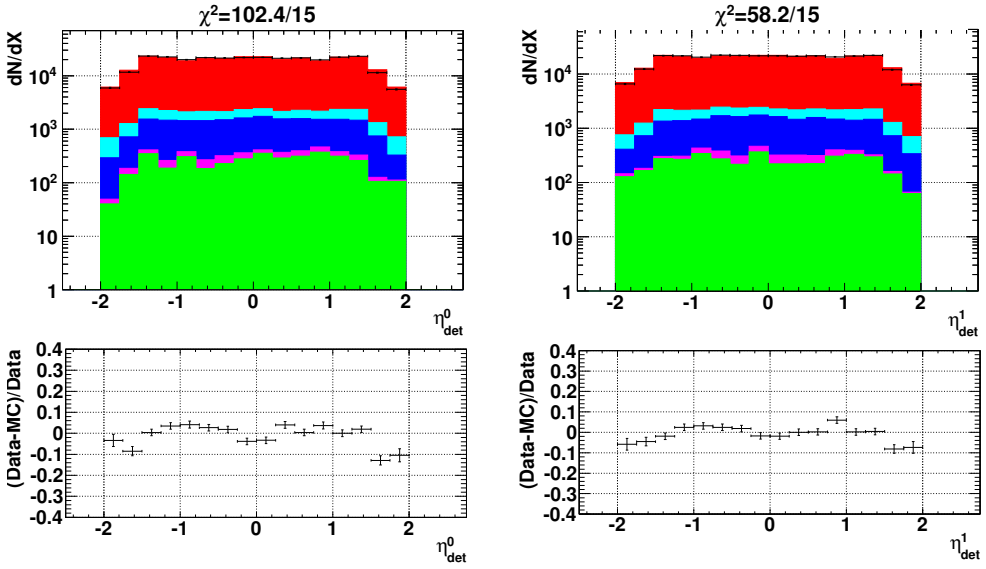

(a) (b)

Figure 5.15: Distribution of η_{det} for muon 0 (left) and muon 1 (right) with all efficiency corrections applied in the $30 < M_{\mu\mu} < 60$ region. χ^2 per degree of freedom calculated using all bins of the spectrum between data and simululations is also presented.

5.4 Optimisation of event selection

5.4.1 Justification of new selection requirements in the low-mass region

The justification of the new selection cut on each variable is performed with cuts on all the other variables applied. In each figure in this section, the cut indicated by the dashed line in the relevant cut variable distribution corresponds to the signal efficiency and background efficiency indicated by an arrow in the corresponding efficiency curve. In this section only the *lepnseg*(3,3) category is presented, as it is the category with the largest statistics. The cut is chosen such that a large fraction of genuine dimuon signal is retained whilst rejecting a large amount of background, i.e., the background efficiency is minimised and the signal efficiency is maximised.

5.4.1.1 Isolation requirements

The selection requirement on the isolation quantities $\mathscr{I}_{cal}[i]$ and $\mathscr{I}_{trk}[i]$ $(i = 0, 1)$ can reject a significant amount of the QCD background. The probability for an event to originate from the QCD background increases with the isolation quantity. These four isolation quantities are arranged in a descending order and recorded by

an array $IOD[j]$ $(j = 0, 1, 2, 3)$. The selection requirement is placed on the largest isolation quantity $IOD[0]$, which was found to provide the best discriminant against the QCD background (See Figure 5.16).

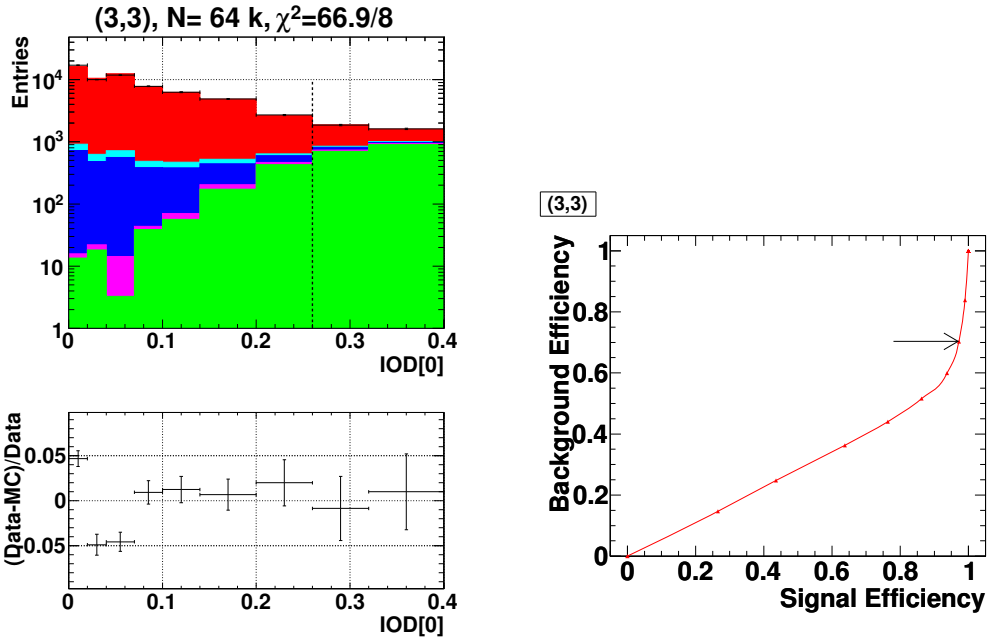

(a) Distribution of the largest isolation quantity with all the other requirements applied in the *lepnseg*(3,3) category.

(b) Signal efficiency versus background efficiency curve for a cut on the largest isolation quantity.

Figure 5.16: Justification of the largest isolation quantity cut in the *lepnseg*(3,3) category in the low-mass region.

5.4.1.2 Pseudo-mass requirements

Events from the Z peak can be misreconstructed to lie in the low mass region due either to mismeasurement of p_T or FSR. This migration background may lead to an underestimate of the transverse momentum of the lower p_T muon and can be suppressed using a modified mass quantity called pseudo-mass. The pseudo-mass mass quantity is calculated in which the magnitude of the transverse momentum of the two leptons are equal, with p_T^1 increased to be equal to p_T^0, the larger of the two lepton transverse momenta. The pseudo-mass M_{pseudo} is defined as

$$M_{pseudo} = \sqrt{2 \times p_T^0 \times p_T^0 \times (cosh(\eta_1 - \eta_2) - cos(\phi_1 - \phi_2))}.$$

The cut is extremely powerful in rejecting migration background, as is apparent in Figure 5.17.

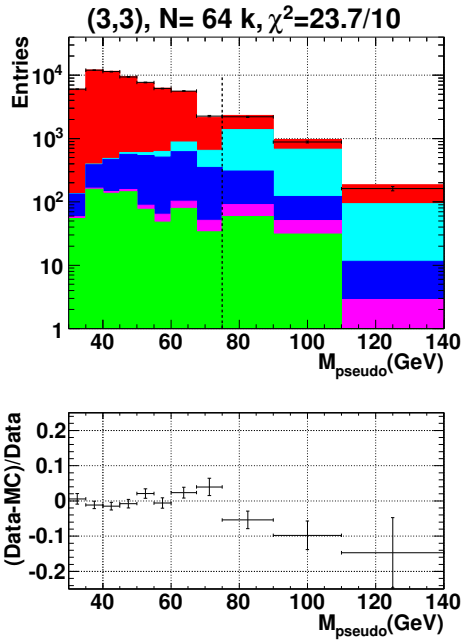

(a) Distribution of pseudo-mass with all the other requirements applied in the *lepnseg*(3,3) category.

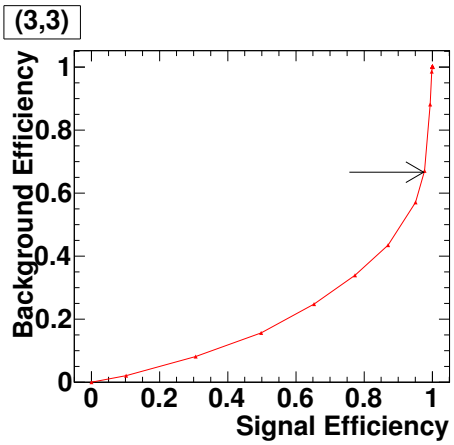

(b) Signal efficiency versus background efficiency curve for a cut on pseudo-mass variable.

Figure 5.17: Justification of the pseudo-mass cut in the *lepnseg*(3,3) category in the low-mass region.

5.4.1.3 Calorimeter energy requirements

The electromagnetic energy and hadronic energy are measured in the ECAL and the HCAL respectively within a narrow cone of $\Delta R < 0.1$ around the muon. There are four calorimeter energy quantities in total, which are sorted in a descending order and stored in $EH[j]$ $(j = 0, 1, 2, 3)$. The selection criteria are imposed on the the largest calorimeter energy $EH[0]$. The distribution of $EH[0]$ and the corresponding efficiency curves are shown in Figure 5.18.

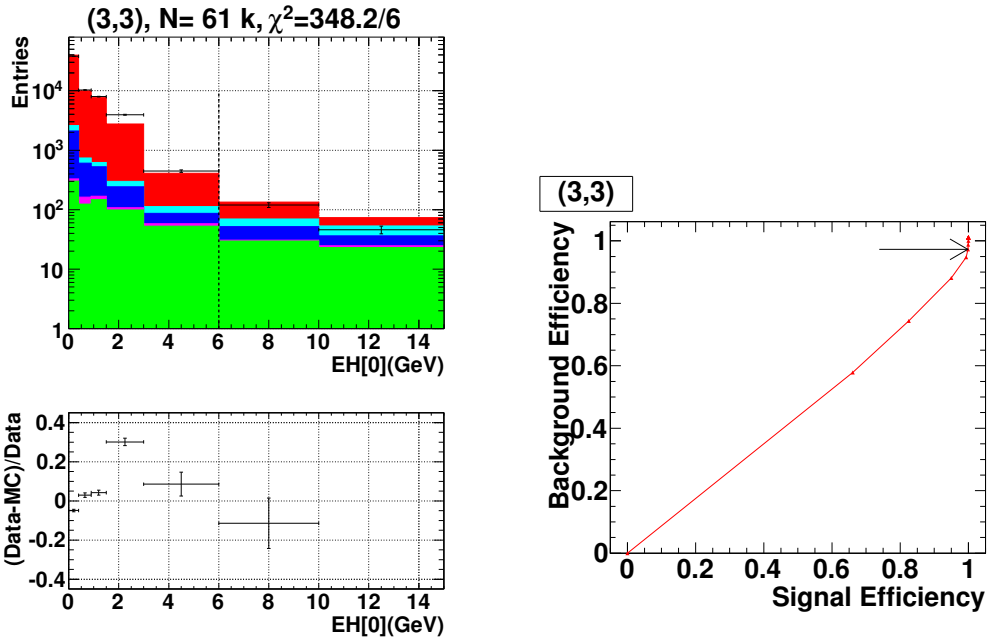

(a) Distribution of the largest calorimeter energy quantity with all the other requirements applied in the *lepnseg*(3,3) category.

(b) Signal efficiency versus background efficiency curve for a cut on the largest calorimeter energy quantity.

Figure 5.18: Justification of the largest calorimeter energy quantity cut in the *lepnseg*(3,3) category in the low-mass region.

5.4.1.4 Particle Identification Number (PID) requirements

The subset of dimuon events containing a third potential lepton candidate is examined. The identification number for the third lepton, represented by *lepid*[2], is the absolute value of the flavour of the highest additional lepton candidate. Figure 5.19 shows the distribution of *lepid*[2]. The value *lepid*[2] = 11 represents an electron-like object in the calorimeter without requiring a matched track in the central tracker. As can be seen in Figure 5.19, the bin *lepid*[2] = 11 is dominated by migration background. Figure 5.19b shows the generator-level particle identification information for these electron candidates, in which *lepid*[2] at generator level (denoted by *lepgenid*[2]) equal to 22 specifically refers to photons [4]. This supports the idea that these electron candidates arise from photons (or conversion electrons) from FSR.

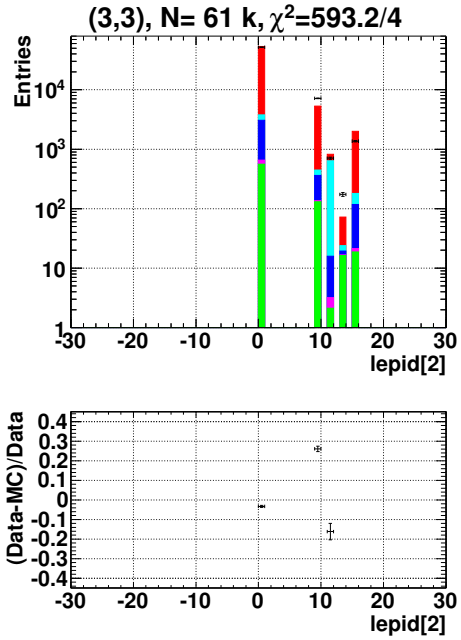

(a) Distribution of *lepid[2]* with all the other requirements applied in the *lepnseg*(3,3) category.

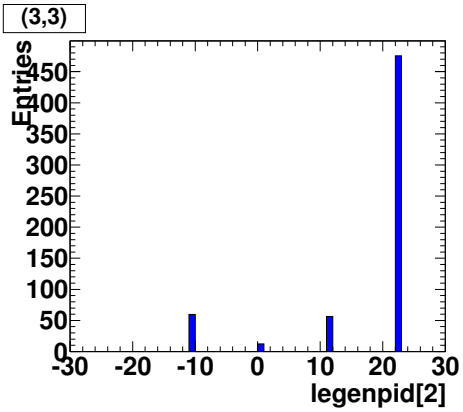

(b) Generator level PID information for third lepton PID equal to 11 at detector level.

Figure 5.19: Justification of the PID cut in the *lepnseg*(3,3) category in the low-mass region.

5.4.2 Summary of cuts in the low-mass region

Table 5.1 illustrates the composition of the data sample passing all the selection requirements in the low-mass region and Table 5.2 summarises the selection cuts and the corresponding signal and background efficiency of each cut. Figure 5.20 shows the distribution of dimuon invariant mass ($M_{\mu\mu}$) distribution with all cuts applied except that on the value of $M_{\mu\mu} < 60$ GeV. This is presented in order to check whether the pseudo-mass cuts have distorted the MC description of the data shape.

Category	Entries	QCD	$W + jet$	Migration	$Z/\gamma^* \to \tau^+\tau^-$	Background	Signal
All new cuts applied							
(3,0) with wire hits	1122	0.004	0.012	0.016	0.105	0.136	0.864
(3,0) without wire hits	1012	0.009	0.009	0.014	0.068	0.100	0.900
(3,1)(3,2)	5939	0.019	0.018	0.014	0.079	0.130	0.870
(1,3)(2,3)	5328	0.021	0.003	0.012	0.080	0.116	0.884
(3,3)	60536	0.012	0.002	0.013	0.045	0.072	0.928
Total	73937	0.013	0.003	0.013	0.052	0.081	0.919

Table 5.1: Composition of the signal region for each category in the low-mass region.

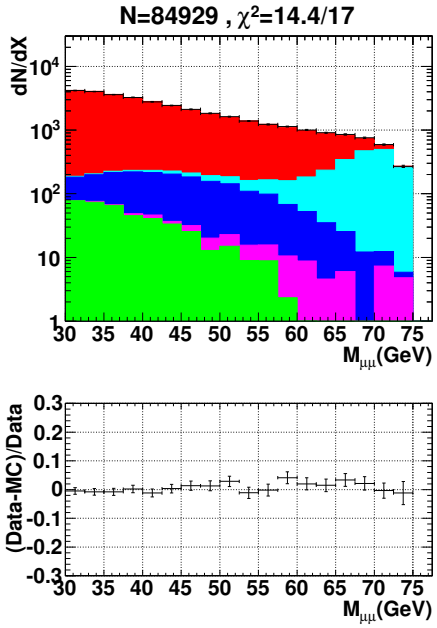

Figure 5.20: Distribution of dimuon invariant mass with all cuts applied except that on the value of $M_{\mu\mu} < 60$ GeV.

5.4.3 List of changes compared to the previously published results in the peak region

There are a few changes in both the event selection cuts and the strategy of efficiency corrections in comparison to the previously published results:

- **Selection cuts**

  The isolation cuts and the cuts on cosmics are tighter and more optimized in order to obtain an event sample of low background. The background fraction after using the latest selection cuts is around 0.16%.

- **Weight-based efficiency corrections**

  The event selection requires at least one $n_{seg} = 3$ muon. The weight-based corrections of muon reconstruction efficiency that took this selection requirement into account in the previously published analysis were slightly incorrect for events with two $n_{seg} = 3$ muons in MC. A better approach is to apply the muon reconstruction efficiency according to the n_{seg} variable of each muon. As a result, the agreement between data and MC in the ϕ_{mod} distribution is improved. This is important since the ϕ^*_η distribution can be distorted by the ϕ_{mod} dependence of the efficiency corrections.

Category (with Number of Events)	Selection Cuts	Signal eff.	Background eff.
(3,0) with wire chamber hits	$IOD[0] < 0.22$	0.958	0.851
	$calisol[1] < 0.07$	0.794	0.524
	$EH[0]$ <3 GeV	0.994	0.892
	M_{pseudo}< 75 GeV	0.977	0.738
	$lepid[2] \neq 11$	0.997	0.929
(3,0) without wire chamber hits	$IOD[0] < 0.14$	0.929	0.742
	$calisol[1] < 0.04$	0.836	0.449
	$EH[0]$ <3 GeV	0.990	0.942
	M_{pseudo}< 75 GeV	0.979	0.716
	$lepid[2] \neq 11$	0.997	0.874
(3,1)(3,2)	$IOD[0] < 0.2$	0.937	0.478
	$EH[0] < 3$ GeV	0.993	0.908
	M_{pseudo}< 75 GeV	0.977	0.702
	$lepid[2] \neq 11$	0.997	0.922
(1,3)(2,3)	$IOD[0] < 0.2$	0.936	0.476
	$EH[0] < 3$ GeV	0.993	0.864
	$M_{pseudo} < 75$ GeV	0.978	0.734
	$lepid[2] \neq 11$	0.997	0.911
(3,3)	$IOD[0]$<0.26	0.972	0.702
	$EH[0]$ <6 GeV	0.998	0.962
	M_{pseudo}<75 GeV	0.977	0.671
	$lepid[2] \neq 11$	0.997	0.850

Table 5.2: A summary of the selection cuts implemented in each *lepnseg* category with the corresponding signal and background efficiency (also denoted as "eff.") at cut value in the low-mass region.

- **Issues in the original analysis**

  The $W + jet$ background was subtracted twice in the original analysis. This causes a relatively large change in the shape of the background-subtracted ϕ^*_η distribution because the $W + jet$ background has a much flatter ϕ^*_η shape than the signal, leading to around one standard deviation away as shown in Figure 5.60 in Section 5.11. $W + jet$ is included in the estimate of the multijets background in the current analysis. The $n_{seg} \geq 0$ efficiency has changed dramatically due to a mistake in the MC simulation for the published results. The previously published analysis included around 2% duplicated events. These are removed in the current analysis.

- **Improvement in the analysis**

  There are some other minor corrections, which make very small changes to the final results. For instance, the kinematic cuts are applied to the final state leptons when evaluating the scale factors in 2D reweighting to ResBos. There are a small number of events that have a $n_{seg} = 3$ muon matched to the

relevant trigger object, but nevertheless failed to fire the single muon trigger. These are taken into account by means of an additional systematic uncertainty.

5.5 Background uncertainty evaluation in the low-mass region

An excellent understanding of the physics background is of great importance in this analysis because the signal is obtained by subtracting the physics background from data. Systematic uncertainties due to the subtraction of physics background will be assessed using control samples predominantly composed of a particular background. The fractional uncertainty assigned to a given background is evaluated by dividing the fractional discrepancy between MC and data in the relevant control plots by the fractional composition of the relevant control sample. The choice of the particular *lepnseg* category to be shown in the plots in this section is such that the background of interest can be distinguished.

Figure 5.21 shows the shapes of the ϕ_η^* distribution predicted by the PYTHIA MC at detector level for the genuine Drell Yan muon pairs and the various physics backgrounds. Both the signal and background ϕ_η^* distributions are normalised to unity. In particular, the ϕ_η^* distribution of the $W+$ jet background stays rather flat over the full ϕ_η^* range. In addition, the $Z/\gamma^* \to \tau^+\tau^-$ background and migration background have a similar shape to that of genuine muon pairs.

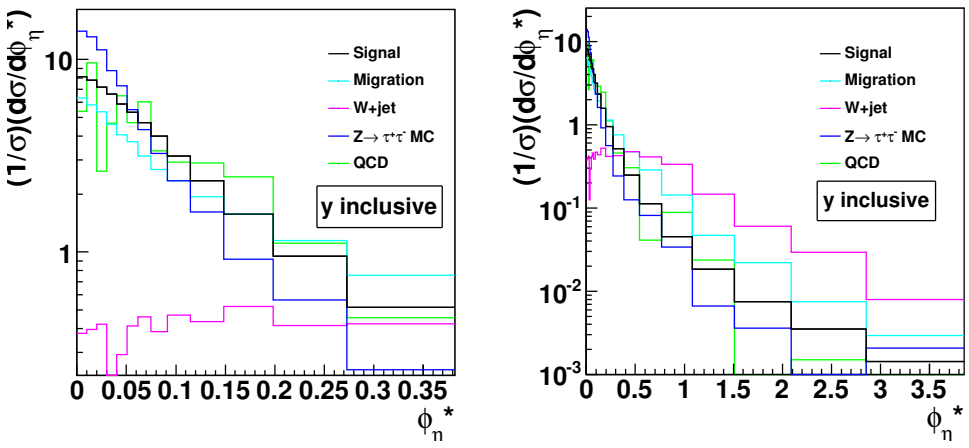

Figure 5.21: Background and signal shape of the normalised differential cross section of ϕ_η^* distribution.

All control samples take advantage of the new variables specifically employed for optimisation of the selection criteria in the low-mass region in Section 5.4.1. The

definition of control samples of each source of the physics background is described as follows.

QCD and $W+$ jet background control sample

The control sample for the QCD background is defined as the event sample rejected exclusively by cuts on the isolation variables $IOD[0]$ and/or $\mathscr{I}_{cal}[i]$. (See Figure 5.22a). The $W+$ jet control sample has the same selection criteria as the QCD control sample, except that the variable $\Delta\phi$, which is the opening angle of the final state leptons, is employed to distinguish the $W+$ jet background from the QCD background (See Figure 5.22b).

Migration background control sample

The control sample for the migration background corresponds to the event sample exclusively eliminated by the the pseudo-mass requirement. A $\pm 30\%$ uncertainty is assigned to the migration background, which is obtained from Figure 5.23.

FSR background control sample

The FSR background control sample (See Figure 5.24 and Figure 5.25 in Section 5.5.1) is the event sample rejected by the $lepid[2] \neq 11$ requirement introduced in Section 5.4.1.4.

$Z/\gamma^* \rightarrow \tau^+\tau^-$ background control sample

The $Z/\gamma^* \rightarrow \tau^+\tau^-$ control sample is inspected by studying the following distributions:

- the sum of track distance of closest approach (represented by $\sum$ trkdca in the following) in the control sample excluded by both $EH[0]$ and $\mathscr{I}_{cal}[1]$ selection criteria (see Figure 5.26a);
- the sum of EM and HAD energy (defined in Section 5.4.1.3), represented by EM + HAD in the plot, for the muon of lower identification quality without $EH[0]$ selection criteria (see Figure 5.26b).

Both distributions have certain regions dominated by the $Z/\gamma^* \rightarrow \tau^+\tau^-$ background. It should be noted the $Z/\gamma^* \rightarrow \tau^+\tau^-$ control sample of the *lepnseg*(3,0) category is the event sample rejected by either $\mathscr{I}_{cal}[1]$ or $EH[0]$ requirements. (see Section 5.5.2 for more details on the $Z/\gamma^* \rightarrow \tau^+\tau^-$ control sample).

Summary of the background systematic uncertainties

Table 5.3 summarises the uncertainty on each background in different *lepnseg* categories.

Category	QCD	Migration	FSR	$W+$ jet	$Z/\gamma^* \to \tau^+\tau^-$
(3,0)(with wire hits)	0.8	0.3	0.5	1	Hadronic(0.4),Muonic(0.1)
(3,0)(without wire hits)	0.4	0.3	0.5	0.4	Hadronic(0.4),Muonic(0.1)
(3,1)(3,2)	0.6	0.3	0.5	0.7	Hadronic(0.4),Muonic(0.1)
(1,3)(2,3)	0.5	0.3	0.5	0.5	Hadronic(0.4),Muonic(0.1)
(3,3)	0.7	0.3	0.5	0.3	Hadronic(0.4),Muonic(0.1)

Table 5.3: Fractional uncertainty of different backgrounds for each *lepnseg* category.

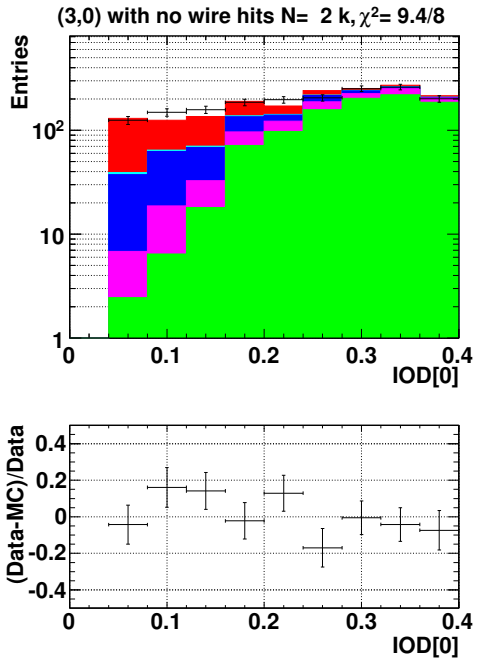

(a) Distribution of the largest isolation quantity in the control region of QCD background for *lepnseg*(3,0) category with no wire chamber hits.

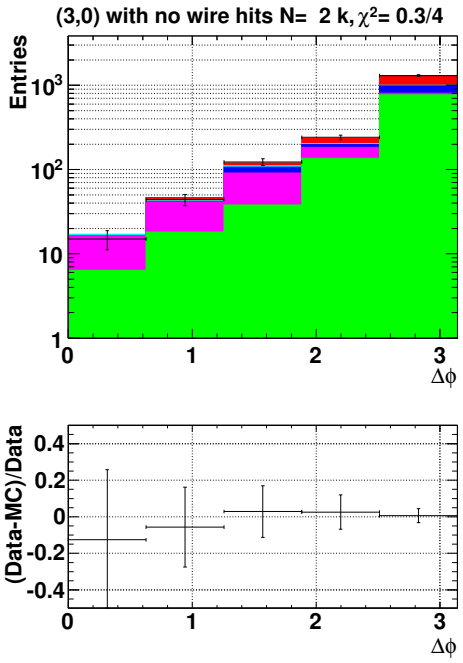

(b) $\Delta\phi$ distribution in QCD control region for *lepnseg*(3,0) category with no wire chamber hits.

Figure 5.22: Estimate of the QCD and $W+$ jet background uncertainty in the QCD background control samples.

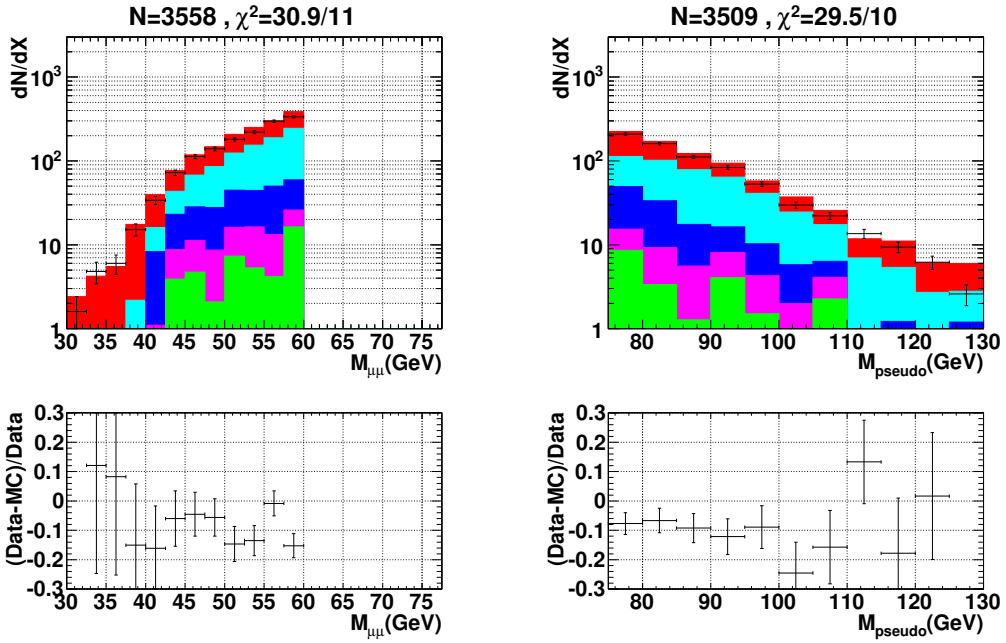

(a) $M_{\mu\mu}$ distribution in the migration control region with all *lepnseg* categories combined

(b) M_{pseudo} distribution in the migration control region with all *lepnseg* categories combined

Figure 5.23: Migration background control samples with all *lepnseg* categories combined.

5.5.1 Constraint on the FSR background uncertainty

It was found that events with $lepid[2] = 11$ are predominantly migration background and the corresponding generator level PID information confirms that these events are FSR events (See Section 5.4.1.4). It is further confirmed by the scatter plot between $M_{\mu\mu\gamma}$ and $M_{\mu\mu}$ in Figure 5.24, where $M_{\mu\mu\gamma}$ is the invariant mass of the "three-body" system. The regions for FSR and initial state radiation (ISR) are indicated by corresponding arrows. The ISR region is irrelevant because we effectively remove these events by the requirement $30 < M_{\mu\mu} < 60$ GeV.

In order to increase the sample statistics, requirements on either $M_{\mu\mu}$ or M_{pseudo} are loosened. The fractional uncertainty assigned to FSR is 50%, as estimated conservatively from Figure 5.25. The fractional uncertainty is estimated by using the bin with the largest deviation between data and MC (the first bin in Figure 5.25b), where the discrepancy between data and MC is around 25% and the migration background composition is around 50%.

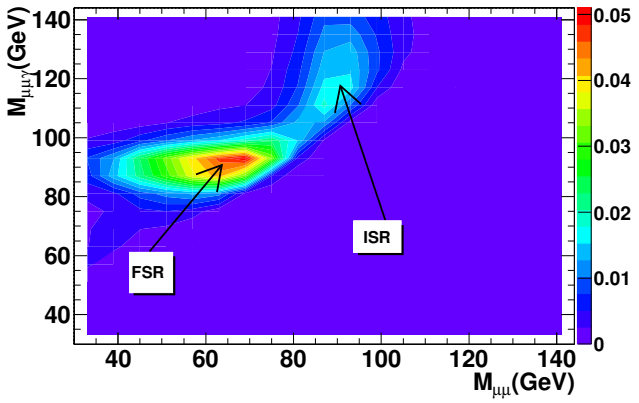

Figure 5.24: Correlation between $M_{\mu\mu\gamma}$ and $M_{\mu\mu}$ for events with *lepid[2] = 11*, no cuts on pseudo-mass and no cuts on $M_{\mu\mu}$ in $Z/\gamma^* \to \mu^+\mu^-$ MC.

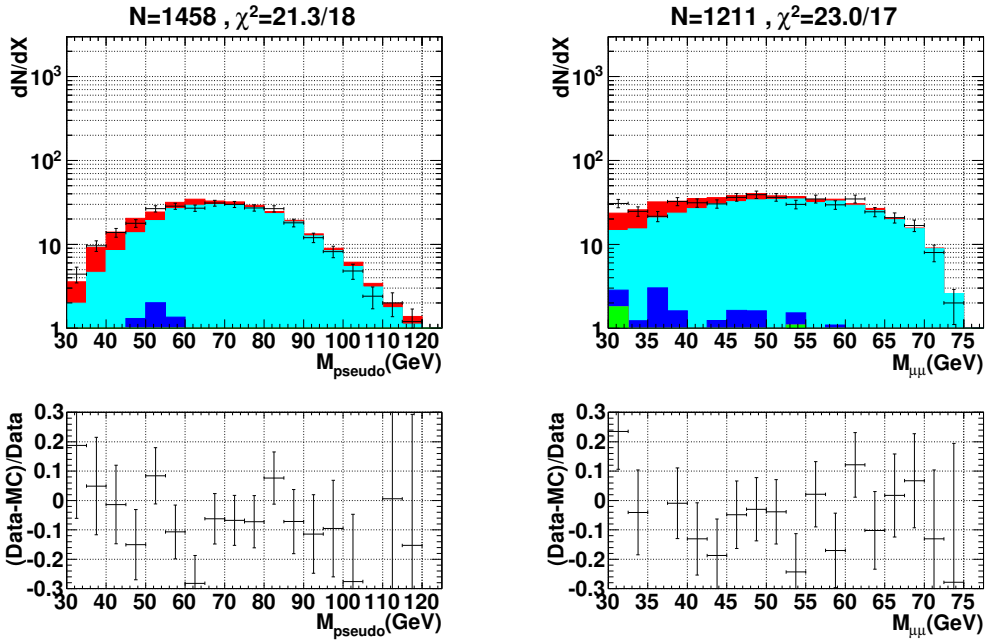

(a) M_{pseudo} distribution in the FSR control region (*lepid[2] = 11* and no cuts on pseudo-mass).

(b) Invariant mass distribution (*lepid[2] = 11* and no cuts on $M_{\mu\mu}$).

Figure 5.25: Control samples for estimate of the FSR background uncertainty.

5.5.2 Constraint on $Z/\gamma^* \to \tau^+\tau^-$ background uncertainty

5.5.2.1 Fraction of genuine muons in the $Z/\gamma^* \to \tau^+\tau^-$ MC

As the $Z/\gamma^* \to \tau^+\tau^-$ background uncertainty arises predominantly from the misidentified hadronic decay products of τ, the uncertainty is evaluated separately for the hadronic decay and muonic τ decays. It is worth noting that the numbers given in Table 5.4 in $Z/\gamma^* \to \tau^+\tau^-$ MC are determined after normalisation to the data. There are two rows of numbers for each *lepnseg* category, where the first row corresponds to muon 0 and the second muon 1. The muon with a low identification quality tends to arise from the hadronic decay of τ in the signal region after selection cuts. To sum up, around 1% of total events in the signal region is due to hadronic decays from the $Z/\gamma^* \to \tau^+\tau^-$ background.

It was decided to vary the hadronic decays in the $Z/\gamma^* \to \tau^+\tau^-$ background by $\pm 40\%$ and the dimuon decays by $\pm 10\%$ (See Figure 5.26) when evaluating the systematic uncertainty due to the $Z/\gamma^* \to \tau^+\tau^-$ background. The motivation for the variations in different decay modes in the $Z/\gamma^* \to \tau^+\tau^-$ background is that it is known that the muonic decays are rather well described by simulations whereas the hadronic decays are poorly understood.

Category	Muon Array	Pions	Kaons	Electrons	Muons	Fraction of genuine muons
Fail EH cuts $Z/\gamma^* \to \tau^+\tau^-$						
(3,0) with wire hits	Muon 0	1	1	2	10	0.767
(3,0) with wire hits	Muon 1	2	1	11	0	0.002
(3,0) without wire hits	Muon 0	0	0	0	3	0.884
(3,0) without wire hits	Muon 1	3	0	0	0	0.000
(3,1)(3,2)	Muon 0	7	0	2	39	0.808
(3,1)(3,2)	Muon 1	25	3	13	7	0.155
(1,3)(2,3)	Muon 0	45	3	9	7	0.103
(1,3)(2,3)	Muon 1	5	0	2	57	0.892
(3,3)	Muon 0	24	1	7	18	0.353
(3,3)	Muon 1	12	0	5	35	0.677
Signal Region $Z/\gamma^* \to \tau^+\tau^-$						
(3,0) with wire hits	Muon 0	2	0	2	109	0.959
(3,0) with wire hits	Muon 1	17	2	50	45	0.399
(3,0) without wire hits	Muon 0	1	0	0	60	0.973
(3,0) without wire hits	Muon 1	26	1	0	35	0.566
(3,1)(3,2)	Muon 0	13	1	5	451	0.960
(3,1)(3,2)	Muon 1	139	16	66	247	0.528
(1,3)(2,3)	Muon 0	194	17	38	198	0.443
(1,3)(2,3)	Muon 1	10	1	5	430	0.963
(3,3)	Muon 0	136	6	30	2542	0.937
(3,3)	Muon 1	89	3	42	2580	0.951

Table 5.4: Origin of muons in $Z/\gamma^* \to \tau^+\tau^-$ MC for each *lepnseg* category failing the *EH[0]* requirements.

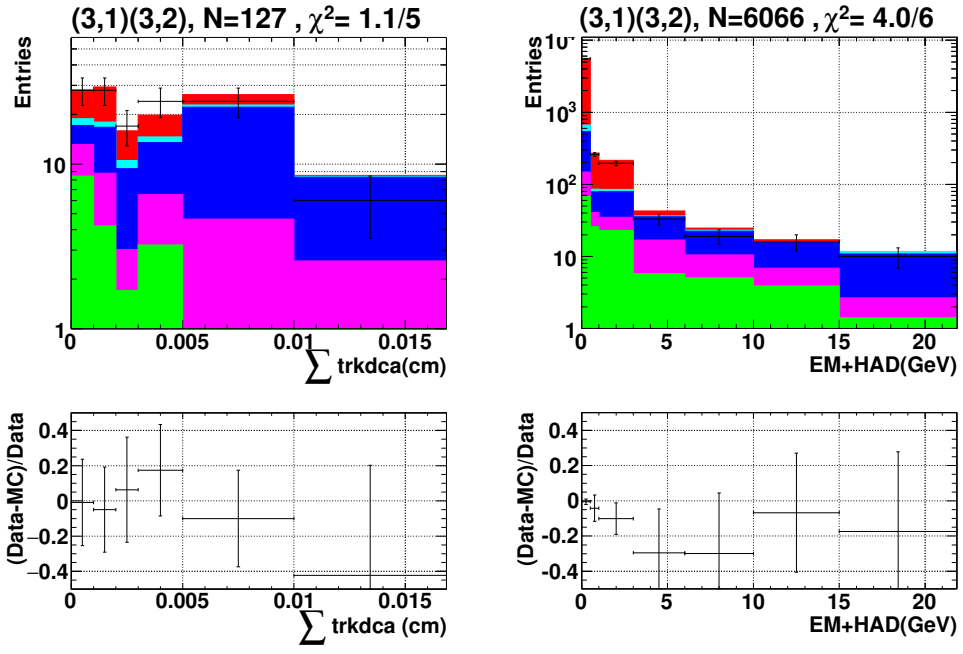

(a) (b)

Figure 5.26: Distribution of (a) $\sum$ trkdca in the control sample excluded by both $EH[0]$ and $\mathscr{I}_{cal}[1]$ selection criteria and (b) EM + HAD for the muon of lower identification quality without $EH[0]$ selection criteria.

5.5.3 Cross-checks of background uncertainty estimations

Cross-checks of the estimated background uncertainties are performed by looking at variations in the data/MC ratios of various distributions after varying background levels according to the uncertainties shown in Table 5.3.

QCD and $W+$ jet background

The nominal distributions for the QCD and $W+$ jet backgrounds are in Figure 5.16 and Figure 5.22b respectively. Figure 5.27 and Figure 5.28 present the data/MC ratios in $IOD[0]$ (QCD background) and $\Delta\phi$ ($W+$ jet background) for the corresponding positive and negative background variations.

Migration background

The nominal distribution for the migration background is in Figure 5.17 and Figure 5.20. The migration background systematic uncertainty is evaluated by reweighting events with $M_Z^{Gen} < 30$ GeV or $M_Z^{Gen} > 70$ GeV but requiring that the third lepton is not a photon or an electron at generator level. Figure 5.29a and Figure 5.29b show the data/MC ratios in terms of $M_{\mu\mu}$ and M_{pseudo} for the positive and negative variations.

FSR background

As for the FSR background, the nominal distribution is presented in Section 5.5.1. The variation in the FSR background is performed by varying events meeting the requirements of genuine muon pairs in addition to an identified radiated photon or electron at generator level with $\Delta_{QED} > 0.5$ GeV by $\pm 50\%$, where Δ_{QED} represents the difference of the dimuon invariant mass at Born level and at bare level. The data/MC ratios in $M_{\mu\mu}$ and M_{pseudo} after variations in the FSR background are illustrated in Figure 5.30.

$Z/\gamma^* \to \tau^+\tau^-$ background

The nominal distribution of $EH[0]$ is shown in Figure 5.18. After variations in the $Z/\gamma^* \to \tau^+\tau^-$ background, a reasonable change is observed in the $EH[0]$ distribution as presented in Figure 5.31, where the discrepancy between data and MC in the range of $2 < EH[0] < 3$ GeV is observed due to relatively poor MC simulation and is not important as the cut is loose at 6 GeV for the *lepnseg*(3,3) category and at 3 GeV for all the other categories.

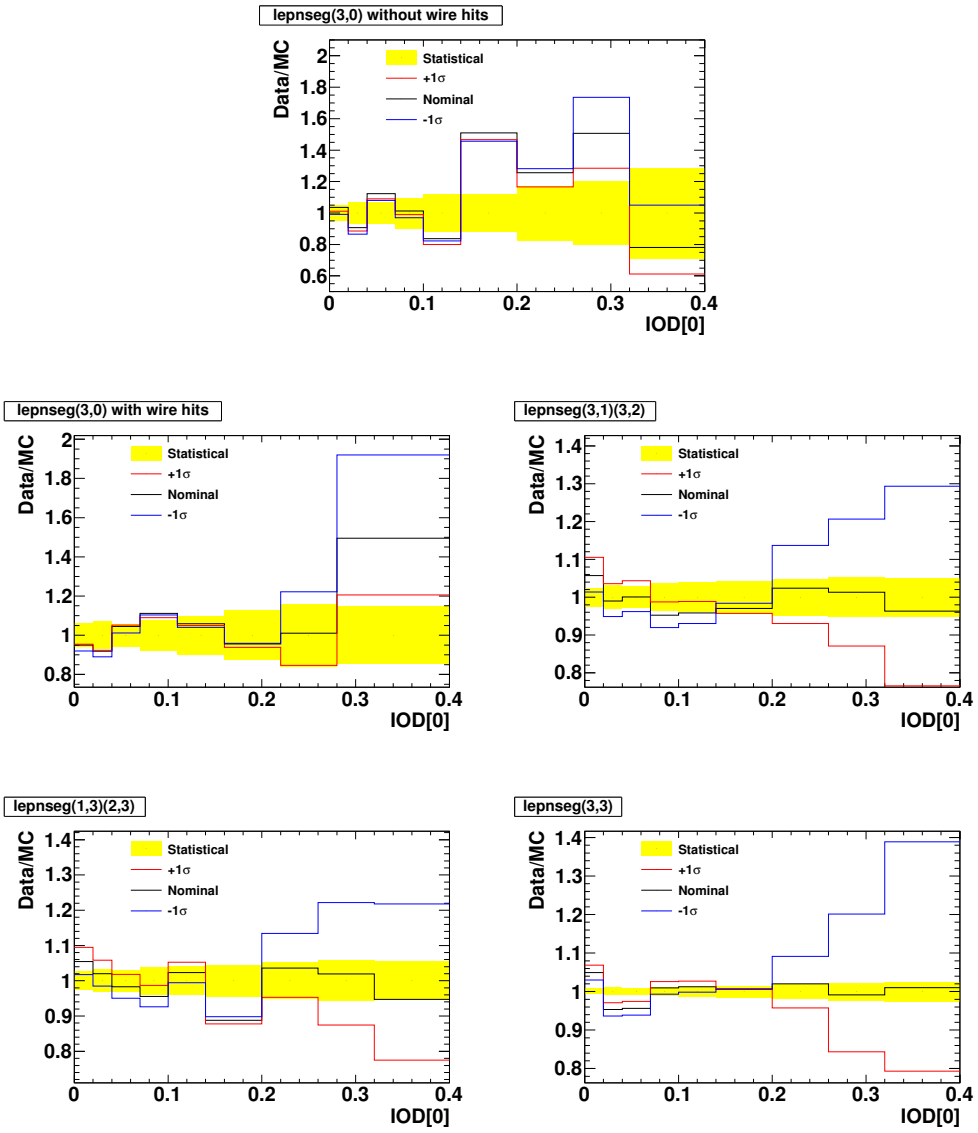

Figure 5.27: Data/MC ratios in $IOD[0]$ distribution after variation of the QCD background with all the other cuts applied for each *lepnseg* category. The yellow band represents the data statistical uncertainties. The plots are made by dropping the isolation requirement on $IOD[0]$ in the corresponding *lepnseg* category.

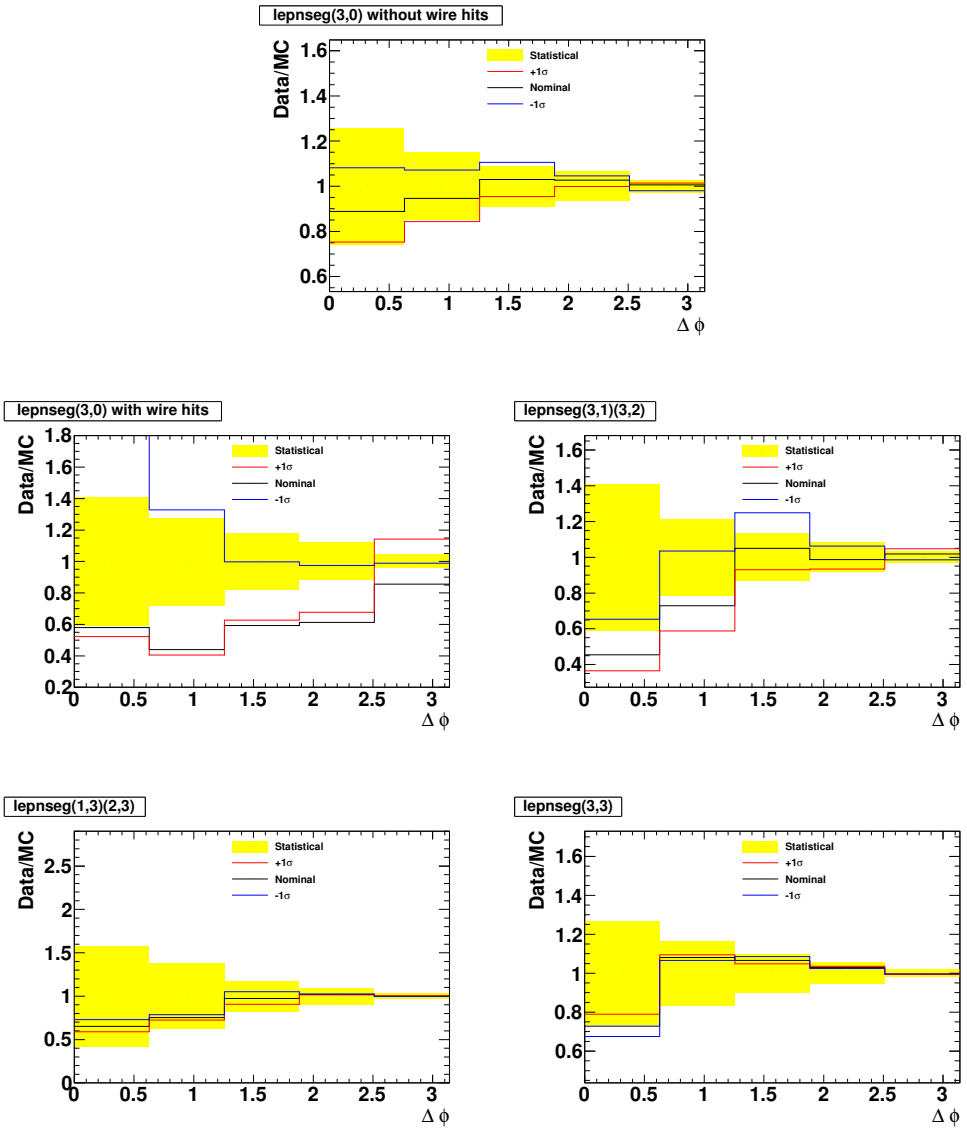

Figure 5.28: Data/MC ratios in $\Delta\phi$ distribution after variations of the $W+$ jet background rejected by isolation cuts for each *lepnseg* category. The yellow band represents the data statistical uncertainties. The plots are made by reversing the isolation requirement on $IOD[0]$ in the corresponding *lepnseg* category.

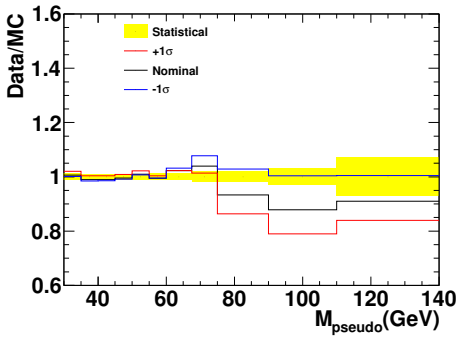

(a) No cuts on M_{pseudo}. Migration background uncertainty cross-check.

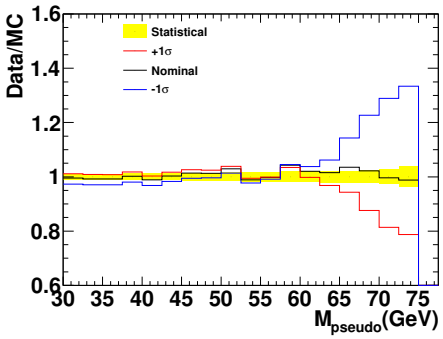

(b) No cuts on $M_{\mu\mu}$. Migration background uncertainty cross-check.

Figure 5.29: Data/MC ratios in $M_{\mu\mu}$ and M_{pseudo} distribution after variations of the migration background with all categories combined. The yellow band represents the data statistical uncertainties.

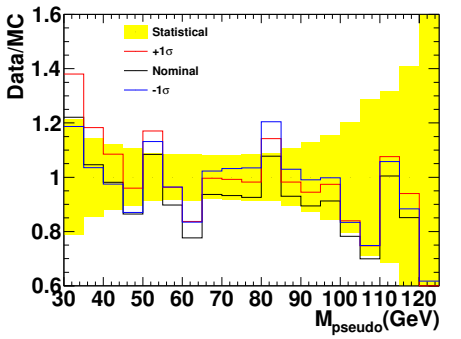

(a) No cuts on M_{pseudo}. FSR background control region.

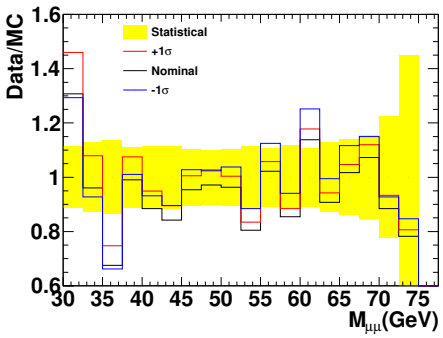

(b) No cuts on $M_{\mu\mu}$. FSR background control region.

Figure 5.30: Data/MC ratios in $M_{\mu\mu}$ and M_{pseudo} distribution after variations of the FSR background with all categories combined. The yellow band represents the data statistical uncertainties.

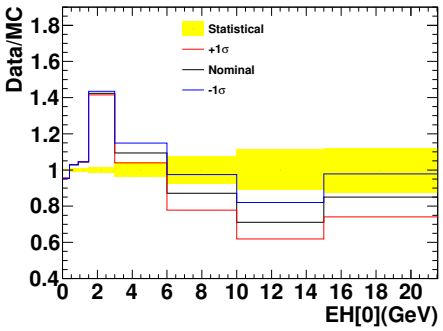

(a) All *lepnseg* categories combined.

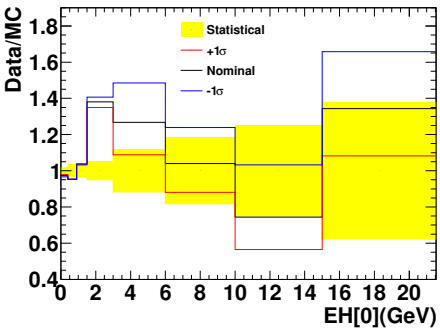

(b) *lepnseg*(3,1)(3,2) category.

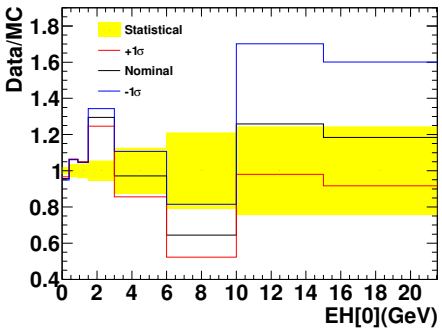

(c) *lepnseg*(1,3)(2,3) category.

Figure 5.31: Data/MC ratios in the $EH[0]$ distribution after variations of the $Z/\gamma^* \rightarrow \tau^+\tau^-$ background. The yellow band represents the data statistical uncertainties. The plots are made by dropping the requirement on $EH[0]$ in the corresponding *lepnseg* category.

5.6 The new scaling factor for the QCD background and overall normalisation in the low-mass region

In the QCD background, which is dominated by $g \to b\bar{b}$, the number of opposite sign (OS) events is expected to be slightly larger than the number of same sign (SS) events. In contrast, other physics background and signal events produce predominantly OS events, particularly noticeable is the $W+$ jet background, which has a strong preference of OS events over SS events. There are two main production mechanisms for the $W+$ jet background, the W boson can be formed via the annihilation of an up-type quark and a down-type quark with the jet coming from initial gluon radiations or via a scatter process where a down-type (up-type) quark couples to a W^- (W^+) boson and a up-type (down-type) quark. The scatter process tends to produce a final state of two muons of opposite charges, for instance, $s \to uW^-$ with $W^- \to \mu^-\bar{\nu}_\mu$ and subsequently $u \to dW^+$ with $W^+ \to \mu^+\nu_\mu$.

The number of QCD background events in the OS signal region is estimated by scaling up the number of SS events that pass all other signal region cuts by the OS/SS ratio determined in the QCD control region. The numbers of OS and SS events in the QCD control sample must be corrected for the expected contributions from all the non-QCD sources.

The MC predictions for $Z/\gamma^* \to \mu^+\mu^-$, $Z/\gamma^* \to \tau^+\tau^-$ and $W+$ jet are first normalised relative to each other and then they are normalised to data after the QCD background subtraction. The overall normalisation constant for the MC predictions S, expressed in terms of the OS/SS ratio R of the QCD background in the signal region and in the QCD control region, reads

$$S_1 = \frac{N_{OS1}^{data} - R_1 \times (N_{SS1}^{data} - S_1 \times N_{SS1}^{MC})}{N_{OS1}^{MC}} \tag{5.1}$$

and

$$S_2 = \frac{N_{OS2}^{data} - R_2 \times (N_{SS2}^{data} - S_2 \times N_{SS2}^{MC})}{N_{OS2}^{MC}}, \tag{5.2}$$

where the subscript "1" represents the signal region and the subscript "2" the QCD control region. N_{OS}^{MC} and N_{SS}^{MC} are the sum of the MC integral for OS and SS respectively including $Z/\gamma^* \to \mu^+\mu^-$, $Z/\gamma^* \to \tau^+\tau^-$ and $W+$ jet MC without normalising to data. N_{OS}^{data} and N_{SS}^{data} are the number of OS and SS events in data.

Rearranging the equations above gives

$$R_1 = \frac{N_{OS1}^{data} - S_1 \times N_{OS1}^{MC}}{N_{SS1}^{data} - S_1 \times N_{SS1}^{MC}} \tag{5.3}$$

and

$$R_2 = \frac{N_{OS2}^{data} - S_2 \times N_{OS2}^{MC}}{N_{SS2}^{data} - S_2 \times N_{SS2}^{MC}}. \tag{5.4}$$

The normalisation constant S and the OS/SS ratio R are assumed to be identical in both the signal and control regions and thus $R_1 = R_2 = R$ and $S_1 = S_2 = S$. As a result, we have a quadratic equation in terms of S. There exist two roots as the solution to the equation and we choose the root that is physical. Substituting S back to Equation 5.1 and Equation 5.2 gives the OS/SS ratio R in the QCD background. Since R in rapidity bins is consistent within the statistical uncertainty (See Table 5.5), the central value in the y-inclusive sample is taken as the OS/SS ratio R for all rapidity bins and the corresponding normalisation constant is calculated.

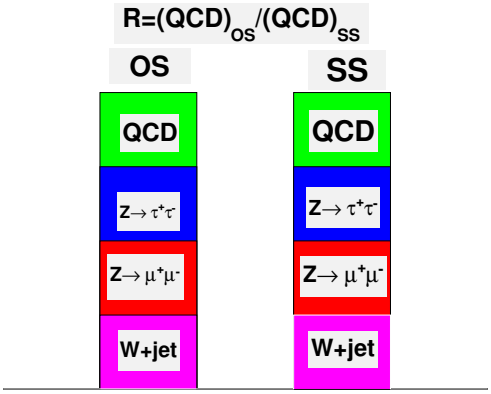

Figure 5.32: Schematic representations of the analytic method to calculate OS/SS ratio and normalisation constant.

OS/SS ratio R			
Category	y inclusive	$\|y\| < 1$	$1 \leq \|y\| < 2$
(3,0) with wire hits	1.00±0.17	1.00±0.16	1.00±1.48
(3,0) without wire hits	1.15±0.07	1.17±0.08	0.75±0.36
(3,1)(3,2)	1.12±0.10	1.11±0.10	1.17±0.38
(1,3)(2,3)	1.19±0.10	1.27±0.11	0.88±0.20
(3,3)	2.77±0.18	2.55±0.18	3.58±0.51

Table 5.5: OS/SS ratio R using the QCD control region and the signal region for each *lepnseg* category. Only statistical uncertainties are shown here.

5.7 Data-MC comparisons

In this section, data are compared to MC predictions in the signal sample passing all the selection criteria in the respective invariant mass regions.

5.7.1 Comparison to the detector-level MC in $70 < M_{\mu\mu} < 110$ GeV region

Data are compared to the detector-level MC for a number of variable distributions as presented in Figures 5.33–5.38. The distributions are shown for two dimuon rapidity regions $0 \leq |y| < 1$ and $1 \leq |y| < 2$. The MC predictions are in good agreement with data. However, if the MC predictions for the observable distribution that could potentially affect the ϕ^*_η distribution deviate from data, additional systematic uncertainty is assigned to cover data/MC differences, as described in Section 5.9. The discrepancies between data and MC in the $(z^0_{dca} + z^1_{dca})/2$ distribution have no effect on the measurement of the ϕ^*_η distribution.

5.7.2 Comparison to the detector-level MC in $30 < M_{\mu\mu} < 60$ GeV region

In this section, the data distributions of relevant physics quantities are compared to the detector-level signal plus background MC predictions as presented in Figure 5.39 and Figure 5.40. In general, we find that the MC describes the data to sufficient accuracy in the low-mass region.

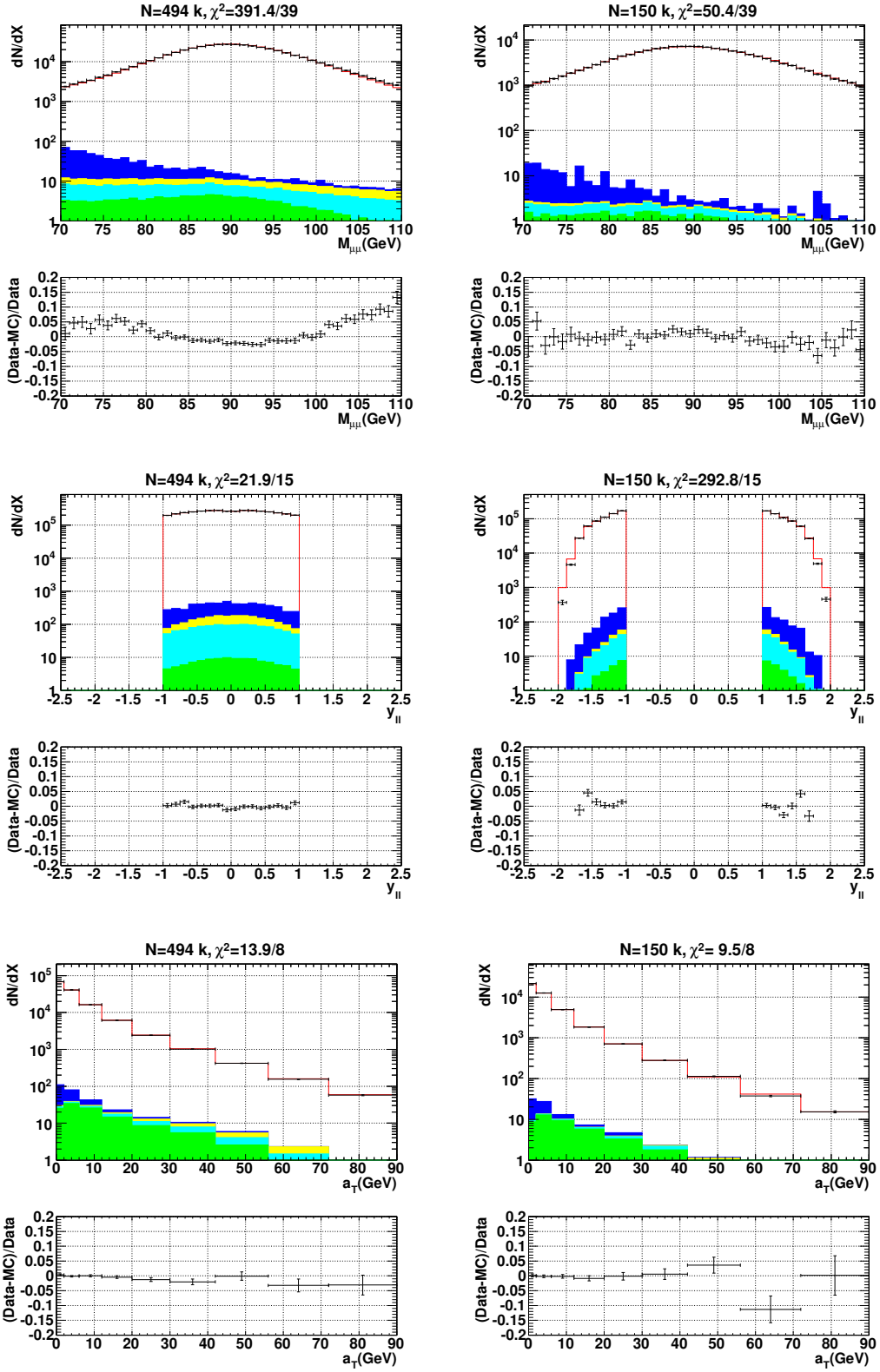

(a) $0 \leq |y| < 1$ (b) $1 \leq |y| < 2$

Figure 5.33: Data versus MC comparison in the distributions of $M_{\mu\mu}$, y_{ll} and a_T for $70 < M_{\mu\mu} < 110$ GeV.

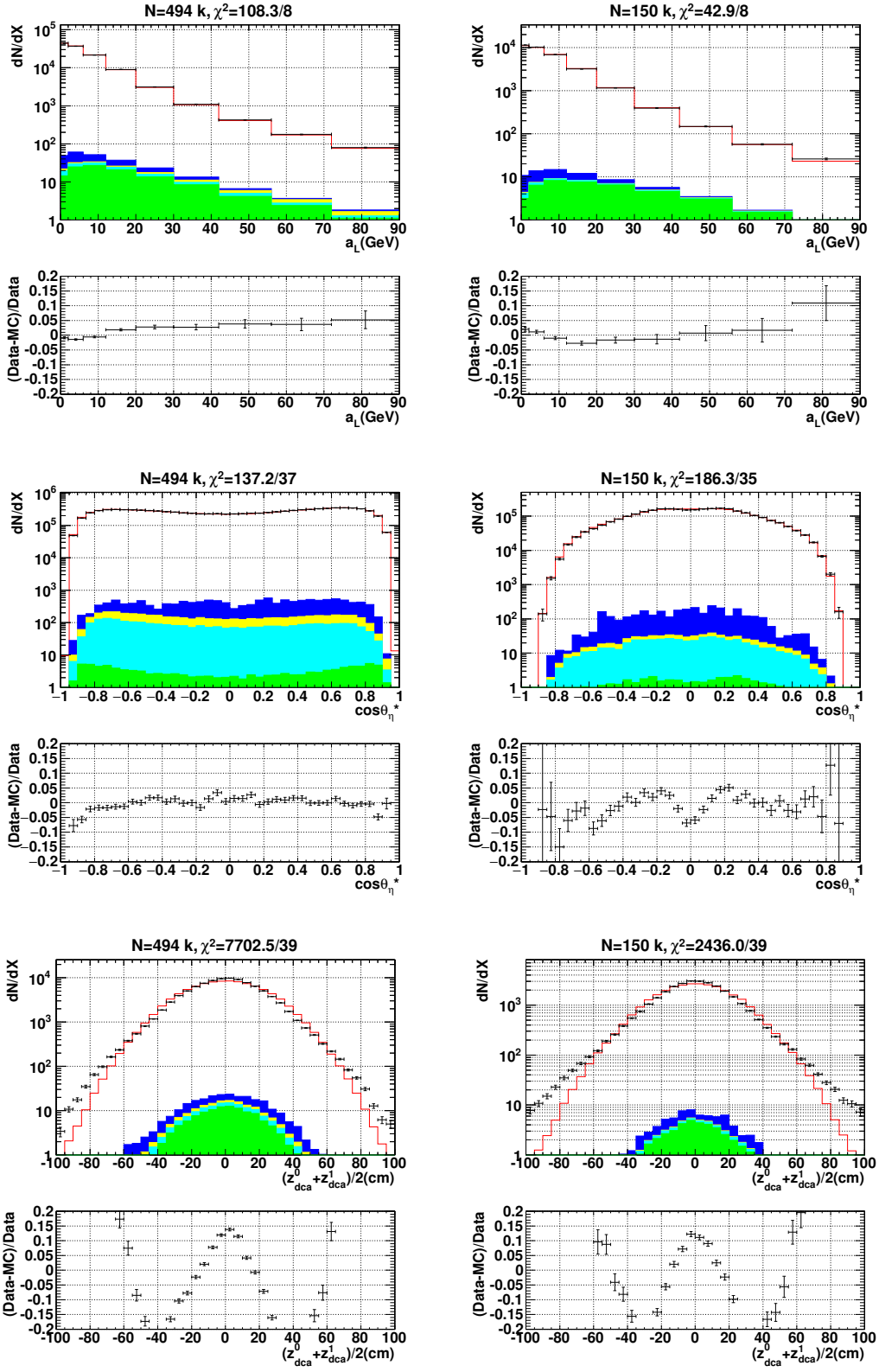

(a) $0 \leq |y| < 1$ (b) $1 \leq |y| < 2$

Figure 5.34: Data versus MC comparison in the distributions of a_L, $\cos\theta^*_\eta$ and $(z^0_{dca} + z^1_{dca})/2$ for $70 < M_{\mu\mu} < 110$ GeV.

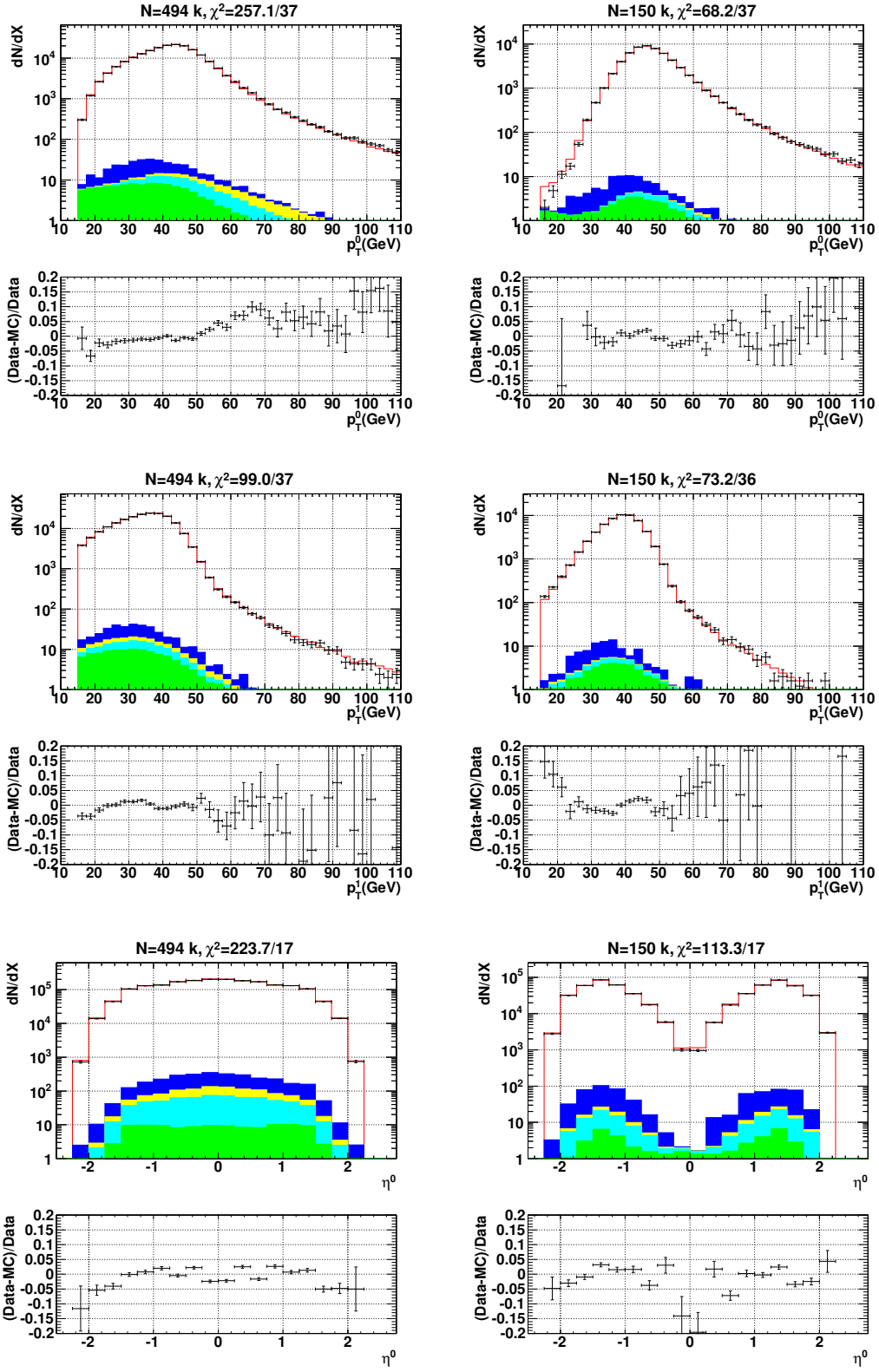

(a) $0 \leq |y| < 1$ (b) $1 \leq |y| < 2$

Figure 5.35: Data versus MC comparison in the distributions of p_T for muon 0 and muon 1 separately and η for muon 0 for $70 < M_{\mu\mu} < 110$ GeV.

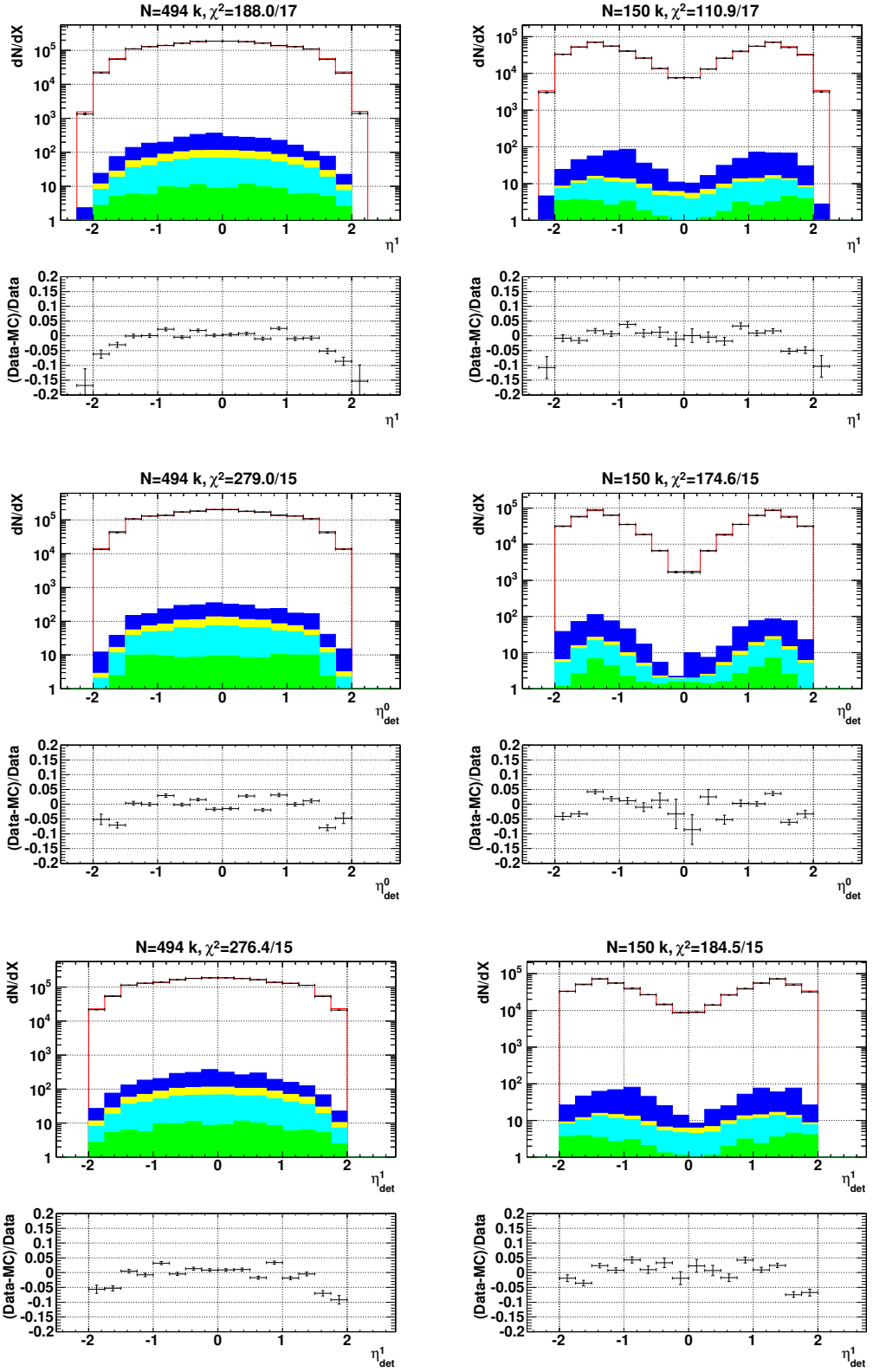

(a) $0 \leq |y| < 1$ (b) $1 \leq |y| < 2$

Figure 5.36: Data versus MC comparison in the distributions of η for muon 1 and η_{det} for muon 0 and muon 1 separately for $70 < M_{\mu\mu} < 110$ GeV.

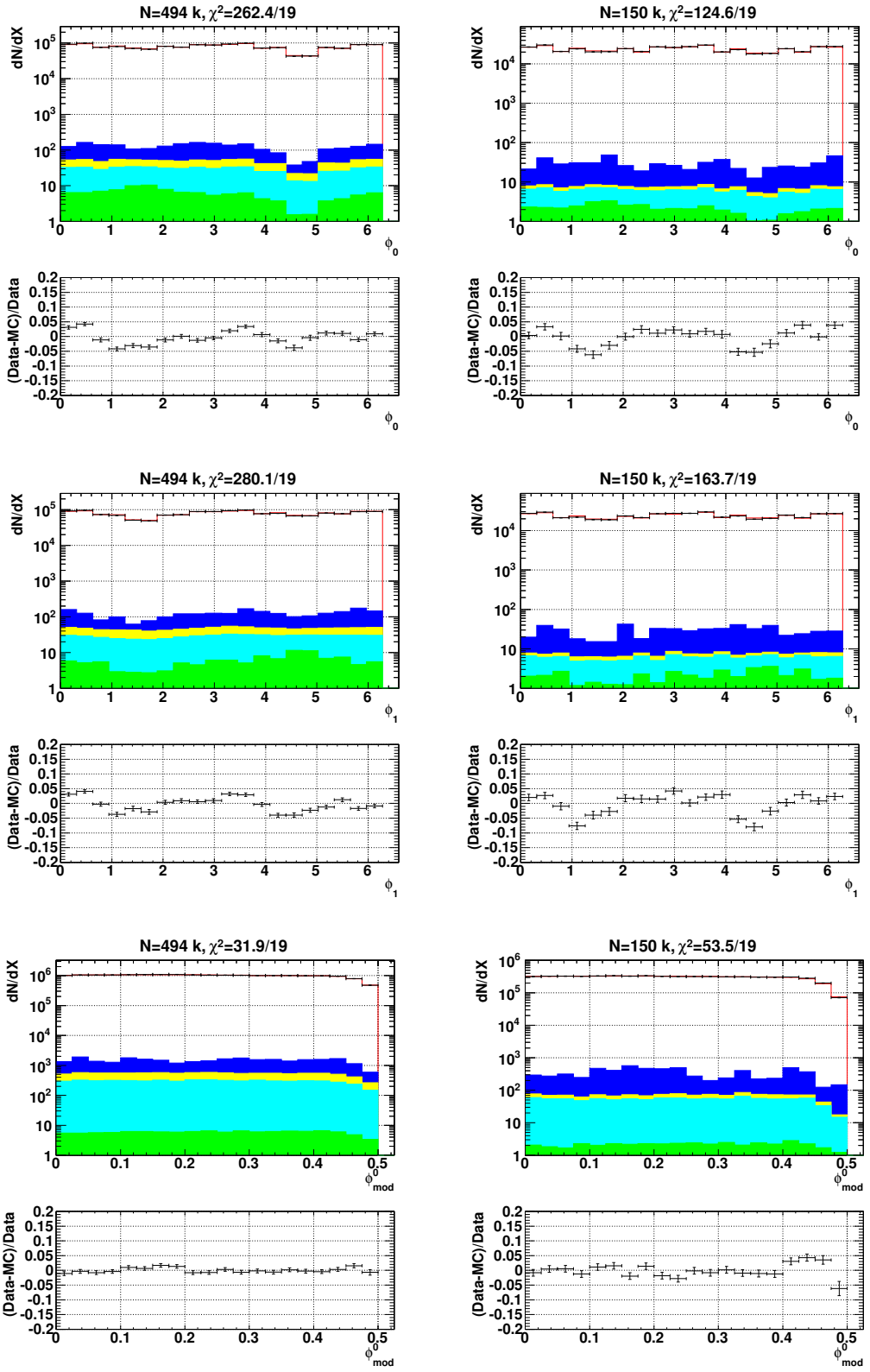

(a) $0 < |y| < 1$ (b) $1 < |y| < 2$

Figure 5.37: Data versus MC comparison in the distributions of ϕ for muon 0 and muon 1 separately and ϕ_{mod} for muon 0 for $70 < M_{\mu\mu} < 110$ GeV.

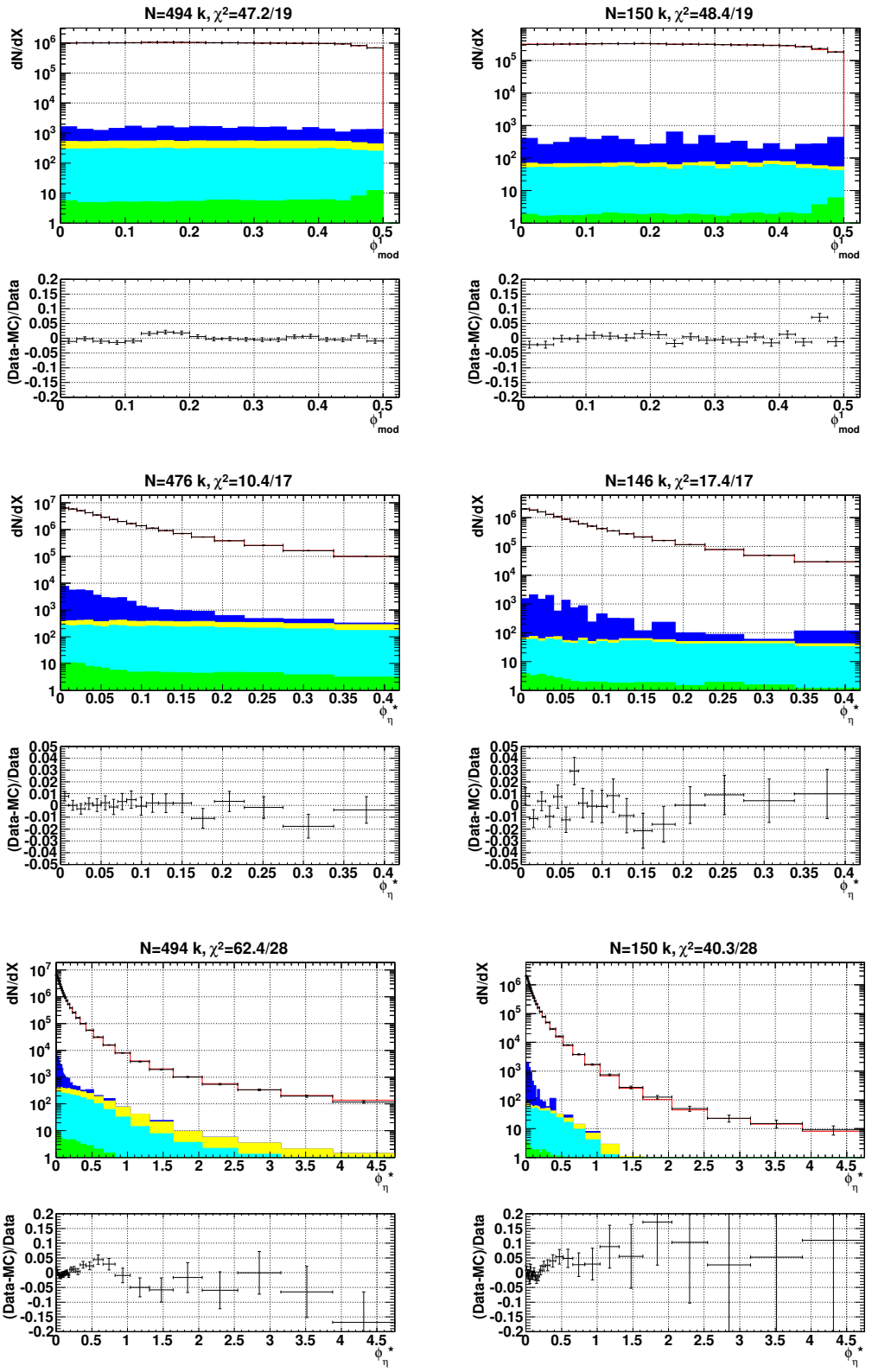

(a) $0 \leq |y| < 1$ (b) $1 \leq |y| < 2$

Figure 5.38: Data versus MC comparison in the distributions of ϕ_{mod} for muon 1 (top), low ϕ^*_η region (middle) and the full range in ϕ^*_η (bottom) for $70 < M_{\mu\mu} < 110$ GeV.

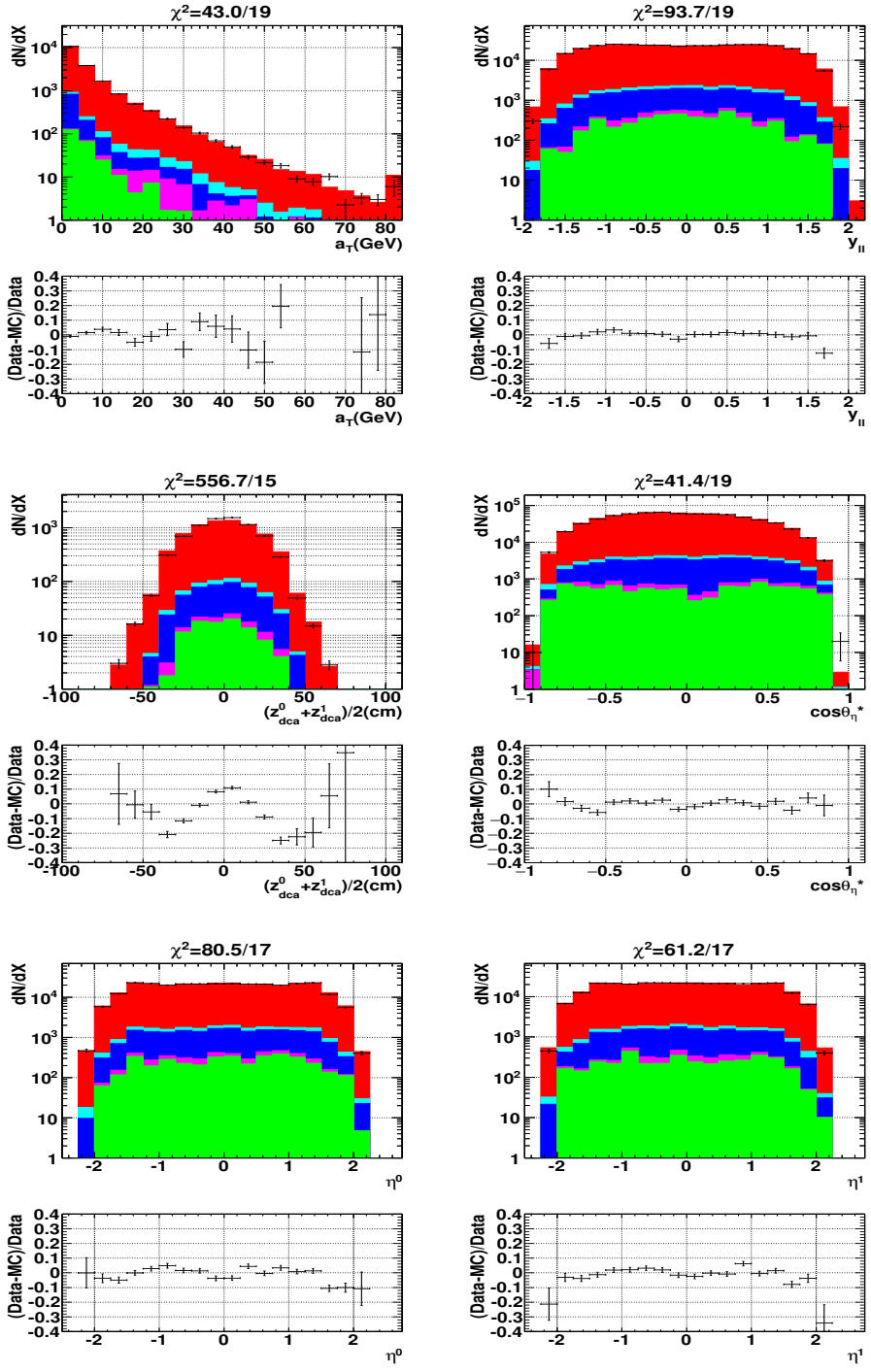

Figure 5.39: Data versus MC comparison for the distributions of a_T, y_{ll}, $(z^0_{dca} + z^1_{dca})/2$, $\cos\theta^*_\eta$, η^0 and η^1 for $30 < M_{\mu\mu} < 60$ GeV.

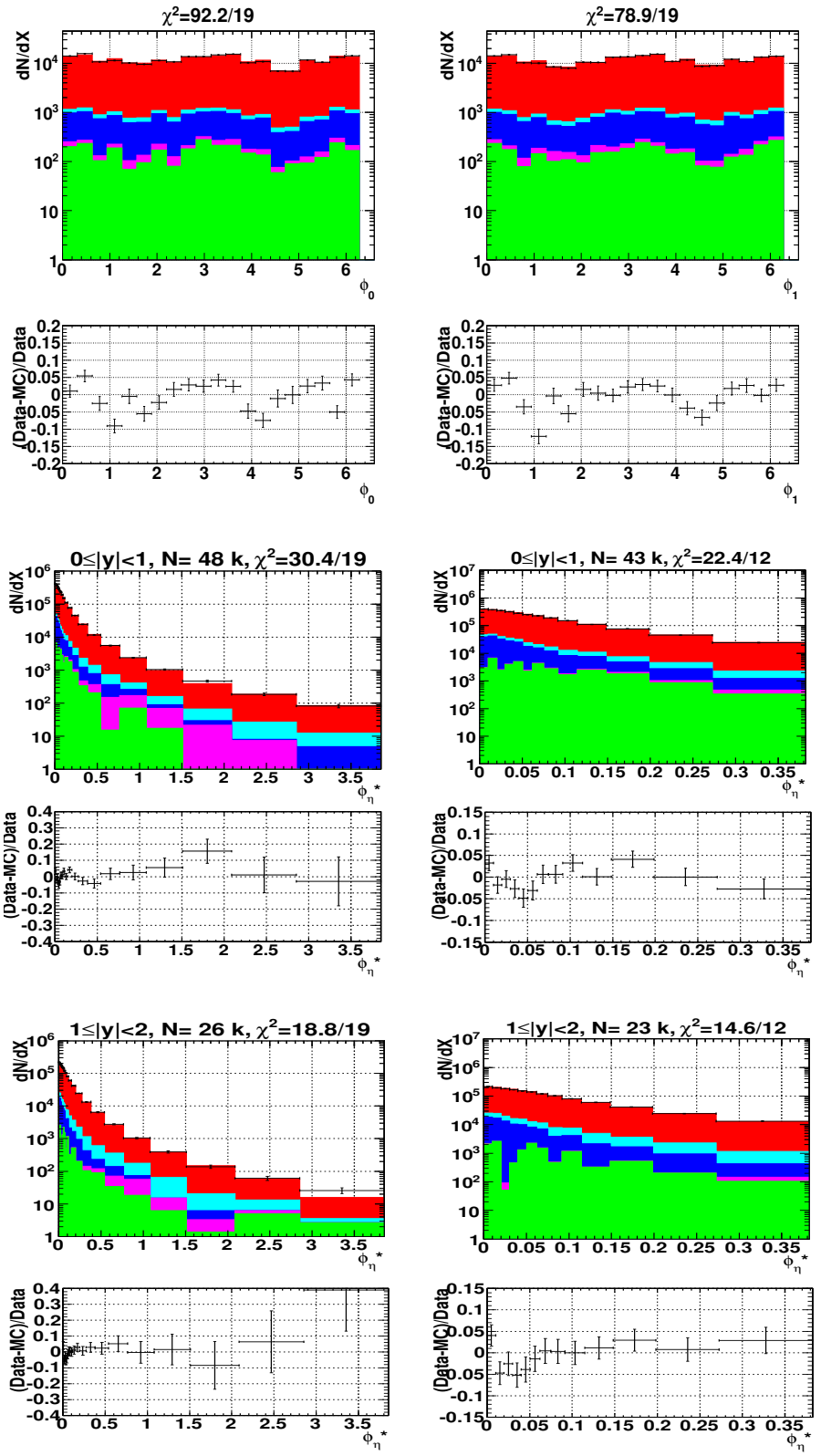

Figure 5.40: Data versus MC comparison for the distributions of ϕ_0 (top left), ϕ_1 (top right), full range in ϕ^*_η (middle and bottom left) and low ϕ^*_η region (middle and bottom right) in two bins of rapidity for $30 < M_{\mu\mu} < 60$ GeV.

5.8 Bin-by-bin corrections

5.8.1 Binning in ϕ_η^*

Peak region

The binning in ϕ_η^* is the same as that used in the previously published analysis [25], where 29 bins are used with the bin width in terms of the bin number i expressed as: $0.01 + 5 \times 10^{-8} \times (i-1)^5$ $(i \geq 1)$. The bin width increases with bin number in order to obtain enough statistics.

Low-mass region

There are 20 bins for the ϕ_η^* distribution, and the bin number i corresponds to a bin width of $0.01 + 4 \times 10^{-7} \times (i-1)^5$ $(i \geq 1)$.

5.8.2 Bin-by-bin corrections

Because the resolution in ϕ_η^* is much better than the width of the above-specified bins leading to high bin purity, a bin-by-bin correction procedure can be applied to correct data back to the particle level. Bin purity is defined as the fraction of events in each bin at detector level that originate from the same bin at generator level determined using $Z/\gamma^* \to \mu^+\mu^-$ Pythia MC.

Peak region

Figure 5.41 demonstrates that the bin purity in ϕ_η^* is adequate to perform such a procedure. The bin-by-bin correction factors are presented in Figure 5.42 with the data statistical uncertainties indicated by the yellow band.

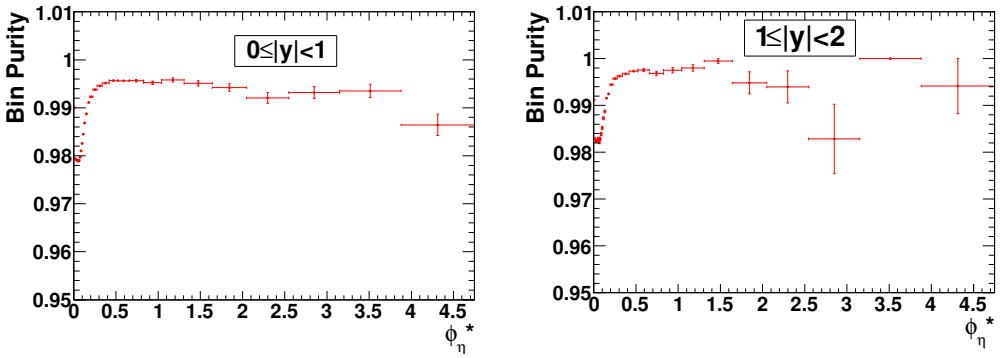

Figure 5.41: Bin purity as a function of ϕ_η^* in two rapidity bins for $70 < M_{\mu\mu} < 110$ GeV.

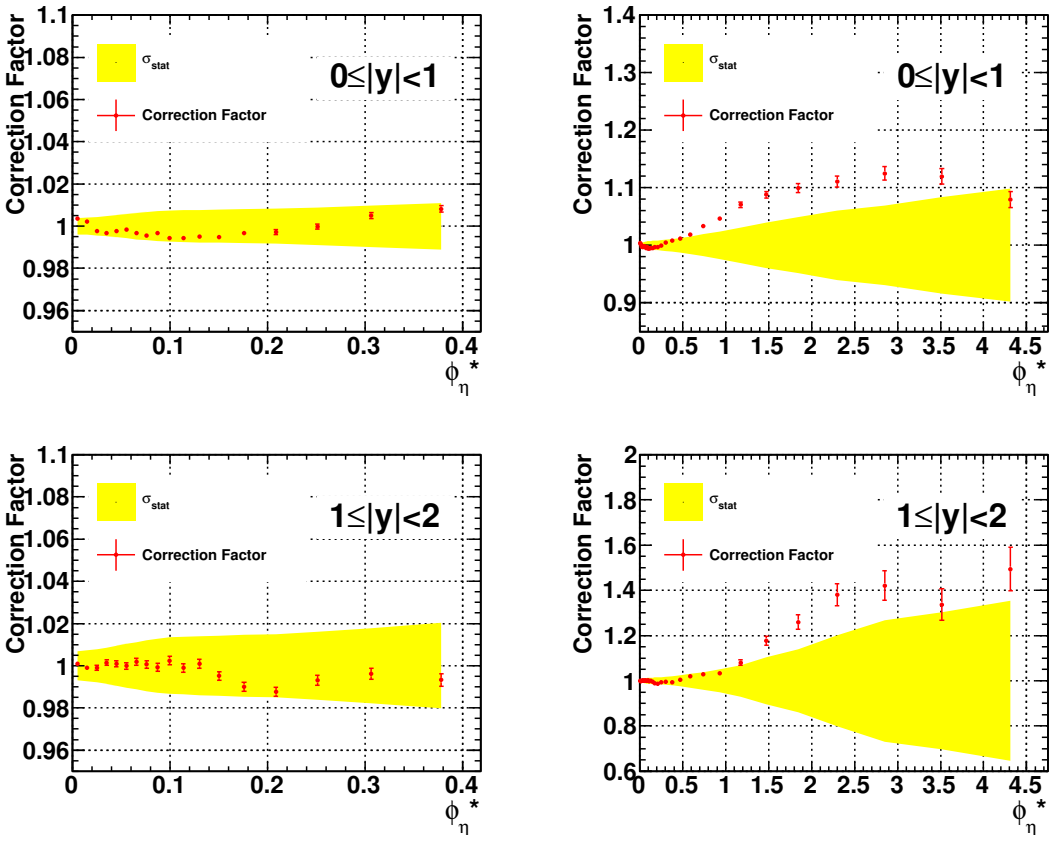

Figure 5.42: Correction factor as a function of ϕ^*_η in two rapidity bins for $70 < M_{\mu\mu} < 110$ GeV. The yellow band represents the data statistical uncertainties.

Low-mass region

The QCD, $Z/\gamma^* \to \tau^+\tau^-$ and $W+$ jet backgrounds are subtracted from the observed data. The migration background is not subtracted. It is taken into account in evaluating the correction factor described below.

Figure 5.43 indicates that the experimental resolution in ϕ^*_η is sufficient to employ bin-by-bin corrections.

The bin-by-bin correction factor within different rapidity ranges is demonstrated in Figure 5.44. The yellow band represents the data statistical uncertainty.

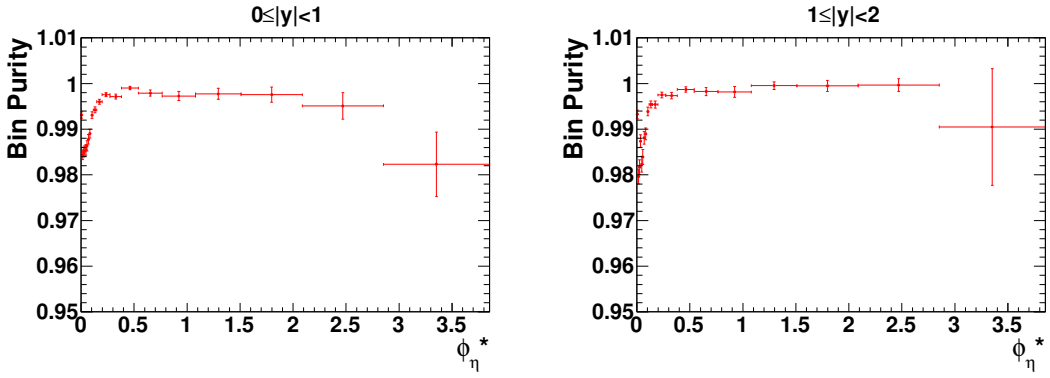

(a) (b)

Figure 5.43: Bin purity as a function of ϕ^*_η in two rapidity bins for $30 < M_{\mu\mu} < 60$ GeV.

5.9 Systematic uncertainties

Figure 5.45 and Figure 5.46 show the systematic uncertainties in each bin of ϕ^*_η in comparison to the statistical uncertainty in the peak and low mass regions respectively. The statistical uncertainties are dominant across all bins of ϕ^*_η. Most of the uncertainties have been evaluated in a fashion consistent with the previously published analysis [25] and the associated variable distributions for the assigned systematics can be found in [71].

- **Background uncertainty**
  - ***WW* and $t\bar{t}$ backgrounds in the peak region**

    The normalisation for WW and $t\bar{t}$ backgrounds are varied by $\pm 20\%$, which is roughly the fractional theoretical uncertainty on the cross sections of these backgrounds.

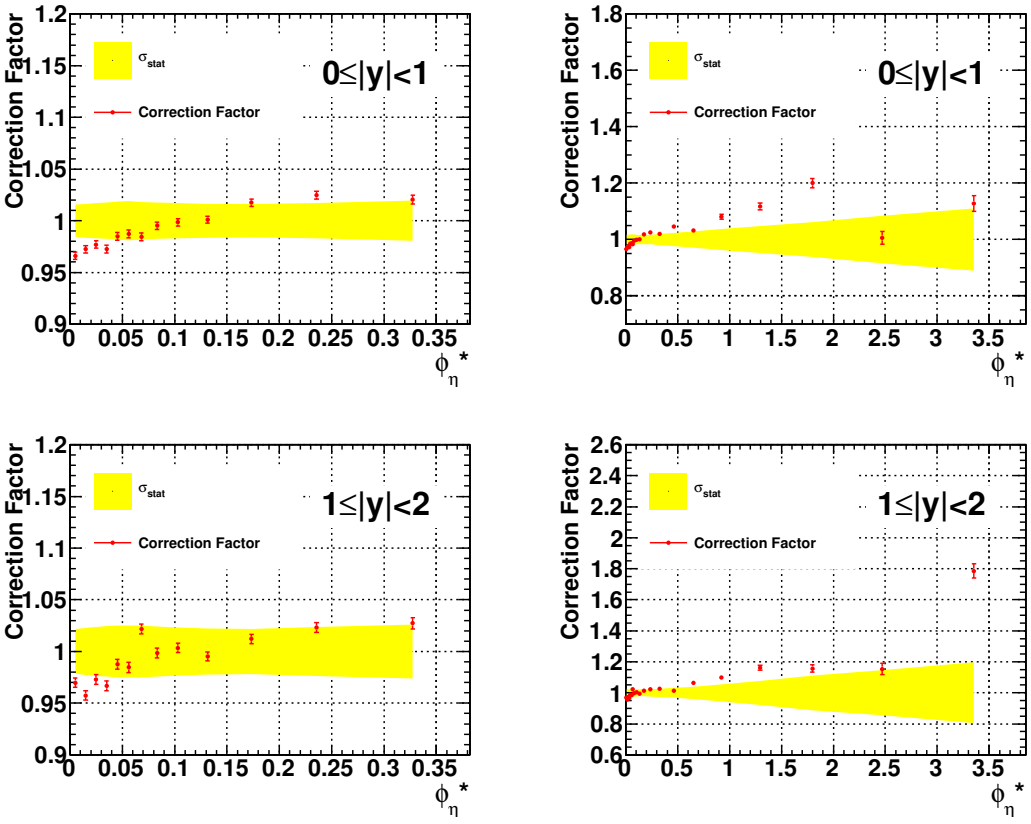

Figure 5.44: Correction factor as a function of ϕ_η^* in two rapidity bins for $30 < M_{\mu\mu} < 60$ GeV. The yellow band represents the data statistical uncertainties.

- **Multijet background in the peak region**

  A ±100% variation in the multijet background is made, which is considered to be conservative. The multijet background is below 0.1% in the peak region such that its effect on the final ϕ^*_η shape is considerably small.

- **Background uncertainties in the low-mass region**

  Each source of physics background is varied up or down by the scale factor in the corresponding *lepnseg* category as shown in Table 5.3.

- **FSR modelling**

  Events with $\Delta_{QED} > 0.5$ GeV are varied by a factor of two in the peak region, where Δ_{QED} is the difference of invariant mass between the Born level and the bare level. As for the low-mass region, events with $\Delta_{QED} > 0.5$ GeV meeting the requirement of a genuine muon pair in addition to a photon or electron at generator level are varied by ±50%. The relatively conservative procedure for evaluating the FSR modelling in the peak region has a negligible effect on the ϕ^*_η distributions because the ϕ^*_η shape is similar with or without FSR in the peak region. However, the ϕ^*_η shape in the low mass region is different for events undergoing FSR and events without FSR as shown in Figure 5.21 in Section 5.5.

- **Momentum resolution and scale**

  The muon momentum scale is varied by ±0.3%. An additional Gaussian smearing with width of 0.001 GeV^{-1} is applied. The systematic variations are such that the systematic uncertainties can cover any difference in data/MC ratios in $M_{\ell\ell}$.

- **Track ϕ and η resolution**

  The ϕ and η resolution parameters are varied by a factor of 1.5, which is a reasonable estimate of the uncertainties on these parameters.

- **Efficiency corrections**

  The ϕ_{mod} and η_{det} distributions are sensitive to efficiency corrections. A ±5% and ±10% variation in the muon reconstruction efficiency is considered to be a reasonable evaluation of the systematic uncertainty for (i) the octant gap region ($\phi_{mod} > 0.45$); (ii) the forward region ($|\eta_{det}| > 1$). Figures 5.47 and 5.48 show the data/MC ratio for ϕ_{mod} and η_{det} distributions with these relative variations applied. An additional ±10% variation in muon reconstruction efficiency is applied to forward rapidity region ($1 < |y| < 2$) to compensate for the data-MC difference.

- **Physics Bias**

  This uncertainty is estimated by multiplying or dividing the K factor determined by the ratio of unfolded data to that of RESBOS in the corresponding mass region to examine the sensitivity of the bin-by-bin corrections to the underlying physics distributions. Figure 5.49 shows the K factor as a function of ϕ^*_η determined in the peak region. The systematic effect on the corrected ϕ^*_η shape is negligible due to the excellent resolution of this variable.

- **Trigger match**

  Around 1.7% events are with $n_{seg} = 3$ muon having passed the trigger match but failed firing the single muon trigger at all three levels. These events were found to be less isolated and were treated as additional systematic uncertainties. It is estimated by switching on and off the single muon trigger.

- **Ad hoc corrections**

  The difference between switching on and off the ad hoc corrections in Section 5.3.4 is treated as an additional source of systematic uncertainty.

- **p_T turn-on effect in the low-mass region**

  Events with $p_T < 15$ GeV are scaled up/down by 10% to evaluate the systematic uncertainty due to additional trigger efficiency corrections. Such a systematic variation is conservative considering the good agreement between data and MC in the muon transverse momentum distribution as shown in Figure 5.14.

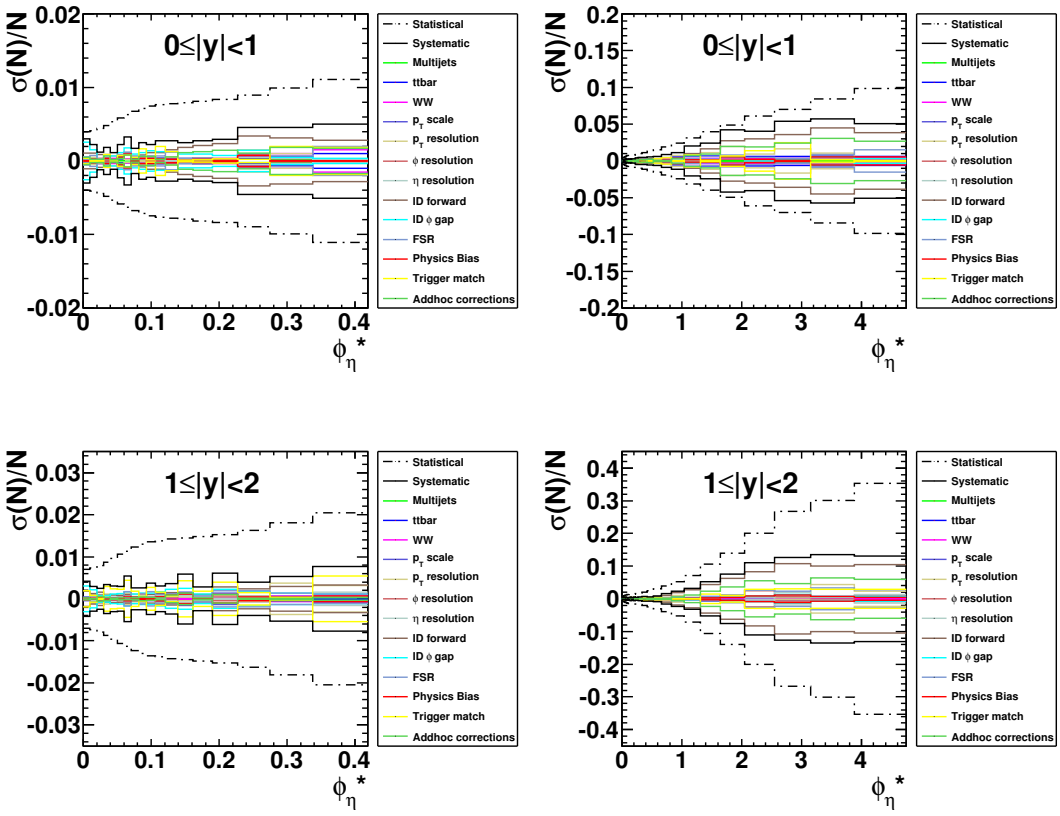

Figure 5.45: Comparison between various experimental systematic uncertainties and the statistical uncertainty as a function of ϕ^*_η in $70 < M_{\ell\ell} < 110$ GeV region. The figure on the left (right) presents the low (full) range of ϕ^*_η.

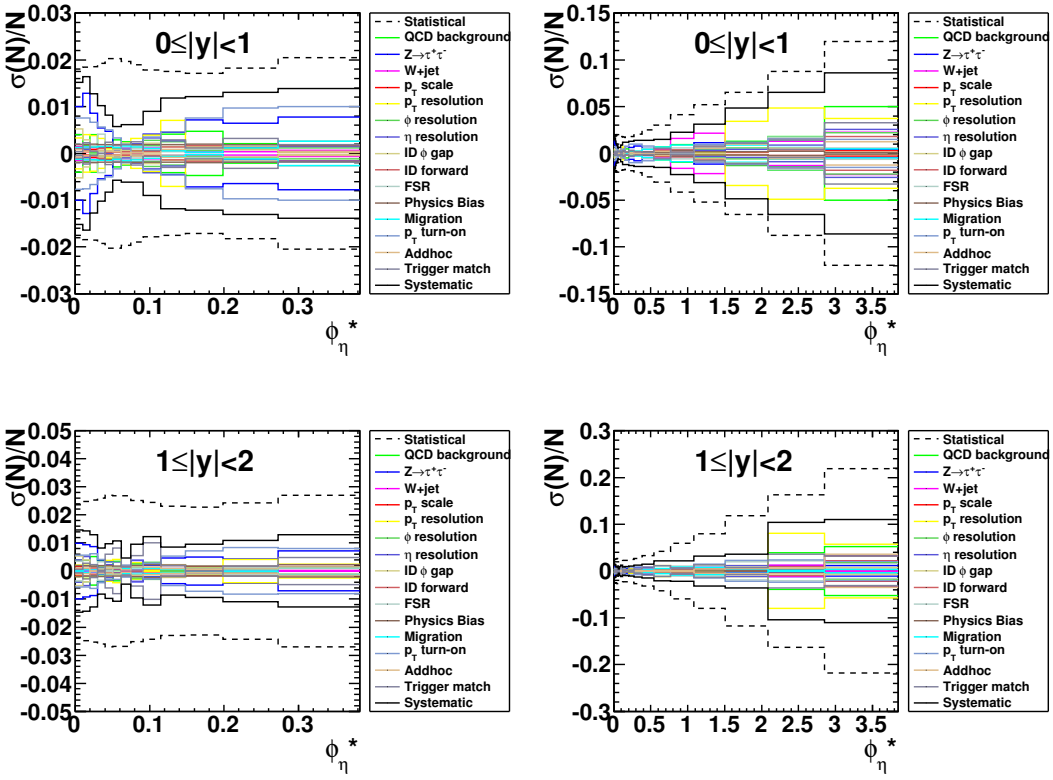

Figure 5.46: Comparison between various experimental systematic uncertainties and the statistical uncertainty as a function of ϕ_η^* in $30 < M_{\ell\ell} < 60$ GeV region. The figure on the left (right) presents the low (full) range of ϕ_η^*.

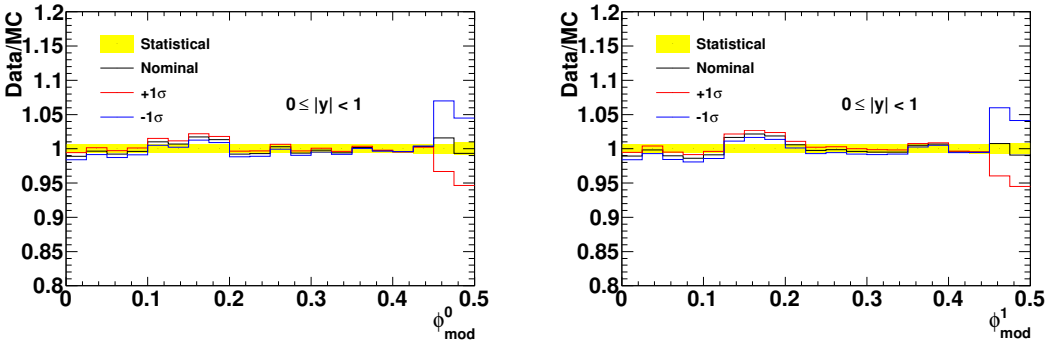

(a) $0 \leq |y| < 1$ (b) $0 \leq |y| < 1$

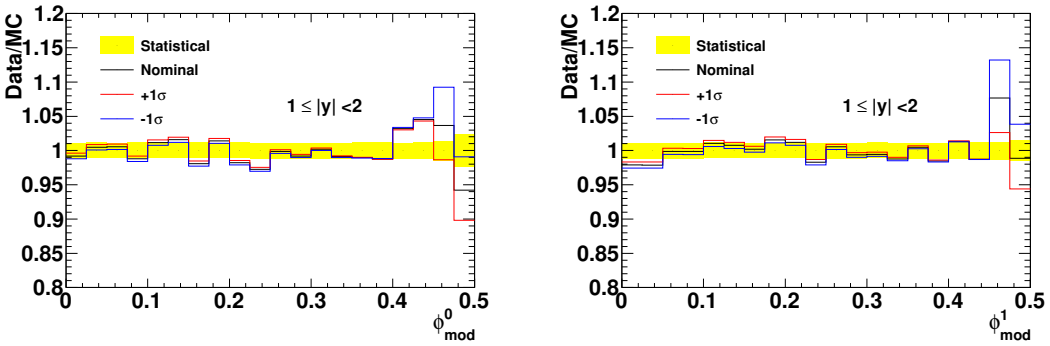

(c) $1 \leq |y| < 2$ (d) $1 \leq |y| < 2$

Figure 5.47: Data/MC ratios in the distribution of ϕ_{mod} arising from the muon ID efficiency systematic variations in the octant gap region for $70 < M_{\ell\ell} < 110$ GeV. The yellow band represents the data statistical uncertainty.

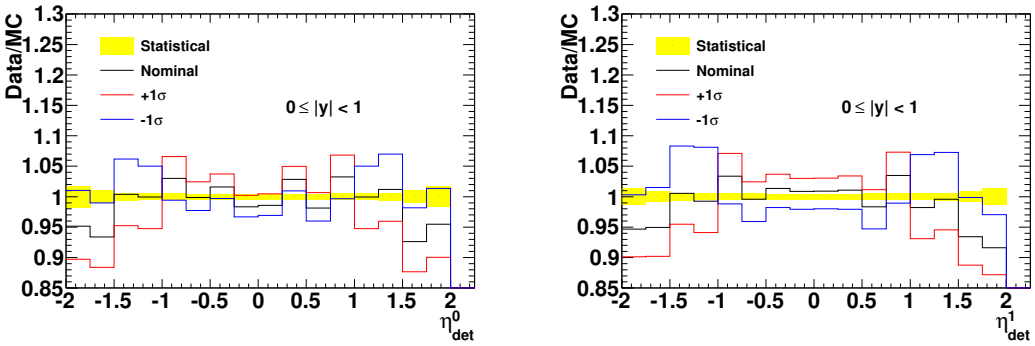

(a) $0 \leq |y| < 1$ (b) $0 \leq |y| < 1$

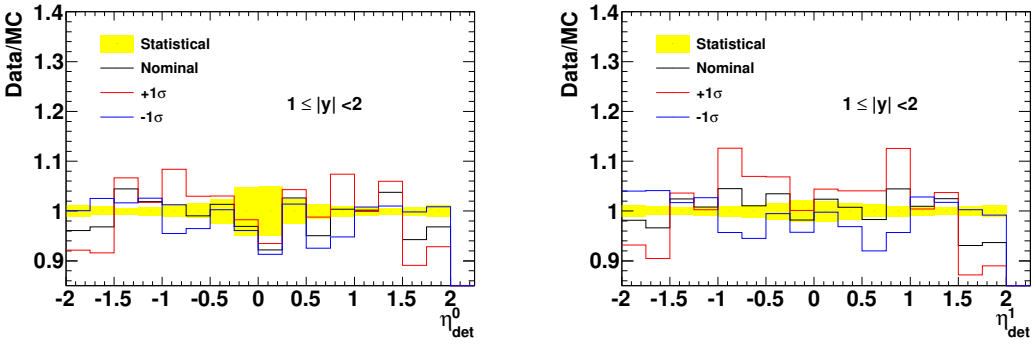

(c) $1 \leq |y| < 2$ (d) $1 \leq |y| < 2$

Figure 5.48: Data/MC ratios in the distribution of η_{det} arising from the muon ID efficiency systematic variations in the forward region for $70 < M_{\ell\ell} < 110$ GeV. The yellow band represents the data statistical uncertainty.

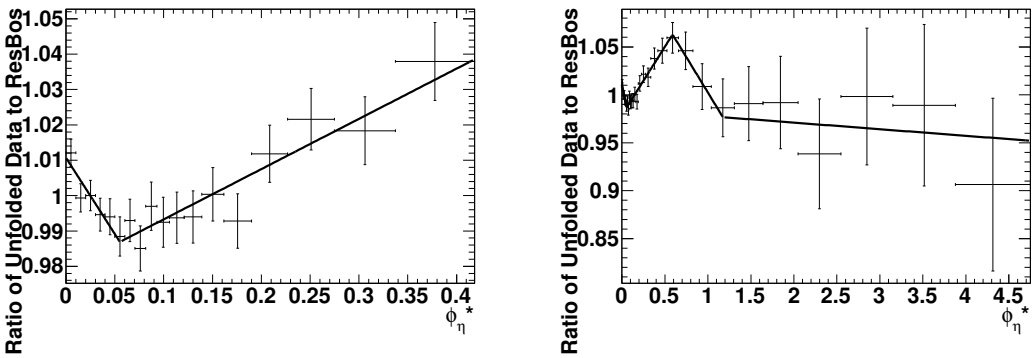

Figure 5.49: Ratio of the unfolded data to the ResBos default prediction for $70 < M_{\ell\ell} < 110$ GeV.

5.10 Comparison to theoretical predictions

5.10.1 Theoretical predictions

The corrected data have been compared to the RESBOS [24,31] predictions and the NNLL+NLO calculations of [34,35].

ResBos

RESBOS generates Z boson events at NNLL+NNLO accuracy. Both the γ^* and Z/γ^* interference contributions are included at NNLL+NLO accuracy. The GNW non-perturbative parameterization in the RESBOS prediction contains a non-perturbative parameter a_Z that must be determined from experimental data. We choose the central values and associated systematic variations for QCD scales and a_Z by following the prescriptions in [24]. The NNLO PDF sets CT10 [72] are implemented in RESBOS and PHOTOS [68] is used to simulate the effects of FSR. The PDF uncertainties of the ϕ^*_η distributions are evaluated by varying each of the 26 eigenvectors in the CT10 PDF sets by 1.6σ corresponding to 90% confidence level.

A NNLL+NLO prediction

The NNLL+NLO predictions of [34,35] use the CTEQ6m [73] NLO PDFs without the effects of FSR or non-perturbative contributions. The central prediction is obtained by setting QCD scales to the dilepton invariant mass at Born level. The scale uncertainties are estimated by varying the three QCD scales[6] between $M_{\ell\ell}/2$ and $2M_{\ell\ell}$, and the ratio of any two of the three QCD scales is required to be bound between 0.5 and 2. The PDF uncertainties are considered negligible in comparison to the QCD scale uncertainties as explained in [34,35].

5.10.2 Results

Peak region

Figure 5.50 presents the comparison of the corrected distributions of ϕ^*_η with predictions from RESBOS in the dimuon channel for two rapidity bins. Figure 5.51 shows the ratio in $(1/\sigma) \times (d\sigma/d\phi^*_\eta)$ of the measured data to that of RESBOS for $70 < M_{\ell\ell} < 110$ GeV. The RESBOS predictions can describe the corrected data distributions accurately within the assigned theoretical uncertainties. In addition, the

[6]The three QCD scales refer to the renormalisation, factorization and resummation scales.

consistency between the updated ϕ^*_η distributions in the dimuon channel and these published measurements in the dielectron channel provides a powerful cross-check.

Figure 5.52 presents the ratio in $(1/\sigma) \times (d\sigma/d\phi^*_\eta)$ of the measured data to the NNLL+NLO predictions from [34, 35]. The NNLL+NLO predictions can describe the detailed ϕ^*_η shape within the assigned QCD scale uncertainties, which are dominated by systematic variations in the resummation scale.

The ratio of the $(1/\sigma) \times (d\sigma/d\phi^*_\eta)$ distribution in the central rapidity region ($|y| < 1$) to that in the forward rapidity region ($1 < |y| < 2$) is illustrated in Figure 5.53. The theoretical predictions from both RESBOS and NNLL+NLO can describe the ratio as a function of ϕ^*_η. The systematic variations for the theoretical uncertainties are performed in a correlated way between the two rapidity regions, and such a procedure leads to a significant reduction in the theoretical uncertainties because of partial cancellations in the ratio. Therefore this ratio with reduced theoretical uncertainties provides a more stringent test of the QCD calculations.

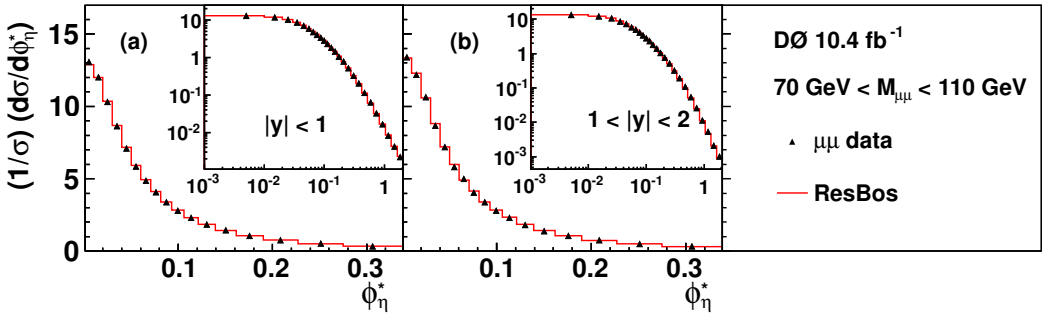

Figure 5.50: Comparison between the measured $(1/\sigma) \times (d\sigma/d\phi^*_\eta)$ and predictions from RESBOS for dimuon events with $70 < M_{\mu\mu} < 110$ GeV in two rapidity bins.

Low-mass region

Figure 5.54 presents the comparison between the measured $(1/\sigma) \times (d\sigma/d\phi^*_\eta)$ with predictions from RESBOS for dimuon events with $30 < M_{\ell\ell} < 60$ GeV in two rapidity bins. The ratio of the measured ϕ^*_η distribution to the predictions from RESBOS is shown in Figure 5.55. The RESBOS predictions can describe the ϕ^*_η shape with reasonable accuracy. However, there is around 20% deficiency from the RESBOS predictions at $\phi^*_\eta > 0.5$, which may be due to a lack of higher order QCD corrections for the γ^* and the Z/γ^* interference contributions. The NNLL+NLO predictions can describe the detailed ϕ^*_η shape accurately within the assigned theoretical uncertainties as shown in Figure 5.56.

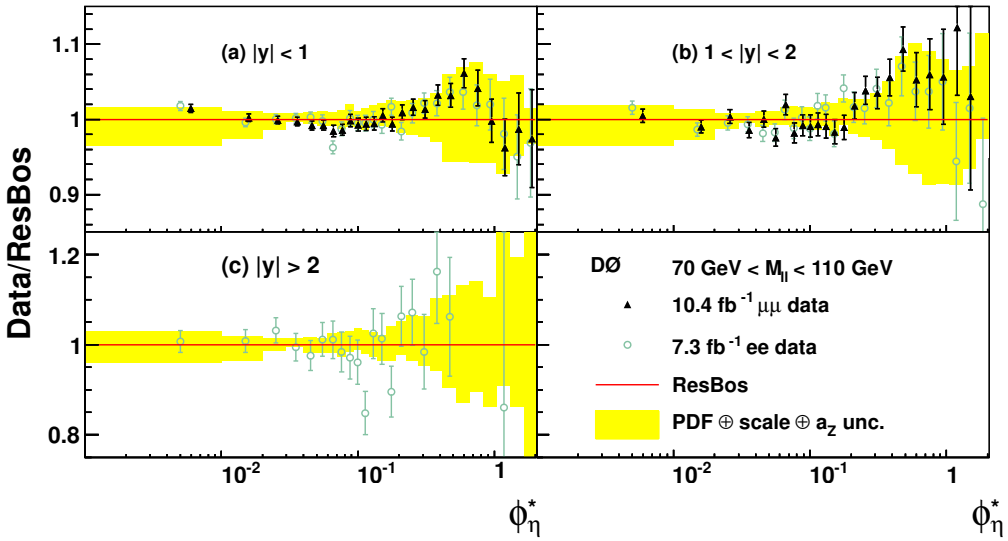

Figure 5.51: Ratio of the corrected ϕ^*_η distributions separately for different rapidity bins of the dielectron and dimuon data to the ResBos predictions for $70 < M_{\ell\ell} < 110$ GeV. The red histograms represent the default ResBos prediction and the yellow band corresponds to the theoretical uncertainty by adding uncertainties for PDFs, QCD scales and the non-perturbative parameter a_Z in quadrature.

High-mass region

A detailed description of the high-mass measurements of ϕ^*_η distributions can be found in [74] and it is shown here for completeness. The data precision is limited by the small statistics in the high-mass region. Figure 5.57 compares the measured ϕ^*_η distributions with the ResBos predictions and Figure 5.58 shows the ratio to the ResBos predictions. The ResBos predictions can describe data reasonably well in the high-mass region.

Comparison between the low-mass and the peak region

Figure 5.59 compares the ϕ^*_η distributions between $30 < M_{\ell\ell} < 60$ GeV and $70 < M_{\ell\ell} < 110$ GeV. As discussed at the start of this chapter, the width of the ϕ^*_η distribution is predicted to increase with decreasing $M_{\ell\ell}$. The measurement agrees with the prediction as shown in Figure 5.59 and ResBos can describe this feature reasonably well.

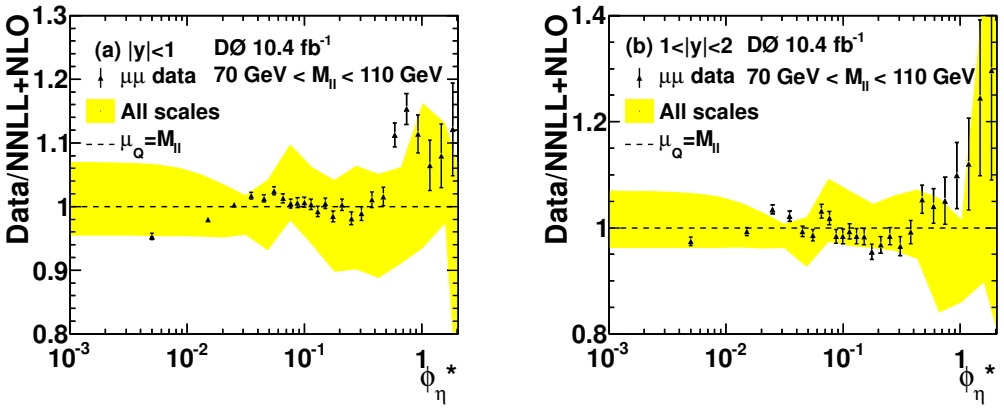

Figure 5.52: Ratio of the corrected ϕ^*_η distributions separately for two rapidity bins of the dimuon data to the NNLL+NLO predictions of Ref. [34, 35] for $70 < M_{\ell\ell} < 110$ GeV. The bold line corresponds to the default NNLL+NLO prediction and the yellow band indicates the theoretical uncertainty by varying QCD scales.

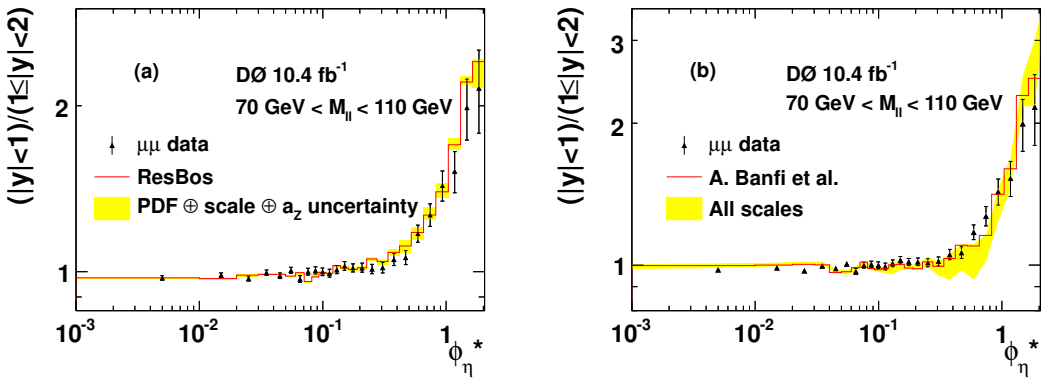

Figure 5.53: Ratio of the corrected $(1/\sigma) \times (d\sigma/d\phi^*_\eta)$ distribution in the central rapidity region ($0 \leq |y| < 1$) to that in the forward rapidity region ($1 \leq |y| < 2$). The corrected dimuon data are compared to the predictions from (a) ResBos and from (b) NNLL+NLO [34, 35]. The data are shown with error bars representing the total uncertainties, assuming uncorrelated uncertainties between the two rapidity regions. The red histograms denote the default theoretical prediction and the yellow bands represent the theoretical uncertainties, accounting for correlations between the two rapidity regions.

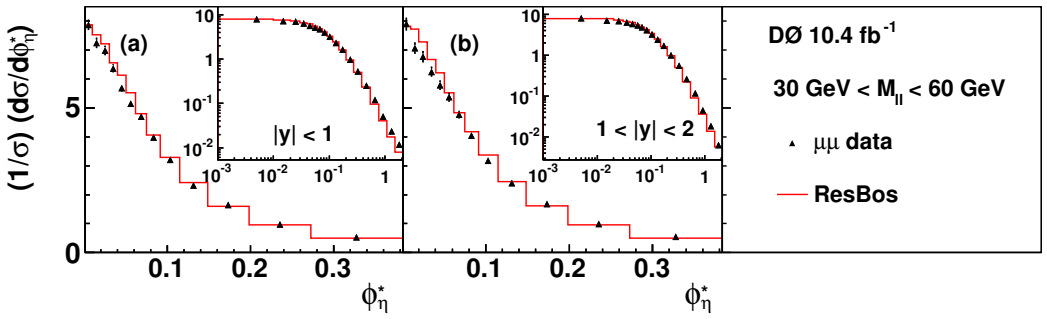

Figure 5.54: Comparison between the measured $(1/\sigma) \times (d\sigma/d\phi^*_\eta)$ and the predictions from ResBos for dimuon events with $30 < M_{\ell\ell} < 60$ GeV in two rapidity bins.

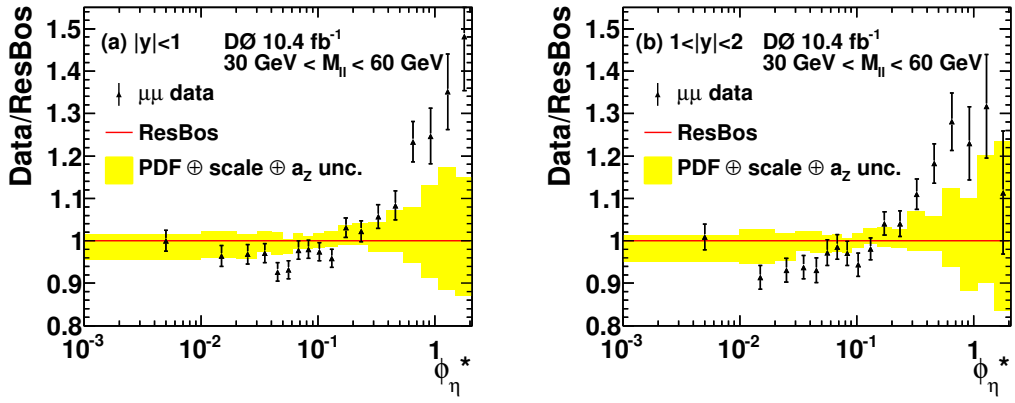

Figure 5.55: Ratio of the corrected ϕ^*_η distributions to the ResBos predictions for $30 < M_{\ell\ell} < 60$ GeV in two rapidity bins. The red histograms represent the default ResBos prediction and the yellow band corresponds to the theoretical uncertainty by adding uncertainties for PDFs, QCD scales and the non-perturbative parameter a_Z in quadrature.

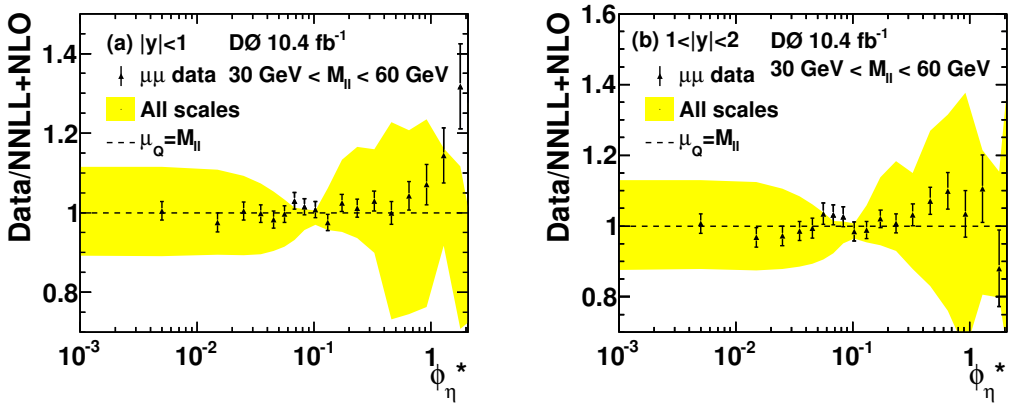

Figure 5.56: Ratio of the corrected distributions of $(1/\sigma) \times (d\sigma/d\phi^*_\eta)$ to the NNLL+NLO predictions of Ref. [34, 35] for $30 < M_{\ell\ell} < 60$ GeV in two rapidity bins. The bold line corresponds to the default NNLL+NLO prediction and the yellow band indicates the theoretical uncertainty by varying QCD scales.

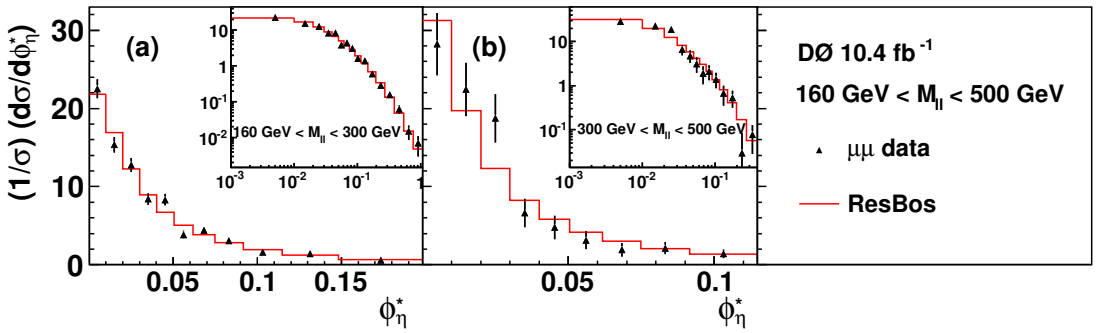

Figure 5.57: Comparison between the measured $(1/\sigma) \times (d\sigma/d\phi^*_\eta)$ and the predictions from ResBos for dimuon events in the region of $160 < M_{\ell\ell} < 300$ GeV and $300 < M_{\ell\ell} < 500$ GeV.

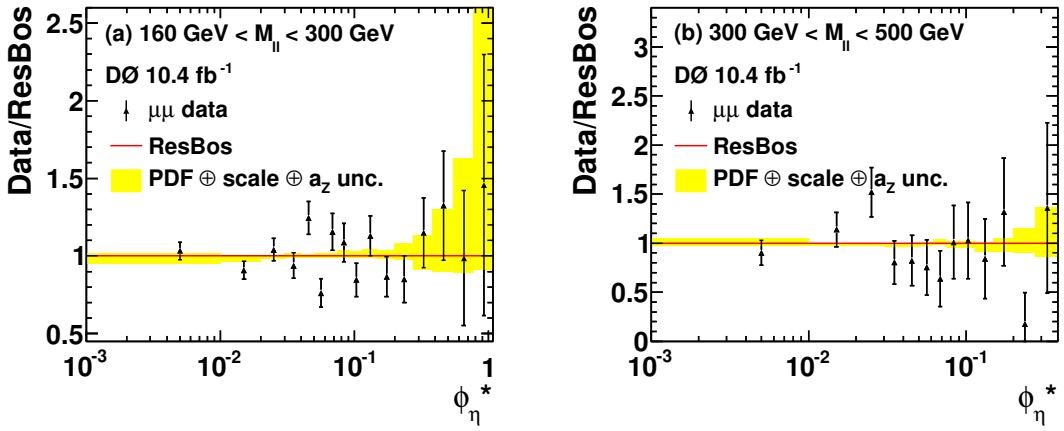

Figure 5.58: Ratio of the corrected ϕ^*_η distributions to the RESBOS predictions separately for $160 < M_{\ell\ell} < 300$ GeV and $300 < M_{\ell\ell} < 500$ GeV. The red histograms represent the default RESBOS prediction and the yellow band corresponds to the theoretical uncertainty by adding uncertainties for PDFs, QCD scales and the non-perturbative parameter a_Z in quadrature.

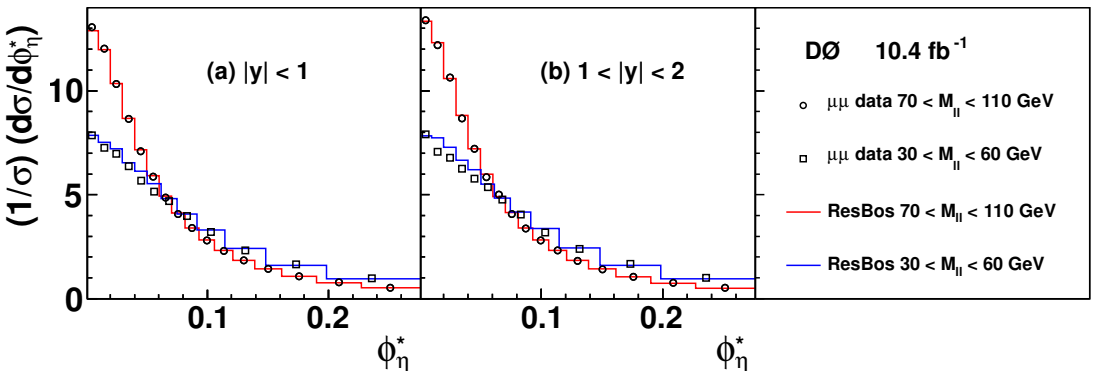

Figure 5.59: Comparison of the $(1/\sigma) \times (d\sigma/d\phi^*_\eta)$ distributions between $30 < M_{\ell\ell} < 60$ GeV and $70 < M_{\ell\ell} < 110$ GeV in two rapidity bins.

5.11 Cross-check with the previously published results in the peak region

In addition to an increased data set a number of changes with regard to the previously published analysis have been introduced for this extended analysis. The difference between the updated and previously published results is within one standard deviation for the normalised differential cross section, as illustrated in Figure 5.60. The systemtic shift in the $(1/\sigma)/(d\sigma/d\phi^*_\eta)$ distribution in the central rapidity bin $(0 \leq |y| < 1)$ arises mainly from that the $W+$ jet background was subtracted twice in the orginal analysis, as described in Section 5.4.3.

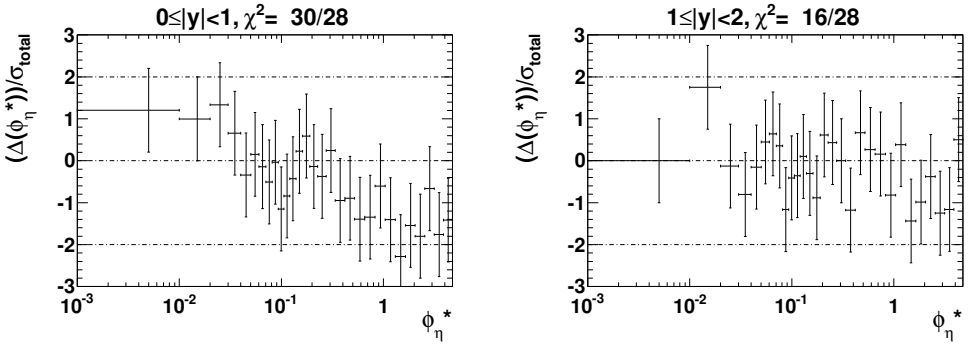

(a) $0 \leq |y| < 1$ (b) $1 \leq |y| < 2$

Figure 5.60: Comparison of the $(1/\sigma)/(d\sigma/d\phi^*_\eta)$ distribution between the current result and the previously published result in bins of rapidity in the dimuon channel for $70 < M_{\ell\ell} < 110$ GeV. $\Delta(\phi^*_\eta)$ denotes the difference with respect to the previously published result. σ_{total} is the quadrature sum of the systematic uncertainty and the statistical uncertainty from the previously published result.

5.12 Conclusion and discussion

A measurement of the transverse momentum of muon pairs for $70 < M_{\ell\ell} < 110$ GeV and $30 < M_{\ell\ell} < 60$ GeV is performed using 10.4 fb^{-1} data from the D0 experiment at Fermilab Tevatron. A new set of cuts was developed in the low-mass region to select a sample of high purity and a systematic study of the background uncertainty was conducted using control samples. The normalised differential cross section in ϕ^*_η is measured in two bins of boson rapidity in both mass regions. A state-of-the-art RESBOS prediction is in excellent agreement with data in bins of boson rapidity for $70 < M_{\ell\ell} < 110$, and is reasonably consistent with data for $30 < M_{\ell\ell} < 60$ GeV. The precision of high-mass region measurements ($160 < M_{\ell\ell} < 300$ GeV

and $300 < M_{\ell\ell} < 500$ GeV) is limited by the statistics and a reasonable agreement between data and the RESBOS predictions is observed. A NLO+NNLL prediction can describe data within uncertainties, considering only the perturbative effects with matched soft gluon resummation. These results including tables for the corrected ϕ_η^* distributions in bins of $M_{\ell\ell}$ and $|y|$ have been published in [40].

The data precision, limited by statistical uncertainties, has already exceeded the size of the theoretical uncertainties in some regions of the ϕ_η^* distribution at the D0 experiment. Further measurements of ϕ_η^* distributions in the Drell-Yan process using 20.3 fb^{-1} pp collision data at $\sqrt{s} = 8$ TeV were also performed with the ATLAS detector [75]. With the extremely high precision of ϕ_η^* distributions at the LHC, the data precision has raised challenges for the current N(N)LO QCD calculations. In order to pin down the theoretical uncertainties, higher order calculations at next-to-NNLO (N^{3}LO) are needed to allow for more stringent tests of the Standard Model.

Chapter 6

Proposed luminosity measurement using the diamond beam monitor

6.1 Overview

One of the detectors used for the luminosity determination at the ATLAS experiment is the beam condition monitor (BCM) [59]. The BCM is made up of four modules on either side of the interaction point at $z = \pm 184$ cm, each of which is composed of two back-to-back diamond sensors and readout chips. The BCM has a geometrical acceptance of $|\eta| \sim 4.2$ and its main objective is to monitor the beam particle losses close to the interaction point. In addition, the bunch-by-bunch luminosity can be determined by the BCM because of its fast response and readout time. One of the main challenges in the LHC Run 2 is the increase in pile-up, which gives rise to induced readout inefficiencies due to high occupancies in the detectors. Luminosity measurements using the BCM will start to saturate due to the large pile-up of events per bunch crossing as the luminosity reaches 10^{34} cm^{-2}s^{-1}. The diamond beam monitor (DBM), which is highly segmented spatially and is not expected to saturate, will complement the existing BCM for the luminosity measurement in LHC Run 2.

The use of the diamond detector has a few advantages over the silicon detector. First, diamond has a larger gap energy ($\sim$ 5.5 eV) between the conduction band and the valence band than silicon ($\sim$ 1 eV). Therefore, diamond has less free charge carriers contributing to noise. The large band gap also gives rise to a low leakage current. In addition, an excellent thermal conductivity reduces the requirement for an extensive cooling system. Finally, diamond is less sensitive to radiation than silicon, hence the diamond detector has an extended lifetime in a radiation-hard environment.

In this chapter we study the hit efficiency of the DBM in the simulation using single-muon events and investigate potential luminosity algorithms using minimum bias[1] pp MC samples. It should be noted that we evaluate the use of the DBM detector for values of the average collisions per bunch crossing (μ) up to 100.

6.2 The DBM detector

The ATLAS pixel detector contains three layers of silicon pixel sensors equipped with FE-I3 front-end pixel readout chips. A fourth layer, the Insertable B-Layer (IBL) [60] has been installed utilising FE-I4 chips. The integrated circuit of the FEI4 chip shown in Figure 6.1 consists of readout for 26880 pixels with 80 columns and 336 rows, giving an active area of 20 mm $\times$ 16.8 mm. The DBM is read out using the same chip.

The DBM is composed of eight telescopes with four telescopes on each side relative to the interaction point, as shown in Figure 6.2, and each telescope is made up of three DBM modules. The distance along the beam direction between two neighbouring DBM modules is 50 mm. In the later text, layer[2] 0 denotes the layer of the DBM modules closest to the interaction point, layer 1 the second closest and layer 2 the furthest. The DBM has a geometrical acceptance of $3.1 < |\eta| < 3.4$, and is positioned at around 1 m in the z direction with respect to the interaction point. In the later text, "A side" refers to the region of $z > 0$ and "C side" refers to the region of $z < 0$ (See Figure 6.2). A schematic diagram of the position and the alignment of a DBM telescope is given in Figure 6.3. A detailed description of the DBM can be found in [76].

6.3 Monte Carlo samples

6.3.1 Single muon samples

One million single muon events of constant $p_T = 100$ GeV were generated with full ϕ coverage for $3.0 < \eta < 3.6$ and $-3.6 < \eta < -3.0$.

[1] Minimum bias refers to events passing a "loose" trigger which selects most evens from the inelastic pp collisions.

[2] "Layer" is just a notation to denote the four DBM modules, the geometrical centre of which share the same position in z.

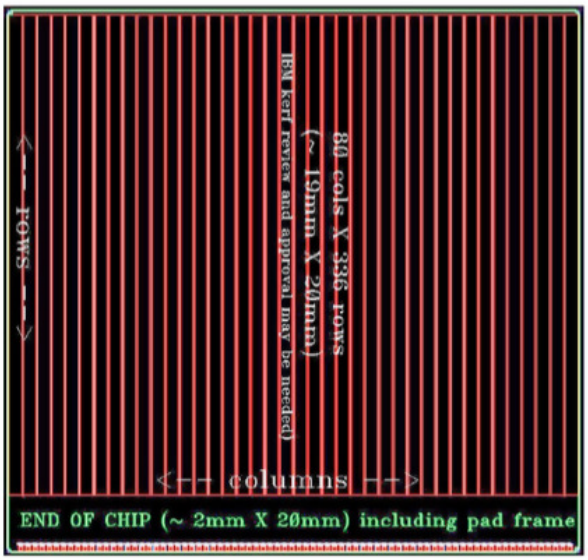

Figure 6.1: Schematic view of the FE-I4 chip, consisting of 336 active rows by 80 columns giving an active area of 20 mm × 16.8 mm [60].

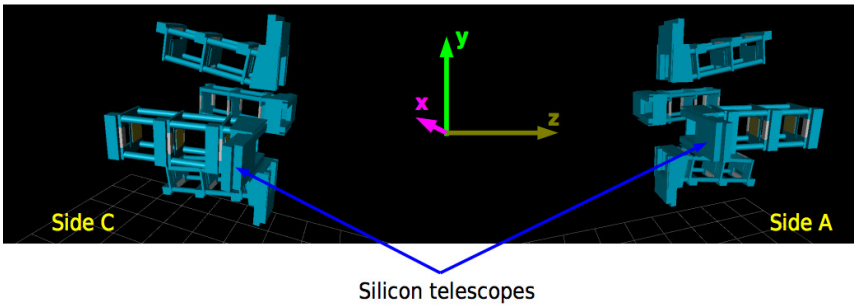

Figure 6.2: A schematic diagram of the DBM geometry [77].

6.3.2 Pile-up *pp* min-bias samples

The pile-up background components considered in the analysis are described as follows:

- In-time pile-up: events originating from additional *pp* collisions present in the same bunch-crossing as the collision of interest.
- Out-of-time-pile-up: events originating from additional *pp* collisions in the successive bunch-crossings before and after the collision of interest. When the detector is sensitive to several bunch crossings or the electronics has an integration time of more than 25 ns, the signal for the collision of interest can be affected by these additional *pp* collisions.

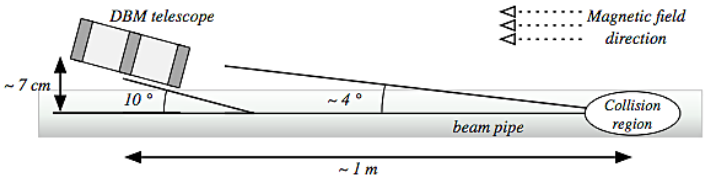

Figure 6.3: A schematic diagram of the position and alignment of a DBM telescope in the ATLAS experiment [76].

The additional *pp* collisions are generated with PYTHIA8 [29] and passed through a GEANT4-based ATLAS detector simulation [78], where PYTHIA8 includes the non-diffractive inelastic, single-diffractive and double-diffractive components of the cross-section. The events mentioned above are overlaid at configurable rates as additional energy deposits in each detector before the energy conversion to the digital signal.

MC samples with a wide range of μ ($1 \leq \mu \leq 100$) values are produced. Each sample contains 2000 events. For the purpose of the study, only the ID simulation is switched on. These samples use single neutrino events[3] as "signal" and multiple *pp* collisions as "background". These events of multiple *pp* collisions are then superimposed on top of the single neutrino events at digitization stage according to the requested μ values.

6.4 DBM cluster reconstruction efficiency studies

In order to validate the DBM configuration in the simulation, the DBM cluster reconstruction efficiency is measured using the single-muon samples described in Section 6.3.1. All plots shown are for the DBM monitor on the C side.

6.4.1 Distribution of the reconstructed DBM clusters

Figure 6.4 shows the number of reconstructed DBM clusters on the C side. It can be observed that the average number of DBM clusters reconstructed for events with tracks passing through the DBM is around 2 as the DBM telescope has limited

[3]Due to the sharply falling distribution of the jet transverse momentum p_T, we usually first produce the single collision samples according to the p_T of the hardest jet, i.e., a high-p_T sample ($p_T > 35$ GeV) and a low-p_T sample ($p_T < 35$ GeV). In order to produce the sample with the requested μ value and to preserve the jet cross section, the low and high p_T samples have to be superimposed on each other with the correct relative fractions. The neutrino signal makes such a procedure convenient because it is invisible to the detector.

geometrical coverage and is not exactly aligned along the track direction. Figure 6.5 illustrates the number of DBM clusters of each layer of the telescope in x and y. The number of reconstructed DBM clusters per x-y bin increases near the beam pipe due to the fact that the density of tracks in η is approximately constant. The total number of DBM clusters reconstructed decreases with the distance from the interaction point in z as a result of the DBM acceptance. Similar results could have been shown from plots of clusters on the A side of the DBM detector.

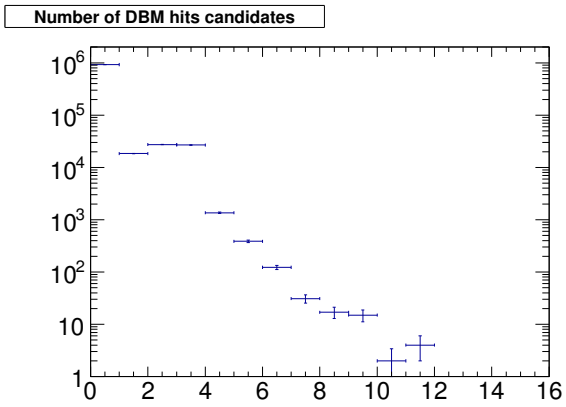

Figure 6.4: Distribution of the number of the reconstructed DBM clusters on the C side.

6.4.2 Algorithm for hit efficiency calculation

Given the production vertex $\vec{v}_0$ and the track direction $\hat{p}$ of the single muon, the trajectory can be calculated and an extrapolation can be made to each layer in a DBM telescope. The cluster reconstruction efficiency ϵ is defined as $\epsilon = N_{rec}^{matched}/N_{truth}$, where N_{truth} is the number of extrapolated DBM clusters using truth level information and $N_{rec}^{matched}$ is the number of reconstructed DBM clusters matched to the extrapolated DBM clusters within a certain distance. In the following extrapolation methods, no energy loss due to interaction with the material is considered.

- Loop over all truth charged particles and the extrapolated hit position within the geometrical acceptance of the DBM is stored.
- Loop over the DBM clusters at detector level and record the reconstructed cluster position.
- For each extrapolated hit, loop over all reconstructed DBM clusters. There are three cases considered:

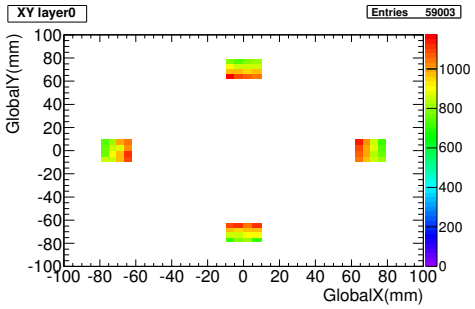

(a) Layer 0

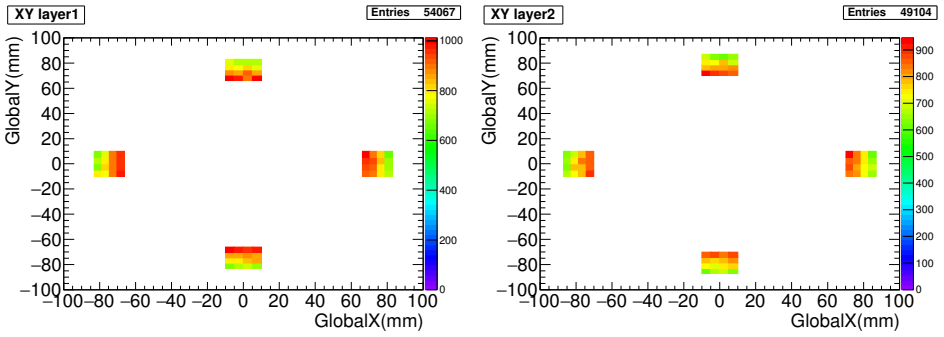

(b) Layer 1

(c) Layer 2

Figure 6.5: Distribution of the number of DBM clusters of each layer of the telescope in x and y.

- the reconstructed hit and the extrapolated hit end up in the same x-y bin;
- the extrapolated hit ends up in an adjacent x-y bin to the reconstructed hit;
- no nearby extrapolated hit is found in the layer.

In the first two cases, the numerator is filled with the position of the reconstructed hit. Otherwise for this extrapolated hit the DBM detector is considered to be inefficient.

- Matched hits are found by minimising the distance between the extrapolated position and the reconstructed cluster position ΔR, which is defined as:

$$\Delta R = \sqrt{(X_{reco} - X_{truth})^2 + (Y_{reco} - Y_{truth})^2}. \tag{6.1}$$

To ensure the hits are found in the same telescope on the same side as the reconstruction level, further requirements on z and ΔR are imposed.

6.4.3 Straight line extrapolation

As the transverse momentum of the muon is around 100 GeV, having a curvature of 1/167 m^{-1} in a 2 T magnetic field, in the first-considered extrapolation method it is assumed that the charged particle track is straight.

The extrapolated position at which the muon hits the DBM plane in terms of the production vertex $\vec{v}_0$ and track direction $\hat{p}$ can be expressed as

$$\vec{v}_x = \vec{v}_0 + s\hat{p}, \tag{6.2}$$

where s is the length of the straight track between the initial position and the DBM plane.

The distance between the origin and the DBM plane d is a constant:

$$\vec{v}_x \cdot \hat{n} = d, \tag{6.3}$$

where $\hat{n}$ is a unit vector normal to the plane of the DBM module.

Substituting Equation 6.2 into Equation 6.3 and re-arranging the equation $s = (d - \vec{v}_0 \cdot \hat{p})/(\hat{p} \cdot \hat{n})$ an expression for $\vec{v}_x$ can be obtained.

6.4.4 Helix extrapolation

In the helix extrapolation method, the magnetic field strength B is assumed to be uniform (2 T) in the ID.

For a helix with initial position $\vec{v}_0(x_0, y_0, z_0)$ and momentum $\vec{P}(p_x, p_y, p_z)$, the projection onto the x-y plane is a circle with following analytical form:

$$(x - x_0 + R\cos\phi_0)^2 + (y - y_0 + R\sin\phi_0)^2 = R^2, \tag{6.4}$$

$$R = \frac{p_T}{qB}, \tag{6.5}$$

where ϕ_0 is the azimuthal coordinate of the initial position $\vec{v}_0$, q is the charge of the particle and p_T is the transverse momentum. $\vec{R}$ represents the radius of the circular trajectory in the transverse plane. It is in the same direction as $\vec{F}$, the force that acts on the particle.

The parameterization of the helix as a function of z is:

$$x\ (z) = x_0 + R[\cos(\phi_0 + h(z - z_0)/(R\tan\lambda)) - \cos\phi_0], \tag{6.6}$$

$$y\ (z) = y_0 + R[\sin(\phi_0 + h(z - z_0)/(R\tan\lambda)) - \sin\phi_0], \tag{6.7}$$

where the dip angle λ is defined as the angle between $\vec{p_T}$ and $\vec{P}$. The helicity h of the helix is -1 for positively charged particles (clockwise) and 1 for negatively charged particles (anticlockwise). In our extrapolation, z is the position of the DBM module.

The intersection between the helix and the DBM module also satisfies the analytical equation of the plane:

$$ax + by + cz + d = 0, \tag{6.8}$$

where (a, b, c) is the unit vector normal to the DBM module and d can be deduced because the centre of the DBM module in the plane is known. As x, y can be expressed as a function of z, substituting Equation 6.6 and Equation 6.7 into Equation 6.8 gives z and we obtain the position of the intersection point.

6.4.5 Validation of the two extrapolation methods

Both the straight line and the helix extrapolation methods have a small mean ΔR, as illustrated in Figure 6.6. This provides a cross-check of the validity of both extrapolation methods.

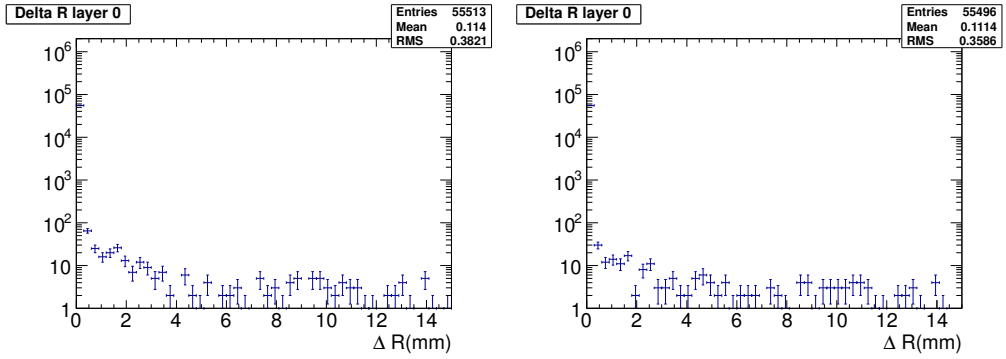

(a) straight line extrapolation (b) helix extrapolation method

Figure 6.6: ΔR distribution for C side of layer 0 for (a) the straight line extrapolation (b) the helix extrapolation method separately.

6.4.6 Results for the helix extrapolation

The distribution of the extrapolated DBM hit positions in x and y on the C side using the helix extrapolation is presented in Figure 6.7. Figure 6.8 presents the

distribution of the reconstructed DBM clusters of each layer of the telescope in x and y on the C side after the algorithm. Figure 6.9 presents the distribution of the DBM hit reconstruction efficiency as a function of x and y on the C side using the helix extrapolation. The overall efficiency is around 77%, which is the same as that obtained from the straight line extrapolation.

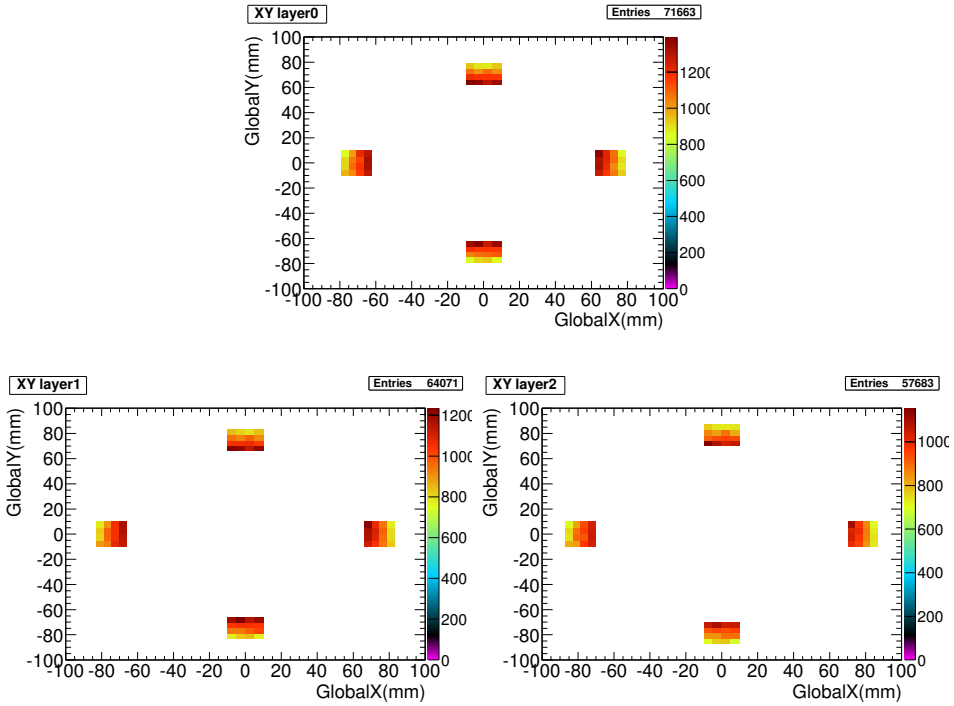

Figure 6.7: Distribution of the extrapolated DBM hits position in x and y on the C side using the helix extrapolation using truth information.

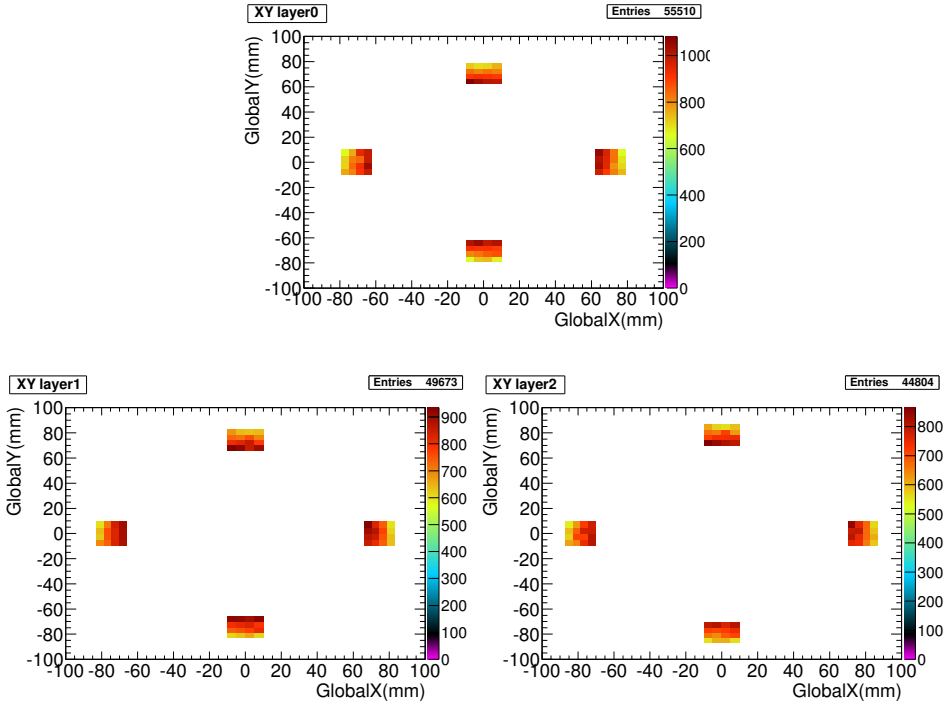

Figure 6.8: Distribution of the reconstructed DBM clusters of each layer of the telescope in x and y on the C side after the algorithm.

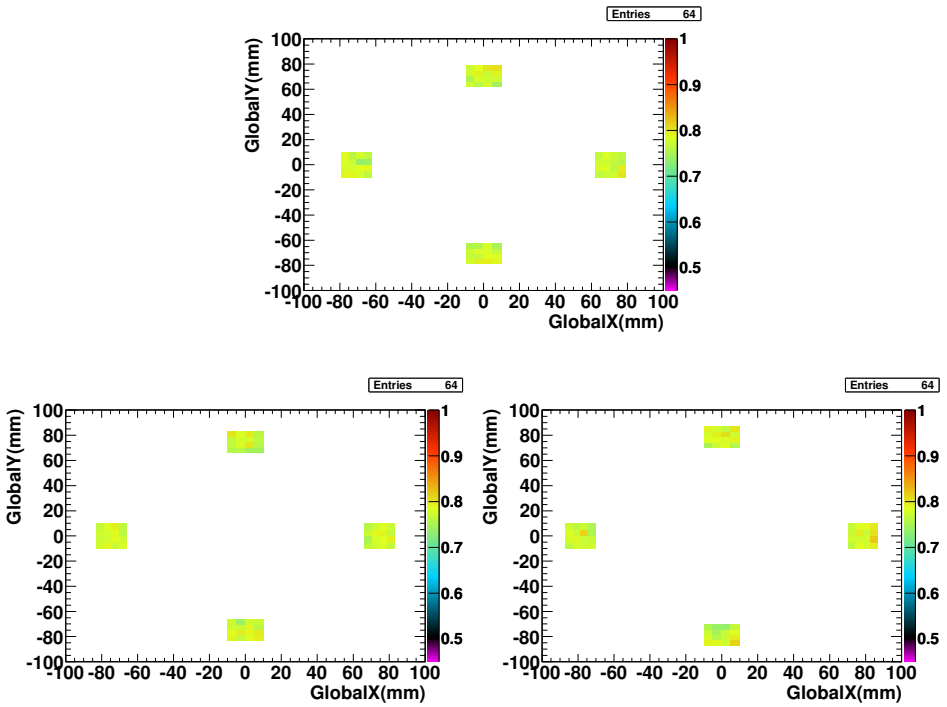

Figure 6.9: Distribution of the DBM hit reconstruction efficiency in x and y on the C side using the helix extrapolation.

6.5 Pile-up response study of the DBM

All pile-up samples used are described in Section 6.3.2. This section mainly concentrates on studying how the relationship between the mean number of DBM clusters changes with μ. All graphs are plotted for the DBM telescopes on the C side only. Similar results could have been shown for clusters on the A side of the DBM detector.

6.5.1 Validation of the pile-up samples

The number of MC truth produced particles is directly proportional to μ as shown in Figure 6.10, which is consistent with expectations. There are around 250 additional particles produced per event per μ. However, the large random deviations of the predicted number of produced particles in terms of μ from a simple linear fit arise from the standard ATLAS pile-up events. Similar effects have been observed in similar studies of other samples; the reason for these fluctuations is not understood.

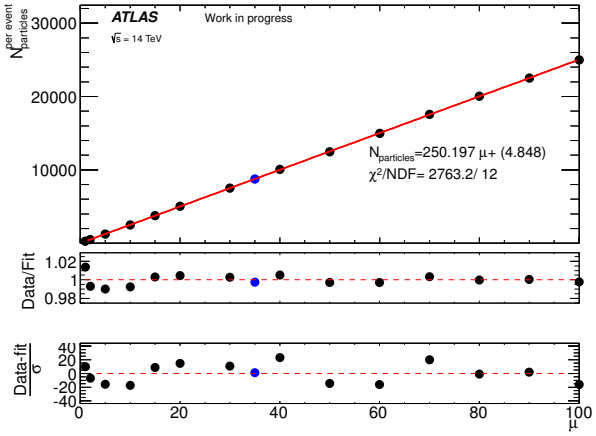

Figure 6.10: The mean number of produced particles per event as a function of μ. The blue point represents $\mu = 35$ sample, which is used below as the test sample for luminosity algorithm validation.

6.5.2 Study of the DBM clusters under pile-up conditions

The distribution of the number of DBM clusters reconstructed on the C side for various μ values is shown from Figure 6.11a to Figure 6.11e. The mean number of DBM clusters reconstructed is directly proportional to μ, as is illustrated in Figure 6.11f. An average rise of approximately 2.25 DBM clusters per μ per event is observed. The pattern of residuals in Figure 6.11f shows similarities with Figure 6.10.

In order to check the dependence of the mean number of DBM clusters on the DBM geometry, we examine the mean number of DBM clusters for each module

separately. Figure 6.12 shows the mean number of DBM clusters per module on the layer 0 on the C side as a function of μ. We define N^{module} as the number of clusters in a given DBM module. An average increase of 0.2 in N^{module} with μ per event is found. Figure 6.13 depicts the relationship between N^{module} in the same DBM telescope on the C side as a function of μ. The slope in N^{module} with per unit μ decreases with distance to the interaction point, ranging from 0.2 on layer 0 to 0.17 on layer 2. This is expected because the DBM module in the outer layer has a smaller acceptance than that in the inner layer.

We further divide each of the 24 DBM modules into four parts according to the quadrants in the local coordinate. The centre of the DBM module is defined as the origin of the local coordinate system. Figure 6.14 shows the mean number of DBM clusters plotted versus μ for the different quadrants in a particular DBM module. The slope of the mean number of DBM clusters versus μ increases as the area covered by the quadrant becomes closer to the beam pipe.

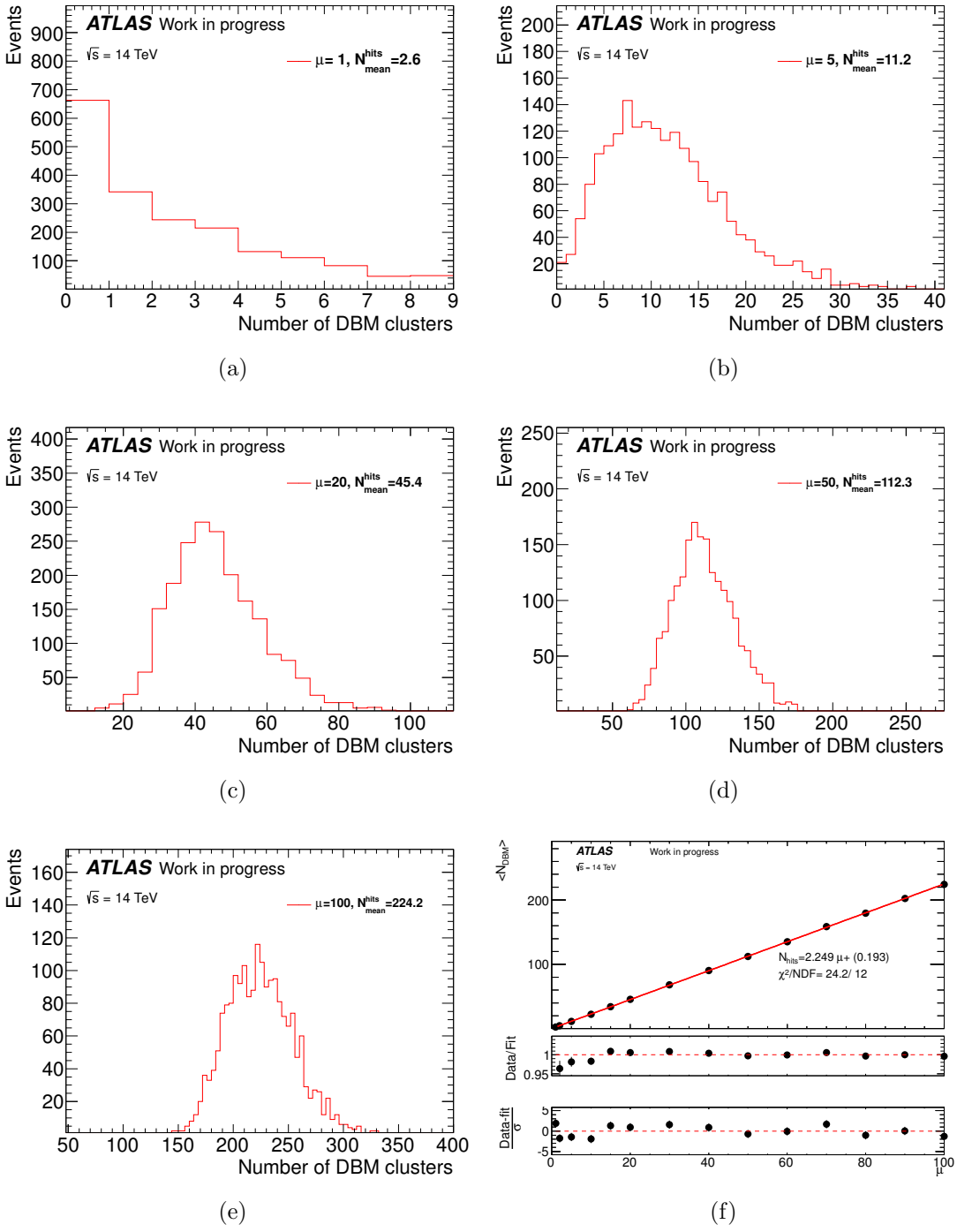

Figure 6.11: (a)-(e) distribution of the number of DBM clusters reconstructed on the C side for various μ values; (f) the mean number of the DBM clusters versus μ on the C side.

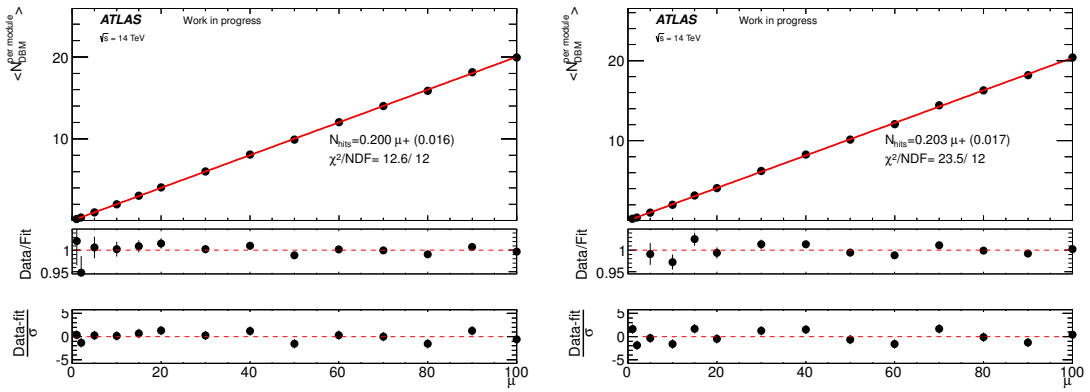

(a) $\phi = 0$

(b) $\phi = \pi/2$

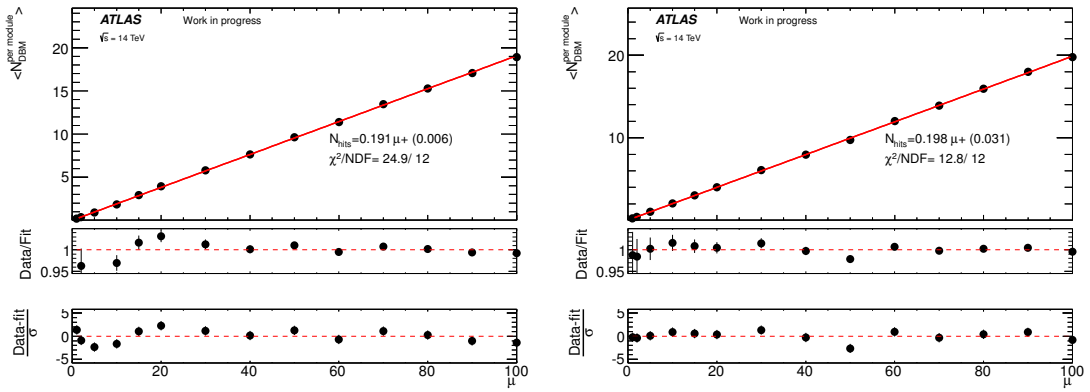

(c) $\phi = \pi$

(d) $\phi = 3\pi/2$

Figure 6.12: The mean number of DBM clusters per module of layer 0 versus μ on the C side.

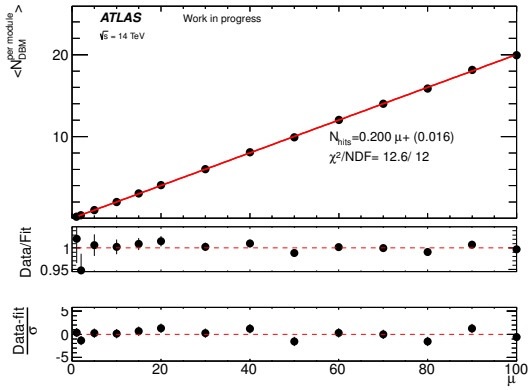

(a) Layer 0

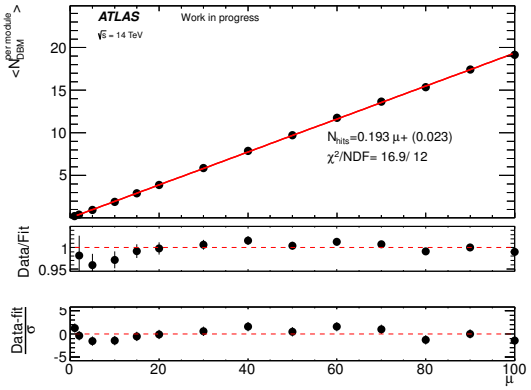

(b) Layer 1

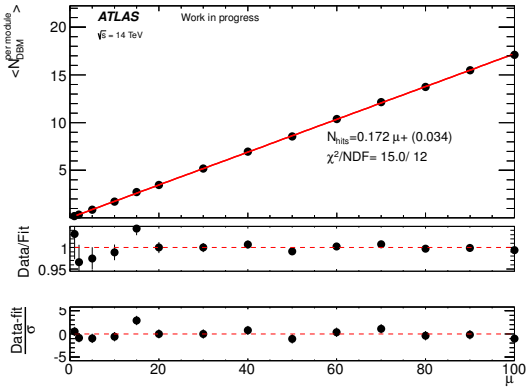

(c) Layer 2

Figure 6.13: The mean number of DBM clusters of different layers versus μ in the $\phi = 0$ telescope on the C side.

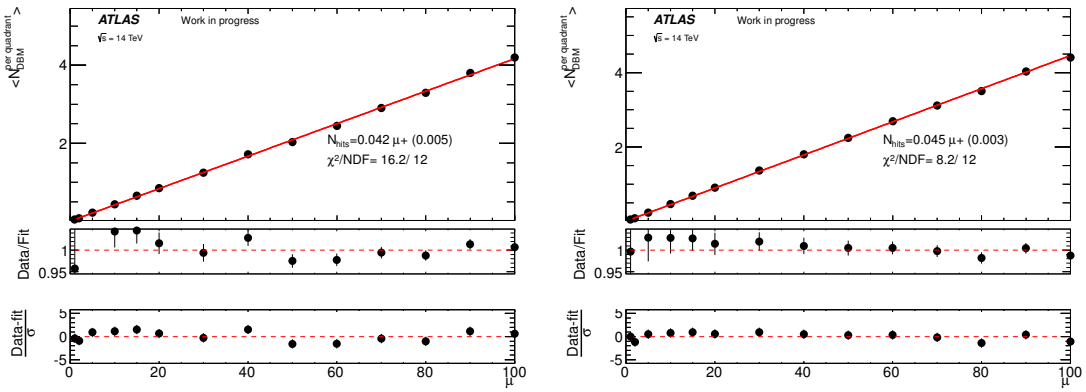

(a) $x \geq 0, y \geq 0$

(b) $x < 0, y \geq 0$

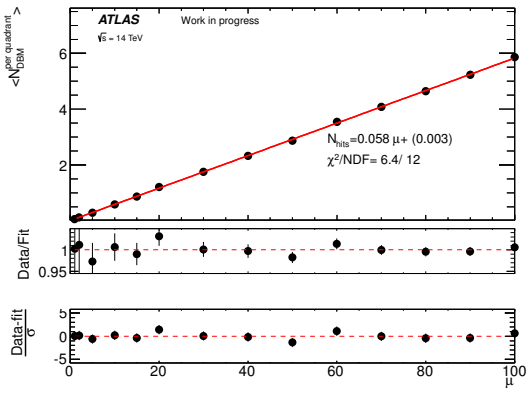

(c) $x < 0, y < 0$

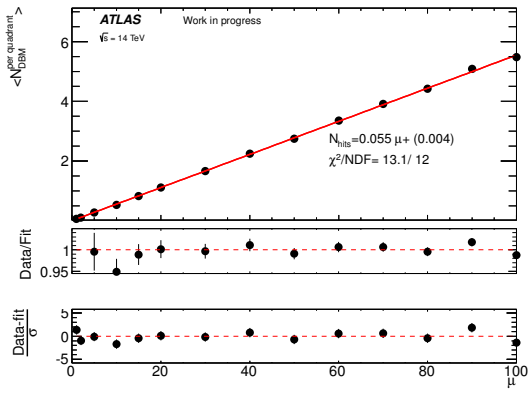

(d) $x \geq 0, y < 0$

Figure 6.14: The mean number of DBM clusters versus μ for different quadrants of the layer 0 module in the $\phi = 0$ telescope on the C side.

6.5.3 Properties of the DBM clusters under pile-up conditions

Figure 6.15 shows the distribution of the column width (Figure 6.15a), the row width (Figure 6.15b) and the mean ToT[4] (Figure 6.15c) of the DBM clusters at $\mu = 30$ and $\mu = 60$ on the C side. The properties of the DBM clusters under pile-up conditions are inspected by looking at the mean cluster row width, the mean column width and the mean ToT, as illustrated in Figure 6.16. All of the quantities stay flat with μ indicating there is no evidence of any pile-up effects that might arise from clusters formed from merging hits produced by particles originating from different pp collisions.

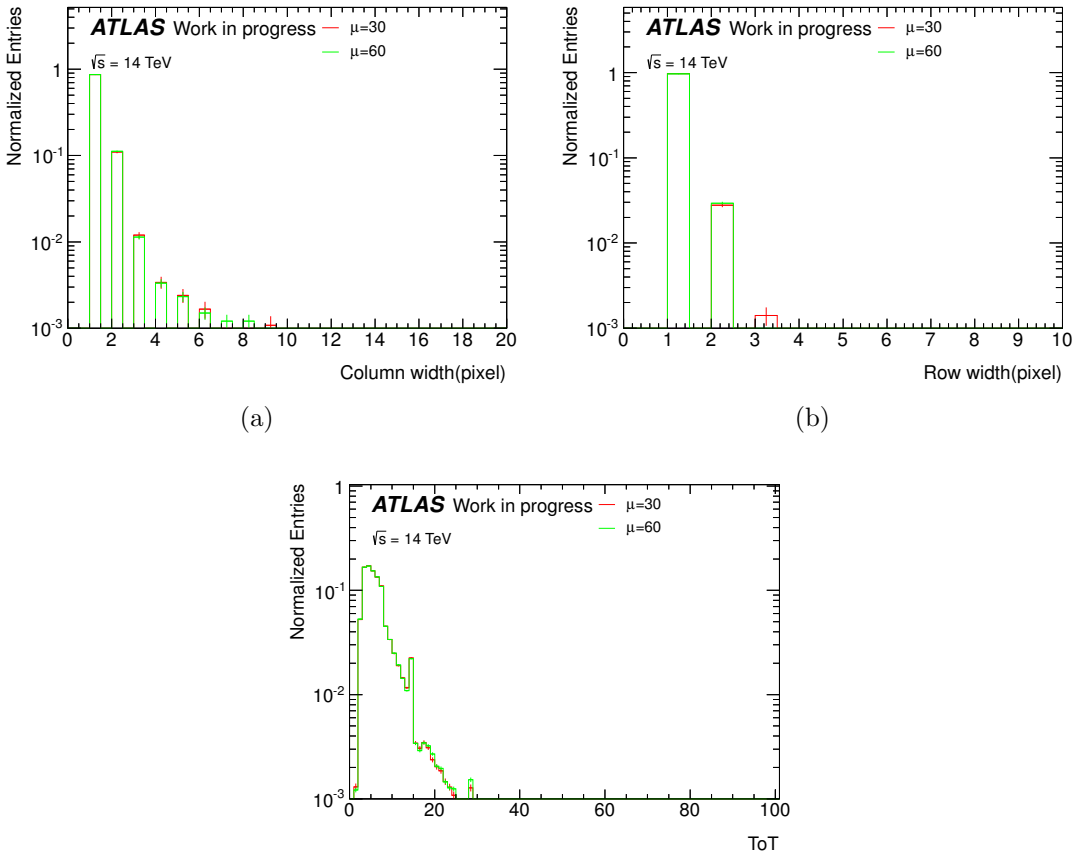

(a) (b)

(c)

Figure 6.15: The normalised distribution of (a) the column width, (b) the row width and (c) the ToT of the DBM clusters at $\mu = 30$ and $\mu = 60$ on the C side.

[4]ToT stands for time over threshold, which is an estimator of collected charge.

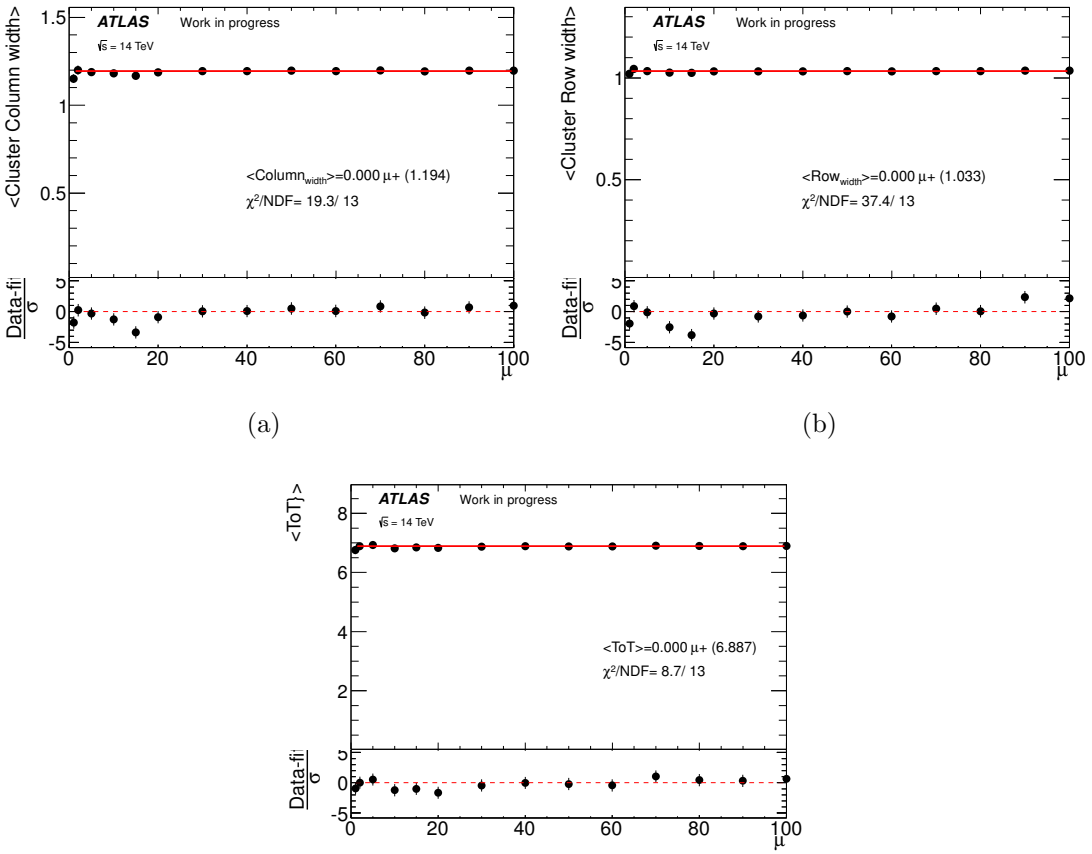

Figure 6.16: Distribution of (a) the mean column width, (b) the mean row width and (c) the mean ToT of the DBM clusters versus μ on the C side.

6.6 A proposed algorithm for luminosity measurement

The observed linearity of the mean number of DBM clusters per module as a function of μ allows us to propose a simple luminosity algorithm. A given observed value of mean number of clusters in a particular DBM module can be converted to a value of μ using the linear relationship appropriate to that particular DBM module. In the real detector the two parameters (offset and slope) would be calibrated in a Van der Meer (vdM) scan [79]. In the MC we can use the linear relationship of the kind shown in Figures 6.12 and 6.13 in lieu of the vdM calibration. In order to validate the method, we employ an independent pile-up sample with $\mu = 35$, which is not included in the fit for the calibration curve.

6.6.1 Validation of the proposed luminosity algorithm

An independent sample with $\mu = 35$ of 2000 events is produced to test the proposed algorithm using the previously obtained "calibration" curve of number of mean DBM clusters versus μ in Section 6.5. The expected mean number of clusters for $\mu = 35$ is ~ 159 in the whole DBM detector. Figure 6.17 shows the extraction of the μ value according to the mean number of DBM clusters of each module in layer 0 of the C side. The extracted μ values of the 24 independent measurements are depicted in Figure 6.18. Averaging over the 24 independent values we obtain $\mu = 34.794 \pm 0.071$. The χ^2 value is 45.1/24 with respect to the input $\mu = 35$, thus validating the proposed algorithm. This is sufficient because the χ^2 is calculated considering the statistical uncertainty only, but the measurement on the luminosity is typically dominated by systematic effects, where the fractional systematic uncertainty is typically at a few percent level [80].

We can further divide each DBM module into four regions according to the quadrants in the local coordinate of the DBM module. Such a procedure will provide 96 independent measurements of the luminosity. Figure 6.19 shows the extracted μ values using the calibration curve of the mean number of DBM clusters in each quadrant of a particular DBM module. Averaging over the 96 independent values we obtain $\mu = 34.799 \pm 0.066$. The distribution of extracted μ values, as presented in Figure 6.20, has $\chi^2 \sim 163.6/96$ with respect to the input $\mu = 35$, thus validating our proposed algorithm.

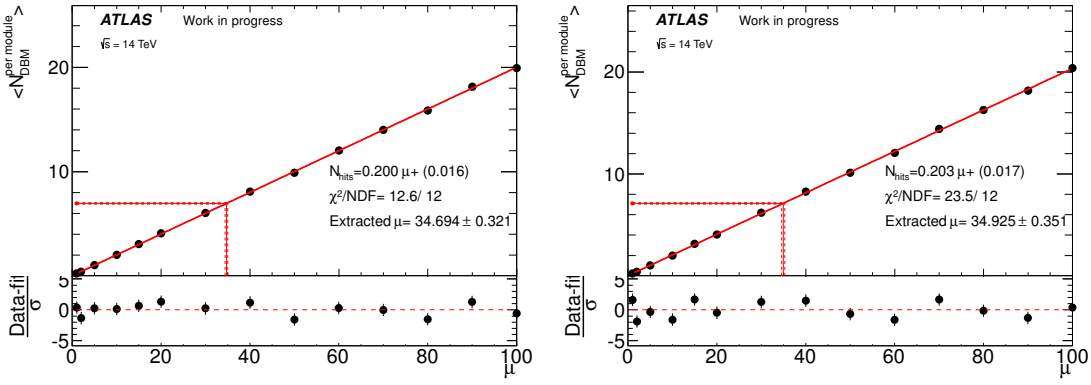

(a) $\phi = 0$ (b) $\phi = \pi/2$

(c) $\phi = \pi$ (d) $\phi = 3\pi/2$

Figure 6.17: Extraction of the μ value using the calibration curve of four DBM modules in layer 0 on the C side.

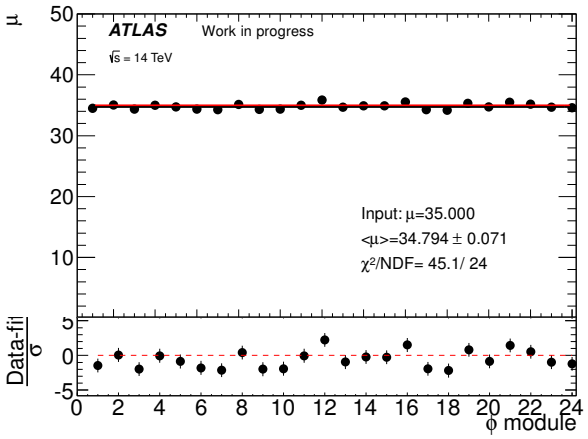

Figure 6.18: The extracted μ from the 24 DBM module measurements.

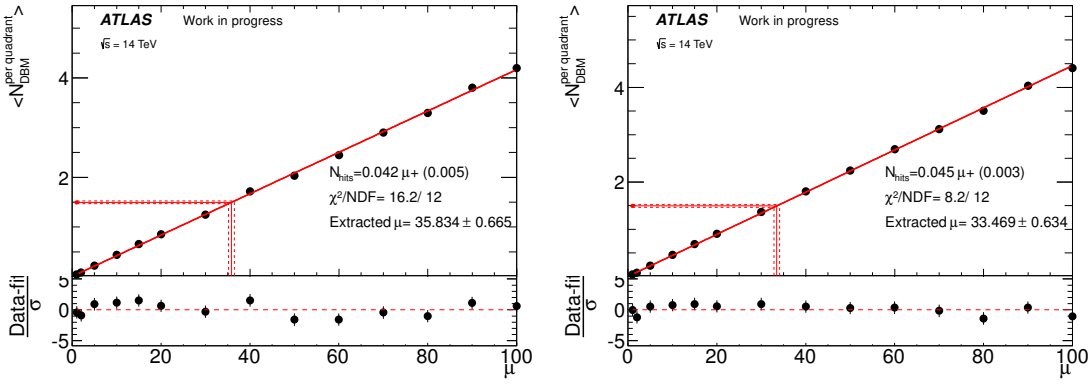

(a) $x \geq 0, y \geq 0$

(b) $x < 0, y \geq 0$

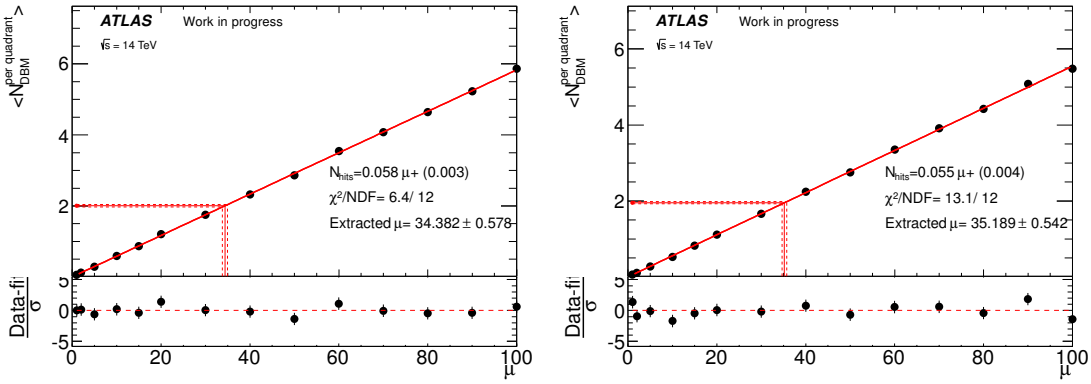

(c) $x < 0, y < 0$

(d) $x \geq 0, y < 0$

Figure 6.19: Extraction of the μ value using the calibration curve in the quadrants of the DBM module for layer 0 of the DBM telescope at $\phi = 0$ on the C side.

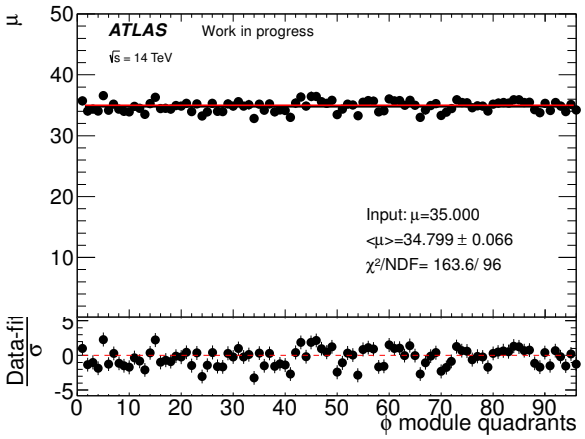

Figure 6.20: The extracted μ from the 96 DBM quadrant measurements.

6.6.2 Robustness of the proposed algorithm to detector effects

This section concentrates on sensitivity studies of the proposed algorithm to noise and inefficiency of certain DBM modules. The DBM can discriminate against non-collision background using the hit information on each DBM module in a particular telescope. If a track leaves two (three) hits on two (three) separate DBM modules in a telescope, this can be used to reject hits arising from non-collision background. No dedicated study on this is performed at the moment.

6.6.2.1 Simulation of inefficiency and noise

The test sample $\mu = 35$ was employed for the sensitivity studies of the proposed algorithm. For the purposes of this study a particular set of DBM modules (or quadrants) was chosen randomly to suffer from inefficiency (or noise). For these chosen modules (or quadrants), the inefficiency is approximately 30% per DBM hit while the probability for counting an extra hit due to noise is 30%. The same set of modules suffered from inefficiency (or noise) for all of the 2000 events in the test sample.

The previously obtained calibration curves of mean number of DBM clusters versus μ, as described in Section 6.5, (i.e., without inefficiency or noise) were used. Figure 6.21 shows the distribution of number of DBM clusters in a particular module (quadrant) with noise or inefficiency.

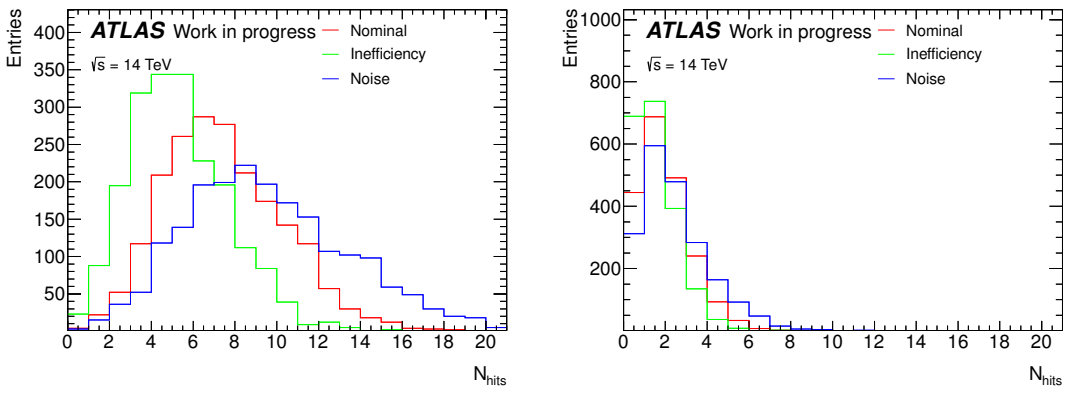

(a) (b)

Figure 6.21: Distribution of the number of DBM clusters for the $\mu = 35$ test sample before and after adding noise or inefficiency (a) for a particular DBM module and (b) for a particular quadrant.

6.6.2.2 The truncated mean algorithm

An iterative approach was used in the truncated mean algorithm described as follows:

- The extracted μ value is averaged for the 24 (96) measurements.
- The χ^2 is calculated for each measurement with respect to the averaged extracted μ.
- A loose χ^2 requirement is applied such that measurements with unreasonable χ^2 are rejected.
- Repeat the above three steps until χ^2 per degree of freedom is no more than 2.

Figure 6.22 shows the distribution of the extracted μ values using the 24 DBM modules for the test sample before and after application of the truncated mean algorithm. Figure 6.23 shows the distribution of the extracted μ values using the 96 DBM quadrants for the test sample before and after application of the truncated mean algorithm. The robustness of the algorithm is validated by the fact that after truncation the mean values of μ, as well as the χ^2 values, are comparable with those obtained in Figures 6.18 and 6.20 without simulation of noise or inefficiency.

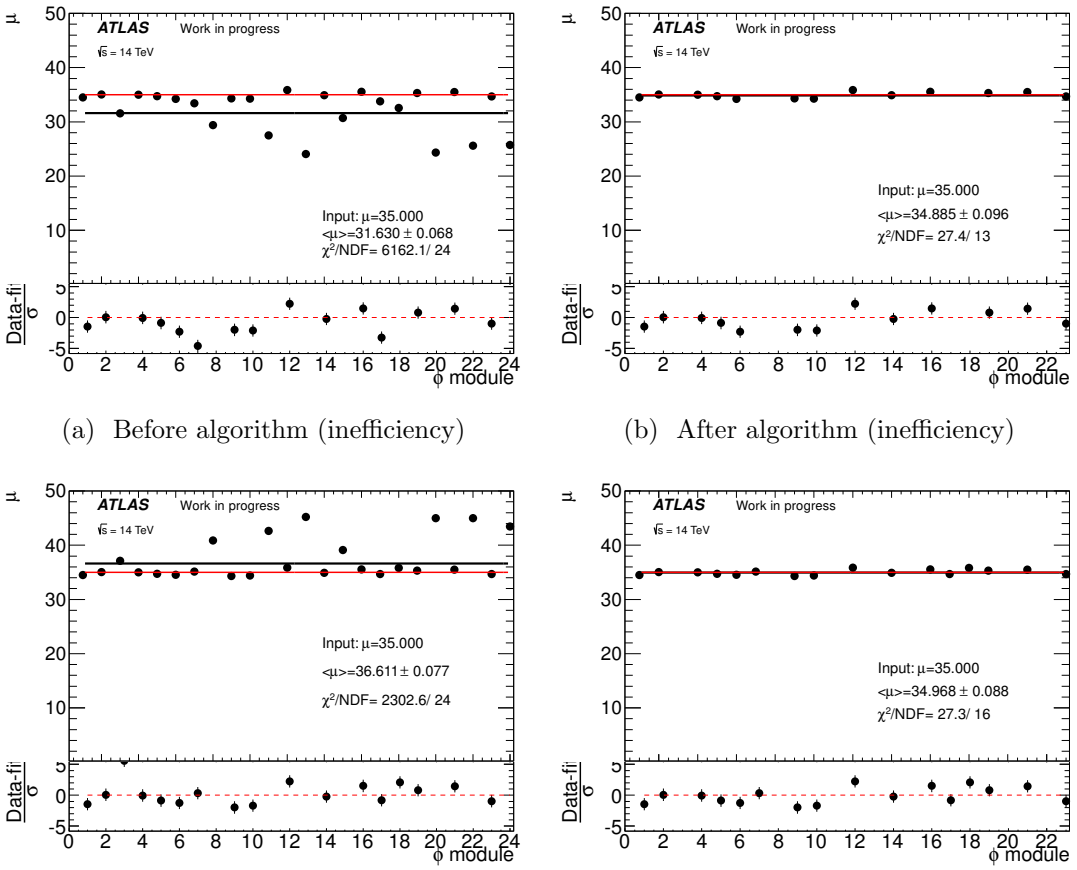

(a) Before algorithm (inefficiency)

(b) After algorithm (inefficiency)

(c) Before algorithm (noise)

(d) After algorithm (noise)

Figure 6.22: Distribution of the extracted μ values for the $\mu = 35$ test sample before and after application of the truncated mean algorithm where certain DBM modules suffered from inefficiency or noise. The red line represents $\mu = 35$ in all four plots. The fit indicated by the black line in the left-hand-side plots shows the actual fit of the 24 DBM module measurements before application of the truncated mean algorithm.

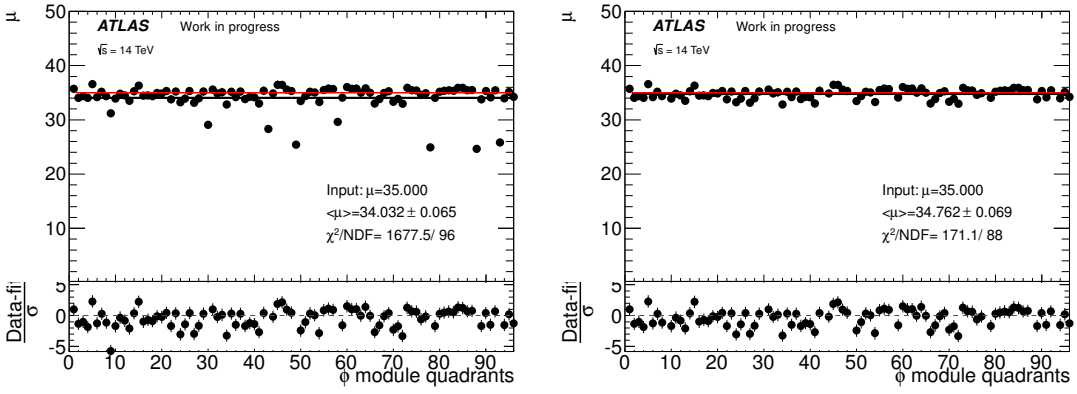

(a) Before algorithm (inefficiency)

(b) After algorithm (inefficiency)

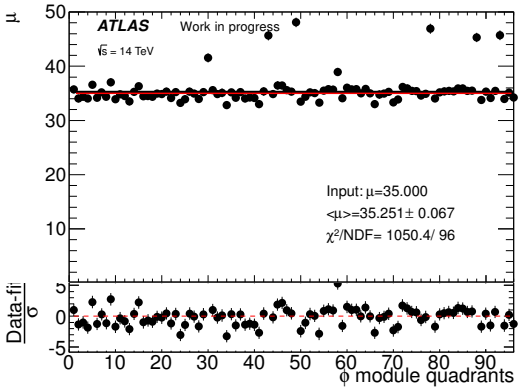

(c) Before algorithm (noise)

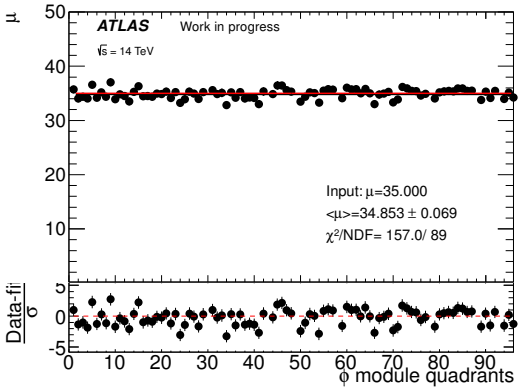

(d) After algorithm (noise)

Figure 6.23: Distribution of the extracted μ values for the $\mu = 35$ test sample before and after application of the truncated mean algorithm where certain DBM quadrants suffered from inefficiency or noise. The red line represents $\mu = 35$ in all four plots. The fit indicated by the black line in the left-hand-side plots shows the actual fit of the 96 DBM quadrant measurements before application of the truncated mean algorithm..

6.7 Conclusion

A study of the reconstruction efficiency of the DBM modules using a single-muon MC was conducted and an overall efficiency of 77% was found. Two extrapolation methods were used for the efficiency measurements and gave consistent results. The efficiency was measured as a function of x and y in the global coordinate of the ATLAS detector.

Using privately-produced pp min-bias MC samples the mean number of DBM clusters was found to increase linearly with μ, such that a simple counting algorithm is possible. The mean cluster width, cluster row width and the ToT stays flat with μ, indicating that there is no evidence of any pile-up effects that might arise from clusters formed from merging hits produced by particles originating from different pp collisions. A luminosity algorithm using the mean number of DBM clusters was proposed and validated. We have shown that for the purposes of cluster counting it is possible to subdivide the DBM detector into individual modules or module quadrants, each of which provides an individual luminosity measurement. By combining these individual measurements using a truncated mean we have shown that the proposed algorithm can be rendered relatively insensitive to certain classes of noise or inefficiency of the DBM modules.

However, the DBM is not operational or recording any data at the ATLAS experiment. Only five telescopes are fully operational at the moment, and the early running period in 2015 led to the bonding wire breakage for the other three telescopes because no safety procedure was implemented to protect these modules. The luminosity algorithm presented in this thesis will be tested using data when the DBM starts running again.

Chapter 7

Isolated diphoton cross section measurements in pp collisions at $\sqrt{s}$ = 8 TeV with the ATLAS detector

7.1 Introduction

We now proceed to the diphoton cross-section measurements at $\sqrt{s} = 8$ TeV using 20.24 fb^{-1} pp collision data as collected by the ATLAS experiment. Both the inclusive and the absolute differential cross sections are measured. The selection criteria for the fiducial cross section at particle level are as follows: $E_{\mathrm{T},1}$ >40 GeV, $E_{\mathrm{T},2}$ >30 GeV, $|\eta| < 2.37$ excluding the crack region of $1.37 < |\eta| < 1.56$, $\Delta R_{\gamma\gamma} > 0.4$ and $E_{\mathrm{T}}^{\mathrm{part.iso.}} < 11$ GeV. $E_{\mathrm{T},1}$ ($E_{\mathrm{T},2}$) refers to the highest (second highest) transverse energy of the photon, $\Delta R_{\gamma\gamma}$ is the separation between the two photons , $E_{\mathrm{T}}^{\mathrm{part.iso.}}$ denotes the calorimeter isolation energy at particle level and the η requirement is placed on each of the two photons. The asymmetric kinematic requirements on the transverse energy are placed to avoid the instability[1] in the fixed order pQCD calculations such as from DIPHOX. The absolute differential cross section is measured in terms of six kinematic variables, namely, $m_{\gamma\gamma}$, $p_{\mathrm{T},\gamma\gamma}$, $\Delta\phi_{\gamma\gamma}$, $|\cos\theta^*_\eta|$, a_{T} and ϕ^*_η, in which $|\cos\theta^*_\eta|$, a_{T} and ϕ^*_η are the three new variables with respect to the 7 TeV analysis. The definitions of these variables are already given in Section 2.6.1.

[1] At low diphoton transverse momentum, resummation of soft and collinear gluon is needed to give a sensible cross section. However, such resummation schemes are not implemented in the fixed-order pQCD calculations of DIPHOX.

The inclusive diphoton cross-section can be measured as follows:

$$\sigma_{fid.} = \frac{N_{\gamma\gamma}^{sig}}{\epsilon_{trig.} C_{total} L}, \tag{7.1}$$

where $N_{\gamma\gamma}^{sig}$ is the extracted diphoton yield from data in the signal region. C_{total} is a correction factor defined as $C_{total} = N_{\gamma\gamma}^{det}/N_{\gamma\gamma}^{true}$, in which $N_{\gamma\gamma}^{det}$ is the number of predicted diphoton events in the signal region at detector level in the diphoton simulation and $N_{\gamma\gamma}^{true}$ is the number of the produced diphoton events in the fiducial volume at truth level. $\epsilon_{trig.}$ represents the trigger efficiency and L is the integrated luminosity. The analysis strategy is to first subtract the background where one or two jets (electrons) are misidentified as photons and then to correct for the detector efficiency and resolution.

7.2 Data and MC samples

The data used in this analysis have been collected by the ATLAS detector in pp collisions at $\sqrt{s} = 8$ TeV. Events in which the calorimeters or the inner detector are not fully operational, or show data quality problems, are excluded. The integrated luminosity after the trigger and the data quality requirements corresponds to 20.24 ± 0.38 fb^{-1} [80].

Diphoton events are generated with both SHERPA 1.4.0 [49] and PYTHIA8 [29]. SHERPA 1.4.0 uses the NLO CT10 [72] PDFs, whereas the LO PDFs CTEQ6L1 [73] are implemented in PYTHIA8. The $Z \to ee$ events are generated using SHERPA [49] or POWHEG+PYTHIA [81].

7.3 Resolution studies of the new variables

A comparison of the resolution of $p_{\mathrm{T},\gamma\gamma}$, a_{T} and ϕ_{η}^{*} using the diphoton SHERPA sample is presented in Figure 7.1. The resolution of both a_{T} and ϕ_{η}^{*} are scaled such that a comparison can be made. It can be observed that ϕ_{η}^{*} has the best resolution and that the resolution of a_{T} and ϕ_{η}^{*} is almost identical when the two photons are back to back. This analysis represents the first measurements of a_{T} and ϕ_{η}^{*} distributions in the diphoton channel.

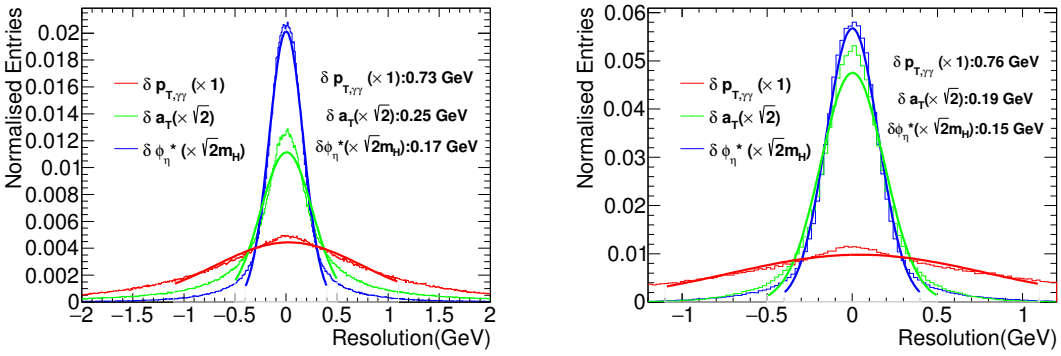

Figure 7.1: The resolution of $p_{\mathrm{T},\gamma\gamma}$ a_{T} and ϕ^*_η using the diphoton SHERPA sample for the inclusive case (left) and $\phi_{acop} < \pi/16$ (right). The resolution of a_{T} and ϕ^*_η is scaled to compare with that of $p_{\mathrm{T},\gamma\gamma}$.

7.4 Event selection

The event selection is as follows:

- *Trigger requirements*: the `g35_loose_g25_loose` trigger chain is used to select the two photons, which is the unprescaled loose diphoton trigger during the whole 2012 data taking period. The LVL1 photon trigger in 2012 uses reduced granularity within a region of 0.1×0.1 in $\Delta\eta \times \Delta\phi$ to determine the transverse energy of the electromagnetic clusters. The trigger chain requires at the Level-3 trigger the presence of two LOOSE (See Section 4.3.2) photon objects with $E_{\mathrm{T},1} > 35$ GeV and $E_{\mathrm{T},2} > 25$ GeV.

- *Primary vertex*: each event must have at least one reconstructed primary vertex with at least three charged tracks associated to it.

- *Two photons acceptance*: each photon candidate must have a pseudorapidity $|\eta_{\mathrm{s2}}|$ measured in the second layer of the ECAL in the pseudorapidity region of $|\eta_{\mathrm{s2}}| < 2.37$ excluding the crack region $1.37 < |\eta_{\mathrm{s2}}| < 1.56$. The photons are arranged in a descending order based on the transverse energy and a pair of photons with the highest transverse energy is selected as input for the diphoton vertex reconstruction.

- *Diphoton vertex*: the diphoton production vertex is determined based on the *photon pointing* method [82], where the position along the beam axis is obtained by the trajectories of both photon candidates with constraints from the average beam spot position. For converted photons, the conversion vertex position is also used as long as there are hits in the silicon detectors associated

to the conversion tracks. A Neural Network algorithm (NN) is used to select the diphoton production vertex according to the photon pointing method with conversion information, the sum of the squared transverse momentum $\sum p_T^2$ and the scalar sum of the transverse momentum $\sum p_T$ of all tracks associated to the reconstructed vertices and the difference in azimuthal angle $\Delta\phi$ between the vertex determined by the vector sum of the tracks momenta and the diphoton system. The pseudorapidity and transverse momentum of each photon candidate are then recalculated using the z-position of the diphoton vertex.

- *Choice of the photon pair*: since the calorimeter isolation energy is measured within a cone of $\Delta R_{\gamma\gamma} < 0.4$, it must be ensured that there is no overlap of energy between the two photons. This is achieved by a requirement on the separation of the reconstructed clusters in the ECAL:

$$\Delta R_{\gamma\gamma} = \sqrt{(\eta_1^{clus} - \eta_2^{clus})^2 + (\phi_1^{clus} - \phi_2^{clus})} > 0.4, \tag{7.2}$$

  where the superscript "clus" indicates that η and ϕ are measured using the cluster information in the ECAL and the subscripts "1" and "2" refer to the highest E_{T}^{γ} (leading) and the second highest E_{T}^{γ} (subleading) photon candidates respectively.

  Both photons are required to be TIGHT (**T**) to reject the potential jet background, and each event has to fulfill $E_{\mathrm{T},1}$ >40 GeV and $E_{\mathrm{T},2}$ >30 GeV.

- *Isolation requirement*: each photon candidate has to pass the requirements on the calorimetric isolation $E_{\mathrm{T}}^{\mathrm{iso}} < 6$ GeV and the track isolation $p_T^{\mathrm{iso}} < 2.6$ GeV. Photon candidates passing the isolation requirement are isolated (**I**).

The events passing the full event selection make up a TIGHT ISOLATED TIGHT ISOLATED (**TITI**) sample, in which the first "TIGHT ISOLATED" (**TI**) refers to the leading photon candidate and the second one refers to the subleading candidate in the selected photon pair candidate.

7.4.1 Corrections to the simulations

A number of corrections have been applied to simulations to improve agreement with data.

Photon identification

The values of the shower shape variables in simulations are corrected using photon-enriched samples to take account of the observed differences of the photon shower shape distributions between data and simulations. In order to correct the observed residual differences in the photon identification efficiencies between MC and data, additional correction factors are applied to simulations. These correction factors are determined using control samples of photons in radiative Z decays, electrons selected with a tag and probe method from $Z \to ee$ decays and photon enriched control samples of known signal composition [83].

Photon isolation corrections to $E_{\mathrm{T}}^{\mathrm{iso}}$

To take into account the observed difference of calorimeter isolation energy distributions between data and simulations, additional corrections to the photon calorimeter isolation energies are determined using inclusive photon samples and applied to improve agreement with data [84].

Pile-up corrections

The MC samples are reweighted to match the pileup conditions of the data according to the distribution of the average number of interactions per bunch crossing μ.

z vertex reweighting

The MC has a slightly wider width of the beam spot along the beam axis (σ_z) than data. A reweighting is applied to match the spread (mean) of the beam spot observed in data ($\sigma_z = 48$ mm).

7.5 Isolation energy distributions for signal and background

The analysis presented here uses both the calorimeter isolation energy and the track isolation energy as well as alternative photon identification criteria (Section 7.5.1) to subtract the hadronic background. This section describes the distribution of the isolation energy quantities for photons, electrons and jets.

7.5.1 Control regions for jets

In order to allow for a data-driven background estimation, a further photon identification selection called the LOOSE′ identification is introduced. For the LOOSE′ identification criteria, all TIGHT requirements are imposed on hadronic and middle layer variables (See Section 4.3.2 for details), whereas for the strip variables only the requirement on $w_{s\,\mathrm{tot}}$ is placed. The objects passing the LOOSE′ selection but failing the TIGHT selection are called NON-TIGHT ($\tilde{\mathbf{T}}$), forming a background control sample dominated by jets with a small contamination from signal events. Alternative definitions, listed in Table 7.1, are implemented to estimate the systematic uncertainties due to the background control region definition. The nominal LOOSE′ selection is referred to as LOOSE′4. Control samples of γj, jγ and jj are formed using data control regions of $\mathbf{TI\tilde{T}I}$, $\mathbf{\tilde{T}ITI}$ and $\mathbf{\tilde{T}I\tilde{T}I}$ respectively.

Name	cuts not applied compared to **T**
LOOSE′2	F_{side}, $w_{s\,3}$
LOOSE′3	F_{side}, $w_{s\,3}$, ΔE
LOOSE′4	F_{side}, $w_{s\,3}$, ΔE, E_{ratio}
LOOSE′5	F_{side}, $w_{s\,3}$, ΔE, E_{ratio}, $w_{s\,\mathrm{tot}}$

Table 7.1: Definition of the various LOOSE′ definitions with respect to the TIGHT photon identification. The definitions of these variables in the table are introduced in Section 4.3.2. LOOSE′4 is taken as the nominal definition of $\tilde{\mathbf{T}}$, which is defined by dropping the requirements on F_{side}, $w_{s\,3}$, ΔE and E_{ratio} with respect to TIGHT. The alternative definitions are used to evaluate the background uncertainty.

7.5.2 Isolation distributions

Figure 7.2 presents the isolation distributions for prompt photons, misidentified electrons and misidentified jets separately with the preselection of $E_{\mathrm{T}}^{\mathrm{iso}} < 10$ GeV and $p_T^{\mathrm{iso}} < 5$ GeV. The jet isolation distributions in γ-jet (also denoted γj) and jet-γ (also denoted jγ)[2] are taken from control regions by requiring one candidate to be **TI** and the other candidate to be $\tilde{\mathbf{T}}$. It can be observed that both calorimeter isolation and track isolation variables have discriminating power against the jet background. Furthermore, the track isolation requirement can also reject a large number of fake photons due to misidentified electrons. The choice of isolation requirements follows the Higgs mass measurements at $\sqrt{s} = 8$ TeV [85].

[2] γj corresponds to a candidate in which the leading candidate is a photon and the subleading candidate is a jet. Similarly in jγ, the leading candidate is a jet and the subleading candidate is a photon.

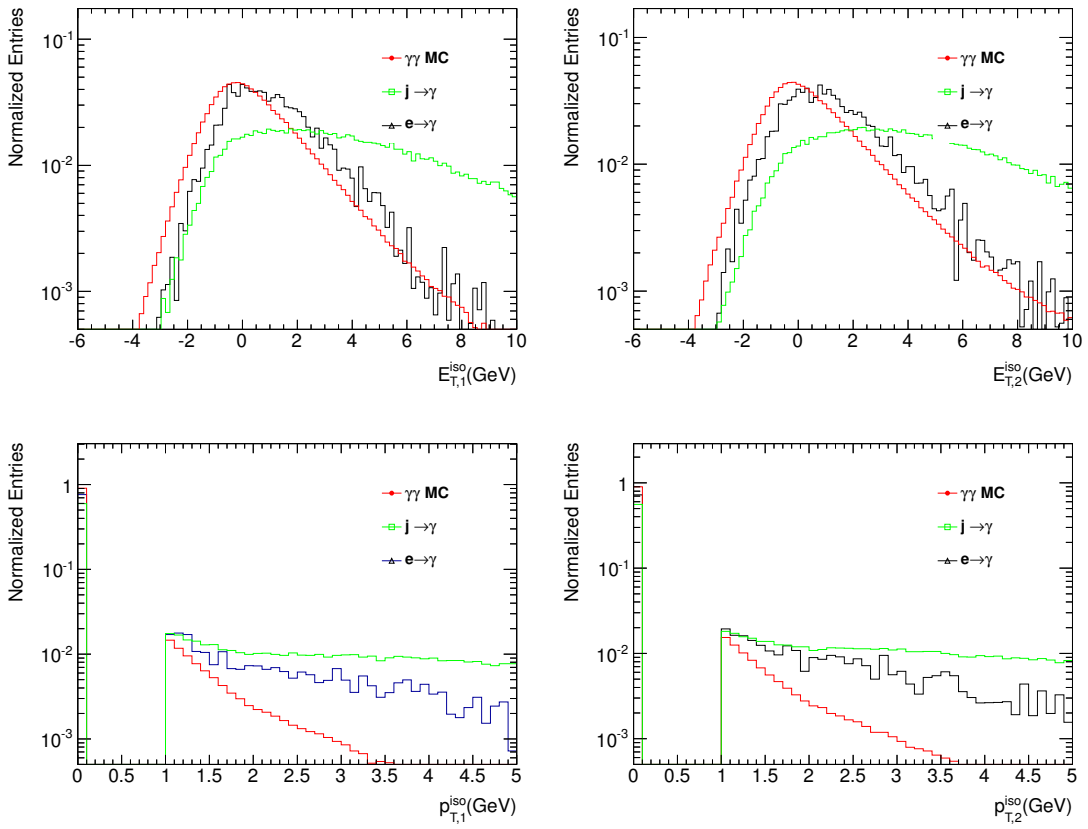

Figure 7.2: Normalized distributions of calorimeter and track isolation profiles for the leading (left) and subleading (right) candidates. The red histograms represent the isolation distribution of prompt photons from the SHERPA $\gamma\gamma$ MC. The bold histograms represent the isolation distributions of misidentified electrons from the $Z \to ee$ MC and the green histograms are the jet distributions taken from $\tilde{\mathbf{T}}$ control regions in data.

Isolation correlations between the two candidates are also investigated. Figure 7.3 shows the isolation correlations in $E_{\mathrm{T}}^{\mathrm{iso}}$ between the two candidates separately for $\gamma\gamma$, γj, jγ and jet-jet (jj) components. The isolation correlations are considered for the jj background whereas they are neglected for the other components in the matrix method described in Section 7.7. Similar isolation correlations between the two selected candidates have been checked for p_T^{iso} as well and they are usually below 1% and safely ignored. Closure tests using a pseudo data sample composed of $\gamma\gamma$, γj, jγ, jj and ee components show that such a treatment of isolation correlations gives unbiased results (Section 7.10.2).

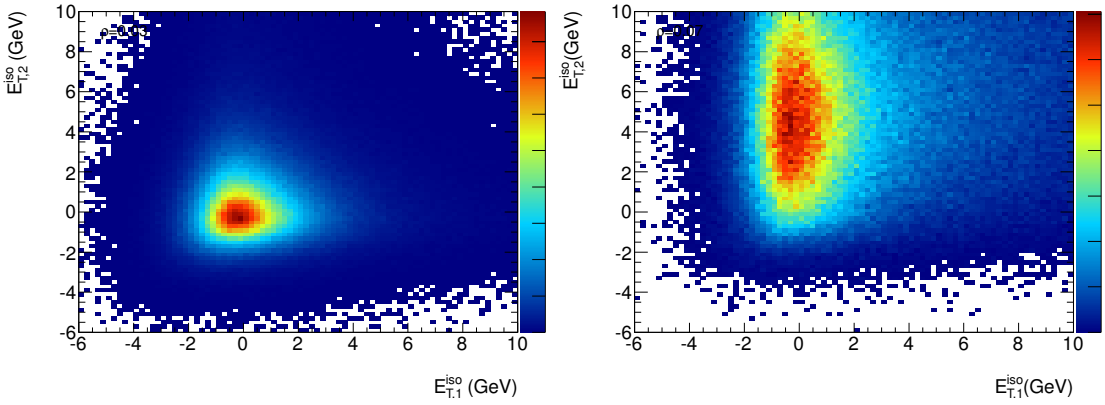

(a) $\gamma\gamma$ (SHERPA) (b) γj (data)

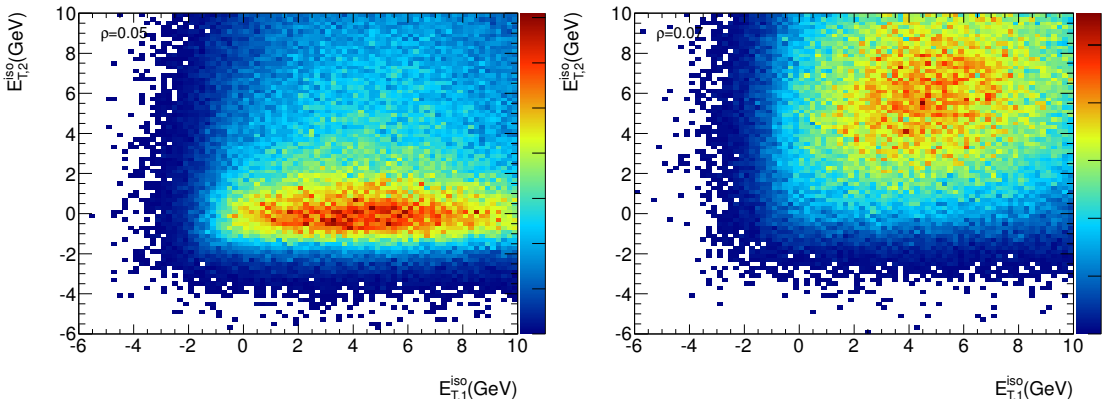

(c) jγ (data) (d) jj (data)

Figure 7.3: 2D distributions of $E_{\mathrm{T}}^{\mathrm{iso}}$ between the leading and subleading candidates for (a) $\gamma\gamma$ taken from SHERPA MC, (b) γj taken from the **TIT̃I** data control samples, (c) jγ taken from the **T̃ITI** data control samples and (d) jj taken from the **T̃IT̃I** data control samples.

7.6 Diphoton yield extraction

After the full event selection, a total of 312,754 data events are retained in the analysis. The main background arises from misidentified jets or electrons.

The sections are organized as follows. An event weighting method called the 4×4 matrix method in Section 7.7 is employed to subtract the hadronic background. The systematic uncertainty due to subtraction of the hadronic background is detailed in Section 7.8.1. The extracted yield after hadronic background subtraction using the matrix method is presented in Section 7.8.2. This is followed by another data-driven method to estimate the electron background of the remaining sample in Section 7.9. Section 7.10.1 gives a brief review of an alternative method to extract the diphoton yield. A closure test is performed to study the performance of the proposed methods in Section 7.10.2.

7.7 4x4 matrix method

The section mainly focuses on the hadronic background subtraction, where the photon here means a photon or an electron. That is, for the purpose of this section the electron background is included in the "signal". The subtraction of the Drell-Yan background is described in Section 7.9.

7.7.1 Description of the method

The event selection and the choice of the pair of photon candidates follows the prescriptions as detailed in Section 7.4, up to the requirement that both photon candidates be **T** and $E_{\mathrm{T}}^{\mathrm{iso}} < 10$ GeV and $p_T^{\mathrm{iso}} < 5$ GeV (**TT** sample). Then the photon candidate can belong to one of the following classifications according to the calorimeter isolation energy $E_{\mathrm{T}}^{\mathrm{iso}}$ and the track isolation energy p_T^{iso}: if $E_{\mathrm{T}}^{\mathrm{iso}} < 6$ GeV and $p_T^{\mathrm{iso}} < 2.6$ GeV, the candidate "passes" (P), otherwise "fails" (F). Therefore the **TT** sample can be classified into four categories, based on the pass/fail status of both candidates, thus obtaining $N_{\mathrm{PP}}^{\mathrm{TT}}$, $N_{\mathrm{PF}}^{\mathrm{TT}}$, $N_{\mathrm{FP}}^{\mathrm{TT}}$, $N_{\mathrm{FF}}^{\mathrm{TT}}$.[3] These can be transferred to the number of events for each final state $N_{\gamma\gamma}^{\mathrm{TT}}$, $N_{\gamma j}^{\mathrm{TT}}$, $N_{j\gamma}^{\mathrm{TT}}$ and N_{jj}^{TT} by solving the following system of four linear equations:

$$\begin{pmatrix} N_{\mathrm{PP}}^{\mathrm{TT}} \\ N_{\mathrm{PF}}^{\mathrm{TT}} \\ N_{\mathrm{FP}}^{\mathrm{TT}} \\ N_{\mathrm{FF}}^{\mathrm{TT}} \end{pmatrix} = \mathbf{E} \begin{pmatrix} N_{\gamma\gamma}^{\mathbf{TT}} \\ N_{\gamma\mathrm{j}}^{\mathbf{TT}} \\ N_{\mathrm{j}\gamma}^{\mathbf{TT}} \\ N_{\mathrm{jj}}^{\mathbf{TT}} \end{pmatrix}. \tag{7.3}$$

E is a 4×4 matrix, whose coefficients describe the probabilities that a given final state produces a certain pass/fail status.

If there were no correlation in isolation status between the two candidates, the matrix **E** would take the following form:

$$\mathbf{E} = \begin{pmatrix} \epsilon_1\epsilon_2 & \epsilon_1 f_2 & f_1\epsilon_2 & f_1 f_2 \\ \epsilon_1(1-\epsilon_2) & \epsilon_1(1-f_2) & f_1(1-\epsilon_2) & f_1(1-f_2) \\ (1-\epsilon_1)\epsilon_2 & (1-\epsilon_1)f_2 & (1-f_1)\epsilon_2 & (1-f_1)f_2 \\ (1-\epsilon_1)(1-\epsilon_2) & (1-\epsilon_1)(1-f_2) & (1-f_1)(1-\epsilon_2) & (1-f_1)(1-f_2) \end{pmatrix}, \tag{7.4}$$

where ϵ_i and f_i ("efficiency" and "fake rate") are the probabilities that a signal photon or a fake candidate respectively, passes the isolation requirement, and $i = 1, 2$

[3] From now on, the first subscript refers to the photon candidate with highest E_{T}^{γ} ("leading"), whereas the second subscript is for the other candidate with the second highest E_{T}^{γ} ("sub-leading") in the selected photon pair.

refers to the leading and subleading candidates, respectively. The evaluation of ϵ_i and f_i coefficients are explained in Section 7.7.2. Since ϵ_i and f_i have strong dependence on $|\eta_{s2}|$ and p_T, it is necessary to estimate the probability for each final state on an event basis.

The same equation can be rewritten on an event-by-event basis, by replacing $N_{\rm PP}^{\rm TT}$, $N_{\rm PF}^{\rm TT}$, $N_{\rm FP}^{\rm TT}$, $N_{\rm FF}^{\rm TT}$ with boolean status variables $B_{\rm PP}^{\rm TT}$, $B_{\rm PF}^{\rm TT}$, $B_{\rm FP}^{\rm TT}$, $B_{\rm FF}^{\rm TT}$ and replacing $N_{\gamma\gamma}^{\rm TT}$, $N_{\gamma j}^{\rm TT}$, $N_{j\gamma}^{\rm TT}$ and $N_{jj}^{\rm TT}$ with event weights $W_{\gamma\gamma}^{\mathbf{TT}}$, $W_{\rm \gamma j}^{\mathbf{TT}}$, $W_{\rm j\gamma}^{\mathbf{TT}}$, $W_{\rm jj}^{\mathbf{TT}}$. For the k-th event in the **TT** sample, Equation 7.3 takes the following form:

$$\begin{pmatrix} B_{\rm PP}^{\rm TT(k)} \\ B_{\rm PF}^{\rm TT(k)} \\ B_{\rm FP}^{\rm TT(k)} \\ B_{\rm FF}^{\rm TT(k)} \end{pmatrix} = \mathbf{E}^{(\rm k)} \begin{pmatrix} W_{\gamma\gamma}^{\rm TT(k)} \\ W_{\rm \gamma j}^{\rm TT(k)} \\ W_{\rm j\gamma}^{\rm TT(k)} \\ W_{\rm jj}^{\rm TT(k)} \end{pmatrix}. \tag{7.5}$$

$B_{XY}^{\rm TT(k)}$ are boolean status variables for the k-th event. For instance, if the k-th event has two **TI** photon candidates, $B_{\rm PP}^{\rm TT(k)} = 1$, $B_{\rm PF}^{\rm TT(k)} = B_{\rm FP}^{\rm TT(k)} = B_{\rm FF}^{\rm TT(k)} = 0$. The event weight $W_{\alpha\beta}^{\rm TT(k)}$ (with $\alpha\beta$ any of $\gamma\gamma$, γj, jγ, jj) can be obtained by inverting the 4×4 matrix in Equation 7.5:

$$\begin{pmatrix} W_{\gamma\gamma}^{\rm TT(k)} \\ W_{\rm \gamma j}^{\rm TT(k)} \\ W_{\rm j\gamma}^{\rm TT(k)} \\ W_{\rm jj}^{\rm TT(k)} \end{pmatrix} = [\mathbf{E}^{(\rm k)}]^{-1} \begin{pmatrix} B_{\rm PP}^{\rm TT(k)} \\ B_{\rm PF}^{\rm TT(k)} \\ B_{\rm FP}^{\rm TT(k)} \\ B_{\rm FF}^{\rm TT(k)} \end{pmatrix}. \tag{7.6}$$

$W_{\alpha\beta}^{\rm TT(k)}$ is not bound between 0 and 1. But its average $\langle W_{\alpha\beta}^{TT} \rangle$ over a large number of data events tends to the probability that the physical final state be $\alpha\beta$. In particular, $W_{\gamma\gamma}^{\rm TT(k)}$ describes how signal-like an event is, and summing $W_{\gamma\gamma}^{\rm TT(k)}$ over all the observed events in the **TT** region gives an estimator of the $\gamma\gamma$ yield in the **TT** sample:

$$N_{\gamma\gamma}^{\mathbf{TT}} = \sum_{k \in \mathbf{TT}} W_{\gamma\gamma}^{\rm TT(k)}. \tag{7.7}$$

In order to estimate the $\gamma\gamma$ yield in the **TITI** sample, the event weight $W_{\gamma\gamma}^{\rm TT(k)}$ must be refined to take into account the probability $(\epsilon_1^{(\rm k)}\epsilon_2^{(\rm k)})$ that both photons fulfill the isolation requirement:

$$N_{\gamma\gamma}^{\mathbf{TITI}} = \sum_{k \in \mathbf{TT}} \epsilon_1^{(k)}\epsilon_2^{(k)} W_{\gamma\gamma}^{\rm TT(k)}. \tag{7.8}$$

Due to the presence of strong statistical correlations between matrix coefficients and $N_{\rm PP}^{\rm TT}$, $N_{\rm PF}^{\rm TT}$, $N_{\rm FP}^{\rm TT}$, $N_{\rm FF}^{\rm TT}$, the bootstrap method is employed to calculate the

statistical uncertainty for the extracted yield as detailed in Section 7.7.8.

7.7.2 Estimation of ϵ and f

A tag and probe sample is selected and we use the "probe" candidate to estimate ϵ or f, where the "tag" refers to one photon candidate and the "probe" refers to the other photon candidate. Three control regions are defined for the evaluation of the matrix coefficients (ϵ and f) for the "probe" candidate:

- Non-tight region ($\tilde{\mathbf{T}}$): as defined in Section 7.5.1. Such a sample is enriched with fake photons but contains a small fraction of prompt photons.
- Non-isolated region ($\tilde{\mathbf{I}}$): $9 < E_{\mathrm{T}}^{\mathrm{iso}} < 24$ GeV and $6 < p_T^{\mathrm{iso}} < 22$ GeV. It is used to ensure the control region is enhanced with fake photons. However, a non-negligible fraction of photons might still be present as described in Section 7.7.5.
- Anti-isolated region ($\tilde{\tilde{\mathbf{I}}}$) : represents a candidate failing the isolation requirement, which is equivalent to the definition of "F". It is used in the fake rate calculation for the tag failing the isolation requirement.

The photon candidates in the probe sample are counted according to whether they pass the identification criterion and whether they pass the isolation requirement. A few assumptions are given as follows:

(1) the ratio α in number of prompt photons of $\tilde{\mathbf{T}}$ to $\mathbf{T}$ is independent of the isolation status. It is estimated from Sherpa MC:

$$\alpha = \frac{n_\gamma^{\tilde{\mathbf{T}}}}{n_\gamma^{\mathbf{T}}} = \frac{n_\gamma^{\tilde{\mathbf{T}}\mathbf{I}}}{n_\gamma^{\mathbf{T}\mathbf{I}}} = \frac{n_\gamma^{\tilde{\mathbf{T}}\tilde{\mathbf{I}}}}{n_\gamma^{\mathbf{T}\tilde{\mathbf{I}}}}. \tag{7.9}$$

(2) the ratio β of number of fake photons from $\mathbf{T}$ to $\tilde{\mathbf{T}}$ is independent of the isolation status. It is data-driven:

$$\beta = \frac{n_j^{\mathbf{T}}}{n_j^{\tilde{\mathbf{T}}}} = \frac{n_j^{\mathbf{T}\mathbf{I}}}{n_j^{\tilde{\mathbf{T}}\mathbf{I}}} = \frac{n_j^{\mathbf{T}\tilde{\mathbf{I}}}}{n_j^{\tilde{\mathbf{T}}\tilde{\mathbf{I}}}}. \tag{7.10}$$

(3) the $\tilde{\mathbf{I}}$ is chosen such that it is enriched with jets faking photons in this control region. However, MC studies show that there is a non-negligible fraction of prompt photons ($\sim 7\%$ in the $\mathbf{TIT\tilde{I}}$ region) for the subleading candidate. The "leakage" of signal $\gamma\gamma$ events into the $\tilde{\mathbf{I}}$ region is subtracted using the $\gamma\gamma$ Pythia sample. Thus

after subtraction of the diphoton signal in the $\mathbf{T\tilde{I}}$ region, Equation 7.10 reads:

$$\beta = \frac{n_j^{\mathbf{T}}}{n_j^{\tilde{\mathbf{T}}}} = \frac{n^{\mathbf{T\tilde{I}}} - n_{\gamma,\mathrm{MC}}^{\mathbf{T\tilde{I}}}}{n^{\tilde{\mathbf{T}}\tilde{\mathbf{I}}}}. \tag{7.11}$$

From these counts, the prompt and fake photon yields n_γ^X and n_j^X can be estimated for any region X. Hence:

$$n_\gamma^{\mathbf{T}} = n^{\mathbf{T}} - n_j^{\mathbf{T}} = n^{\mathbf{T}} - \beta n_j^{\tilde{\mathbf{T}}} = n^{\mathbf{T}} - \beta(n^{\tilde{\mathbf{T}}} - n_\gamma^{\tilde{\mathbf{T}}}) = n^{\mathbf{T}} - \beta(n^{\tilde{\mathbf{T}}} - \alpha n_\gamma^{\mathbf{T}}). \tag{7.12}$$

$n_\gamma^{\mathbf{T}}$ can be solved:

$$n_\gamma^{\mathbf{T}} = \frac{n^{\mathbf{T}} - \beta n^{\tilde{\mathbf{T}}}}{1-\alpha\beta}; \qquad n_\gamma^{\mathbf{TI}} = \frac{n^{\mathbf{TI}} - \beta n^{\tilde{\mathbf{T}}\mathbf{I}}}{1-\alpha\beta}. \tag{7.13}$$

Similarly for $n_j^X = n^X - n_\gamma^X$, therefore:

$$n_j^{\mathbf{T}} = \frac{\beta}{1-\alpha\beta}(n^{\tilde{\mathbf{T}}} - \alpha n^{\mathbf{T}}); \qquad n_j^{\mathbf{TI}} = \frac{\beta}{1-\alpha\beta}(n^{\tilde{\mathbf{T}}\mathbf{I}} - \alpha n^{\mathbf{TI}}). \tag{7.14}$$

The ϵ and f can be expressed as:

$$\epsilon = \frac{n_\gamma^{\mathbf{TI}}}{n_\gamma^{\mathbf{T}}} = \frac{n^{\mathbf{TI}} - \beta n^{\tilde{\mathbf{T}}\mathbf{I}}}{n^{\mathbf{T}} - \beta n^{\tilde{\mathbf{T}}}}; \qquad f = \frac{n_j^{\mathbf{TI}}}{n_j^{\mathbf{T}}} = \frac{n^{\tilde{\mathbf{T}}\mathbf{I}} - \alpha n^{\mathbf{TI}}}{n^{\tilde{\mathbf{T}}} - \alpha n^{\mathbf{T}}}. \tag{7.15}$$

7.7.3 Requirements on the tag candidate

The following requirements are applied on the tag:

- In order to measure ϵ and f in the $\gamma\gamma$, γj and jγ final states, all tag candidates are required to be **TI**. For photon isolation efficiency ϵ, it is independent of the isolation status of the other candidate. It was found that forcing non-isolation on the tag in the calculation of the fake rate for the γj and jγ components would enhance jj contamination in our "tag and probe" sample.

- In the fourth column (jj components), we explicitly require the tag candidate to be $\tilde{\mathbf{T}}$ such that the tag is enriched with fake photons. Furthermore, to take into account the isolation correlations in the jj background component, conditional probabilities are used, requiring the tag candidate to pass the isolation criteria or not:

$$f_1 f_2 \to \frac{1}{2}\left[f_1 f_2^{\hat{\mathrm{P}}} + f_1^{\hat{\mathrm{P}}} f_2\right], \tag{7.16}$$

$$f_1(1-f_2) \to \frac{1}{2}\left[f_1\left(1-f_2^{\hat{\mathrm{P}}}\right)+f_1^{\hat{\mathrm{F}}}\left(1-f_2\right)\right], \tag{7.17}$$

where $\hat{\mathrm{P}}$ and $\hat{\mathrm{F}}$ denote the pass/fail status of the tag. The ambiguity in the choice of tag is solved by taking both choices and averaging them. f_i refers to the fake rate in the di-jet system with only the preselection isolation requirement on the tag candidate.

Hence the 4x4 matrix **E** takes the following structure:

$$\mathbf{E} = \begin{pmatrix} \epsilon_1^{\hat{\mathrm{P}}}\epsilon_2^{\hat{\mathrm{P}}} & \epsilon_1^{\hat{\mathrm{P}}}f_2^{\hat{\mathrm{P}}} & f_1^{\hat{\mathrm{P}}}\epsilon_2^{\hat{\mathrm{P}}} & \frac{1}{2}\left[f_1 f_2^{\hat{\mathrm{P}}}+f_1^{\hat{\mathrm{P}}}f_2\right] \\ \epsilon_1^{\hat{\mathrm{P}}}\left(1-\epsilon_2^{\hat{\mathrm{P}}}\right) & \epsilon_1^{\hat{\mathrm{P}}}\left(1-f_2^{\hat{\mathrm{P}}}\right) & f_1^{\hat{\mathrm{P}}}\left(1-\epsilon_2^{\hat{\mathrm{P}}}\right) & \frac{1}{2}\left[f_1\left(1-f_2^{\hat{\mathrm{P}}}\right)+f_1^{\hat{\mathrm{F}}}\left(1-f_2\right)\right] \\ \left(1-\epsilon_1^{\hat{\mathrm{P}}}\right)\epsilon_2^{\hat{\mathrm{P}}} & \left(1-\epsilon_1^{\hat{\mathrm{P}}}\right)f_2^{\hat{\mathrm{P}}} & \left(1-f_1^{\hat{\mathrm{P}}}\right)\epsilon_2^{\hat{\mathrm{P}}} & \frac{1}{2}\left[\left(1-f_1\right)f_2^{\hat{\mathrm{F}}}+\left(1-f_1^{\hat{\mathrm{P}}}\right)f_2\right] \\ \left(1-\epsilon_1^{\hat{\mathrm{P}}}\right)\left(1-\epsilon_2^{\hat{\mathrm{P}}}\right) & \left(1-\epsilon_1^{\hat{\mathrm{P}}}\right)\left(1-f_2^{\hat{\mathrm{P}}}\right) & \left(1-f_1^{\hat{\mathrm{P}}}\right)\left(1-\epsilon_2^{\hat{\mathrm{P}}}\right) & \frac{1}{2}\left[\left(1-f_1\right)\left(1-f_2^{\hat{\mathrm{F}}}\right)+\left(1-f_1^{\hat{\mathrm{F}}}\right)\left(1-f_2\right)\right] \end{pmatrix}, \tag{7.18}$$

where $\epsilon_i^{\hat{\mathrm{P}}}$ refers to the isolation efficiency given that the tag candidate passes the isolation requirement. $f_i^{\hat{\mathrm{P}}}$ in the last three columns refers to the fake rate in the γj, jγ and jj systems provided the tag candidate passes the isolation requirement.

7.7.4 Dependence of photon isolation efficiencies on kinematic variables

The isolation efficiencies vary as a function of p_T and $|\eta_{s2}|$[4] as well as the variable of interest in diphoton Sherpa MC, as presented in Figure 7.4[5]. For instance, the low-mass region ($0 < m_{\gamma\gamma} < 50$ GeV) in Figure 7.4b is sensitive to the fragmentation component, and thus having typically lower photon isolation efficiencies than the relatively high-mass region ($80 < m_{\gamma\gamma} < 90$ GeV) in Figure 7.4c. Similarly, the difference in photon isolation efficiency between $0 < p_{T,\gamma\gamma} < 5$ GeV and $20 < p_{T,\gamma\gamma} < 30$ GeV is non-negligible. These sub-samples in the specific phase space possess unique kinematic properties compared to inclusive photon isolation efficiencies as shown in Figure 7.4a.

When evaluating a differential distribution as a function of a kinematic variable (e.g. $m_{\gamma\gamma}$) the efficiencies are evaluated as a function of p_T, η and the relevant variable.[6] This is referred to as the 3D matrix method. A closure test, as depicted

[4]The nominal p_T binning for the leading candidate: $[25, 45, 55, 75, 600]$ GeV; the nominal p_T binning for the subleading candidate is:$[25, 45, 55, 75, 600]$ GeV; the nominal η binning is: $[0, 0.6, 1.37, 1.56, 1.81, 2.37]$.

[5]In MC, the isolation efficiency is set to 1 if there are no events in the probed phase space.

[6]Due to limited statistics, the binning in the 3D isolation efficiency or fake rates for variables of interest. $m_{\gamma\gamma}$: $[0, 50, 70, 80, 90, 100, 115, 150, 1800]$; $p_{\mathrm{T},\gamma\gamma}$:$[0, 5, 10, 20, 30, 45, 80, 750]$; $\Delta\phi_{\gamma\gamma}$:$[0, 1.5, 2.25, 2.65, 2.9, 3.05, 3.1416]$; $|\cos\theta^*_\eta|$: $[0, 0.16, 0.32, 0.52, 0.8, 1]$; a_{T}: $[0, 4, 10, 20, 30, 45, 80, 450]$; ϕ^*_η:$[0, 0.02, 0.039, 0.072, 0.114, 0.165, 0.312, 0.524, 1.153, 260000]$.

in Section 7.10.2, shows that the 3D matrix method does much better than the 2D matrix method in the differential spectrum.

7.7.5 Studies for tight non-isolated region

The estimation of photon isolation efficiencies assumed the contamination of prompt photons in the $\mathbf{T\tilde{I}}$ region is negligible, as was assumed in the previous 7 TeV analysis [45]. Further studies are performed using $\gamma\gamma$ SHERPA and PYTHIA MC after scaling the cross section to match that of the data [7]. Table 7.2 presents the number of events in the respective control regions for data and MC predictions. For the leading candidate, the contamination from the diphoton signal in the $\mathbf{T\tilde{I}}$ region is almost negligible. As for the subleading candidate, the PYTHIA MC predicts more than ten times the diphoton yield in the $\mathbf{T\tilde{I}}$ region predicted by SHERPA. The PYTHIA sample overestimates the ratio of fragmentation photons to direct photons. However, the isolation tails of SHERPA are underestimated due to the requirement that the separation ΔR between a parton and a photon is greater than 0.3. This leakage from fragmentation photons in the $\mathbf{TIT\tilde{I}}$ region cannot be ignored and is corrected. The PYTHIA prediction is taken as default for subtracting the diphoton signal in the $\mathbf{T\tilde{I}}$ region and the difference between $\gamma\gamma$ SHERPA and PYTHIA MC is taken as a systematic uncertainty which is symmetrized.

Figure 7.5 shows the extracted β_2 and ϵ_2 from collision data using scaled $\gamma\gamma$ PYTHIA (left) and SHERPA (right) respectively for subtracting the diphoton signal leakage in the $\mathbf{TIT\tilde{I}}$ region. β_2 derived using PYTHIA $\gamma\gamma$ MC (Figure 7.5a) gives a -10% change in comparison to that derived using SHERPA $\gamma\gamma$ MC (Figure 7.5b) for the diphoton signal leakage subtraction in the $\mathbf{TIT\tilde{I}}$ region, giving a -0.5% to -2% change in ϵ_2 as shown in Figure 7.5c and Figure 7.5d.

Control region	data	$\gamma\gamma$ Sherpa	$\gamma\gamma$ Pythia
$\mathbf{\tilde{T}IT\tilde{I}}$	15732	163	258
$\mathbf{TIT\tilde{I}}$	31417	257	2852

Table 7.2: The diphoton signal events in the $\mathbf{T\tilde{I}}$ region as predicted by SHERPA and PYTHIA separately. The diphoton signal leakage in the $\mathbf{\tilde{T}\tilde{I}}$ region is negligible.

[7] The SHERPA cross section is scaled by 1.3 and PYTHIA by 1.39 separately. The scaling factor is the ratio of the data-driven estimate of the $\gamma\gamma$ signal over that of the corresponding MC predictions in the **TITI** region.

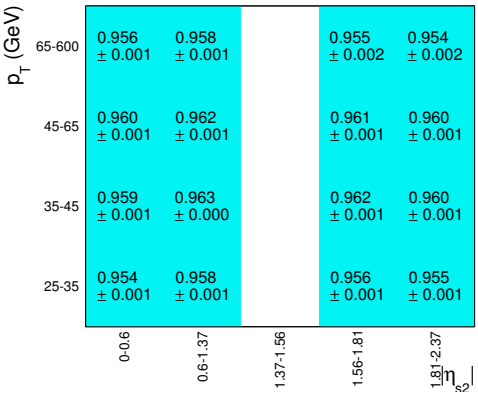

(a) Inclusive

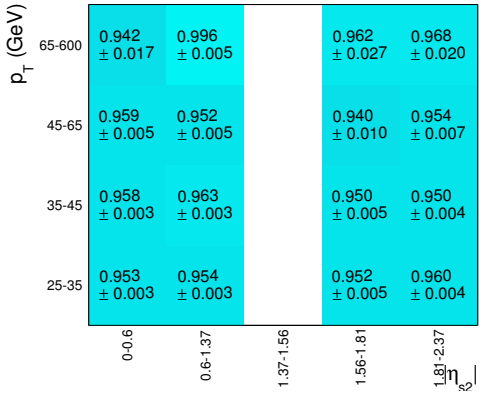

(b) $0 < m_{\gamma\gamma} < 50$ GeV

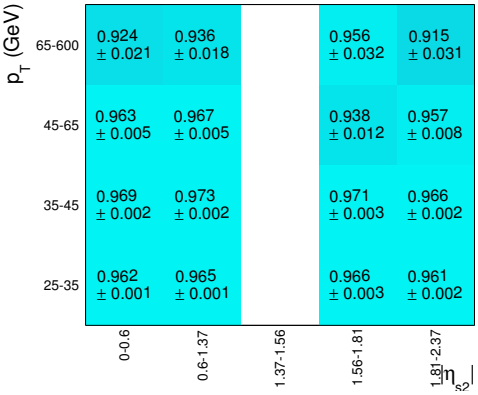

(c) $70 < m_{\gamma\gamma} < 80$ GeV

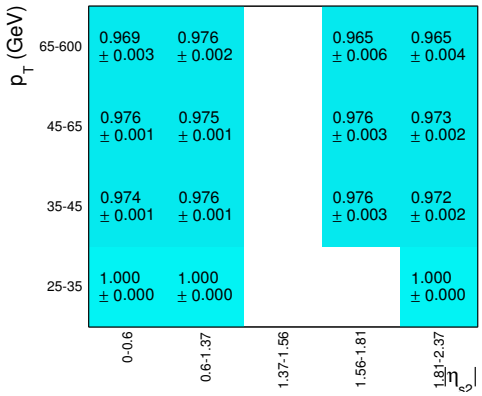

(d) $0 < p_{T,\gamma\gamma} < 5$ GeV

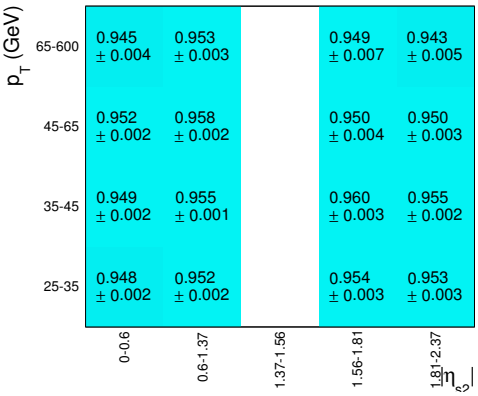

(e) $20 < p_{T,\gamma\gamma} < 30$ GeV

Figure 7.4: Extracted photon isolation efficiency of the subleading candidate from diphoton SHERPA MC in terms of p_T and $|\eta_{s2}|$ for (a) inclusive case, (b) $0 < m_{\gamma\gamma} < 50$ GeV, (c) $70 < m_{\gamma\gamma} < 80$ GeV, (d) $0 < p_{T,\gamma\gamma} < 5$ GeV and (e) $20 < p_{T,\gamma\gamma} < 30$ GeV.

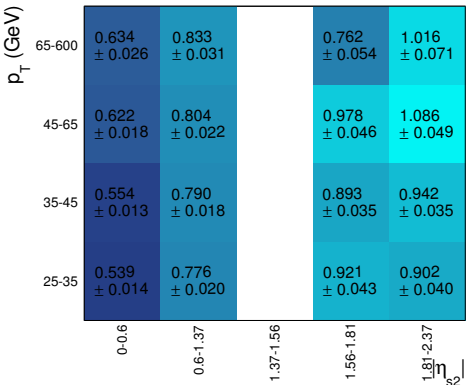

(a) β_2 derived using PYTHIA $\gamma\gamma$ MC

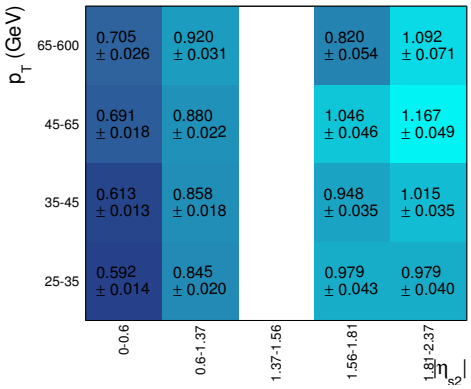

(b) β_2 derived using SHERPA $\gamma\gamma$ MC

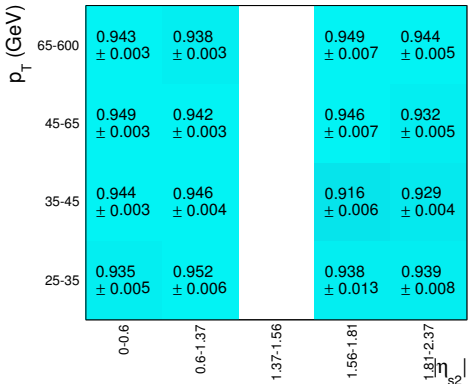

(c) Data-driven ϵ_2 using PYTHIA for β_2 calculation

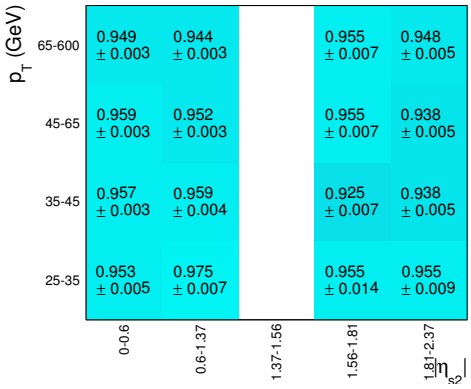

(d) Data-driven ϵ_2 using SHERPA for β_2 calculation

Figure 7.5: Extracted β_2 and ϵ_2 from collision data using the scaled $\gamma\gamma$ PYTHIA (left) and SHERPA (right) predictions for the diphoton signal leakage subtraction in the **TIT$\tilde{\text{I}}$** region.

7.7.6 Effects of fakes from electrons on data-driven isolation efficiencies

At around the Z-mass peak region (∼90 GeV), the data-driven isolation efficiencies in p_T and $|\eta_{s2}|$ were found to be significantly below the prediction from diphoton SHERPA MC samples as shown in Figure 7.6. The effect is particularly visible in the endcap region ($1.56 < |\eta_{s2}| < 2.37$), where the fake rates due to misidentified electrons can be much larger than in the barrel region. These photon candidates due to electron mis-identifications are a "special" group of photons, which tends to possess more EM activities and thus lower photon isolation efficiencies (Figure 7.6a).

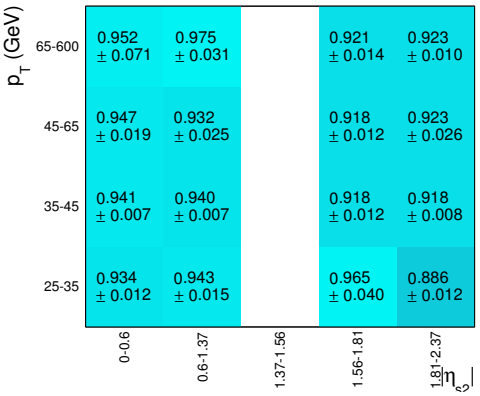

(a) Data-driven

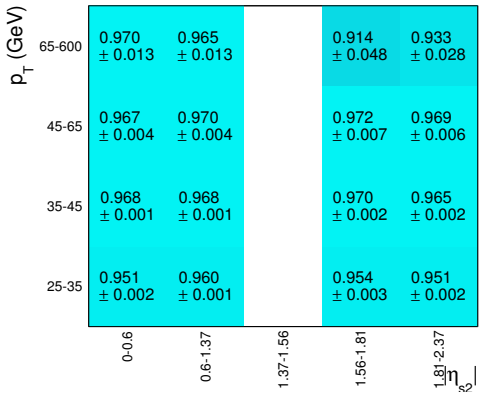

(b) Diphoton Sherpa MC

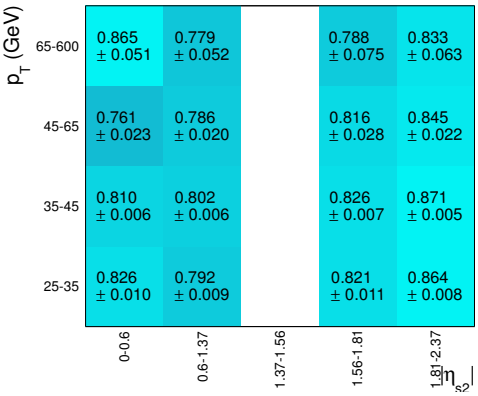

(c) Drell-Yan MC

Figure 7.6: Extracted photon isolation efficiency of the subleading candidate as a function of p_T and $|\eta_{s2}|$ for $80 < m_{\gamma\gamma} < 90$ GeV for (a) collision data and predictions from (b) the diphoton SHERPA MC and (c) the Drell-Yan MC.

7.7.7 Extracted isolation efficiency and fake rate

For the inclusive yield, ϵ and f are evaluated as a function of p_T and $|\eta_{s2}|$. As for the differential spectrum, ϵ and f are evaluated in p_T and $|\eta_{s2}|$ as well as the variable of

interest for the leading and subleading candidates separately. Neighbouring bins are grouped together where the number of events is low, particularly at low and high edges of p_T. Since the photon isolation efficiencies or the fake rates might have a strong dependence on the particular variable bin, bins are only merged along the p_T axis. The statistical correlations between neighbouring bins are taken into account using the bootstrap technique as illustrated in Section 7.7.8.

Figure 7.7 illustrates the extracted photon isolation efficiency in bins of p_T and $|\eta_{s2}|$. The photon isolation efficiency has a strong dependence on $|\eta_{s2}|$, where the photon isolation efficiency in the barrel region ($|\eta_{s2}| < 1.37$) is higher than in the endcap region ($1.56 < |\eta_{s2}| < 2.37$) due to the presence of misidentified electrons. It is fairly dependent on p_T. The isolation fake rate in the γ-jet (jet-γ) system is presented in Figure 7.8. The isolation fake rate decreases rapidly with p_T and has a fairly strong dependence on $|\eta_{s2}|$. Figure 7.9 shows the fake rate extraction for the jj background (4th column in equation 7.18), where the tag candidate is explicitly required to be $\tilde{\mathbf{T}}$. The extracted fake rate for the jj background has a strong dependence on the isolation status of the tag. For instance, the fake rate with the tag passing the isolation criteria is higher than that with the tag failing the isolation criteria.

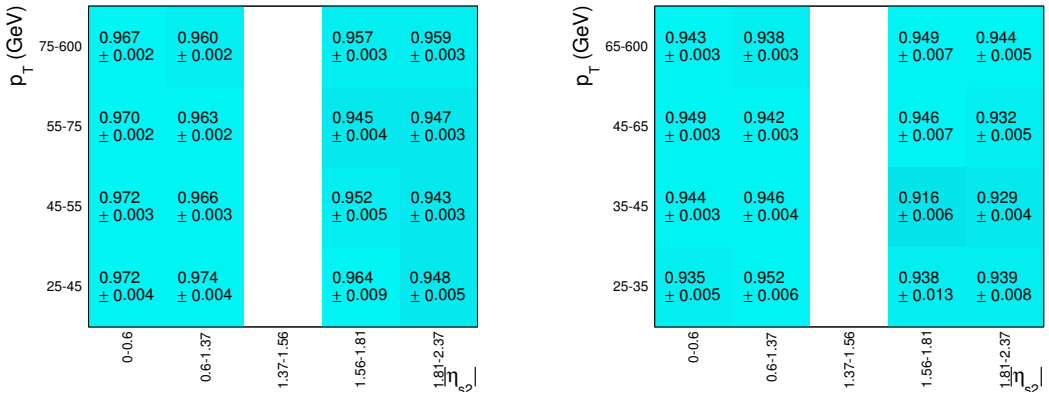

Figure 7.7: Extracted photon isolation efficiency of the leading (left) and subleading (right) candidates from collision data as a function of p_T and $|\eta_{s2}|$ with the tag candidate passing the **TI** requirement.

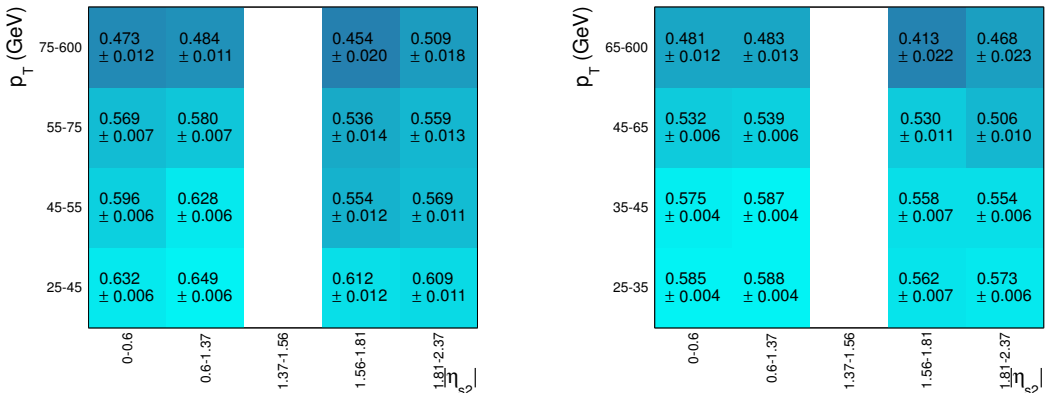

Figure 7.8: Extracted fake rates of the leading (left) and subleading (right) candidates in the γj and jγ background respectively from collision data as a function of p_T and $|\eta_{s2}|$ and with the tag candidate passing the **TI** requirement.

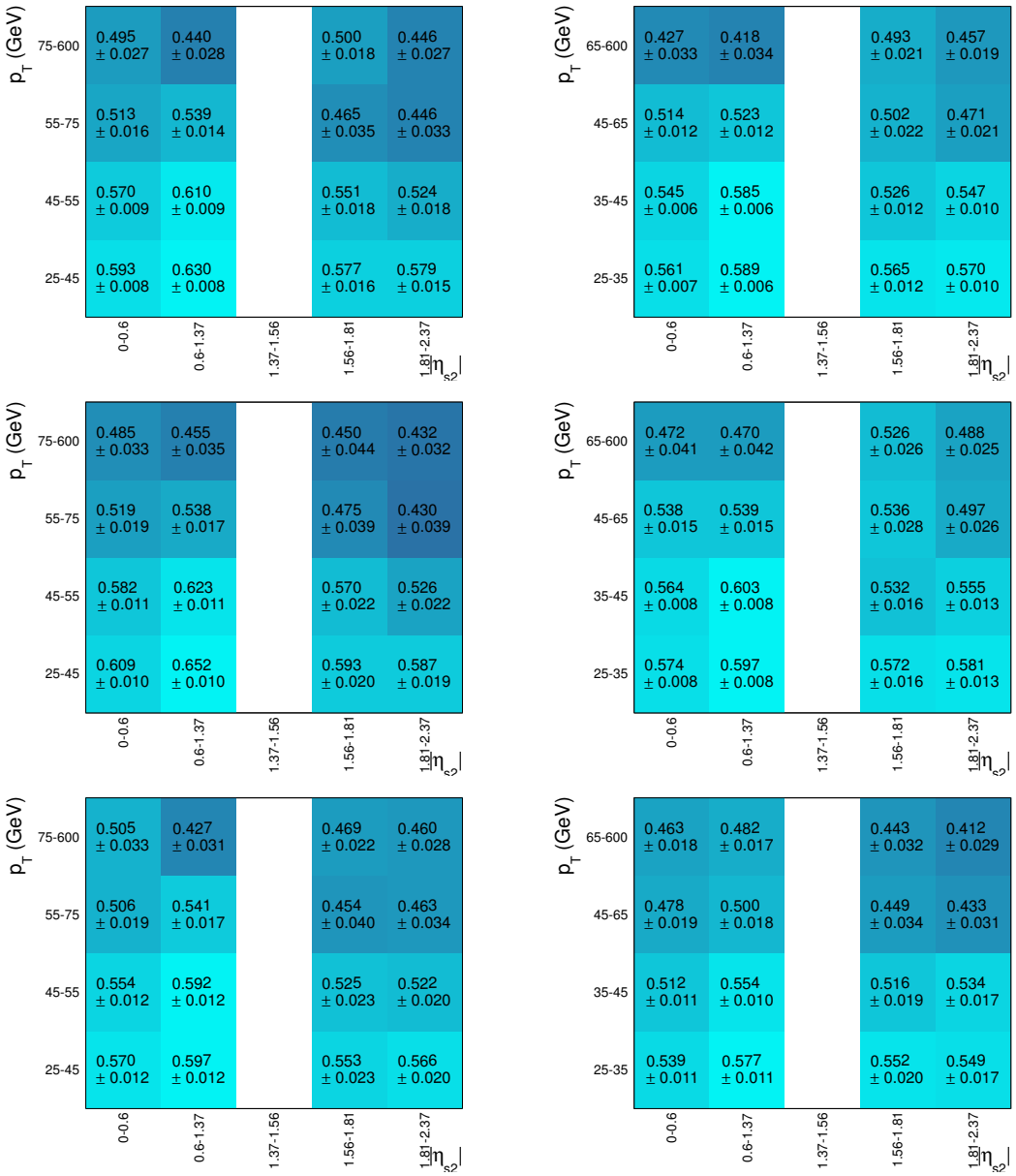

Figure 7.9: Extracted fake rate of the di-jet system of the leading (left) and subleading (right) candidates from collision data as a function of p_T and $|\eta_{s2}|$ with the tag candidate fulfilling the requirement of $\tilde{\mathbf{T}}$ (top), $\tilde{\mathbf{T}}\mathbf{I}$ (middle) and $\tilde{\mathbf{T}}\tilde{\tilde{\mathbf{I}}}$ (bottom).

7.7.8 Bootstrap technique in matrix method

The bootstrap technique [86] is applied manually in the matrix method to estimate the statistical uncertainty, which takes account of strong statistical correlations between the data-driven matrix coefficients and $N_{\mathrm{PP}}^{\mathrm{TT}}$, $N_{\mathrm{PF}}^{\mathrm{TT}}$, $N_{\mathrm{FP}}^{\mathrm{TT}}$, $N_{\mathrm{FF}}^{\mathrm{TT}}$. It is described as follows:

- 1000 toy experiments of data are produced, where each event in data passing Loose′4 is assigned a weight drawn randomly from a Poisson distribution of mean 1.
- In the first loop, calculate the matrix coefficients ϵ and f in Equation 7.5 for each toy experiment.
- In the second loop, calculate the event weights for each toy experiment.
- The inclusive $\gamma\gamma$ yield of 1000 toy experiments using the 2D matrix method is presented in Figure 7.10 and the distribution follows a Gaussian. The extracted nominal inclusive yield in $\gamma\gamma$,γj, jγ, jj and the mean inclusive yield of 1000 toy experiments are listed in Table 7.3. The mean yield of 1000 toy experiments is in excellent agreement with the nominal yield within the uncertainty on the mean value.
- One naively expects the root of mean squared (RMS) of these 1000 toy experiments gives the correct statistical uncertainty, both for the inclusive yield and for the differential cross-section in variables of interest. However, the large statistical fluctuations in the 3D efficiencies or fake rates have resulted in a "non-Gaussian" tail.
- In order to obtain the correct RMS of the distribution, we first apply a very loose cut for the yield to be within 25 standard deviations of statistical uncertainty from the nominal mean value and then calculate the RMS of the distribution, which eliminates the very extreme tail of the distribution. After which we require the yield to be within three RMS around the mean value. Then this "truncated" RMS is recalculated and treated as the statistical uncertainty of the yield. The procedure is applied in the 3D matrix method for the differential spectrum only. In addition, any difference between the nominal yield and the mean of the 1000 toy experiments is added in quadrature with the statistical uncertainty returned by the bootstrap method, which is the final statistical uncertainty.

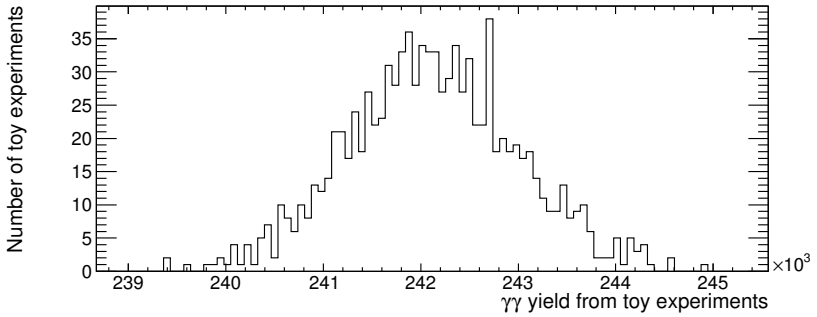

Figure 7.10: The $\gamma\gamma$ inclusive yield distribution of the 1000 toy experiments.

Final state	Nominal	Toy experiments
$\gamma\gamma$	242155	242116±874
γj	45175	45165±529
jγ	17974	17992±425
jj	7450	7461±228

Table 7.3: Signal ($\gamma\gamma$) and background (γj, jγ, jj) nominal yields and the mean inclusive yields with RMS of 1000 toy experiments in the **TITI** region.

7.7.9 The differential spectrum

The extracted differential spectra in terms of the kinematic variables $m_{\gamma\gamma}$, $p_{\mathrm{T},\gamma\gamma}$, $\Delta\phi_{\gamma\gamma}$, $|\cos\theta^*_\eta|$, a_{T} and ϕ^*_η are illustrated in Figures 7.11, for the $\gamma\gamma$, γj+jγ and jj final states. The "Guillet shoulder" [41] can be observed in the $p_{\mathrm{T},\gamma\gamma}$ and a_{T} spectra due to an enhancement of the fragmentation component. The diphoton signal purity as a function of $m_{\gamma\gamma}$, $p_{\mathrm{T},\gamma\gamma}$, $\Delta\phi_{\gamma\gamma}$, $|\cos\theta^*_\eta|$, a_{T} and ϕ^*_η is presented in Figure 7.12. The diphoton signal purity increases with $m_{\gamma\gamma}$ as expected because the fake rate decreases rapidly with p_T as shown in Figure 7.8 and Figure 7.9.

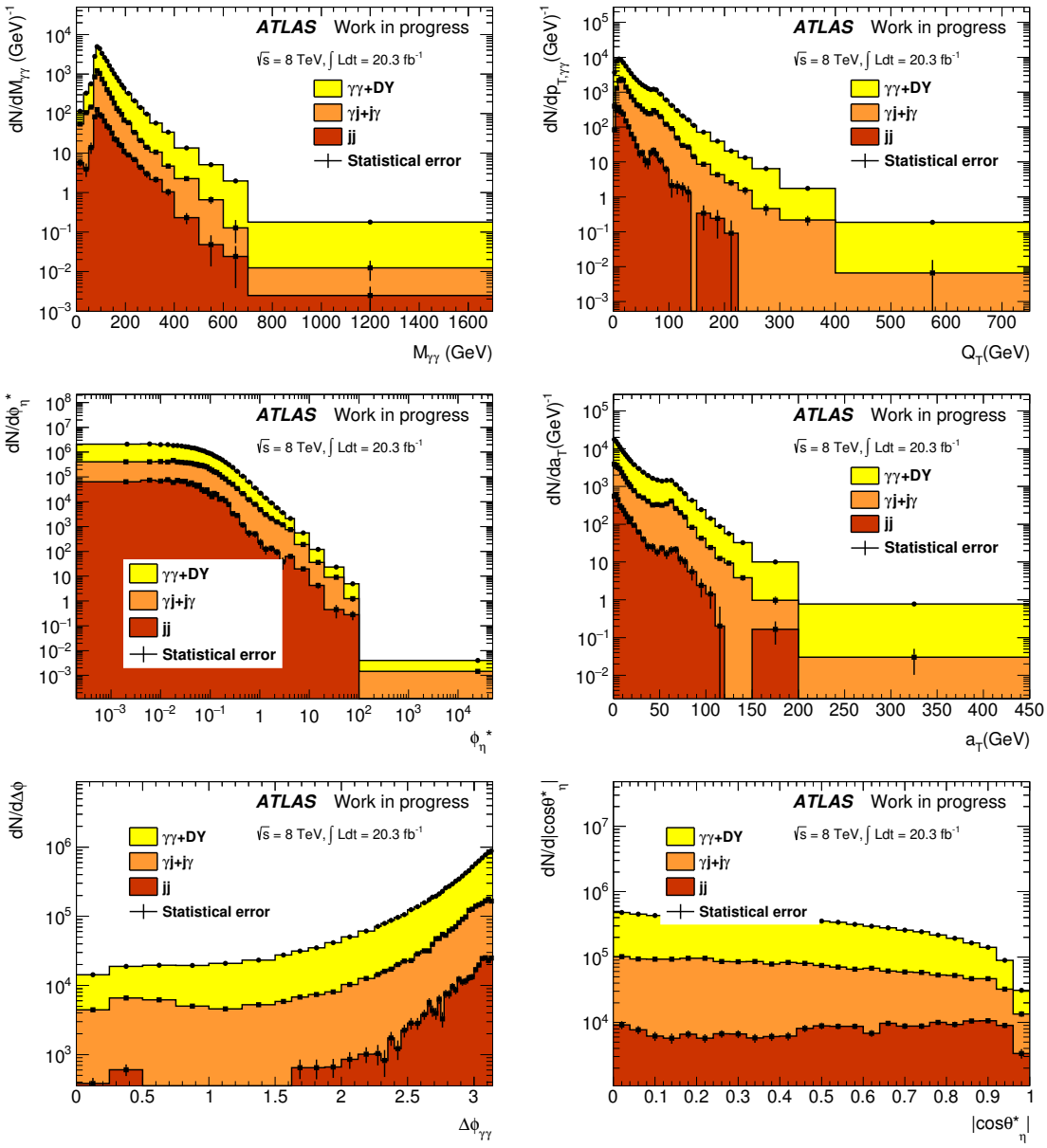

Figure 7.11: The extracted differential spectrum in terms of $m_{\gamma\gamma}$, $p_{\mathrm{T},\gamma\gamma}$, ϕ^*_η, a_{T}, $\Delta\phi_{\gamma\gamma}$ and $|\cos\theta^*_\eta|$ for the $N_{\gamma\gamma}$ (yellow), $N_{\gamma\mathrm{j}} + N_{\mathrm{j}\gamma}$ (orange), and N_{jj} (light red) contributions. Only the statistical uncertainty (black line) is shown here.

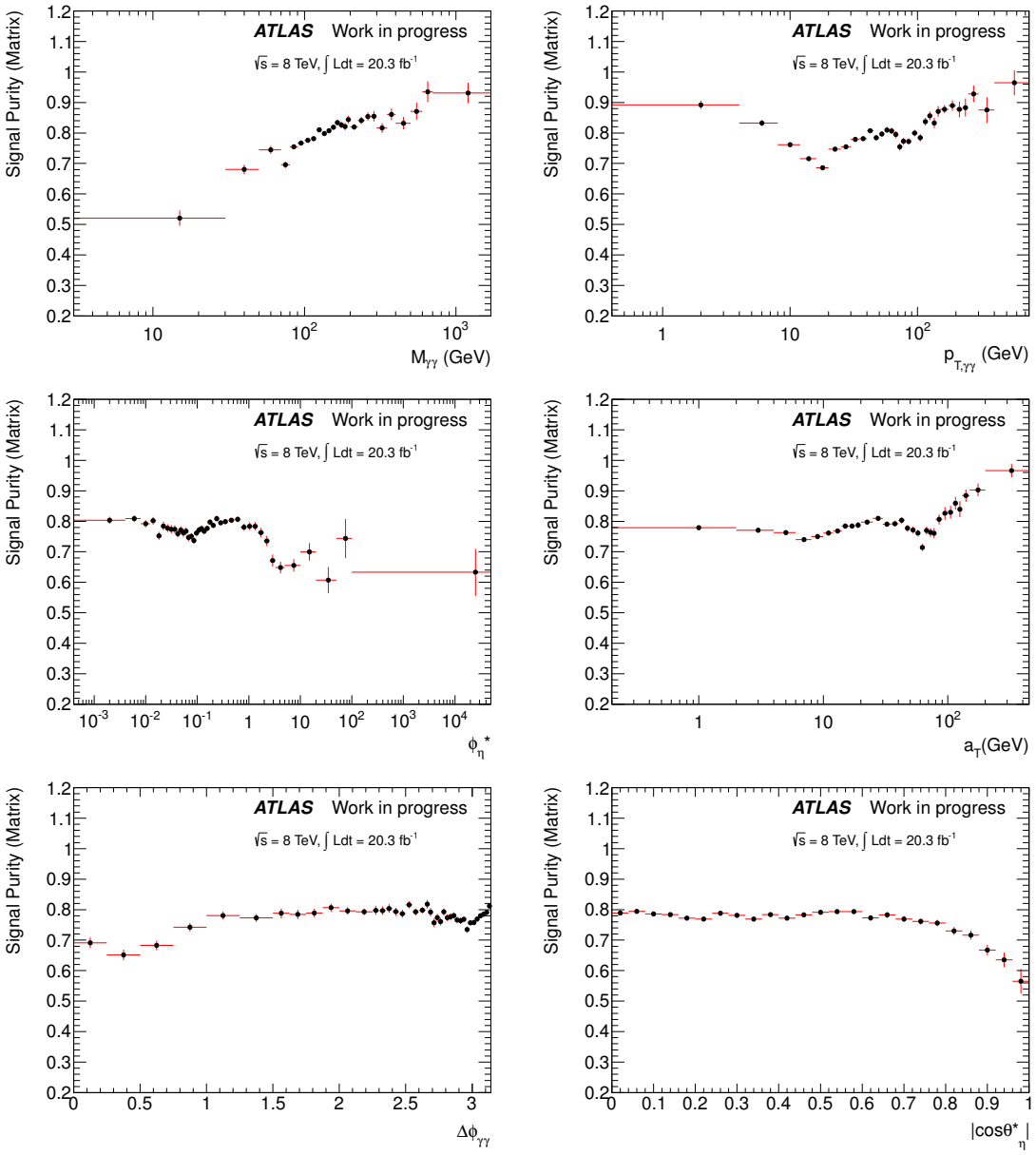

Figure 7.12: The extracted diphoton signal purity in terms of $m_{\gamma\gamma}$, $p_{\mathrm{T},\gamma\gamma}$, ϕ^*_η, a_{T}, $\Delta\phi_{\gamma\gamma}$ and $|\cos\theta^*_\eta|$. Only the statistical uncertainty (red line) is shown here and is obtained using the bootstrap method.

7.8 Final results from the matrix method

7.8.1 Background systematic uncertainties in the matrix method

The following systematic effects have been considered for the matrix method.

- **$\tilde{\mathbf{T}}$ definition**
  The nominal choice of the jet control sample is comprised of events passing the Loose′4 selection but failing the **T** criteria. The analysis is repeated using alternative $\tilde{\mathbf{T}}$ definitions in which events fail the **T** requirement but pass the Loose′2, Loose′3 or Loose′5 requirements (See Section 7.5.1). The largest difference is considered as the systematic uncertainty. As the jet properties are extrapolated from the $\tilde{\mathbf{T}}$ region to the **T** region, such a variation is considered to cover the systematic effects due to the correlation between tightness and isolation in jets.

- **Photon ID systematics**
  The photon identification leakage factor $\alpha = n^{\gamma}_{\tilde{\mathbf{T}}}/n^{\gamma}_{\mathbf{T}}$, defined as the ratio of $\tilde{\mathbf{T}}$ photons to **T** photons in Equation 7.9 in Section 7.7.2, is estimated directly from $\gamma\gamma$ MC. It is related to the **T** photon identification efficiency determined with respect to the Loose′4 (also denoted as L' in the following equation) sample $\epsilon_{T|L'}$:

$$\alpha = \frac{n^{\gamma}_{\tilde{\mathbf{T}}}}{n^{\gamma}_{\mathbf{T}}} = \frac{n^{\gamma}_{\tilde{\mathbf{T}}} + n^{\gamma}_{\mathbf{T}}}{n^{\gamma}_{\mathbf{T}}} - 1 = \frac{1}{\frac{n^{\gamma}_{\mathbf{T}}}{n^{\gamma}_{\tilde{\mathbf{T}}}+n^{\gamma}_{\mathbf{T}}}} - 1 = \frac{1}{\epsilon_{T|L'}} - 1. \tag{7.19}$$

  Using the photon identification efficiency scale factors and their systematic uncertainties derived by the e/γ performance group [83], we can calculate the corresponding change in α using Equation 7.19.

- **$\tilde{\mathbf{I}}$ region definition**
  An additional systematic uncertainty arises due to the choice of non-isolated region $\tilde{\mathbf{I}}$ ($9 < E_{\mathrm{T}}^{\mathrm{iso}} < 24$ GeV and $6 < p_T^{\mathrm{iso}} < 22$ GeV) to normalise the $\tilde{\mathbf{T}}$ sample before extraction of the photon isolation efficiency. The related systematic effect is evaluated by changing the $\tilde{\mathbf{I}}$ requirements to one of the following criteria:

  - $7 < E_{\mathrm{T}}^{\mathrm{iso}} < 17$ GeV and $6 < p_T^{\mathrm{iso}} < 22$ GeV
  - $11 < E_{\mathrm{T}}^{\mathrm{iso}} < 40$ GeV and $6 < p_T^{\mathrm{iso}} < 22$ GeV

- $9 < E_{\mathrm{T}}^{\mathrm{iso}} < 24$ GeV and $4 < p_T^{\mathrm{iso}} < 15$ GeV
- $9 < E_{\mathrm{T}}^{\mathrm{iso}} < 24$ GeV and $8 < p_T^{\mathrm{iso}} < 40$ GeV

These ranges are chosen such that the control region has similar statistics to the default choice. The maximum deviation from the nominal result is then taken as a systematic uncertainty.

- **$\gamma\gamma$ signal leakage in the $\tilde{\mathbf{I}}$ region**
  Another source of systematic uncertainty arises from the photon signal leakage particularly for the subleading candidate in the $\tilde{\mathbf{I}}$ region, as explained in Section 7.7.5. The systematic uncertainty is taken as the difference between the SHERPA and PYTHIA predictions for the $\mathbf{T\tilde{I}}$ region and the systematic uncertainty of the final yield is symmetrized.

- **Difference between the inclusive yield using the 2D matrix method and the integrated yield of the differential spectrum**
  Table 7.4 shows the total signal and background yields returned by the matrix method if computed in the inclusive case using the 2D matrix method or by decomposing it with respect to the different diphoton variables and then integrating over the bins using the 3D matrix method. A maximum of 0.2% difference is observed in the diphoton signal purity and is considered as an additional systematic uncertainty in the inclusive case.

Variables	$N_{\gamma\gamma+DY}$	$N_{\gamma j}$	$N_{j\gamma}$	N_{jj}
Inclusive	242155	45175	17974	7450
$m_{\gamma\gamma}$	242130	45079	17638	7908
ϕ_η^*	242498	44656	17455	8146
a_T	242297	44964	17480	8012
Q_T	242089	45393	17481	7791
$\Delta\phi$	242680	44663	17480	7931
$cos\theta_\eta^*$	241978	45020	17999	7757
Shift	$^{+525}_{-177}$	$^{+218}_{-519}$	$^{+25}_{-519}$	$^{+696}_{0}$

Table 7.4: Total signal and background yields returned by the matrix method if computed in the inclusive case using the 2D matrix method or by decomposing it with respect to the different diphoton variables and then integrating over the bins using the 3D matrix method. The maximum difference is taken as an additional systematic uncertainty in the inclusive case.

7.8.2 Matrix method results

Inclusive yields

A summary of the dominant uncertainties is reported in Table 7.5. Most of the systematic uncertainties are data-driven except for the systematic effects from the photon ID description defined in Equation 7.9 and the signal leakage in the $\tilde{\mathbf{I}}$ region as detailed in Section 7.7.5. The dominant systematic uncertainty arises from the Loose′ variation and the signal leakage in the $\tilde{\mathbf{I}}$ region. Table 7.6 shows the extracted yield with the statistical uncertainty and the total systematic uncertainty.

	Photon ID	$\tilde{\mathbf{T}}$ definition	$\tilde{\mathbf{I}}$ definition	$\tilde{\mathbf{I}}$ signal leakage	Variable
$\gamma\gamma$	+2968 -2980	+7664 -5990	+635 -1189	+4721 -4721	+525 -177
γj	+1204 -1466	+3634 -5583	+981 -596	+4536 -4536	+218 -519
$j\gamma$	+1100 -1084	+1243 -1279	+134 -399	+155 -155	+25 -519
jj	+676 -418	+1114 -802	+121 -48	+339 -339	+696 0

Table 7.5: List of the main systematic uncertainties considered in the matrix method. The numbers shown here are the difference with respect to the nominal yield for each source of systematic uncertainty for both signal and background components. Central values use the Loose′4 preselection and Sherpa leakage factors in input. The signal leakage in the $\tilde{\mathbf{I}}$ region is taken from Pythia for the nominal yield. The signal leakage in the $\tilde{\mathbf{I}}$ region is detailed in Section 7.7.5. The last column termed "Variable" represents the difference between the integrated yield over bins of the differential spectra using the 3D matrix method and the inclusive yield estimated using the 2D matrix method as presented in Table 7.4.

	Event yield	Fractions in the **TITI** sample
$\gamma\gamma$	242155 ± 874 (stat.) $^{+9514}_{-8276}$ (syst.)	77.43% ± 0.28% (stat.) $^{+3.04}_{-2.65}$% (syst.)
γj	45175 ± 529 (stat.) $^{+6020}_{-7384}$ (syst.)	14.44% ± 0.17% (stat.) $^{+1.92}_{-2.36}$% (syst.)
jγ	17974 ± 425 (stat.) $^{+1673}_{-1807}$ (syst.)	5.75%± 0.14% (stat.) $^{+0.53}_{-0.58}$% (syst.)
jj	7450± 228 (stat.) $^{+1521}_{-967}$ (syst.)	2.38% ± 0.07% (stat.) $^{+0.49}_{-0.31}$% (syst.)

Table 7.6: Total yields for two candidates passing the **TITI** criteria. The extracted event yields for $\gamma\gamma$, γj, jγ and jj are shown in the second column with the fraction of the corresponding component in the **TITI** sample in the third column. Both the statistical and total systematic uncertainties are listed. The statistical uncertainty is estimated using a bootstrap technique as explained in Section 7.7.8.

Differential spectrum

The systematic uncertainties on the differential spectra are evaluated in a consistent way to the inclusive yield. The relative systematic uncertainties in bins of $m_{\gamma\gamma}$, $p_{\mathrm{T},\gamma\gamma}$,

$\Delta\phi_{\gamma\gamma}$, $|\cos\theta^*_\eta|$, a_{T} and ϕ^*_η are illustrated in Figure 7.13. Systematic uncertainties in the differential spectra are dominated by variations in the $\tilde{\mathbf{T}}$ definition in almost all bins at around the 2% to 4% level. Other main systematic effects include variations in the signal leakage in the $\tilde{\mathbf{I}}$ region for some particular phase space (e.g. $\sim$2% for $2.7 < \Delta\phi_{\gamma\gamma} < 3.15$) and variations of the photon ID descriptions by MC, which stays almost flat ($\sim$ 1.5%). The extracted differential spectrum with statistical and total error per bin are presented in Figure 7.14.

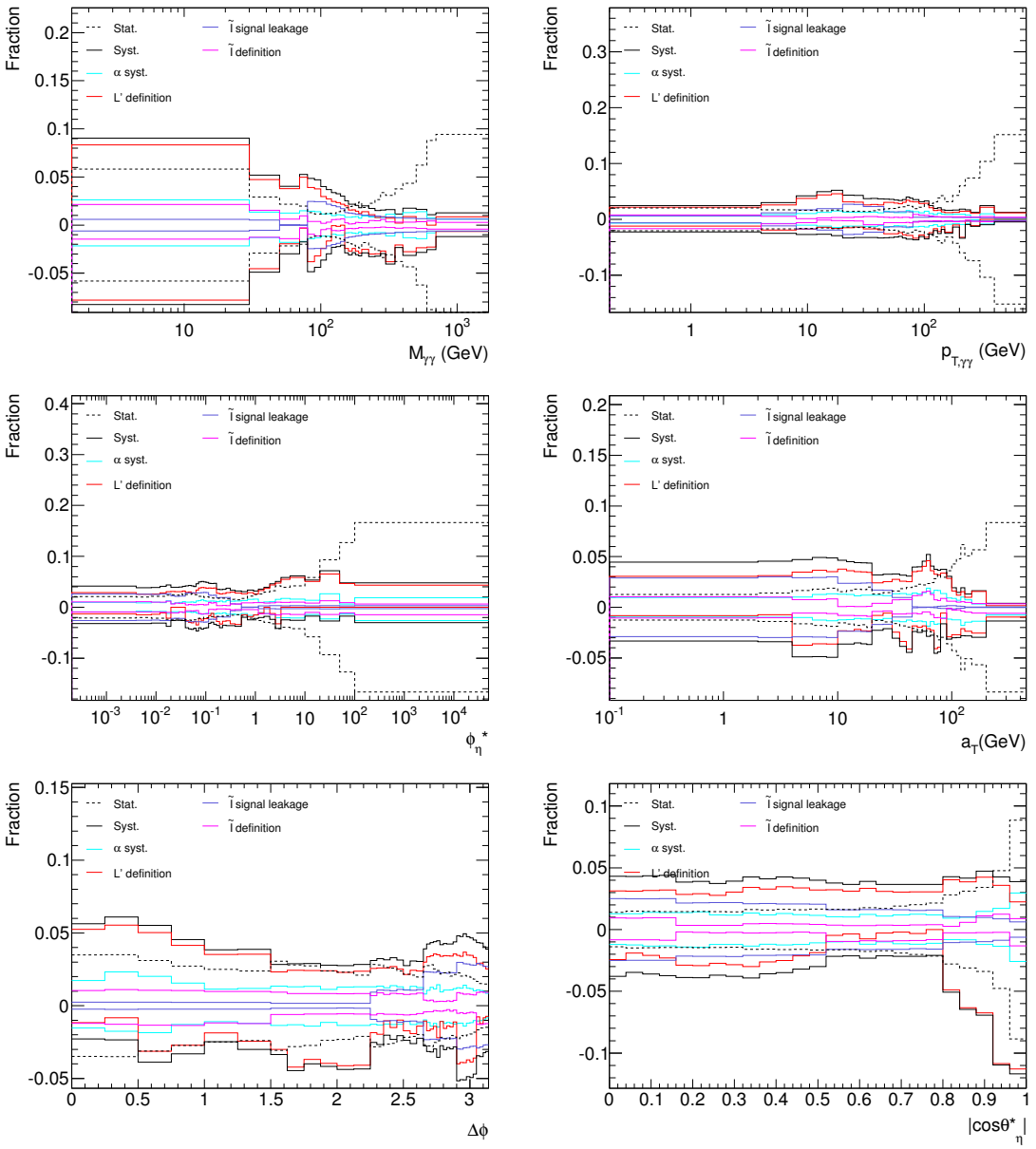

Figure 7.13: Relative systematic uncertainties on the diphoton yield as a function of $m_{\gamma\gamma}$, $p_{\mathrm{T},\gamma\gamma}$, ϕ^*_η, a_{T}, $\Delta\phi_{\gamma\gamma}$ and $|\cos\theta^*_\eta|$.

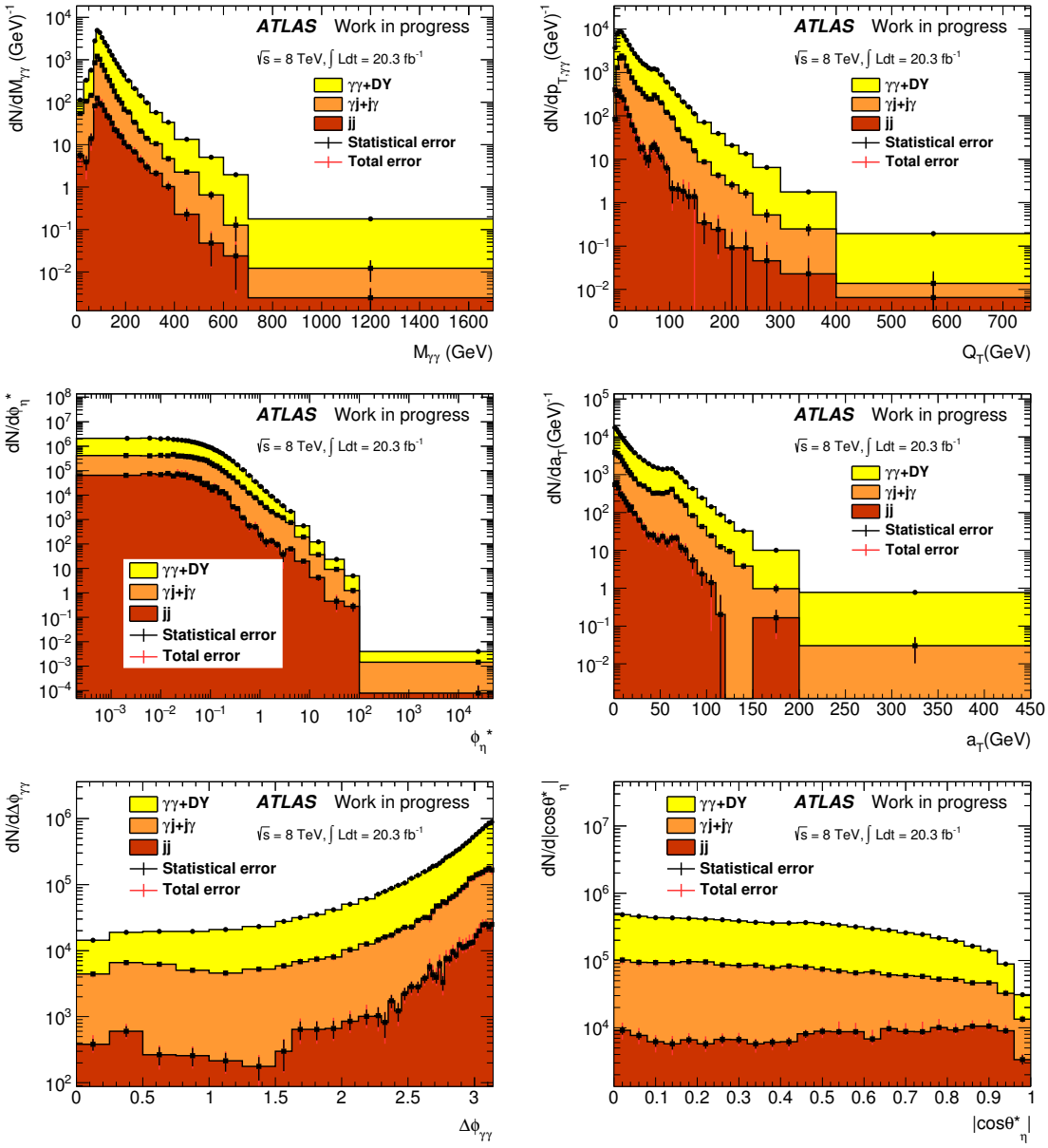

Figure 7.14: The extracted differential spectrum in terms of $m_{\gamma\gamma}$, $p_{\mathrm{T},\gamma\gamma}$, ϕ^*_η, a_T, $\Delta\phi_{\gamma\gamma}$ and $|\cos\theta^*_\eta|$ for the $N_{\gamma\gamma}$ (yellow), $N_{\gamma\mathrm{j}} + N_{\mathrm{j}\gamma}$ (orange), and N_{jj} (light red) contributions. Statistical uncertainty (black line) and total uncertainty (red line) are represented. Yields and errors are normalised to the bin width.

7.9 Background from isolated electrons

The matrix method leaves the final states containing isolated electrons untouched after hadronic background subtraction. An electron can be wrongly reconstructed as a converted photon if the tracker fails to associate a B-layer hit to the track or it associates a spurious conversion track to it. For instance, an excess of $e\gamma$ two-body final states with an invariant mass close to that of the Z boson is a clear indication misidentification of $e \to \gamma$.

Several physics processes can contribute to such a background:

- final states with both electrons misidentified as photons ($Z/\gamma^* \to ee$, $WW \to e\nu e\nu$ and $WZ \to e\nu ee$).
- final states with one genuine photon and one electron wrongly reconstructed as a photon ($\gamma Z \to \gamma ee$ and $\gamma W \to \gamma e\nu$).

7.9.1 Objects selection

The photon selection is the same as in Section 7.4. The electron candidates are required to pass the same isolation requirement and satisfy the TIGHT++ electron identification criteria [87]. To ensure electrons are not reconstructed at the same time as photons, the electron is considered as a photon clone if it fulfills:

$$\Delta R_{e\gamma} = \sqrt{(\eta_e^{clus} - \eta_\gamma^{clus})^2 + (\phi_e^{clus} - \phi_\gamma^{clus})^2} < 0.05, \tag{7.20}$$

where $\Delta R_{e\gamma}$ is the separation between the reconstructed electron and photon clusters in the ECAL.

For the two-body final-states, an event can be reconstructed as ee, $e\gamma$ or $\gamma\gamma$. For the ee and $e\gamma$ final states, the electron track is required to be associated with the primary vertex. The $\gamma\gamma$ event selection in the $Z \to ee$ MC strictly follows the selection requirements detailed in Section 7.4.

7.9.2 Electron background estimation

The $e \to \gamma$ fake rates can be extracted by examining the number of the reconstructed ee, $e\gamma$ and γe events with invariant mass around the Z-boson mass region. For single electron and photon final states, N_x represents the number of the observed final states containing an object *reconstructed as* x (x can be either e or γ) which satisfies the **TI** selection criteria, and n_x represents the number of reconstructed

final states containing *a true object* x. Thus, the observed counts N_γ, N_e can be expressed in terms of the true counts n_γ, n_e by the following linear equations:

$$\begin{pmatrix} N_\gamma \\ N_e \end{pmatrix} = \begin{pmatrix} \varepsilon_\gamma & \rho_{e\to\gamma} \\ \rho_{\gamma\to e} & \varepsilon_e \end{pmatrix} \times \begin{pmatrix} n_\gamma \\ n_e \end{pmatrix}, \tag{7.21}$$

where ε_γ (ε_e) corresponds to the probability for a true γ (e) to be identified as such and fulfill the **TI** requirement, $\rho_{e\to\gamma}$ is the probability for a true electron to be identified as a **TI** photon, $\rho_{\gamma\to e}$ represents the probability for a true photon to be identified as a **TI** electron.

Equation 7.21 takes a simpler form once we incorporate the efficiencies into the n_x counts, i.e., $N_x^{\text{sig}} = \varepsilon_x n_x$, and then the fake rates can be expressed as $f_{e\to\gamma} = \rho_{e\to\gamma}/\varepsilon_e$ and $f_{\gamma\to e} = \rho_{\gamma\to e}/\varepsilon_\gamma$. Hence Equation 7.21 becomes:

$$\begin{pmatrix} N_\gamma \\ N_e \end{pmatrix} = \begin{pmatrix} 1 & f_{e\to\gamma} \\ f_{\gamma\to e} & 1 \end{pmatrix} \times \begin{pmatrix} N_\gamma^{\text{sig}} \\ N_e^{\text{sig}} \end{pmatrix}, \tag{7.22}$$

where $N_{\gamma/e}^{\text{sig}}$ corresponds to the number of true γ/e that are identified as such and fulfills the **TI** criteria. $f_{e\to\gamma}$ and $f_{\gamma\to e}$ essentially represent the ratio between the number of objects that are wrongly identified and those correctly identified:

$$f_{e\to\gamma} = \frac{N_{e\to\gamma}}{N_{e\to e}}; \tag{7.23}$$

$$f_{\gamma\to e} = \frac{N_{\gamma\to e}}{N_{\gamma\to\gamma}}. \tag{7.24}$$

For two-body final states, N_{xy} denotes the observed number of the two-body final states which are *reconstructed as* xy and satisfy the **TITI** selection criteria, and N_{xy}^{sig} denotes the number of *true* final states xy passing the **TITI** selection criteria. Since the fake rates for an electron to be wrongly reconstructed as a photon depend on particularly the momentum of the initial electrons, the choice of the asymmetric cuts on momentum of the reconstructed photons leads naturally to the distinction of the fake rates for the leading and subleading candidates, where the superscript "1" refers to the leading candidate and the superscript "2" refers to the subleading

candidate. Thus one can obtain N_{xy}^{sig} by solving the following linear equations:

$$\begin{pmatrix} N_{\gamma\gamma} \\ N_{e\gamma} \\ N_{\gamma e} \\ N_{ee} \end{pmatrix} = \begin{pmatrix} 1 & f_{e\to\gamma}^1 & f_{e\to\gamma}^2 & \alpha_{ee\to\gamma\gamma} f_{e\to\gamma}^1 f_{e\to\gamma}^2 \\ f_{\gamma\to e}^1 & 1 & f_{\gamma\to e}^1 f_{e\to\gamma}^2 & f_{e\to\gamma}^2 \\ f_{\gamma\to e}^2 & f_{\gamma\to e}^2 f_{e\to\gamma}^1 & 1 & f_{e\to\gamma}^1 \\ \alpha_{\gamma\gamma\to ee} f_{\gamma\to e}^1 f_{\gamma\to e}^2 & f_{\gamma\to e}^2 & f_{\gamma\to e}^1 & 1 \end{pmatrix} \begin{pmatrix} N_{\gamma\gamma}^{\text{sig}} \\ N_{e\gamma}^{\text{sig}} \\ N_{\gamma e}^{\text{sig}} \\ N_{ee}^{\text{sig}} \end{pmatrix}. \tag{7.25}$$

$\alpha_{ee\to\gamma\gamma}$ and $\alpha_{\gamma\gamma\to ee}$ are introduced to account for correlations in the $e\to\gamma$ and $\gamma\to e$ fake rates in the two-body final states, as detailed in Section 7.9.3.

After the manipulation of the matrix, one can obtain $N_{\gamma\gamma}^{\text{sig}}$, $N_{e\gamma}^{\text{sig}}$, $N_{\gamma e}^{\text{sig}}$ and N_{ee}^{sig}. As for $N_{\gamma\gamma}$, it can be decomposed as a sum of the contributions from the true xy final states:

$$N_{\gamma\gamma} = N_{\gamma\gamma}^{\text{sig}} + N_{e\gamma}^{*} + N_{\gamma e}^{*} + N_{ee}^{*}; \tag{7.26}$$

$$N_{e\gamma}^{*} = f_{e\to\gamma}^1 N_{e\gamma}^{\text{sig}}; \quad N_{\gamma e}^{*} = f_{e\to\gamma}^2 N_{\gamma e}^{\text{sig}}; \quad N_{ee}^{*} = \alpha_{ee\to\gamma\gamma} f_{e\to\gamma}^1 f_{e\to\gamma}^2 N_{ee}^{\text{sig}}. \tag{7.27}$$

The number of the electron background events $N_{ee+e\gamma+\gamma e}$ is

$$N_{ee+e\gamma+\gamma e} = N_{e\gamma}^{*} + N_{\gamma e}^{*} + N_{ee}^{*} = N_{\gamma\gamma} - N_{\gamma\gamma}^{\text{sig}}. \tag{7.28}$$

7.9.3 Extraction of the $e\to\gamma$ and $\gamma\to e$ fake rates

$f_{e\to\gamma}$ can be extracted from two-body decays in data by looking at the number of the reconstructed ee, $e\gamma$ and γe events observed with a pair invariant mass consistent with that of objects coming from the Z boson decay. The fake rates for the leading and the subleading electrons, represented by $f_{e\to\gamma}^1$ and $f_{e\to\gamma}^2$ respectively, are evaluated by counting the observed number of ee (N_{ee}), $e\gamma$ ($N_{e\gamma}$) and γe ($N_{\gamma e}$) events with invariant mass close to the Z-mass region:

$$f_{e\to\gamma}^1 = \frac{N_{\gamma e}}{N_{ee}}; \quad f_{e\to\gamma}^2 = \frac{N_{e\gamma}}{N_{ee}} \quad \text{(data-driven)}. \tag{7.29}$$

The estimations of $f_{e\to\gamma}^1$ and $f_{e\to\gamma}^2$ are completely data-driven as explained in Section 7.9.4.

The fake rate for both photons to be misidentified electrons can be determined from the $Z\to ee$ MC:

$$f_{ee\to\gamma\gamma} = \frac{N_{\gamma\gamma}}{N_{ee}} \quad (Z\to ee \text{ MC}). \tag{7.30}$$

A correlation factor $\alpha_{ee\to\gamma\gamma}$ is introduced to account for the correlation in $e \to \gamma$ misidentification fake rates between $ee \to \gamma\gamma$ and $ee \to e\gamma$ ($ee \to \gamma e$) determined from $Z \to ee$ MC:

$$\alpha_{ee\to\gamma\gamma} = \frac{f_{ee\to\gamma\gamma}}{f^1_{e\to\gamma} f^2_{e\to\gamma}} = \frac{N_{\gamma\gamma}/N_{ee}}{N_{\gamma e}/N_{ee} N_{e\gamma}/N_{ee}} = \frac{N_{\gamma\gamma} N_{ee}}{N_{\gamma e} N_{e\gamma}} \quad (Z \to ee \text{ MC}). \tag{7.31}$$

The correlation factor is approximately 1 if the photon misidentification fake rate is independent of the other candidate. However, this is not the case as the track isolation energy needs the information of the primary vertex from the two candidates.

Similarly, a photon can be mis-reconstructed as an electron. The fake rates for the leading and subleading photons, denoted as $f^1_{\gamma\to e}$ and $f^2_{\gamma\to e}$ respectively, can be determined from $\gamma\gamma$ SHERPA MC and are defined as follows:

$$f^1_{\gamma\to e} = \frac{N_{e\gamma}}{N_{\gamma\gamma}}; \quad f^2_{\gamma\to e} = \frac{N_{\gamma e}}{N_{\gamma\gamma}} \quad (\gamma\gamma \text{ SHERPA MC}). \tag{7.32}$$

The fake rate for both electrons to be misidentified as photons can be obtained from the $\gamma\gamma$ SHERPA MC:

$$f_{\gamma\gamma\to ee} = \frac{N_{ee}}{N_{\gamma\gamma}} \quad (\gamma\gamma \text{ SHERPA MC}). \tag{7.33}$$

The correlation factor for $\gamma\gamma \to ee$, determined from the $\gamma\gamma$ SHERPA MC, is introduced and defined as:

$$\alpha_{\gamma\gamma\to ee} = \frac{f_{\gamma\gamma\to ee}}{f^1_{\gamma\to e} f^2_{\gamma\to e}} = \frac{N_{ee}/N_{\gamma\gamma}}{N_{\gamma e}/N_{\gamma\gamma} N_{e\gamma}/N_{\gamma\gamma}} = \frac{N_{\gamma\gamma} N_{ee}}{N_{\gamma e} N_{e\gamma}} \quad (\gamma\gamma \text{ SHERPA MC}). \tag{7.34}$$

7.9.4 Extraction of $e \to \gamma$ fake rates from data

Using Equation 7.29, $f^1_{e\to\gamma}$ and $f^2_{e\to\gamma}$ can be measured in a mass window ($[80, 100]$ GeV) around the Z peak region for ee and $e\gamma$ (γe) events. The E_T cuts are lowered to be 30 GeV for both leading and subleading candidates to avoid the distortion of the Z mass distribution due to the E_T turn-on effects.

The electrons misidentified as photons are reconstructed using the energy calibration parameters for photons. Therefore, the invariant mass is slightly shifted by 1 GeV compared to the correct calibration (Figure 7.15a) because the inner tracker used for the electron reconstruction has a slightly better resolution than the calorimeter. In order to correctly estimate the electron background in $\gamma\gamma$ contributions, an energy correction of -1.5% is applied to the electrons to recompute the variables (Figure 7.15b).

A convolution of a double-sided Crystal ball function and a Breit-Wigner distribution with a fixed Z boson width of $\Gamma_Z = 2.495$ GeV is applied to fit the mass peak, as presented in Figure 7.16 with a bold line, where the defined mass window is $[80, 100]$ GeV for the extraction of fake rates. An exponential fit was used to subtract the hadronic background in $e\gamma$ (γe) data for the purpose of estimating $e \to \gamma$ fake rates in data. The slope of the exponential shape was determined using $120 < M_{XY} < 240$ GeV region for the ee and $e\gamma$ (γe) final states respectively. Table 7.7 compares the number of the observed ee, $e\gamma$, γe and $\gamma\gamma$ events between MC predictions and data. A summary of the $e \to \gamma$ fake rates determined from data and MC as well as correlation factors are illustrated in Table 7.8.

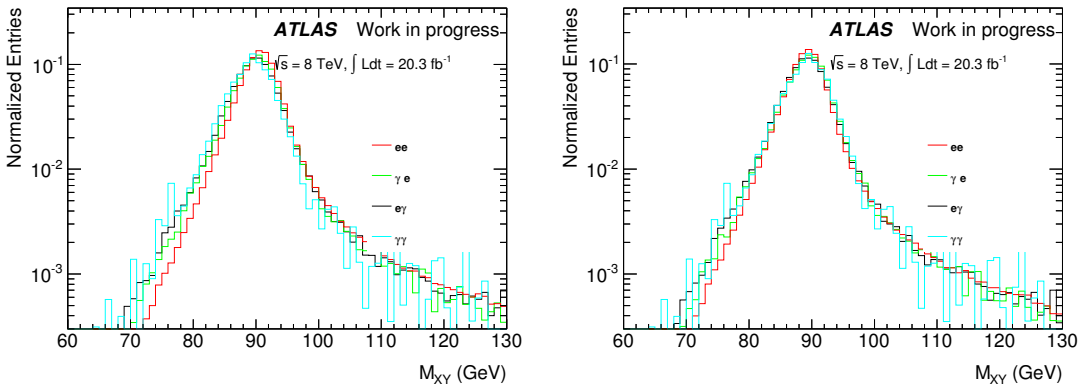

(a) Before energy corrections for e

(b) After energy corrections for e

Figure 7.15: Normalized invariant mass distribution of ee (red histograms), $e\gamma$ (blue histograms), γe (green histograms) and $\gamma\gamma$ (cyan histograms) from $Z \to ee$ SHERPA MC. A 1 GeV shift in the invariant mass peak position between $\gamma\gamma$ and ee final states is observed in MC before the energy correction shift for electrons.

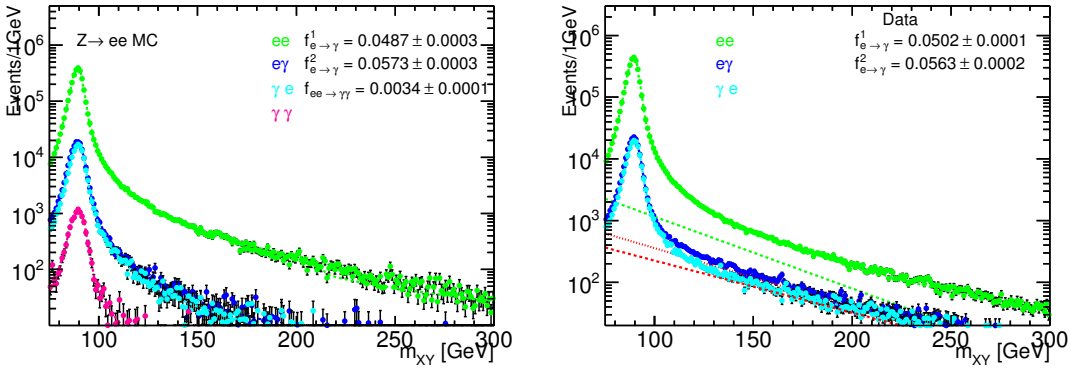

(a) Sherpa MC (b) Data

Figure 7.16: Invariant mass distribution of ee, $e\gamma$ and γe in (a) MC and (b) data. In Figure 7.16b, the dashed line represents the exponential shape used to subtract the hadronic background for ee (green dashed), $e\gamma$ (red dotted) and γe (red dashed) in data. The $\gamma\gamma$ invariant mass distribution (left) is also shown as pink dots.

The following systematic uncertainties on $e \to \gamma$ fake rates are considered.

- E_T cuts: the nominal E_T cuts used for the estimation of fake rates were chosen in order not to create a distortion of the m_{XY} shape. It has been checked using $Z \to ee$ MC that changing the E_T requirements to the nominal ones has a small effect on $e \to \gamma$ fake rates.

- fit region of the invariant mass for the fake rate: the fake rate is estimated in the Z-mass peak region and applied everywhere. A systematic uncertainty is obtained by taking the difference between the nominal fake rate determined from the $Z \to ee$ MC and the one recomputed with $E_T^1 < 30$ GeV and $E_T^2 < 30$ GeV across the whole mass region.

- exponential shape component for the hadronic background for ee and $e\gamma$ final states: to take into account the processes with fake electrons or photons due to hadronic background, an exponential shape component is considered. But processes with a genuine photon (e.g. $W\gamma$ events) could have a component without resonant events. To account for such systematic effects, the fake rate is computed without the exponential component in data.

- calibration of the ee and $e\gamma$ yields: for the nominal yield, an energy correction of -1.5% is applied to the electrons to recompute the variables in both data and MC; the energy corrections are turned off to estimate the systematic effects due to this procedure in data.

Table 7.9 summarises the systematic uncertainties on $e \to \gamma$ fake rates. The dominant systematic uncertainties arise from the use of exponential shape component for the hadronic background subtraction in the observed ee, $e\gamma$ and γe final states.

	N_{ee}	$N_{e\gamma}$	$N_{\gamma e}$	$N_{\gamma\gamma}$
$Z \to ee$ MC	2749103	157664	133847	9474
$\gamma\gamma$ MC	5	394	406	52535
data	3085285	174017	153207	-

Table 7.7: Events of xy pair reconstructed in MC and data for 80< M_{XY} <100 GeV, used for extraction of fake rates. MC is normalised to the integrated luminosity of data.

	$f^1_{e\to\gamma}$	$f^2_{e\to\gamma}$	$\alpha_{ee\to\gamma\gamma}$
$Z \to ee$ MC	0.0487±0.0003	0.0574±0.0003	1.2343±0.0267
$Z \to ee$ data	0.0502±0.0001	0.0563±0.0002	-

Table 7.8: Summary of $e \to \gamma$ fake rates measured from data and MC. Only the statistical uncertainty is given.

	$f^1_{e\to\gamma}$	$f^2_{e\to\gamma}$	$\alpha_{ee\to\gamma\gamma}$
E_T cuts	0.0009	-0.0008	0.0321
Fit region	0.0004	0.0012	0.0004
Exponential shape	0.0011	0.0028	0
Energy calibration	-0.0008	-0.0001	-0.0059

Table 7.9: Summary of systematic uncertainties on $f^1_{\gamma\to e}$, $f^2_{\gamma\to e}$ and $\alpha_{ee\to\gamma\gamma}$. The dominant systematic uncertainty arises due to the use of the exponential shape to subtract the hadronic background faking electrons or photons.

7.9.5 Extraction of $\gamma \to e$ fake rates from MC

Using Equation 7.32, $f^1_{\gamma\to e}$ and $f^2_{\gamma\to e}$ can be determined from the diphoton SHERPA MC. We use the nominal E_T requirements here and the fake rates are computed across the whole mass spectrum. The $\gamma \to e$ fake rates are below 1% as shown in Table 7.10. Strictly speaking, one should use three-body decay of $Z \to ee\gamma$ and $Z \to eee$ around the Z-mass peak region in data as done in [46] to determine $\gamma \to e$ fake rates. However, the data sample only contains hundreds of events for $Z \to ee\gamma$ and $Z \to eee$ even after lowering the requirement on E_T of the three objects to 25 GeV. $\gamma \to e$ fake rate was found to have a small effect on the electron

background estimation and it is varied by 100% in the inclusive case as a cross-check in Section 7.9.7.

	$f^1_{\gamma\to e}$	$f^2_{\gamma\to e}$	$\alpha_{\gamma\gamma\to ee}$
$\gamma\gamma$ MC	0.0084±0.0001	0.0086±0.0001	1.3850±0.1434

Table 7.10: Summary of $\gamma \to e$ fake rates measured in the diphoton SHERPA MC. Only statistical uncertainties are given.

7.9.6 Impurity estimation in differential spectra

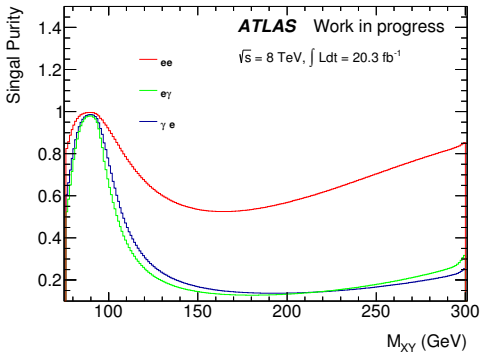

Figure 7.17: Signal purity as a function of m_{XY} for the observed $e\gamma$, γe and ee final states separately determined using Figure 7.16b. The signal purity is defined as the ratio of genuine $e\gamma$ (ee) events to genuine $e\gamma$ (ee) events plus the hadronic background.

For all kinematic variables of interest, we carry out the following procedures.

- The hadronic background in $e\gamma$, γe and ee final states can be subtracted using an exponential shape as shown in Figure 7.16b; the fraction of genuine $e\gamma$, γe and ee events can be parameterized as a function of m_{XY} (Figure 7.17) and propagated into the differential spectrum of other kinematic variables. For signal purities outside the defined mass ranges, we use the signal purity with a non-zero value closest to that bin.

- The histogram of $h_{\gamma\gamma}$, $h_{e\gamma}$, $h_{\gamma e}$ and h_{ee} for the reconstructed (observed) $\gamma\gamma$, $e\gamma$ γe and ee final states in data, passing the **TITI** selection, are filled. For each event in $h_{e\gamma}$, $h_{\gamma e}$ and h_{ee}, instead of filling with the data event weight 1, they are filled event by event with the signal purity parameterized as a function of the invariant mass and are shown respectively in Figure 7.17. As a result, we obtained $N_{\gamma\gamma}$, $N_{e\gamma}$, $N_{\gamma e}$ and N_{ee} after hadronic background subtraction, the left hand side of Equation 7.25.

- Using Equation 7.25, one can obtain the number of true final states of $\gamma\gamma$, $e\gamma$, γe and ee. With Equation 7.27, one can determine the contribution to the electron background in the observed $\gamma\gamma$ state in terms of $N^{\text{sig}}_{e\gamma}$, $N^{\text{sig}}_{\gamma e}$ and N^{sig}_{ee} respectively. It should be noted here that $f^1_{e\to\gamma}$ and $f^2_{e\to\gamma}$ are determined with hadronic background subtraction using the exponential shape.

- In this step, the $\gamma\gamma$ histogram with hadronic background subtracted is kept the same, but we fill $h_{e\gamma}$, $h_{\gamma e}$ and h_{ee} with a normal event weight of 1 for each event passing the **TITI** selection, i.e., no background subtraction for $e\gamma$, γe and ee final states. And use $e \to \gamma$ fake rates without hadronic background subtraction. Thus the electron background can be recomputed using Equation 7.27.

- Since processes with a genuine photon could have a component without resonant events for the observed $e\gamma$ and γe final states, the central value is taken as the average obtained using Equation 7.25 with and without hadronic background subtraction. The systematic uncertainty is taken as half the difference between the extracted electron background with and without hadronic background subtraction in the observed $e\gamma$, γe and ee samples.

- For each histogram bin, the impurity I_e can be determined:

$$I_e[bin] = 1 - \frac{h^{\text{sig}}_{\gamma\gamma}[bin]}{h_{\gamma\gamma}[bin]}, \tag{7.35}$$

  where $h^{\text{sig}}_{\gamma\gamma}$ is the histogram filled with the extracted $\gamma\gamma$ yield after the electron background subtraction.

- The statistical uncertainty is obtained by varying each input parameter in Equation 7.25 by one standard statistical deviation. Although there is a small degree of statistical correlations between different input parameters in Equation 7.25, such correlations are ignored because they have negligible effect on the extracted diphoton yield considering the impact of the total statistical uncertainty from the electron background on the diphoton yield is below 0.1%.

- The systematic uncertainty on $f^1_{e\to\gamma}$, $f^2_{e\to\gamma}$ and $\alpha_{ee\to\gamma\gamma}$, except the use of the exponential shape to subtract hadronic background in the ee, γe and ee final states, are propagated through the matrix to the inclusive yield as well as each bin in the differential spectrum. Each systematic variation is performed separately with and without hadronic background subtraction in the $e\gamma$, γe

and ee final states, which is then averaged. As a result, the difference with respect to the nominal value is taken as a systematic uncertainty.

7.9.7 Results

The number of events with or without hadronic background subtracted for the observed ee, $e\gamma$ and γe final states are shown in Table 7.11, in which the number of observed $\gamma\gamma$ final state is only shown after background subtraction as estimated in Section 7.7. The fraction of the hadronic background in the observed ee state is $\sim$2% whereas it is $\sim$10% in the $e\gamma$ state as returned by the exponential shape. The number of the electron background events extracted with or without hadronic background subtracted for the observed ee, $e\gamma$ and γe final states are shown in Table 7.12. The nominal value of the electron background contribution in the $\gamma\gamma$ final state is taken as the average of the derived electron background events with or without the hadronic background subtraction in the observed $e\gamma$, γe and ee final states. A summary of the systematic uncertainties on the number of electron background is illustrated in Table 7.13. The dominant systematic uncertainty is due to the treatment of the subtraction of the hadronic background. The number of the estimated electron background is 11,083 $\pm$ 221 (stat.) $\pm$ 1310 (syst.).

The $\gamma \to e$ fake rates has been varied by $\pm$100% to check its effect, which gives $\pm$220 on the number of the electron background. Such a variation is quite conservative and this is only done as a cross-check.

The bin-by-bin impurities with the associated systematic uncertainties and the effect of subtraction of electron background are shown for $m_{\gamma\gamma}$, $p_{\mathrm{T},\gamma\gamma}$ and ϕ^*_η in Figure 7.18, and a_{T}, $\Delta\phi_{\gamma\gamma}$ and $|\cos\theta^*_\eta|$ in Figure 7.19.

Data (Observed)	$N_{\gamma\gamma}$	$N_{e\gamma}$	$N_{\gamma e}$	N_{ee}
Background subtraction	242129 $\pm$ 874	157487 $\pm$ 379	144453 $\pm$ 367	2782145 $\pm$ 1646
No subtraction	-	185646 $\pm$ 431	163524 $\pm$ 404	2847967 $\pm$ 1688

Table 7.11: The number of events with or without hadronic background subtraction in the observed $e\gamma$, γe and ee final states in data. The observed number of $\gamma\gamma$ final state is with hadronic background subtracted, as explained in Section 7.7.

	Electron background
Background subtraction	9806 ± 211 (stat.)
No subtraction	12360 ± 231 (stat.)
Average	11083 ± 221 (stat.)

Table 7.12: The number of electron background events in the observed $\gamma\gamma$ state with or without hadronic background subtraction for the observed $e\gamma$, γe and ee final states.

E_T cuts	Fit region	Calibration	Exponential shape
272	74	-88	1276

Table 7.13: Systematic uncertainties on the estimated number of the electron background events. All systematic uncertainties are symmetrized for the final results.

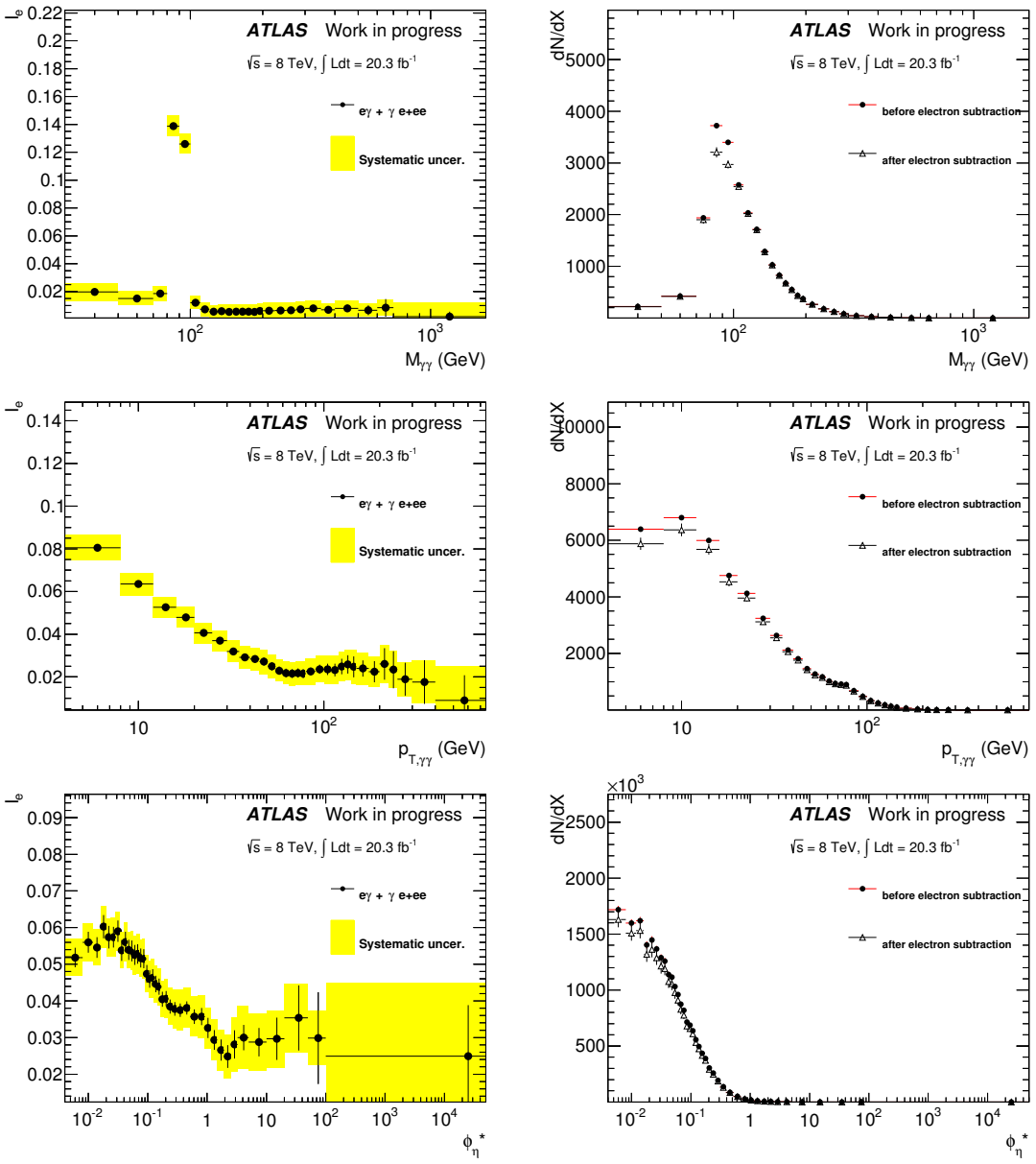

Figure 7.18: Bin by bin electron impurity (left) and differential **TITI** yield before and after electron background subtraction (right) for $m_{\gamma\gamma}$, $p_{\mathrm{T},\gamma\gamma}$ and ϕ^*_η.

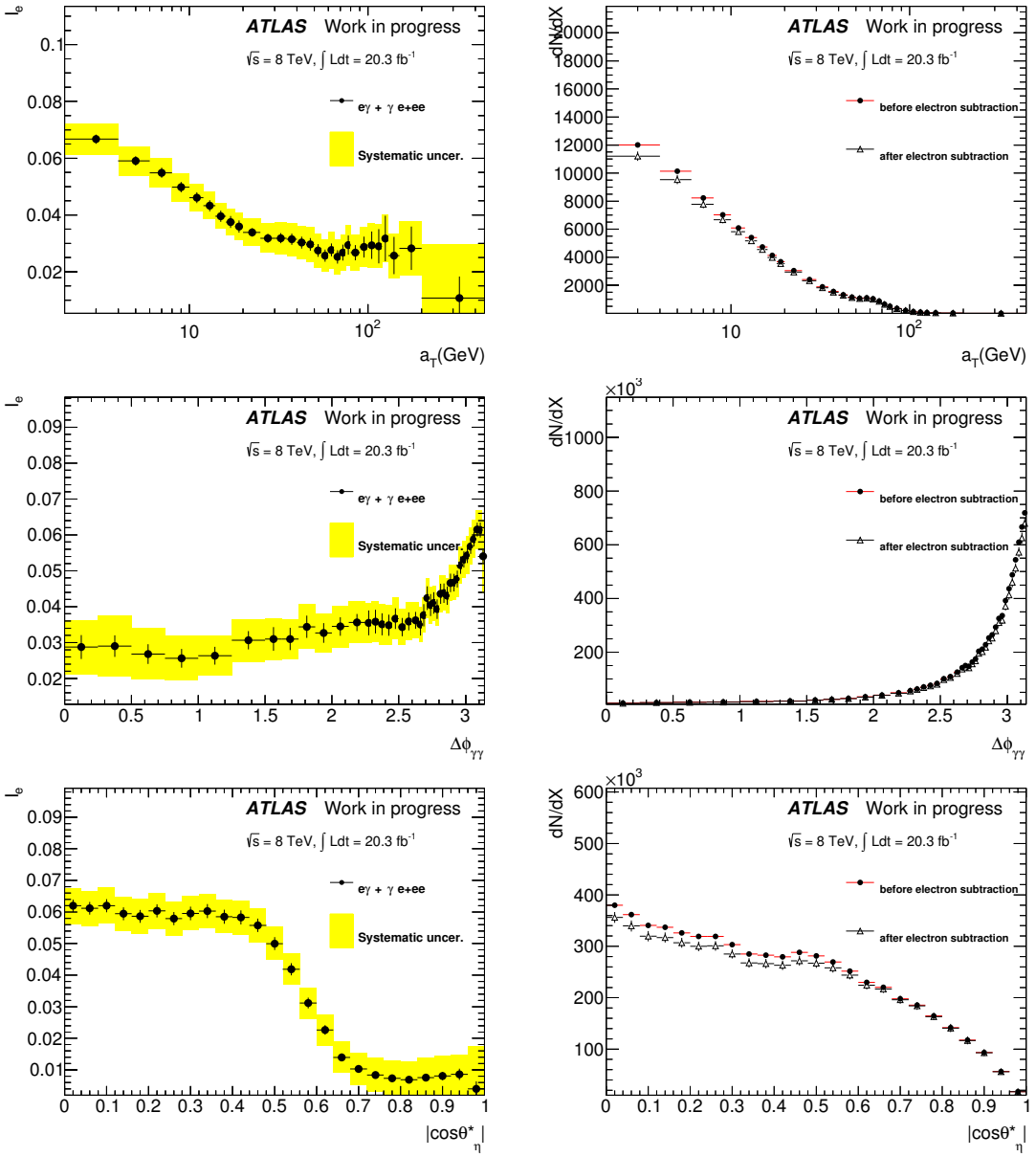

Figure 7.19: Bin by bin electron impurity (left) and differential **TITI** yield before and after electron background subtraction (right) for a_{T}, $\Delta\phi_{\gamma\gamma}$ and $|\cos\theta^{*}_{\eta}|$.

7.10 An alternative method and closure tests

7.10.1 2D fit method

An alternative method to decompose the data sample is the 2D fit method, which uses a maximum likelihood fit to the two-dimensional distributions of $E_{\mathrm{T}}^{\mathrm{iso}}$ of the two photon candidates. This method was developed by others and so a brief introduction to the 2D fit method is given in Appendix A.

The main systematic uncertainties for the 2D fit method arise due to the photon isolation profile description in the $\gamma\gamma$ MC, $\tilde{\mathbf{T}}$ definition variations and the photon ID description in the $\gamma\gamma$ MC.

7.10.2 Closure tests

A pseudo-data sample of known compositions, containing around the same amount of $\gamma\gamma$, γj, jγ, jj and ee as in the real data is produced to validate both methods. The $\gamma\gamma$ and ee events are taken from Sherpa and Powheg+Pythia samples respectively to keep the correlations between the two candidates. The γj, jγ and jj events are built using $\mathbf{T}\tilde{\mathbf{T}}$, $\tilde{\mathbf{T}}\mathbf{T}$ and $\tilde{\mathbf{T}}\tilde{\mathbf{T}}$ regions in data. For the $\tilde{\mathbf{T}}$ leg (jet control sample), the ratio from $\mathbf{T}$ to $\tilde{\mathbf{T}}$ derived in Equation 7.10 is employed to extrapolate the jet component back to the $\mathbf{T}$ region in the pseudo data. This is effectively ignoring the correlations between tightness and isolation for jets. For the $\mathbf{T}$ leg in the γj and jγ control samples, we replace the $\mathbf{T}$ leg by a random photon from the Sherpa $\gamma\gamma$ sample with similar E_{T}^{γ} and $|\eta_{s2}|$

The electron background remains untouched for the closure test of the matrix method. No biases can be observed inclusively for the 2D or 3D matrix method as listed in Table 7.14. However, relatively large discrepancies for the 2D matrix method in the differential spectrum are found whereas no bias is observed in the differential spectra using the 3D matrix method as depicted in Figure 7.20. The closure tests have been performed for the 2D fit method and no bias on the $\gamma\gamma$ yield inclusively or in the differential spectrum is observed.

7.11 Comparison between the two methods

The two methods have in common the use of shower shape variables, calorimetric isolation and track isolation energy, to distinguish the photon signal from the hadronic background, and the data-driven estimation of jet background relying on the $\tilde{\mathbf{T}}$ control region. For these reasons, they cannot be considered as completely

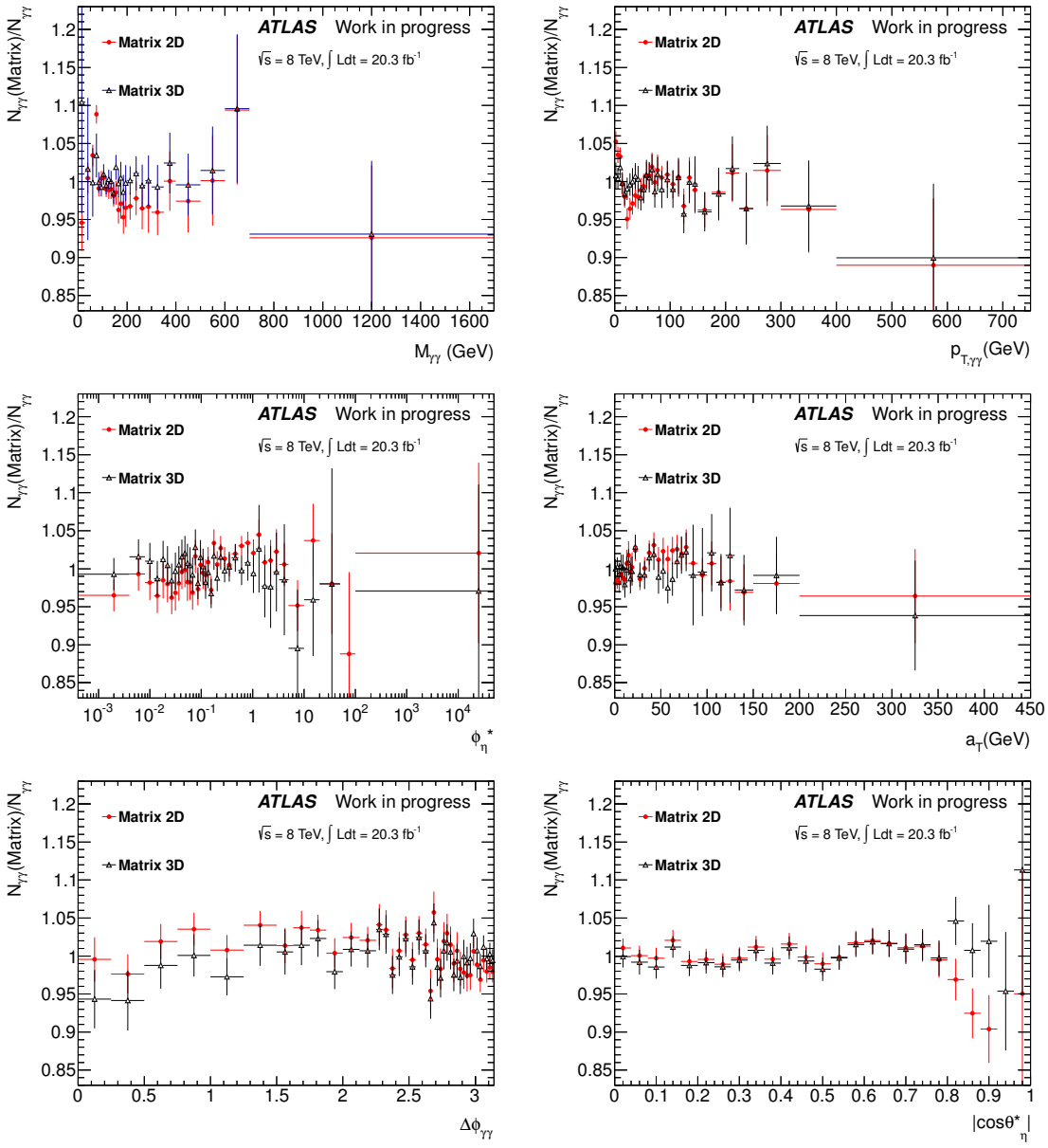

Figure 7.20: Ratio of the 2D (3D) matrix method signal yield to the actual signal yield as a function of $m_{\gamma\gamma}$, $p_{\mathrm{T},\gamma\gamma}$, ϕ^*_η, a_T, $\Delta\phi_{\gamma\gamma}$ and $|\cos\theta^*_\eta|$. Uncertainties shown are statistical uncertainties. Biases are observed in certain regions of variables when using the 2D matrix method while no bias is observed using the 3D matrix method.

Process	Actual yield	2D Matrix Method	3D Matrix Method
$\gamma\gamma$ + DY	243,584	243,428±899	244,530±1969
γj	45,000	46,389±663	45,396±1407
jγ	18,000	17,608±492	16,802±1220
jj	7000	6167±308	6864±935

Table 7.14: Closure test for the 2D and 3D matrix methods. The *ee* component is included in the pseudo-data. The output from both the 2D and 3D matrix methods gives a consistent $\gamma\gamma$ yield compared to the actual yield. The statistical fluctuations are slightly larger in the 3D matrix case. The bootstrap method described in Section 7.7.8 is used to extract the statistical uncertainty.

independent and therefore their outcomes cannot be combined.

7.11.1 Inclusive yield comparison

The inclusive yield of the two data-driven techniques are illustrated in Table 7.15. The yields obtained from the 4x4 matrix method is compatible with the 2D fit method within the systematic uncertainty.

Event Entry	2D Fit	4x4 matrix
$N_{\gamma\gamma}$	235,392 ± 1,022 (stat.) $^{+8,070}_{-8,672}$ (syst.)	231,072 ± 901 (stat.) $^{+9658}_{-8437}$ (syst.)
$N_{\gamma j}$	45,465 ± 672 (stat.) $^{+8,470}_{-8,780}$ (syst.)	45175 ± 529 (stat.) $^{+6167}_{-7457}$ (syst.)
$N_{j\gamma}$	18,699 ± 590 (stat.) $^{+4,391}_{-4,693}$ (syst.)	17974 ± 425 (stat.) $^{+1728}_{-1868}$ (syst.)
N_{jj}	4,873 ± 352 (stat.) $^{+2,096}_{-1,461}$ (syst.)	7450 ± 228 (stat.) $^{+1804}_{-1469}$ (syst.)
$N_{ee+e\gamma}$	8,275 ± 680 (stat.) $^{+2,777}_{-1,396}$ (syst.)	11,083 ± 221 (stat.) $^{+1310}_{-1310}$ (syst.)
Sum	312704	312754

Table 7.15: Yields for the 2D fit and 4x4 matrix method determined for a sample of two photon candidates passing **TITI** criteria. Both signal and background components are in agreement between the two methods within the quoted systematic uncertainties.

7.11.2 Comparison of differential spectra between the two background decomposition techniques

The $\gamma\gamma$ differential spectra obtained with the 2D fit method and matrix method are compared in Figures 7.21, Figure 7.22 and Figure 7.23. The yields from the two methods are consistent with each other for all variables.

A comparison of the γj + jγ + jj background between the 2D fit and the matrix method was performed, as illustrated in Figure 7.24. The hadronic background obtained from the 3D matrix method and 2D fit method is in good agreement.

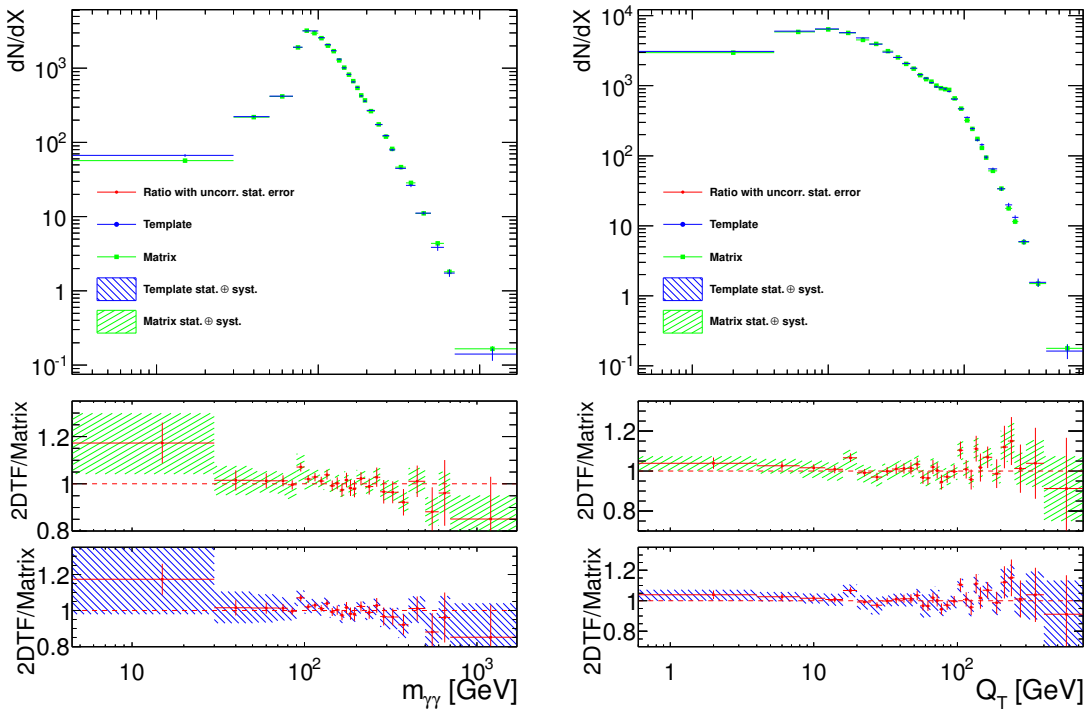

Figure 7.21: Comparison of the $\gamma\gamma$ yield between the matrix method (green points with error bars) and the 2D fit method (blue points with error bars) in $m_{\gamma\gamma}$ and $p_{\mathrm{T},\gamma\gamma}$. The green band represents the total uncertainties from the matrix method and the total uncertainties from the 2D fit method are indicated by the blue band. The ratio (red dots with error bars) of the diphoton yield of the 2D fit method to that of the matrix method is calculated assuming no statistical correlations between the two methods.

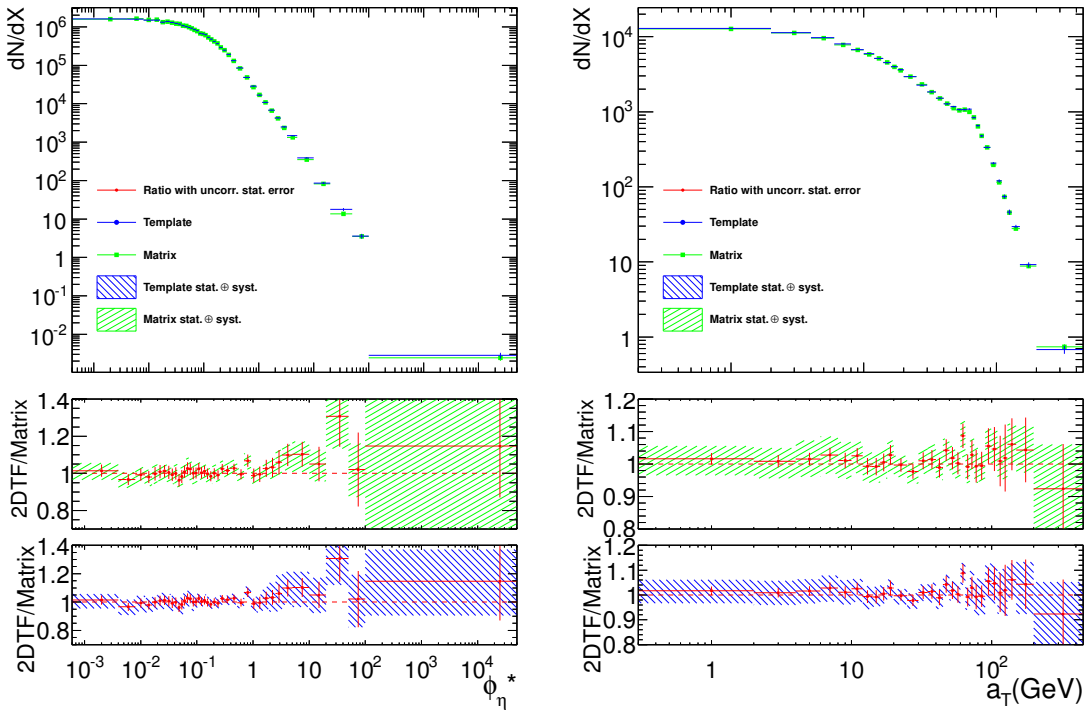

Figure 7.22: Comparison of the $\gamma\gamma$ yield between the matrix method (green points with error bars) and the 2D fit method (blue points with error bars) in ϕ_η^* and a_{T}. The green band represents the total uncertainties from the matrix method and the total uncertainties from the 2D fit method are indicated by the blue band. The ratio (red dots with error bars) of the diphoton yield of the 2D fit method to that of the matrix method is calculated assuming no statistical correlations between the two methods.

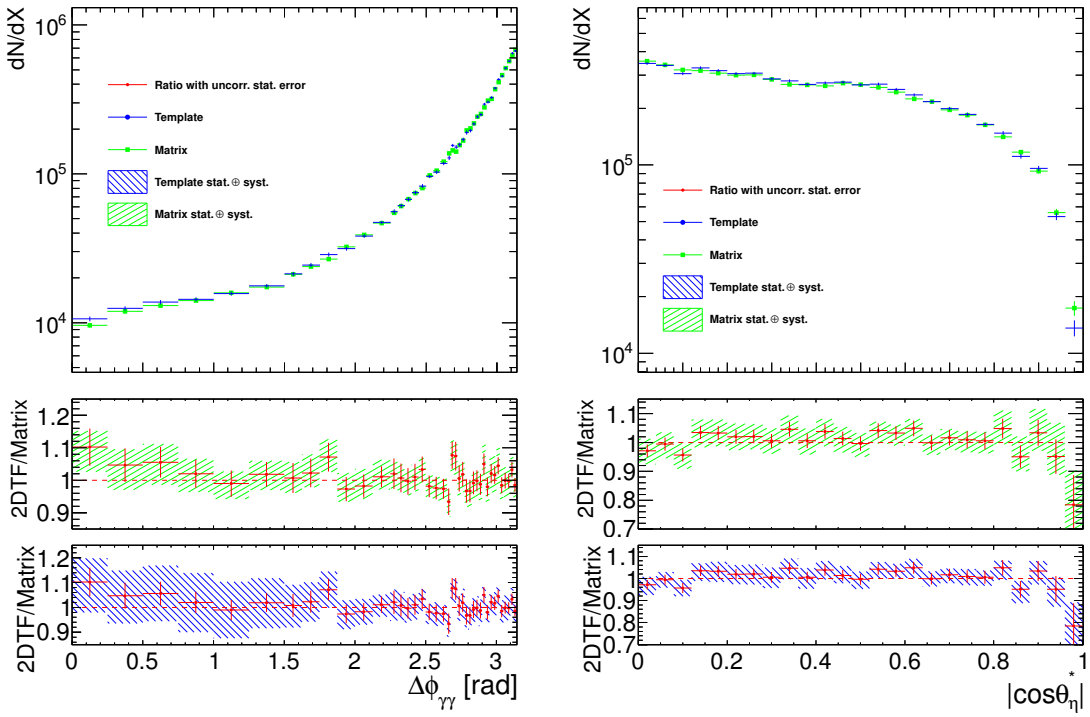

Figure 7.23: Comparison of the $\gamma\gamma$ yield between the matrix method (green points with error bars) and the 2D fit method (blue points with error bars) in $\Delta\phi_{\gamma\gamma}$ and $|\cos\theta^*_\eta|$. The green band represents the total uncertainties from the matrix method and the total uncertainties from the 2D fit method are indicated by the blue band. The ratio (red dots with error bars) of the diphoton yield of the 2D fit method to that of the matrix method is calculated assuming no statistical correlations between the two methods.

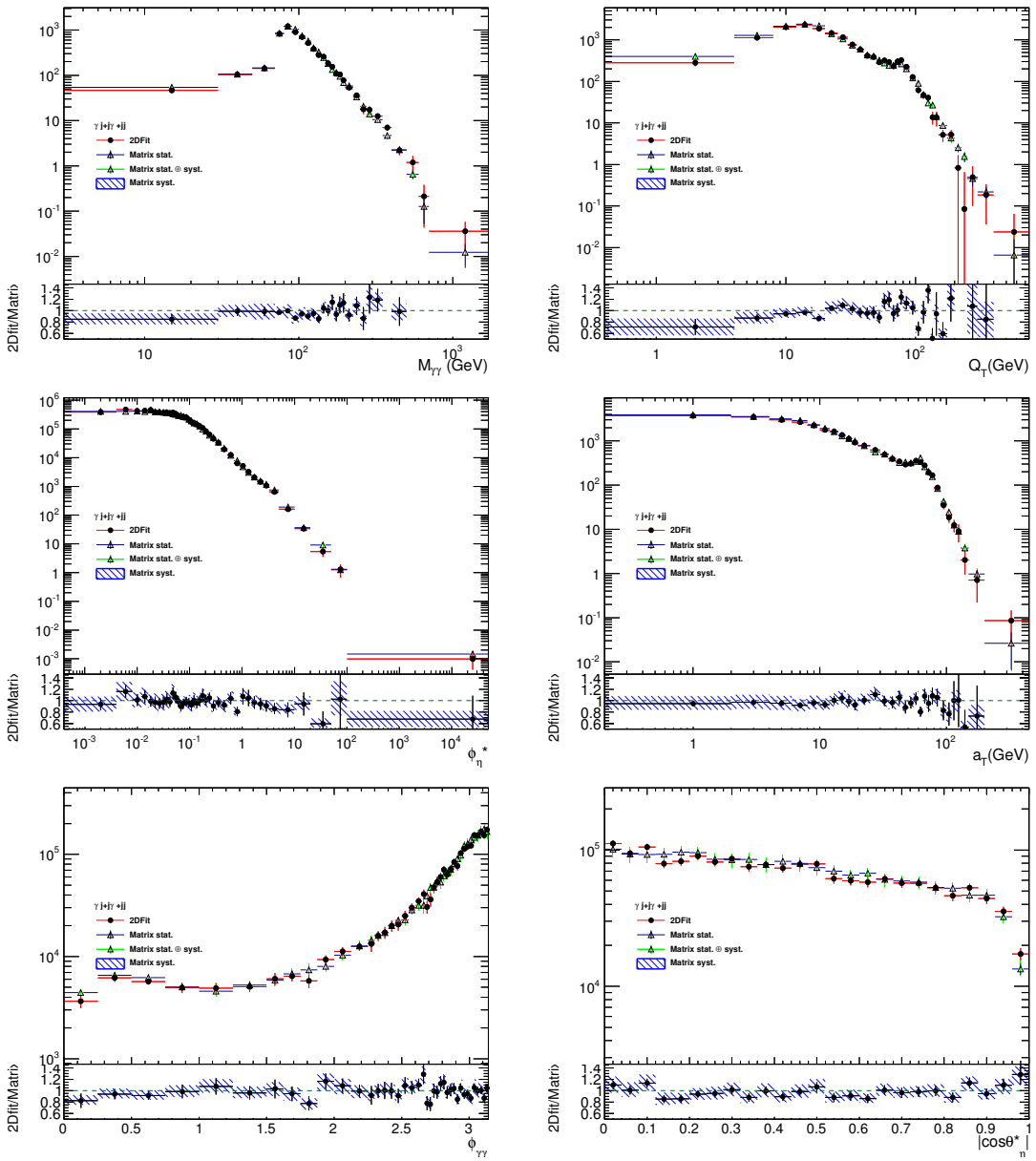

Figure 7.24: Comparison of the γj + jγ + jj yield between the matrix method (triangle) and the 2D fit method (black dots) in terms of $m_{\gamma\gamma}$, $p_{\mathrm{T},\gamma\gamma}$, ϕ^*_η, a_T, $\Delta\phi_{\gamma\gamma}$ and $|\cos\theta^*_\eta|$. Systematic uncertainties are only shown for the matrix method and the error bars of the 2D fit method represent statistical uncertainties.

7.11.3 Comparison between the matrix method and the 2D fit method considering uncertainty correlations

One naively expects there is a strong correlation in the statistic and systematic uncertainties between the two data-driven techniques due to a common use of shower shape variables and isolation requirements. Using the measurement in all bins of the differential spectra, the correlation in statistical uncertainties and relevant systematic uncertainties between the 2D fit method and the matrix method is shown in Figure 7.25. Table 7.16 shows the global correlation factors for the relevant correlated uncertainties using these measurements in all bins of the six kinematic variables. These global correlation factors in Table 7.16 were used as input to compute the uncorrelated systematic uncertainties in the differential spectrum comparison between the two data-driven methods. The photon ID systematic uncertainty between the two methods are considered to be 100% correlated and not included in the following comparisons.

The inclusive yield ratio of the 2D fit method to that of the matrix method considering uncertainty correlations is 1.0187 ± 0.0014 (stat.) $^{+0.0492}_{-0.0466}$ (syst.). Figure 7.26 shows the ratio in the differential spectra of the 2D fit method to that of the matrix method considering uncertainty correlations. The agreement between the matrix method and the 2D fit method in the differential spectra is excellent. There are some bins in which systematic uncertainties do not cover the residual differences.

	Stat.	Loose′2	Loose′5
2D fit	1022	-4011	3587
matrix method	901	-5990	7664
Correlation factor	0.947	0.19	0.27

Table 7.16: Global correlation factors for uncertainties determined from measurements in all bins of $\gamma\gamma$ differential spectra.

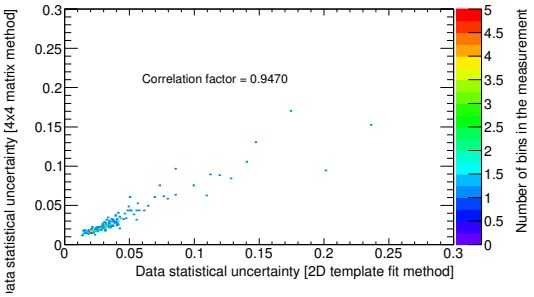

(a) Statistical correlation

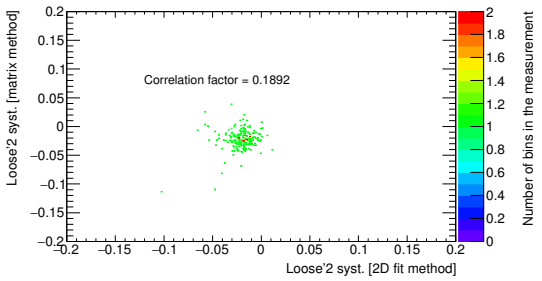

(b) Loose′2 systematics correlation

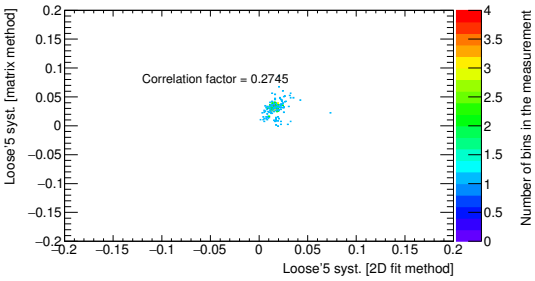

(c) Loose′5 systematics correlation

Figure 7.25: Correlation of statistical (systematic) uncertainties between the 2D fit method and the 3D matrix method using all bins of $\gamma\gamma$ differential spectra in the measurement. The correlations considered between the two methods are (a) Statistical uncertainties, (b) Loose′2 systematic uncertainty and (c) Loose′5 systematic uncertainty.

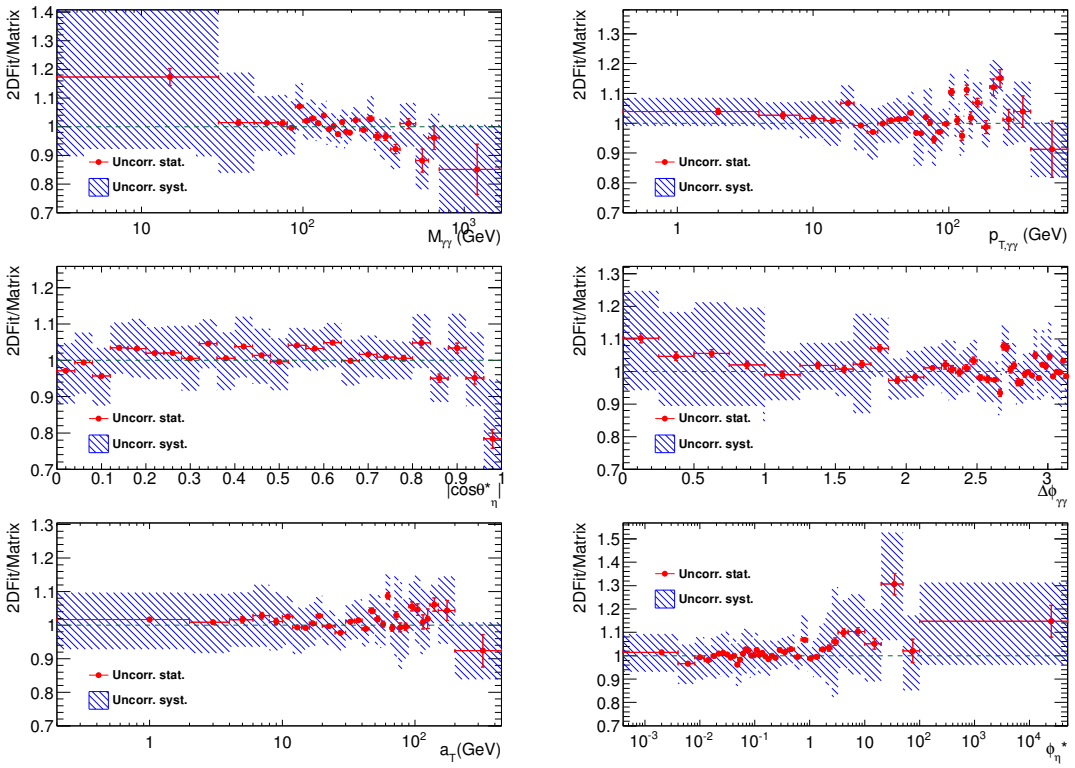

Figure 7.26: Ratio of the $\gamma\gamma$ yield of the differential spectra of the 2D fit method to that of the matrix method taking into account uncertainty correlations. The red points with error bars represent the ratio of the diphoton yield of the 2D fit method to that of the matrix method and uncorrelated statistical uncertainty. The blue band represents the uncorrelated systematic uncertainties between the two methods.

7.12 Unsmearing studies

7.12.1 Particle-level isolation

At detector level, calorimeter and track isolation requirements are imposed to reduce the hadronic background, which produces "fake" photons in the secondary decays of the boosted mesons (e.g. π^0). These fake photons arising from the hadronic background are not described accurately in the MC because the production processes are non-perturbative and rely on the hadronization model of the simulation.

At particle level, a requirement on the isolation energy is needed to decrease the fraction of the fragmentation photons, which are less well understood. In order to mimic the experimental isolation requirement, two definitions have been proposed. The nominal definition is called "fixed cone" by summing the hadronic energy in a fixed cone around the photon. An alternative definition of the isolation energy is known as "Frixione isolation" [88]. It is such that the theoretical calculations are independent of the fragmentation photon contributions. This particular feature makes higher order calculations feasible, and thus the Frixione isolation definition is often used in fixed order pQCD calculations. However, this definition does not correspond to the fixed cone definition in the experiment and implementation of the Frixione isolation in the experiment is not possible.

The general principle of unfolding the detector level distributions to the truth level distributions is to minimize the model dependence of the measurement and therefore we define a fiducial volume at particle level that is as close as possible to detector level requirements. The calorimeter isolation energy correlations between detector level and particle level are investigated in detail.

Figure 7.27 shows the results of a linear fit of particle-level isolation energy $E_{\mathrm{T}}^{\mathrm{part.iso.}}$ and calorimeter isolation energy $E_{\mathrm{T}}^{\mathrm{iso}}$ using both Sherpa and Pythia simulations for the leading and subleading photons separately, where the optimal requirement on $E_{\mathrm{T}}^{\mathrm{part.iso.}}$ to minimize the model dependence is around 11-12 GeV from both event generators. Since Sherpa is used as default for the unfolding procedure, we require $E_{\mathrm{T}}^{\mathrm{part.iso.}} < 11$ GeV.

7.12.2 Track isolation efficiency

The track isolation efficiency ϵ_{II} is defined as follows:

$$\epsilon_{II} = \frac{N_{calo,trk}^{TT}}{N_{calo}^{TT}}, \tag{7.36}$$

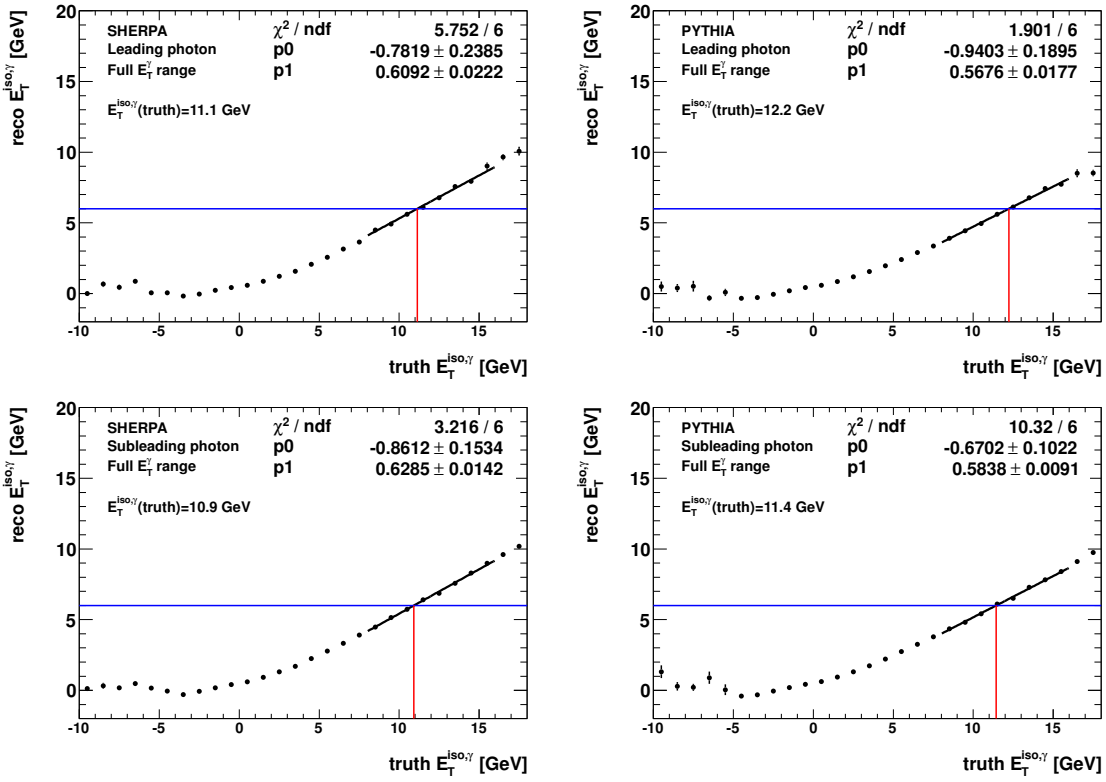

Figure 7.27: Relationship between particle-level isolation energy $E_T^{\mathrm{iso},\gamma}$ and calorimeter isolation energy $E_T^{\mathrm{iso},\gamma}$, as described by the SHERPA (left) and PYTHIA (right) diphoton MC, for the leading (top) and subleading (bottom) photons separately. A linear fit associates the cut on $E_{\mathrm{T}}^{\mathrm{iso}}$ (horizontal line) with the corresponding optimal cut at particle level (vertical line).

where $N^{TT}_{calo,trk}$ is the number of the diphoton events passing all selection requirements, and N^{TT}_{calo} is the number of the diphoton events when the track isolation is not applied. It is difficult to apply the track isolation requirement at particle level due to the track isolation efficiency dependence on the hadronization model. Therefore, it is important to check the description of the track isolation efficiency in simulations using data-driven methods. Previously in the ATLAS $H \to \gamma\gamma$ analysis [89], the track isolation requirement is also applied and the calorimeter and track isolation efficiency is examined using radiative decays in $Z \to ee\gamma$ control samples and a tag and probe technique in $Z \to ee$ samples. Scale factors are derived and have a strong dependence on the transverse energy E_T, which range from 0.996 at 40 GeV to 0.989 at 100 GeV per photon. However, these scale factors do not include contributions from fragmentation photons or converted photons.

Table 7.17 presents the comparison of the inclusive track isolation efficiency between the data-driven method and predictions from Sherpa and Pythia. Figure 7.28 shows the comparison between extracted track isolation efficiency using the matrix method and predictions from Sherpa and Pythia in terms of different kinematic observables. The track isolation efficiency is flat from both the data-driven method and simulations. Further comparisons were made for different background components, as presented in Figure 7.29. Another cross-check is to look at the comparison of the track isolation shape between data and simulations. Figure 7.30 compares the normalised track isolation distribution of data to Sherpa and Pythia predictions. Large discrepancies in the tail of the distributions were observed confirming the track isolation efficiency difference between the data-driven method and the predictions from simulations.

As the amount of background present in the sample is quite different with or without track isolation, the background systematic uncertainties associated with track isolation efficiencies are also evaluated and illustrated in Table 7.18. For photon ID systematics, variations in the diphoton yield have a positive correlation with variations in the track isolation efficiency. However, for the $\tilde{\mathbf{T}}$ definition variations, an anti-correlation between changes in the diphoton yield and track isolation efficiency was found. In order to take into account these correlations, a data-driven track isolation efficiency was propagated through the analysis to estimate the cross section in the defined fiducial region as introduced in Section 7.13.1. A data-driven photon isolation efficiency using the matrix method as a function of various kinematic variables is applied to the MC for the results shown below.

	data	$\gamma\gamma$ SHERPA	$\gamma\gamma$ PYTHIA
ϵ_{II}	0.926 ± 0.004	0.967 ± 0.000	0.958 ± 0.000

Table 7.17: The diphoton track isolation efficiency comparison between the data driven method, SHERPA and PYTHIA. The statistical uncertainty on data is shown. The statistical uncertainty on the MC predictions is less than 0.001.

	Photon ID	$\tilde{\mathbf{T}}$ definition	$\tilde{\mathbf{I}}$ definition	$\tilde{\mathbf{I}}$ signal leakage	electron background
$\gamma\gamma$	+2968 -2980	+7664 -5990	+635 -1189	+4721 -4721	+1310 -1310
ϵ_{II}	+0.012 -0.013	-0.021 +0.014	-0.002 +0.002	-0.008 +0.008	-0.004 +0.003

Table 7.18: Systematic uncertainties of the diphoton yield and the corresponding changes in the diphoton track isolation efficiency.

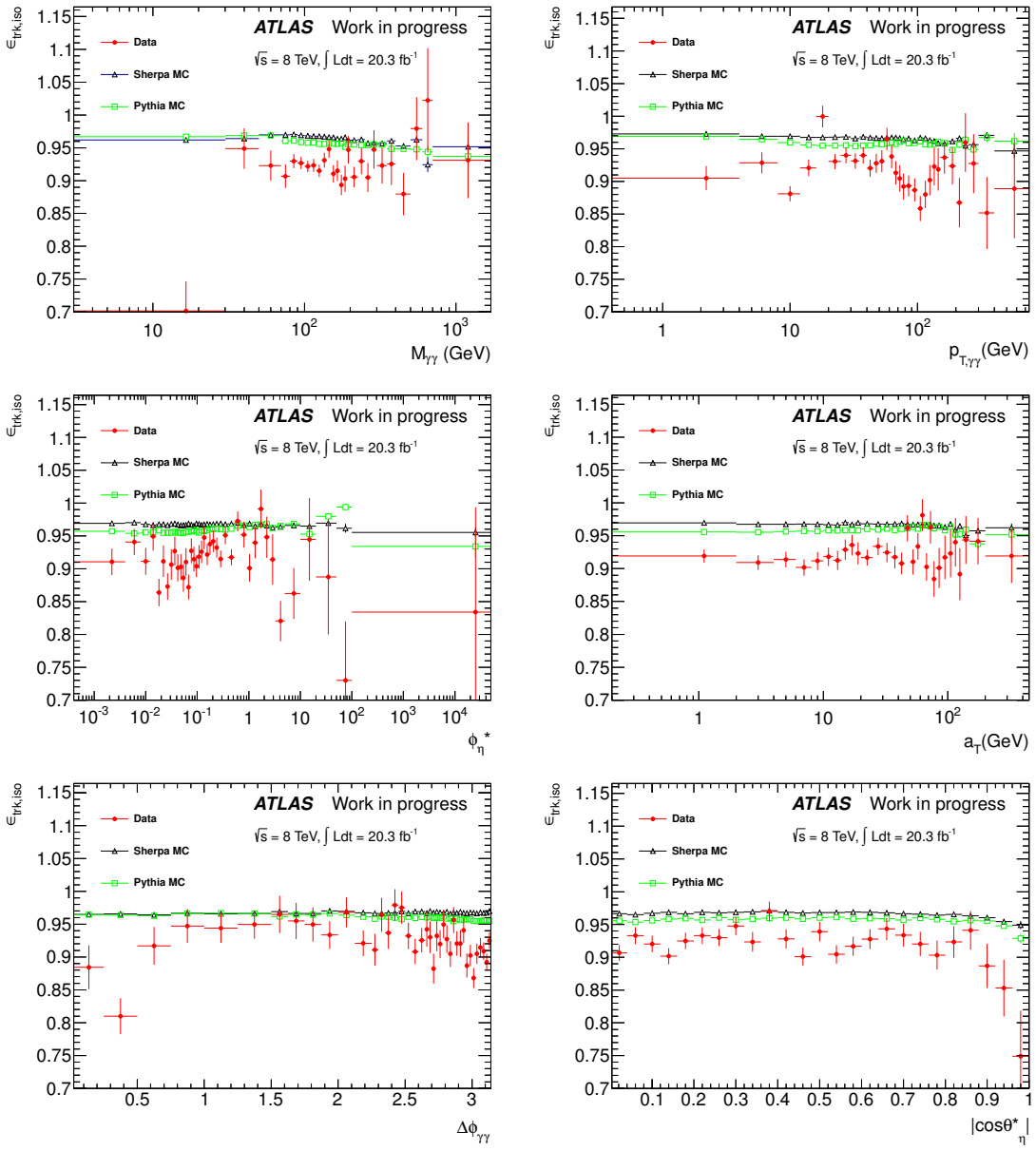

Figure 7.28: Comparison between the extracted track isolation efficiency using the matrix method and predictions from SHERPA and PYTHIA as a function of $m_{\gamma\gamma}$, $p_{\mathrm{T},\gamma\gamma}$, ϕ^*_η, a_{T}, $\Delta\phi_{\gamma\gamma}$ and $|\cos\theta^*_\eta|$.

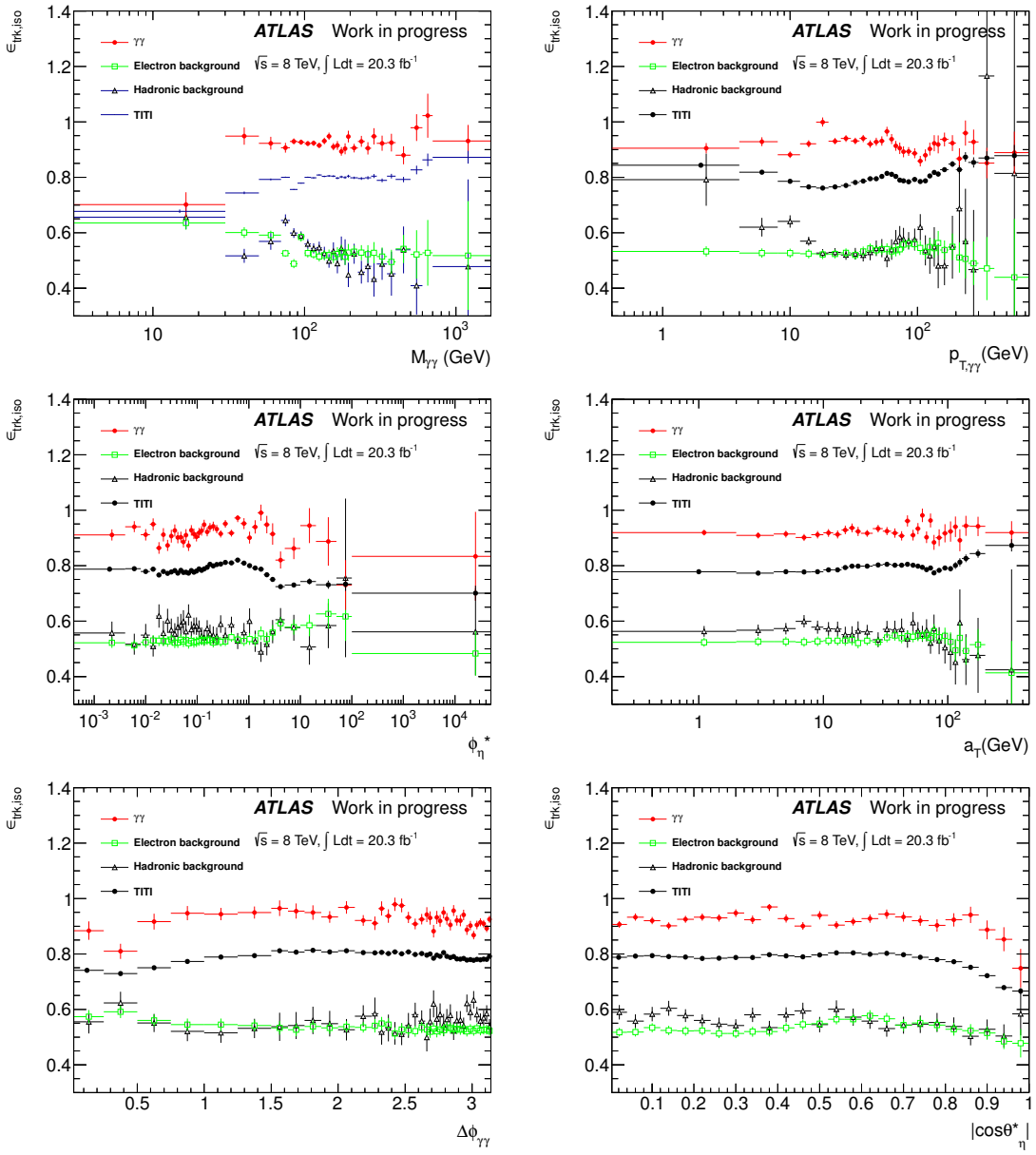

Figure 7.29: Track isolation efficiency using the matrix method for different background components as a function of $m_{\gamma\gamma}$, $p_{\mathrm{T},\gamma\gamma}$, ϕ^*_η, a_T, $\Delta\phi_{\gamma\gamma}$ and $|\cos\theta^*_\eta|$. The **TITI** in the histogram represents the data efficiency without any background subtraction.

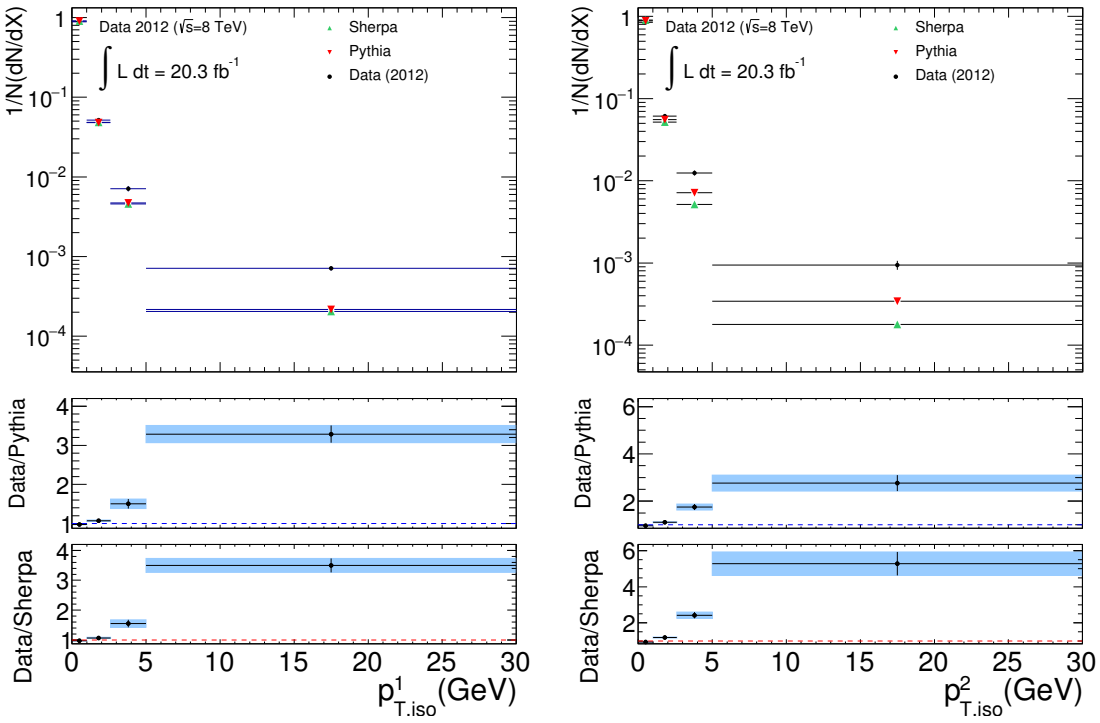

Figure 7.30: Normalized track isolation distributions using data-driven methods compared to predictions from SHERPA and PYTHIA for the leading (left) and subleading photons (right). Large discrepancies between data and simulations are observed in the tail of the distributions. Only the statistical uncertainty is shown for data and MC predictions.

7.12.3 Bin purity and reconstruction efficiencies

The bin purity is defined as the fraction of events in each bin at detector level that originate in the same bin at the generator level on an event-by-event basis. The bin purity is a measure of the migration into and out of the bins at detector level. This accounts for resolution effects leading to migration between bins and fake events that are reconstructed in a given distribution at detector level but have no counterpart at particle level. The reconstruction efficiency is the fraction of events in each bin at particle level that end up in the same bin at detector level. The reconstruction efficiency not only takes into account resolution effects that cause bin migrations, but also is a reflection of efficiency losses arising from object identification and reconstruction.

The bin purity and the reconstruction efficiency are shown in Figure 7.31 and Figure 7.32. Figure 7.33 presents the response matrix for each kinematic variable, which demonstrates the degree of migrations between different bins of the true and reconstructed diphoton kinematic variables. The bin purity across all the variables are above 75%. In particular, the bin purity in $|\cos\theta^*_\eta|$ is around 95%. The reconstruction efficiency in bins of the kinematic variables varies between 40% and 70%.

The bin-by-bin correction factor C_i is defined as follows:

$$C_i = \frac{N_i^{det}}{N_i^{part}}, \tag{7.37}$$

where N_i^{det} is the number of events in bin i for a given distribution passing detector level requirements (**TITI**), and N_i^{part} is the number of the selected events fulfilling the particle level fiducial cuts. Figure 7.34 shows the bin-by-bin correction factors in terms of the six variables and the distribution of the correction factors stays flat.

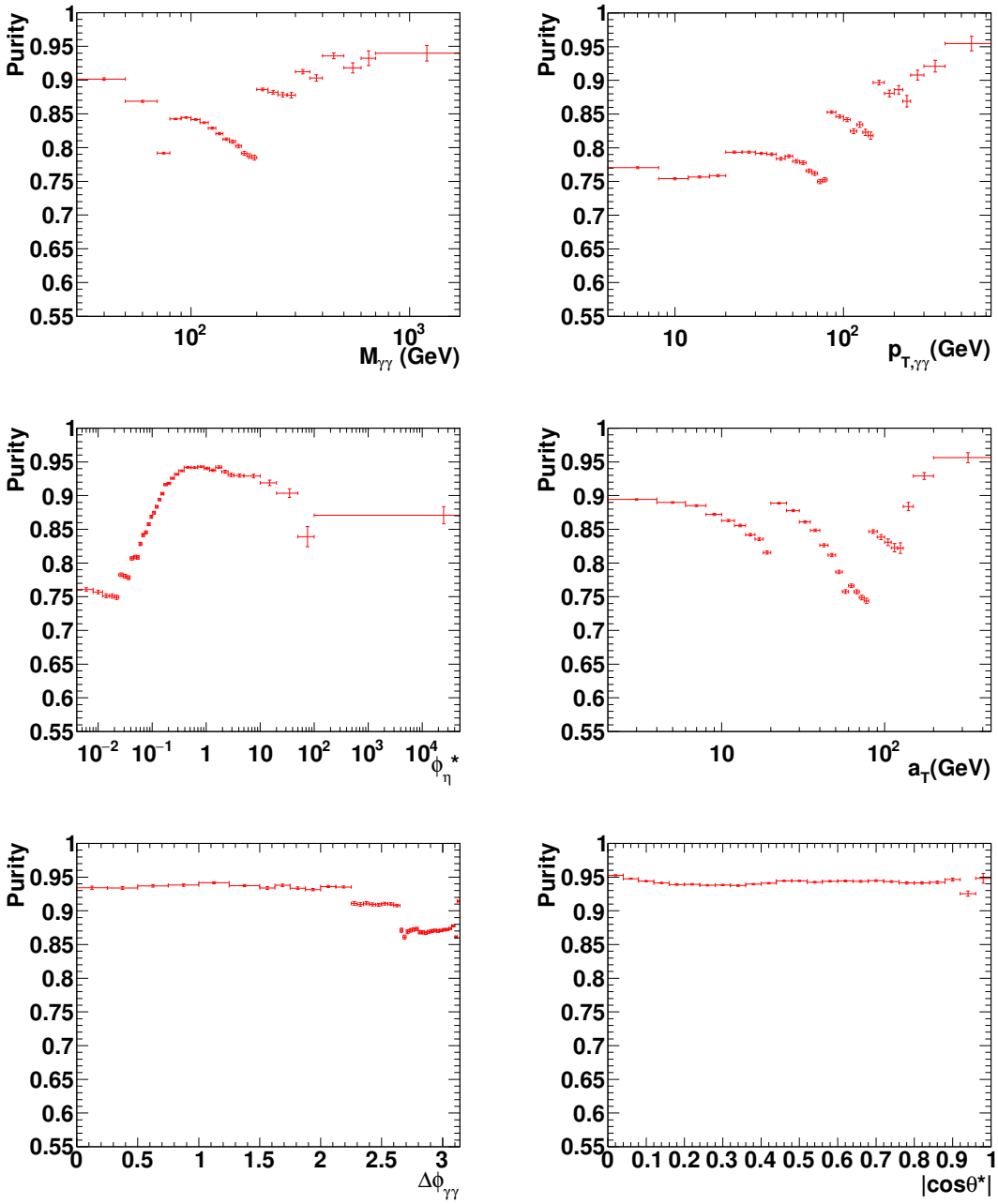

Figure 7.31: Bin purity as a function of $m_{\gamma\gamma}$, $p_{\mathrm{T},\gamma\gamma}$, ϕ_η^*, a_T, $\Delta\phi_{\gamma\gamma}$ and $|\cos\theta_\eta^*|$ in the SHERPA diphoton samples.

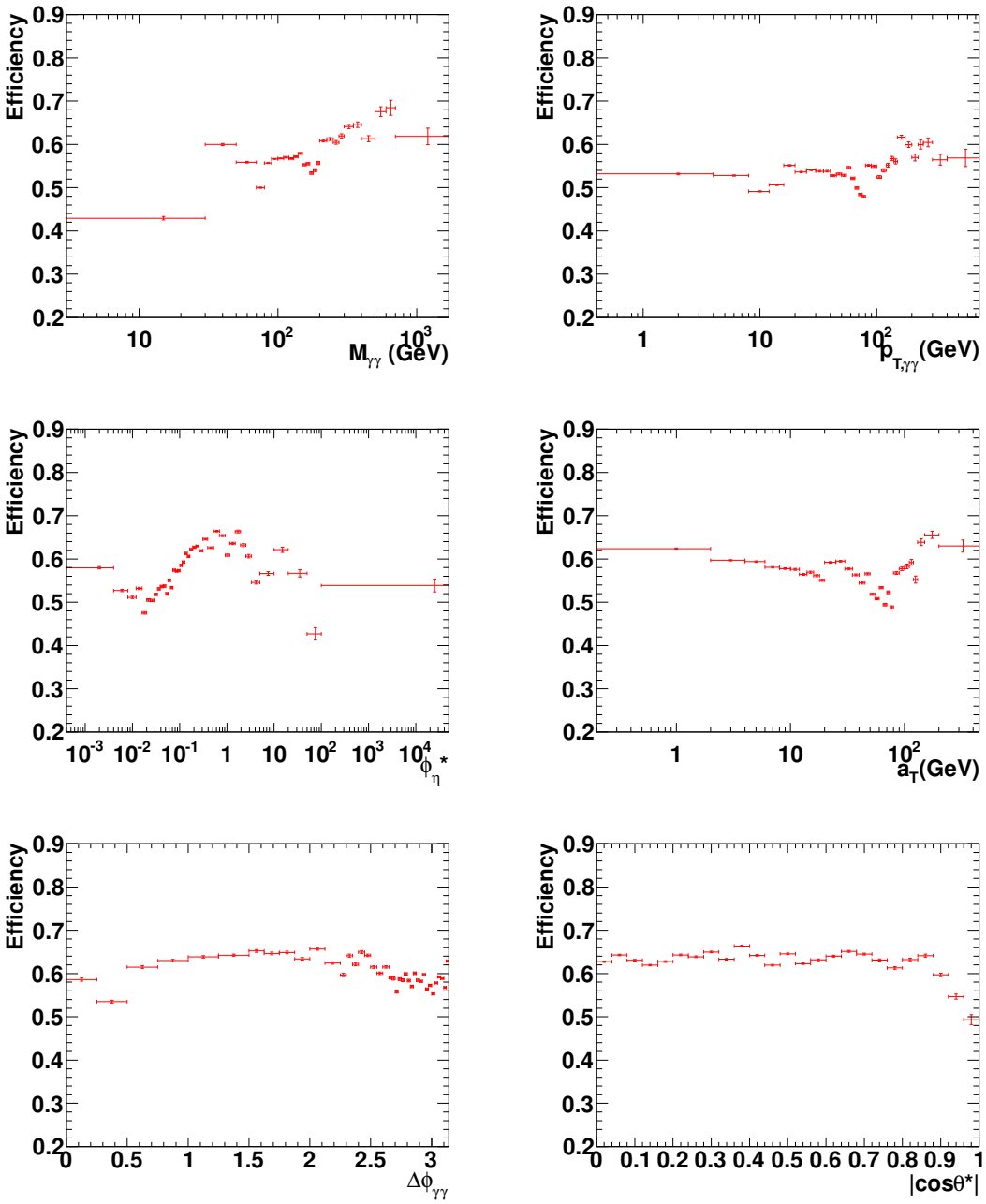

Figure 7.32: Reconstruction efficiency as a function of $m_{\gamma\gamma}$, $p_{\mathrm{T},\gamma\gamma}$, ϕ^*_η, a_T, $\Delta\phi_{\gamma\gamma}$ and $|\cos\theta^*_\eta|$ in the SHERPA diphoton samples.

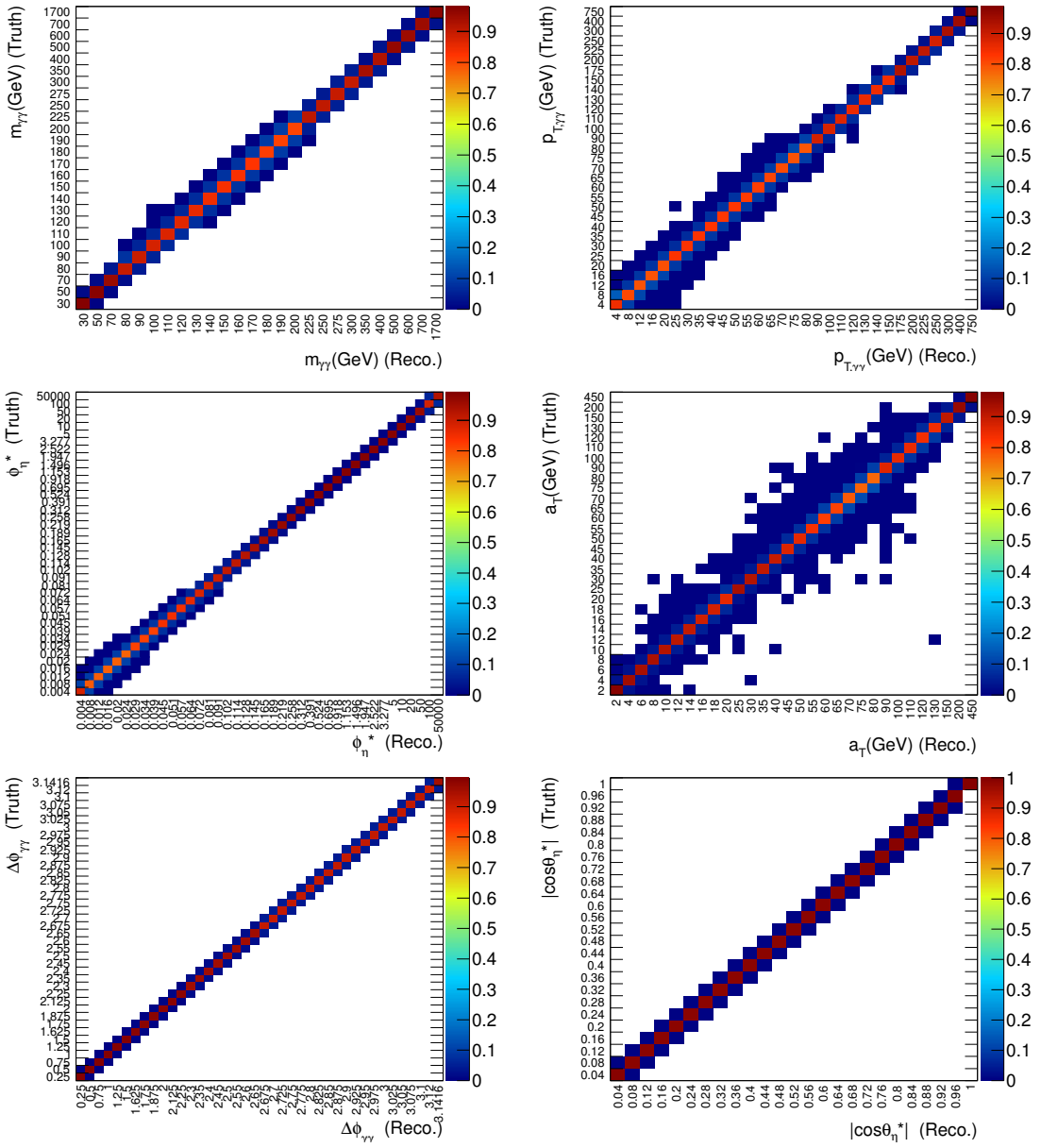

Figure 7.33: Response matrices as a function of $m_{\gamma\gamma}$, $p_{\mathrm{T},\gamma\gamma}$, ϕ^*_η, a_T, $\Delta\phi_{\gamma\gamma}$ and $|\cos\theta^*_\eta|$ after normalisation by row in the SHERPA diphoton samples.

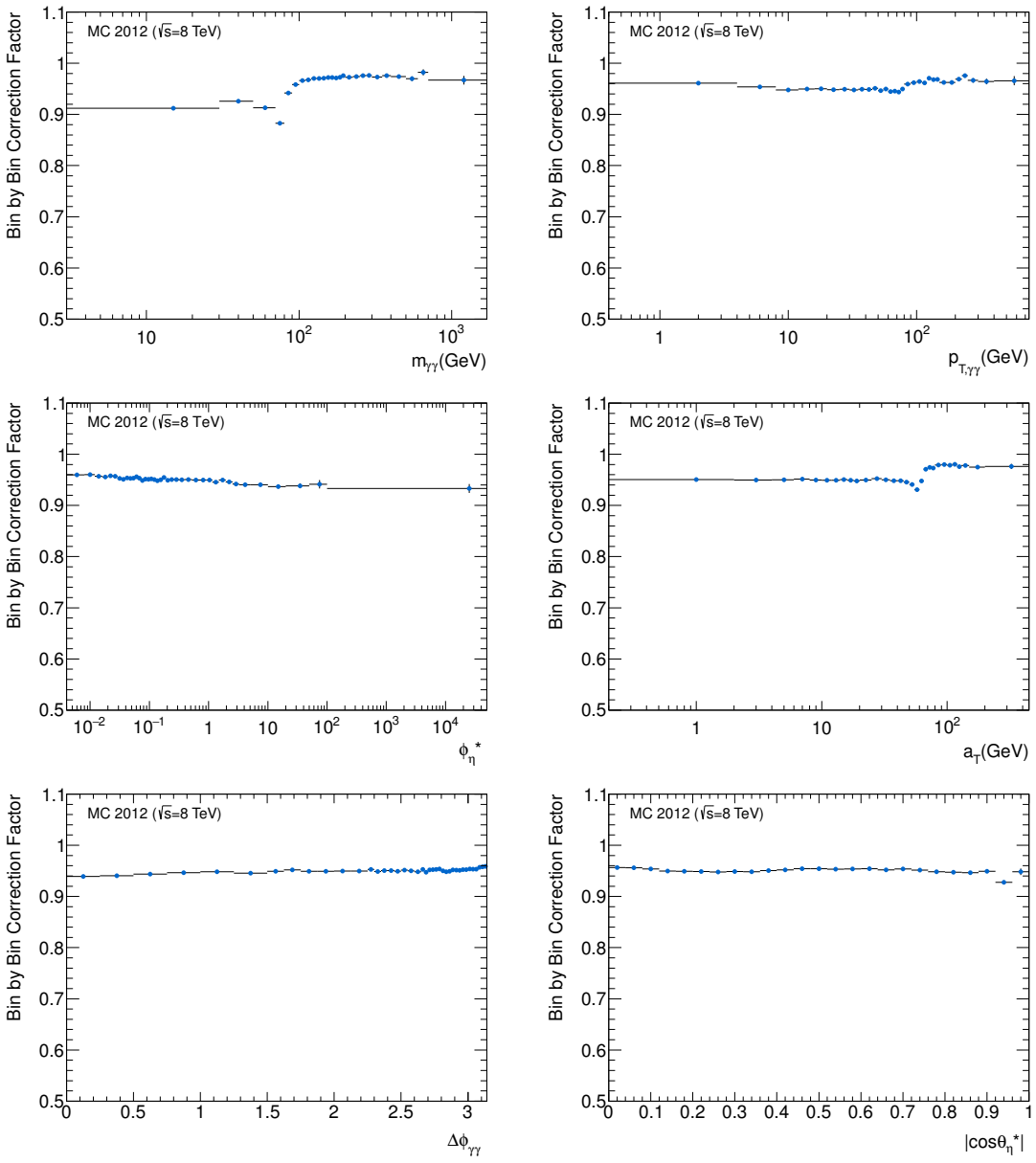

Figure 7.34: Bin-by-bin correction factor as a function of $m_{\gamma\gamma}$, $p_{\mathrm{T},\gamma\gamma}$, ϕ^*_η, a_T, $\Delta\phi_{\gamma\gamma}$ and $|\cos\theta^*_\eta|$ in the SHERPA diphoton samples.

7.13 Unfolding

7.13.1 Cross section measurement

In order to propagate the data-driven track isolation efficiencies throughout the analysis, the cross-section introduced in Equation 7.1 can be written in the following form:

$$\sigma_{fid.} = \frac{N_{\gamma\gamma}^{\mathbf{TITI},trackiso.}}{\epsilon_{II}^{data}\epsilon_{trig.}C_{total}^{calo}L}, \tag{7.38}$$

where $N_{\gamma\gamma}^{\mathbf{TITI},trackiso.}$ is the extracted diphoton yield from data in the **TITI** region with both the calorimeter requirement and the track isolation requirement applied and ϵ_{II}^{data} represents the data-driven track isolation efficiency. C_{total}^{calo} is defined as $C_{total}^{calo} = N_{\gamma\gamma}^{\mathbf{TT},calo}/N_{\gamma\gamma}^{true}$, in which $N_{\gamma\gamma}^{\mathbf{TT},calo}$ is the number of predicted **TT** diphoton events with only the calorimeter isolation requirement and $N_{\gamma\gamma}^{true}$ is the number of the produced diphoton events in the fiducial volume at truth level. Because a strong correlation between the track isolation efficiency and the extracted diphoton yield exists when varying background-related systematics, $N_{\gamma\gamma}^{\mathbf{TITI},trackiso.}$ and ϵ_{II}^{data} has to be varied in a correlated way.

One can write ϵ_{II}^{data} in terms of the diphoton yield:

$$\epsilon_{II}^{data} = \frac{N_{\gamma\gamma}^{\mathbf{TITI},trackiso.}}{N_{\gamma\gamma}^{\mathbf{TITI},notrackiso.}}, \tag{7.39}$$

where $N_{\gamma\gamma}^{\mathbf{TITI},notrackiso.}$ is the diphoton yield when the track isolation requirement is not applied. Substituting Equation 7.39 into Equation 7.38, we can obtain the following form:

$$\sigma_{fid.} = \frac{N_{\gamma\gamma}^{\mathbf{TITI},notrackiso.}}{\epsilon_{trig.}C_{total}^{calo}L}, \tag{7.40}$$

where the measurement is effectively insensitive to the presence of the track isolation efficiencies. In the actual analysis, we stick to Equation 7.39, though it is equivalent to Equation 7.40.

The differential cross section as a function of $m_{\gamma\gamma}$, $p_{\mathrm{T},\gamma\gamma}$, $\Delta\phi_{\gamma\gamma}$, $|\cos\theta_{\eta}^{*}|$, a_{T} and ϕ_{η}^{*}, generally denoted by X, is calculated for each bin i of X^{true}:

$$\frac{d\sigma_i}{dX} = \frac{N_{\gamma\gamma,i}^{\mathbf{TITI},trackiso.}}{\epsilon_{II,i}^{data}\epsilon_{trig.}C_{total,i}^{calo}L\Delta X}, \tag{7.41}$$

where the trigger efficiency is the same across all bins of the six kinematic variables.

7.13.2 Bayesian iterative unfolding

The iterative unfolding method [90] is more robust against the underlying generator distributions than bin-by-bin corrections, and it is based on Bayes' theorem. True yields in each bin of the X spectrum are iteratively reproduced starting from a detector response matrix and a MC truth prior. The conditional probability for an event in the E_j bin of the reconstructed X spectrum to have originated from an event generated in the C_i bin of the truth X spectrum is given as follows:

$$P(C_i|E_j) = \frac{P(E_j|C_i)P_0(C_i)}{\sum_{l=1}^{B_C} P(E_j|C_l)P_0(C_l)}, \tag{7.42}$$

where $P(E_j|C_i)$ represents the conditional probability for an event generated in the C_i bin of the true spectrum to be observed in the E_j bin of the reconstructed spectrum, $P_0(C_i)$ is the probability for an event to be generated in the C_i bin at truth level and B_C corresponds to the total number of bins of the true spectrum that end up in the E_j bin of the reconstructed spectrum. $P(E_j|C_i)$ represents the detector response matrix obtained from simulation samples (Figure 7.33), which has no dependence on the true distributions and the dependence is controlled by the $P_0(C_i)$ term. Starting from the prior true distributions $P_0(C_i)$ and the response matrix $P(E_j|C_i)$ from simulation samples, one can calculate $P(C_i|E_j)$ in the first iteration. This probability can be then used to compute the number of events in the C_i bin of the true spectrum, $\hat{n}(C_i)$, using the number of observed events in the E_j bin of the reconstructed spectrum, $\hat{n}(E_j)$:

$$\hat{n}(C_i) = \frac{1}{\epsilon_{trig.}} \sum_{j=1}^{B_E} n(E_j)P(C_i|E_j), \tag{7.43}$$

where B_E corresponds to the number of bins in the reconstructed spectrum that contain events that originate from the C_i bin of the true spectrum. The probability distribution $P_0(C_i)$ at truth level can be then recalculated by normalizing the sum of $\hat{n}(C_i)$ to unity, which can be used as input for the next iteration in Equation 7.42. The procedure described above is iterated until a stable spectrum is obtained. It can be observed in Figure 7.35 that 5 iterations are sufficient for the analysis.

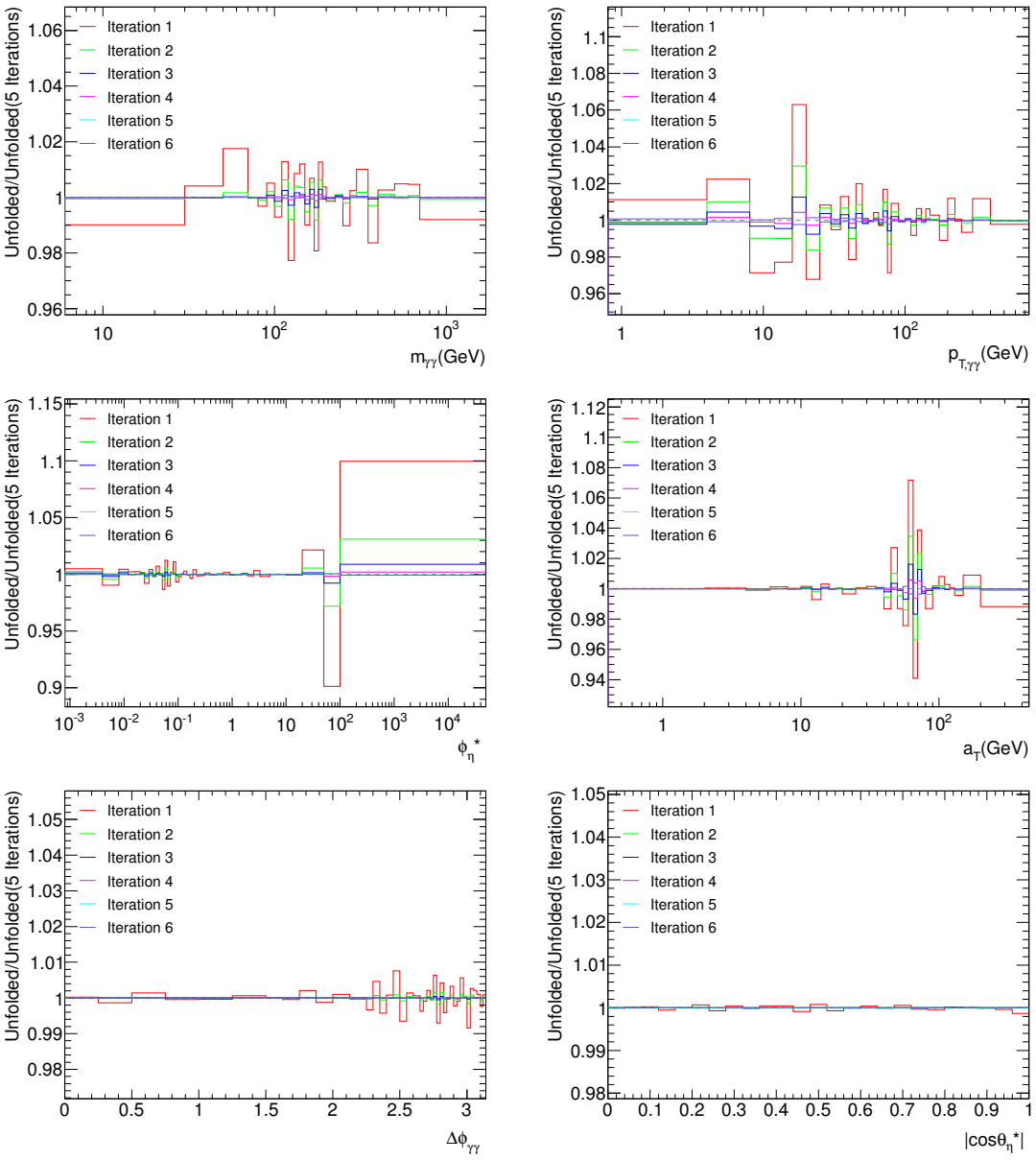

Figure 7.35: Unfolded spectra in terms of the number of iterations normalised to the ones with 5 iterations using the SHERPA diphoton samples for the response matrix and MC truth prior as a function of $m_{\gamma\gamma}$, $p_{\mathrm{T},\gamma\gamma}$, ϕ^*_η, a_T, $\Delta\phi_{\gamma\gamma}$ and $|\cos\theta^*_\eta|$.

7.14 Summary of uncertainties

The nominal fiducial cross section is obtained by using the LOOSE′4 definition and the corresponding response matrix from the $\gamma\gamma$ SHERPA simulation. The trigger efficiency was evaluated using a bootstrap method and radiative $Z \to ee\gamma$ decays using the method described in [91]. The value of the trigger efficiency is $99.47^{+0.13\%}_{-0.17\%}$, which is considered to be the same across all bins of the kinematic variables.

The inclusive fiducial cross-section is estimated using Equation 7.38. The iterative Bayesian unfolding is used only for the differential spectra.

A summary of the systematic uncertainty for the inclusive yield is given in Table 7.19. Figure 7.39 compares the total systematic uncertainty to the total statistical uncertainty in the differential spectra.

The measured inclusive diphoton cross section using the matrix method is: $16.97 \pm 0.09(\text{stat}) \, ^{+1.10}_{-0.93}$ (syst) $^{+0.03}_{-0.02}$ (trigger) $^{+0.33}_{-0.32}$(lumi) pb.

Background uncertainties

For each of the background uncertainties explained in Section 7.8.1 and the electron background uncertainty, the diphoton track isolation efficiency is evaluated and the corresponding response matrix is calculated. The difference with respect to the nominal unfolded cross section is taken as a systematic uncertainty. The systematic effect on the diphoton track isolation efficiency due to background variations is illustrated in Table 7.18. Figure 7.36 shows the background-related systematic uncertainties as a function of the six kinematic variables. The background uncertainties are dominated by the definition of the background from jets.

Photon energy scale and resolution

There are 65 (7) nuisance parameters for describing the photon energy scale (resolution), each of these nuisance parameters used in the photon calibration [61] is varied by $\pm 1\sigma$ to obtain a distorted response matrix and the difference with respect to the nominal is added in quadrature. Figure 7.37 presents the uncertainties due to the photon energy scale and resolution in terms of the six kinematic variables.

Calorimeter isolation distribution

The data-driven isolation corrections in [84] have been applied in the nominal case to improve the MC description of the photon calorimeter isolation profile, which

is varied by its associated systematic effects on the response matrix. Figure 7.38 presents the systematic uncertainty due to the calorimeter isolation description, the diphoton vertex reconstruction and underlying physics distributions.

Diphoton vertex reconstruction

The diphoton vertex is reconstructed using a NN algorithm described in Section 7.4. The corrected z position is used to compute the corrected pseudorapidity and transverse momentum of the candidate. The z position could deviate from the true position by a significant amount. In order to evaluate the systematic uncertainty due to diphoton vertex reconstruction, the event weight is varied by $\pm 5\%$ given the reconstructed diphoton vertex position along the z axis is 0.3 mm away from the true vertex. These values are chosen by following a $Z \to ee$ study of the vertex reconstruction efficiency in the $H \to \gamma\gamma$ analysis [92]. An additional normalisation factor is applied to obtain the same number of events as the nominal case. Therefore this systematic variation has no effect on the inclusive fiducial cross section by construction but can affect the differential spectrum.

Underlying physics distributions

The underlying physics distributions of the six variables are reweighted to the data distributions to test the sensitivity of the unfolding procedure to the input physics distributions. The effect is negligible as the iterative Bayesian unfolding is insensitive to the underlying physics distributions.

Luminosity and trigger efficiency

The trigger efficiency is taken to be $99.47^{+0.13\%}_{-0.17\%}$ and the luminosity has an uncertainty of $\pm 1.9\%$. The uncertainties are propagated throughout the whole analysis for both the inclusive and differential cross section measurements.

Difference between the integrated yield and the inclusive yield

A small difference between the integrated yield of the differential spectrum and the inclusive yield is observed and this systematic uncertainty is only considered for the inclusive case. The resultant systematic uncertainty is smaller than the statistical uncertainty of the inclusive yield.

	Cross-section difference (pb)	Cross-section difference (%)
Statistics(data)	±0.086	±0.51
Statistics(MC)	±0.012	±0.073
Background	+1.1/-0.93	6.8/-5.7
Isolation shift	0.0094/-0.0098	0.056/-0.058
Isolation smearing	0.00026/0.00096	0.0015/0.0057
z vertex reweighting	0./0.	0./0.
Photon energy resolution	0.0033/-0.0016	0.02/-0.0095
Photon energy scale	0.13/-0.13	0.79/-0.78
Integrated yield	+0.039/-0.013	0.23/-0.077

Table 7.19: Summary of the uncertainties for the inclusive diphoton fiducial cross section obtained using the matrix method. The last row termed as "Integrated yield" is the difference between the inclusive yield and the integrated yield over the bins of the differential spectra.

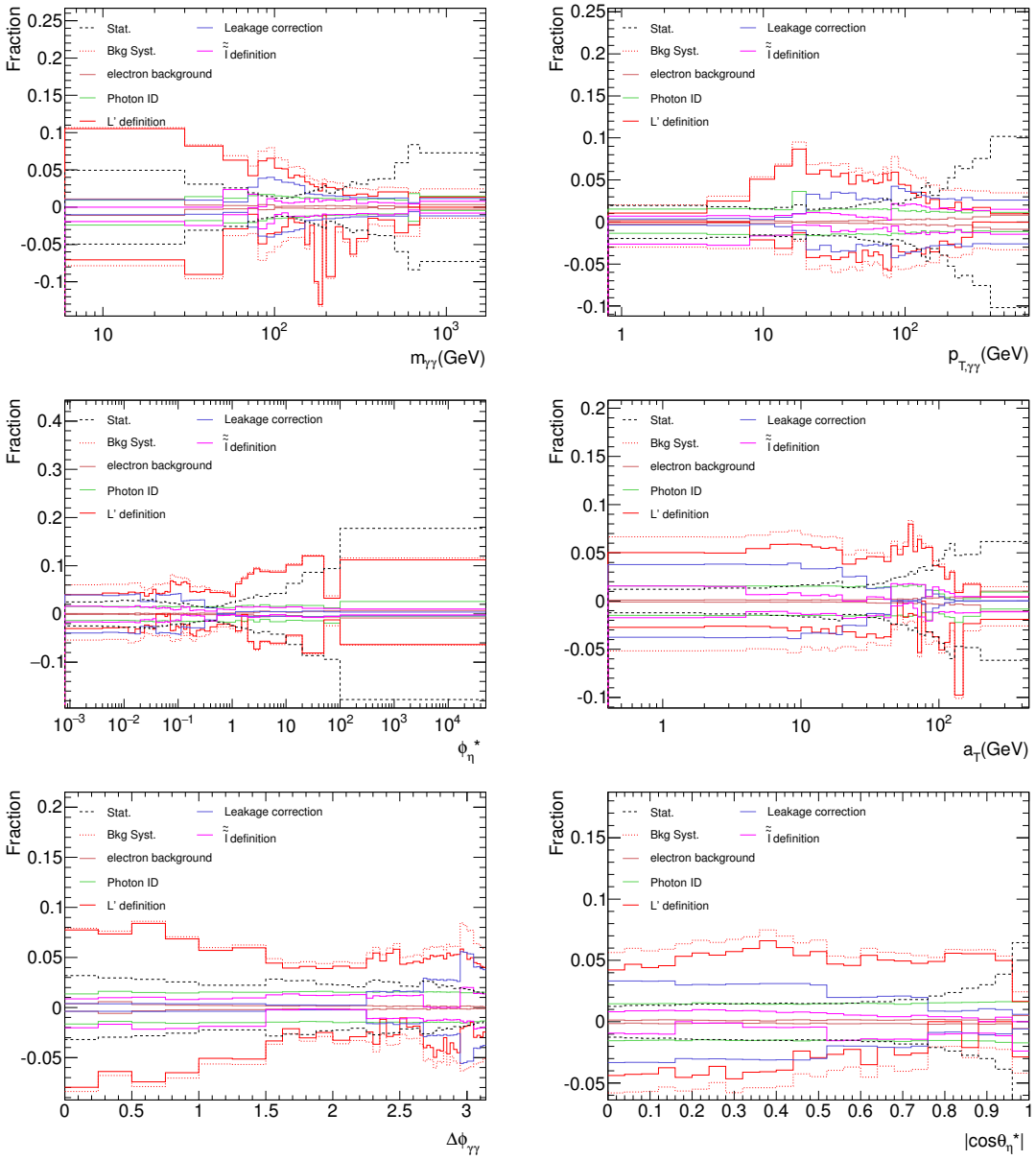

Figure 7.36: Systematic uncertainties related to the background estimation in data as a function of $m_{\gamma\gamma}$, $p_{\mathrm{T},\gamma\gamma}$, ϕ_η^*, a_T, $\Delta\phi_{\gamma\gamma}$ and $|\cos\theta_\eta^*|$.

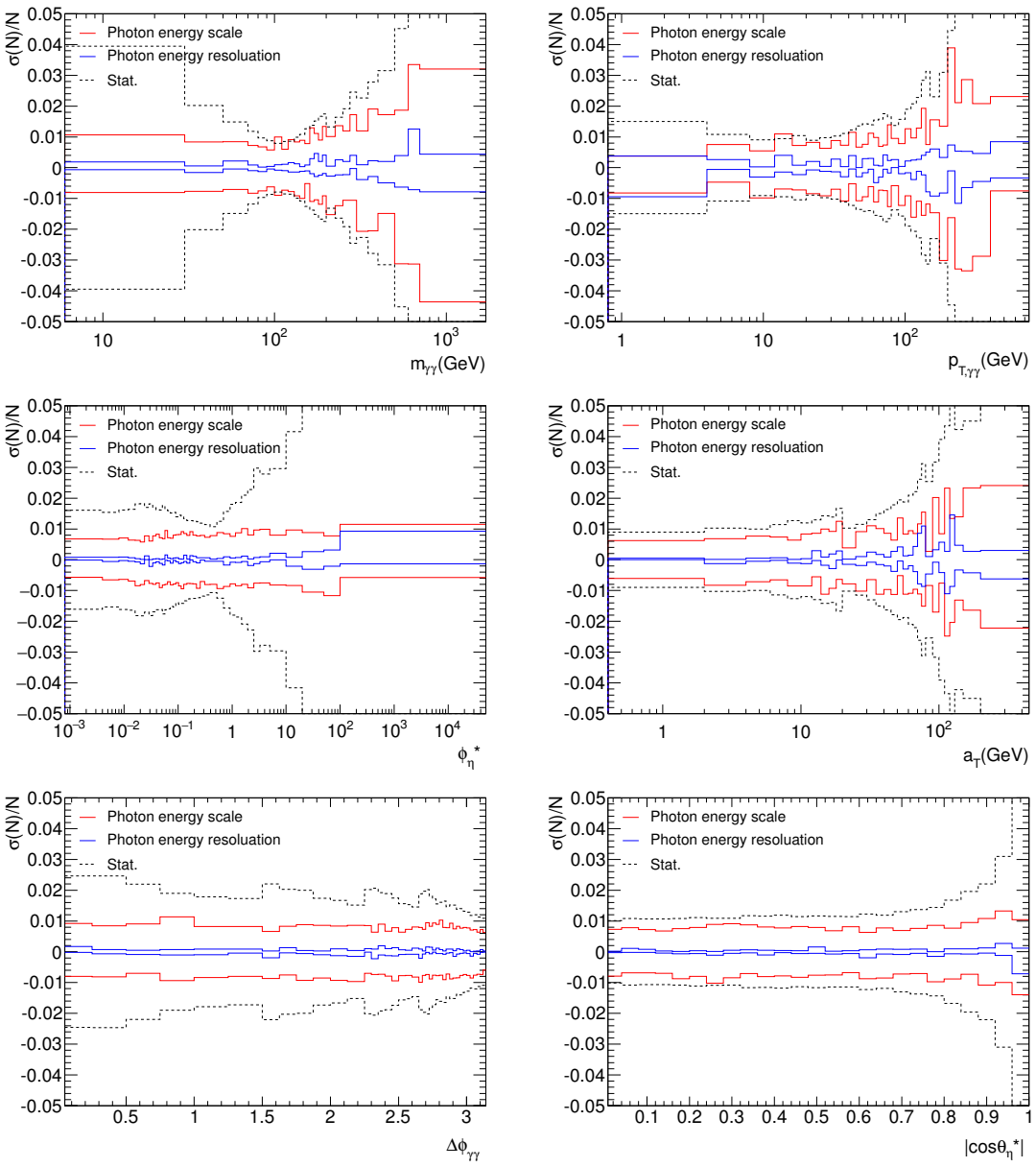

Figure 7.37: Systematic uncertainties related to the MC description of the photon energy resolution and scale uncertainties as a function of $m_{\gamma\gamma}$, $p_{\mathrm{T},\gamma\gamma}$, ϕ^*_η, a_{T}, $\Delta\phi_{\gamma\gamma}$ and $|\cos\theta^*_\eta|$.

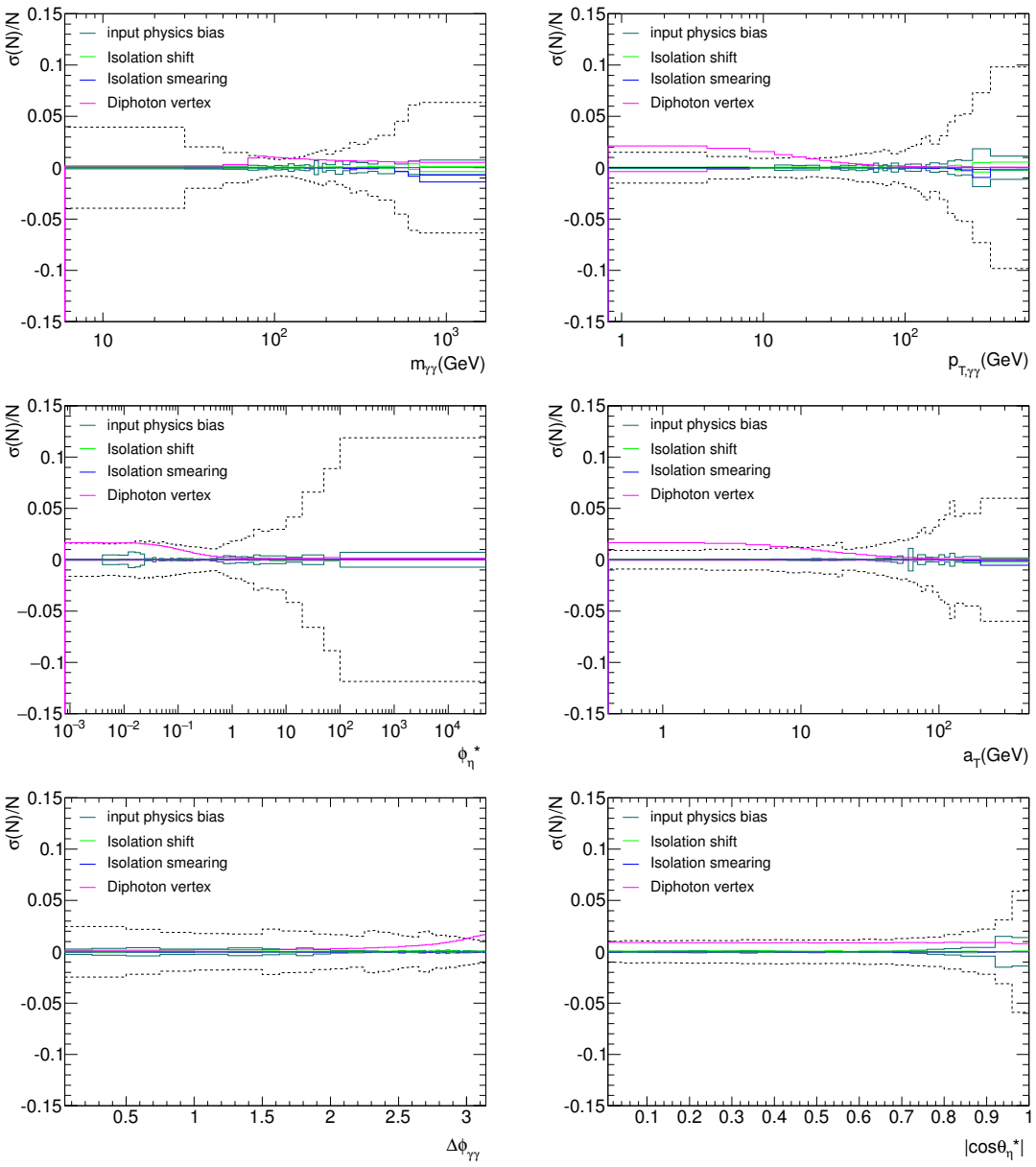

Figure 7.38: Systematic uncertainties related to the MC description of the photon isolation and the diphoton vertex reconstruction as a function of $m_{\gamma\gamma}$, $p_{\mathrm{T},\gamma\gamma}$, ϕ^*_η, a_T, $\Delta\phi_{\gamma\gamma}$ and $|\cos\theta^*_\eta|$.

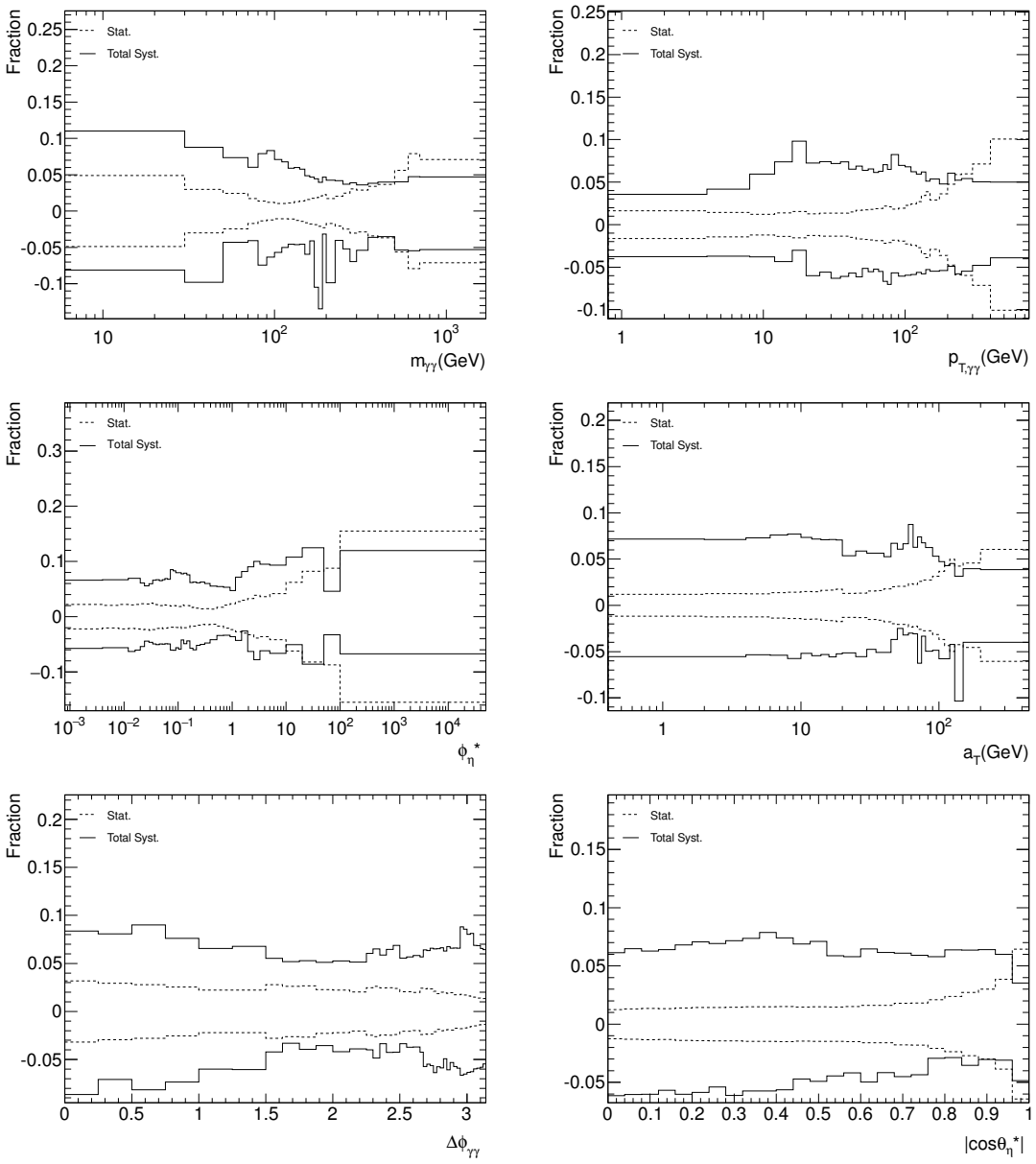

Figure 7.39: Total systematic uncertainties in comparison to the statistical uncertainties for the differential spectrum as a function of $m_{\gamma\gamma}$, $p_{\mathrm{T},\gamma\gamma}$, ϕ_η^*, a_T, $\Delta\phi_{\gamma\gamma}$ and $|\cos\theta_\eta^*|$.

7.15 Comparison to theoretical predictions

The unfolded data are compared to a number of theoretical predictions described as follows. The fixed order predictions at N(N)LO accuracy are produced at parton level without underlying events or hadronization. The non-perturbative effects are a few percent and are neglected in the following N(N)LO fixed order calculations.

Sherpa 1.4.0 and Pythia8

Both Sherpa 1.4.0 [49] and Pythia8 [29] predict the diphoton production process at LL+LO accuracy. The total fiducial cross section predicted by Sherpa 1.4.0 (Pythia8) is 12.53 pb (11.81 pb). For the differential spectrum, an overall scale factor of 1.44 (1.35) is applied to compare the shape between data and predictions. Such a large scaling factor arises due to missing higher order contributions to the diphoton cross section. Figure 7.40 and Figure 7.41 compare data with predictions from Sherpa 1.4.0 and Pythia8. Pythia8 gives a much better description than Sherpa 1.4.0 in terms of the $m_{\gamma\gamma}$ spectrum. Sherpa 1.4.0 generally reproduces the data shape except the $m_{\gamma\gamma}$ spectrum with better accuracy than Pythia8.

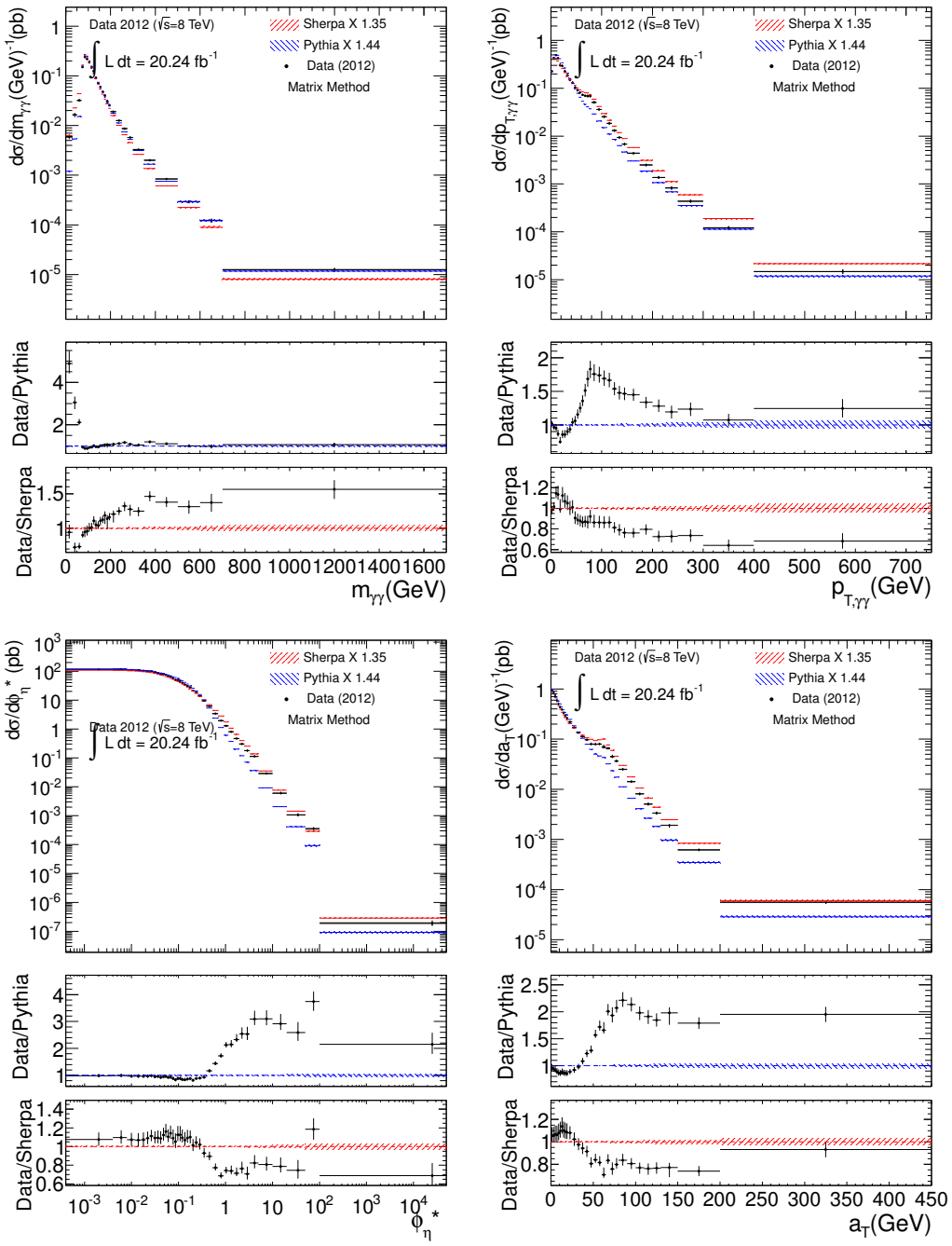

Figure 7.40: Comparison between unfolded distributions and the SHERPA and PYTHIA MC predictions for $m_{\gamma\gamma}$, $p_{\mathrm{T},\gamma\gamma}$, ϕ^*_η and a_{T}. The SHERPA (PYTHIA) MC distributions have been scaled to the total data cross section, by a factor of 1.35 (1.44). Data are shown as black dots with error bars indicating the total uncertainties. The SHERPA and PYTHIA predictions with corresponding statistical uncertainties are represented by red and blue bands respectively.

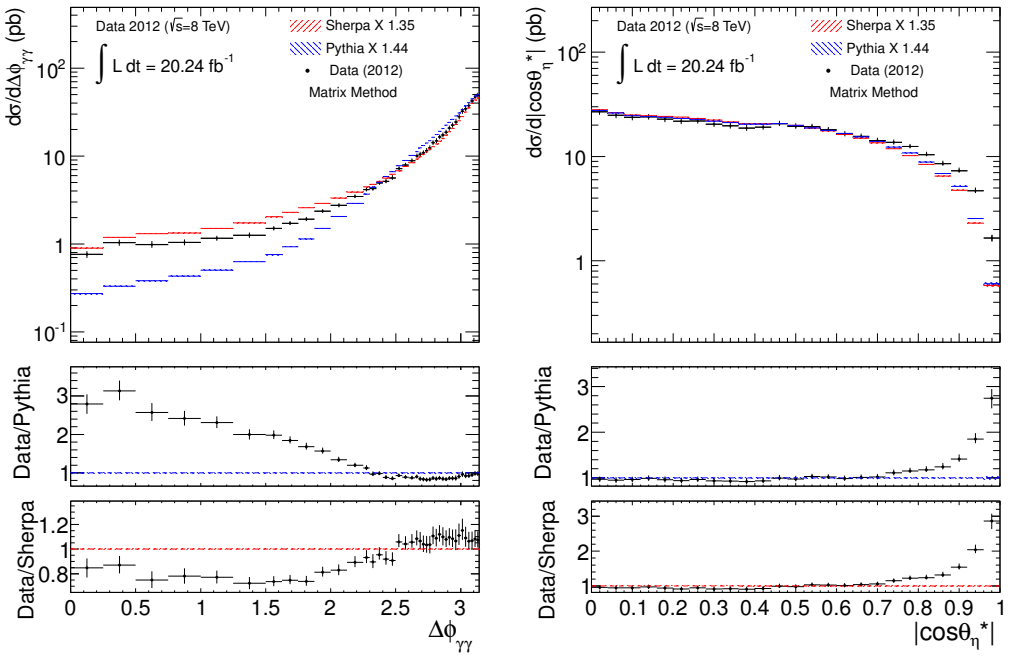

Figure 7.41: Comparison between unfolded distributions obtained and the SHERPA and PYTHIA MC predictions for $\Delta\phi_{\gamma\gamma}$ and $|\cos\theta^*_\eta|$. The SHERPA (PYTHIA) MC distributions have been scaled to the total data cross section, by a factor of 1.35 (1.44). Data are shown as black dots with error bars indicating the total uncertainties. The SHERPA and PYTHIA predictions with corresponding statistical uncertainties are represented by red and blue bands respectively.

DIPHOX and ResBos

The DIPHOX predictions [32] implement an almost NLO pQCD calculation with the NLO PDF set CT10 in which the box process ($gg \to \gamma\gamma$) is predicted at LO. DIPHOX includes contributions from events in which one or both photons originate from fragmentation. The QCD scale uncertainties are evaluated by varying the renormalisation, factorization and fragmentation scales between $m_{\gamma\gamma}/2$ and $2m_{\gamma\gamma}$, which are the dominant theoretical uncertainties. The predicted fiducial cross-section is 10.80 ± 0.04 (stat.) $^{+1.50}_{-1.18}$ (syst.) pb, where the systematic uncertainty is the quadrature sum of the scale uncertainty and the PDF uncertainty.

The ResBos predictions [51–53] include all NLO perturbative contributions of the hard process, i.e., the gluon-gluon scattering box diagram contribution is also at NLO in contrast to the DIPHOX generator, which only accounts for it at LO. In addition, ResBos predictions include all-orders resummation of initial state gluon radiation to NNLL accuracy. These contributions are especially important at low values of the diphoton transverse momentum or equivalently when the two photons are back-to-back in the azimuthal plane ($\Delta\phi_{\gamma\gamma} \sim \pi$) where fixed order calculations yield integrable singularities. As for the treatment of the contribution from fragmentation photons, ResBos predictions do not introduce fragmentation functions but adopt a simplified approach as detailed in [52] to include these contributions. No scale variations for ResBos predictions are provided and hence the fractional uncertainties are taken from DIPHOX as the theoretical uncertainties. The inclusive diphoton cross-section predicted by ResBos is 12.26 ± 0.05 (stat.) $^{+1.70}_{-1.34}$ pb. A rather large deviation of NLO pQCD calculations from data is observed due to a lack of higher order contributions.

The comparison between data and the NLO predictions from DIPHOX and ResBos is shown in Figure 7.42 and Figure 7.43. It can be observed that ResBos gives a better description of the data shape at high $\Delta\phi_{\gamma\gamma}$ and low a_{T} where contributions from resummation of soft gluons are important. However, DIPHOX provides a slightly better description of the data shape around the Guillet shoulder region of the $p_{\mathrm{T},\gamma\gamma}$ and a_{T} spectra and at low $m_{\gamma\gamma}$ region where there is an enhancement of fragmentation components. Both NLO predictions give a good description of the $m_{\gamma\gamma} > 80$ GeV region and both predictions fail at $|\cos\theta^*_\eta| > 0.8$.

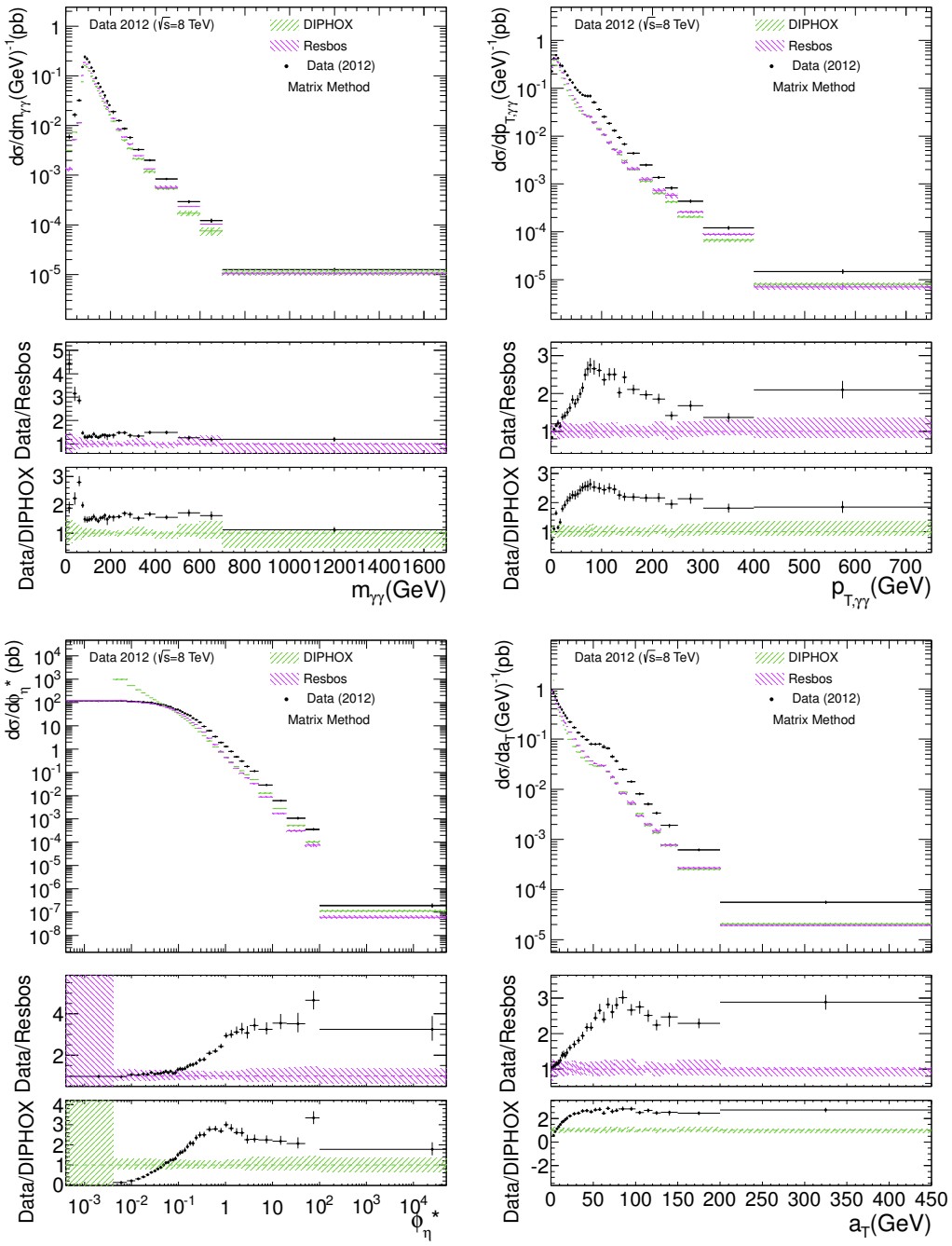

Figure 7.42: Comparison between unfolded distributions and the NLO predictions from DIPHOX and ResBos for $m_{\gamma\gamma}$, $p_{\mathrm{T},\gamma\gamma}$, ϕ^*_η and a_{T}. Data are shown as black dots with error bars indicating the total uncertainties. The DIPHOX and ResBos predictions with corresponding theoretical uncertainties are represented by pink and green bands respectively for the ratio plots. Only statistical uncertainties are shown for the differential spectrum for predictions from DIPHOX and ResBos.

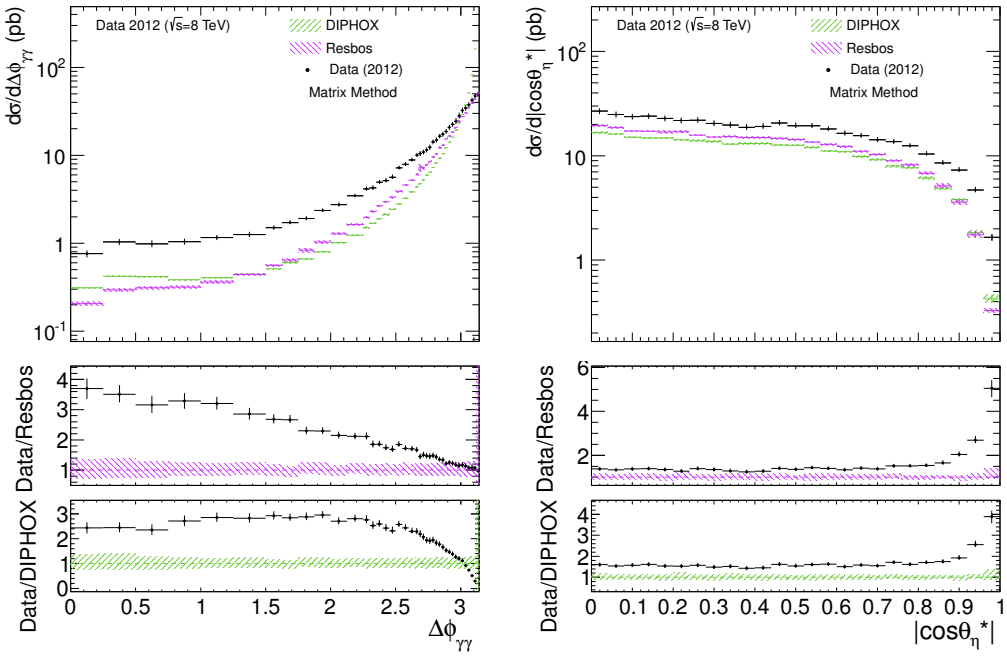

Figure 7.43: Comparison between unfolded distributions and the NLO predictions from DIPHOX and ResBos for $\Delta\phi_{\gamma\gamma}$ and $|\cos\theta^*_\eta|$. The DIPHOX and ResBos predictions with corresponding theoretical uncertainties are represented by pink and green bands respectively for the ratio plots. Only statistical uncertainties are shown for the differential spectrum for predictions from DIPHOX and ResBos.

2γNNLO

2γNNLO provides a NNLO pQCD calculation using a Frixione [88] isolation criterion. Only the central value of the prediction is available at the moment and the predicted fiducial cross section is 13.94 pb. Figure 7.44 compares data to the 2γNNLO predictions. A slightly better agreement with data than the NLO predictions from DIPHOX and ResBos is observed. Since no theoretical uncertainties are available, no conclusion can be made here.

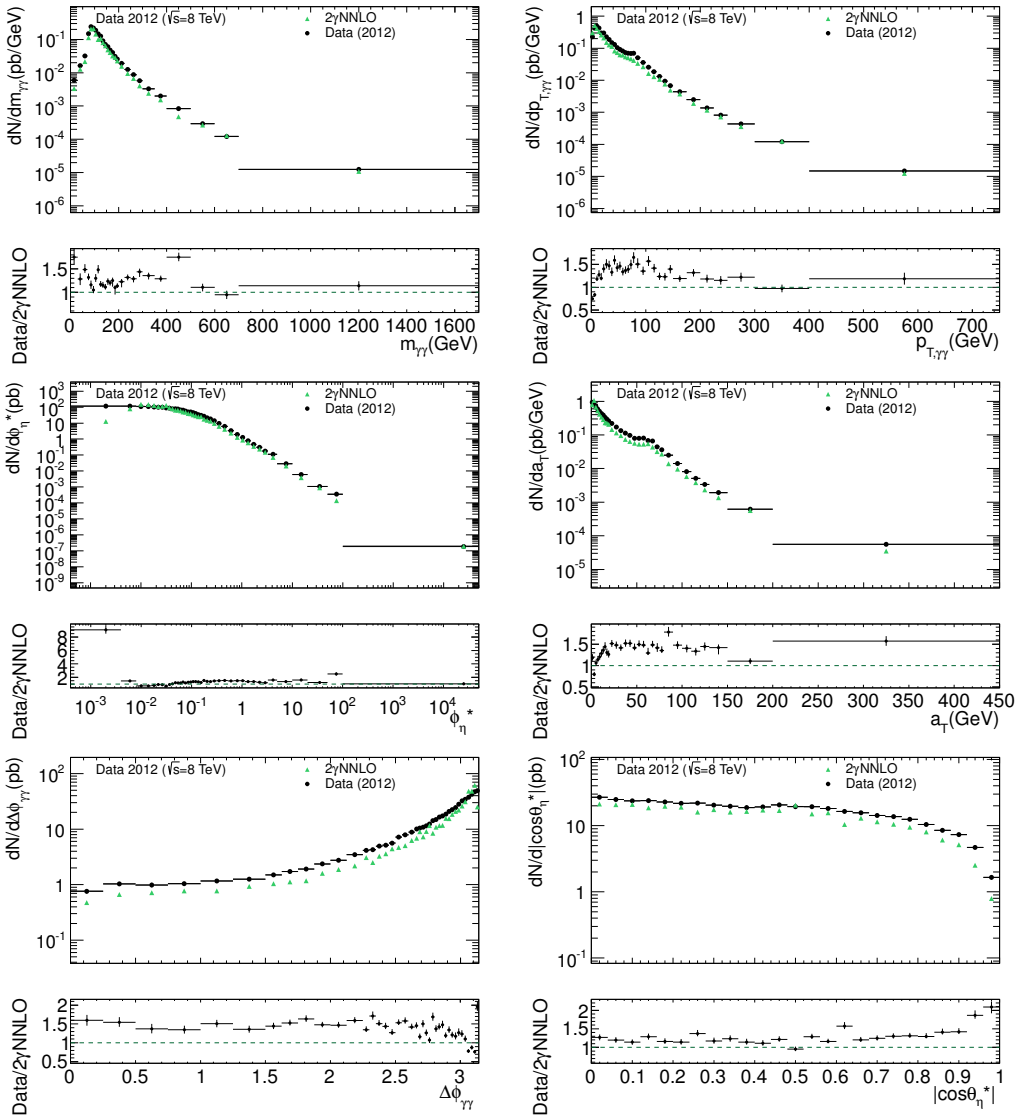

Figure 7.44: Comparison between unfolded distributions and the NNLL+NNLO predictions for $m_{\gamma\gamma}$, $p_{\mathrm{T},\gamma\gamma}$, $\Delta\phi_{\gamma\gamma}$, $|\cos\theta^*_\eta|$, a_{T} and ϕ^*_η. Data are shown as black dots with error bars indicating the total uncertainties. Only the central value is given for the NNLO predictions.

Sherpa 2.2α

Sherpa 2.2α generates the diphoton production process at NLO accuracy. Matrix elements are generated using Comix [93] and OpenLoops [94] for $\gamma\gamma$ and $\gamma\gamma$ + jet production at NLO accuracy and $\gamma\gamma$ + 2 jets and $\gamma\gamma$ + 3 jets at LO accuracy. The simulation uses the NNLO PDF set NNPDF [20]. The predicted inclusive fiducial cross section is 16.36 $\pm$ 0.08 (stat.) pb. Figure 7.45 shows the comparison of data distributions to the predictions from Sherpa 2.2α. The predictions from Sherpa 2.2α can describe the data within the data uncertainties except for $m_{\gamma\gamma} > 200$ GeV and $|\cos\theta^*_\eta| > 0.9$.

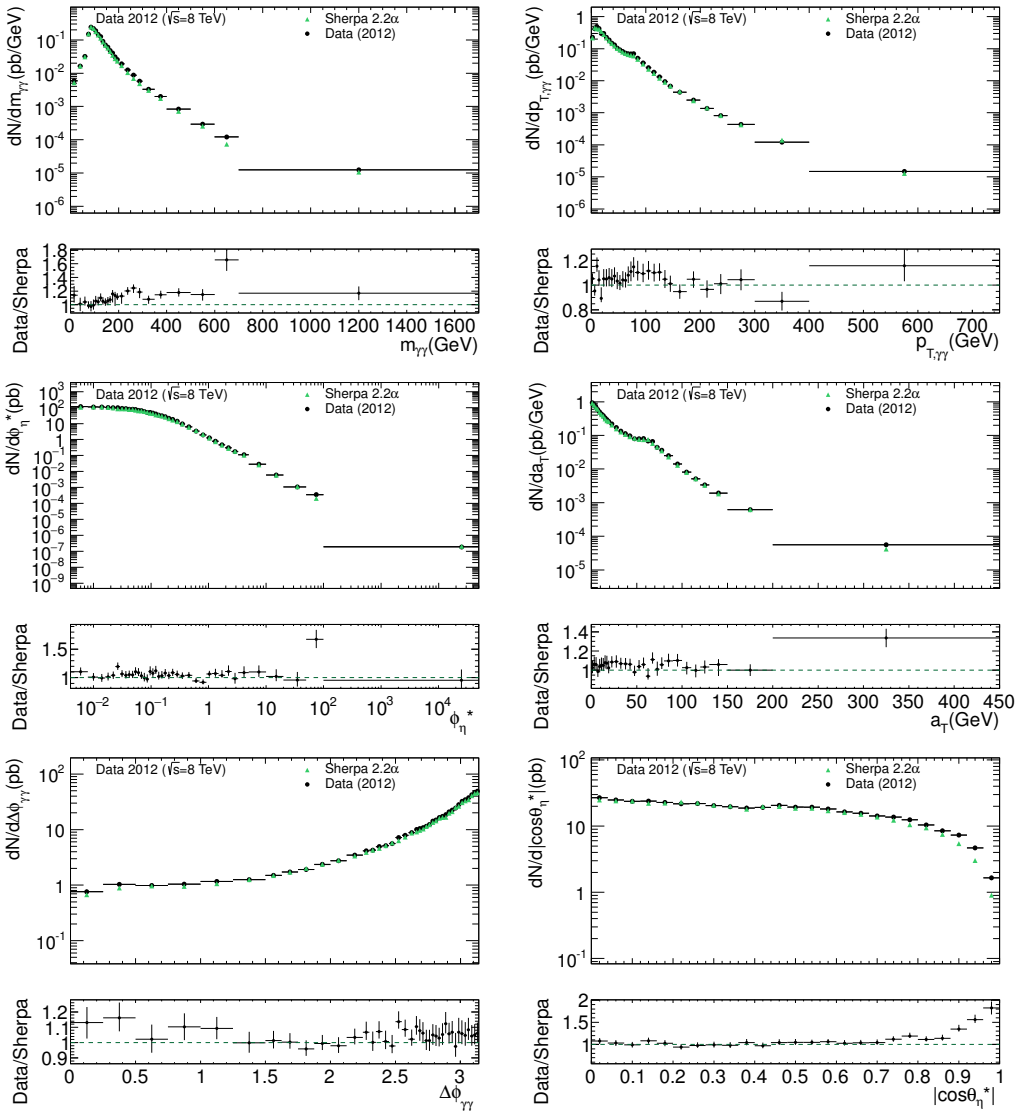

Figure 7.45: Comparison between unfolded distributions and the NLO Sherpa predictions $m_{\gamma\gamma}$, $p_{\mathrm{T},\gamma\gamma}$, $\Delta\phi_{\gamma\gamma}$, $|\cos\theta^*_\eta|$, a_{T} and ϕ^*_η. Data are shown as black dots with error bars indicating the total uncertainties.

7.16 Conclusion

Using 20.24 fb^{-1} data collected by the ATLAS experiment in 2012, measurements of cross-section for the diphoton production in pp collisions at $\sqrt{s} = 8$ TeV have been presented. The data were corrected for background and detector inefficiency and resolution. The measured inclusive $pp \to \gamma\gamma + X$ cross section in the defined fiducial phase space is
16.97 ± 0.09 (stat) $^{+1.10}_{-0.93}$ (syst) $^{+0.03}_{-0.02}$ (trigger) $^{+0.33}_{-0.32}$ (lumi) pb.
In addition, six differential cross sections have been measured in the same fiducial phase space. Both the inclusive and differential cross sections have been compared to MC event generators and fixed-order pQCD calculations. The inclusive cross section is underestimated by LO parton shower event generators Sherpa 1.4.0 and Pythia8 as well as NLO pQCD calculations DIPHOX and ResBos due to missing higher order contributions. No conclusion can be made for the 2γNNLO predictions due to an absence of theoretical uncertainties. The Sherpa 2.2α predictions ($\sigma_{fid}^{Sherpa} = 16.36 \pm 0.08$ (stat.) pb) are consistent with the measured cross section. Table 7.20 summarises the measured inclusive fiducial cross section and the various predictions. In terms of the differential cross sections, Sherpa 1.4.0 can give a better description of data than Pythia8 except at high $m_{\gamma\gamma}$. Pythia8 is missing higher order contributions, but is compensated by the parton shower at low $p_{\mathrm{T},\gamma\gamma}$, a_{T} and ϕ^*_η and for $\Delta\phi_{\gamma\gamma}$ around π. In these regions, fixed order calculations fail but the ResBos predictions using resummation techniques of multiple soft gluons give accurate predictions. Sherpa 2.2α was found to describe data well except for $|\cos\theta^*_\eta| > 0.9$ and in high $m_{\gamma\gamma}$ regions.

	Fiducial cross section (pb)
Data	$16.97\ ^{+1.15}_{-0.99}$ (total)
Sherpa 1.4.0	12.53 ± 0.01 (stat.)
Pythia8	11.81 ± 0.01 (stat.)
DIPHOX	$10.80\ ^{+1.50}_{-1.18}$ (total)
ResBos	$12.26\ ^{+1.70}_{-1.34}$ (total)
2γNNLO	13.94
Sherpa 2.2α	16.36 ± 0.08 (stat.)

Table 7.20: Comparison between the measured fiducial cross section and various MC predictions. Data are shown with the total uncertainty by adding the statistical uncertainty and systematic uncertainties in quadrature. For predictions from Sherpa 1.4.0, Pythia8 and Sherpa 2.2α, only statistical uncertainties are given. The DIPHOX and ResBos predictions are presented with the theoretical uncertainties. Only the central prediction is available for the 2γNNLO prediction.

Chapter 8

Conclusion

Using 10.4 fb^{-1} data collected by the D0 experiment, we measure the normalized differential cross section of ϕ^*_η in the Drell-Yan process in bins of dimuon invariant mass and dimuon rapidity. This represents the first measurement of the ϕ^*_η distribution away from the Z-mass peak. A prediction from RESBOS is found to describe data within the assigned theoretical uncertainty except at $\phi^*_\eta > 0.5$ in the mass region $30 < M_{ll} < 60$ GeV. A NNLL+NLO prediction is in excellent agreement with data within theoretical uncertainties. Further measurements of the ϕ^*_η distributions are performed by the ATLAS collaboration at $\sqrt{s} = 8$ TeV [75], which are still dominated by statistical uncertainties. As more data are recorded at the ATLAS experiment, the systematic uncertainties will become dominant in the ϕ^*_η measurements.

Using 20.24 fb^{-1} data collected by the ATLAS experiment, we present both the inclusive and differential cross sections of prompt photon pairs. A prediction from SHERPA including higher-order corrections can describe the data with reasonable accuracy whereas the other event generators are unable to provide a reasonable description of data due to a lack of higher-order corrections. This new version of SHERPA predictions can be used as the background model in the $H \to \gamma\gamma$ analysis and new physics searches with a pair of photons as the final state. This is also the first measurement of a_T and ϕ^*_η distributions in the diphoton channel. Further analysis at the LHC with more data can benefit from the improved background decomposition methods adopted in this thesis. As the measurement precision is limited by systematic effects, a more careful treatment of the background can potentially reduce the systematic uncertainty.

Bibliography

[1] D. Wark, *The hunt for Majorana neutrinos hots up*, Nature **510** (2014) 224.

[2] ATLAS and CMS Collaboration, G. Aad et al., *Combined Measurement of the Higgs Boson Mass in pp collisions at $\sqrt{s} = 7$ and 8 TeV with the ATLAS and CMS Experiments*, Phys. Rev. Lett. **114** (2015) 191803.

[3] G. 't Hooft, *Naturalness, chiral symmetry, and spontaneous chiral symmetry breaking*, NATO ASI Series B **59** (1980) 135.

[4] Particle Data Group Collaboration, K. Olive et al., *Review of Particle Physics*, Chin. Phys. C **38** (2014) 090001.

[5] S. Weinberg, *A model for leptons*, Phys. Rev. Lett. **19** (1967) 1264.

[6] A. Salam, *Weak and electromagnetic interactions*, Proceedings of the 8th Nobel Symposium on Elementary Particle Theory, Relativistic Groups and Analyticity (1969) 367–377.

[7] S. L. Glashow, *Partial symmetries of weak interactions*, Nul. Phys. **22** (1961) 579.

[8] P. Higgs, *Broken Symmetries and the Masses of Gauge Bosons*, Phys. Lett. **13** (1964) 508.

[9] F. Englert and R. Brout, *Broken Symmetry and the Mass of Gauge Vector Mesons*, Phys. Lett. **13** (1964) 321.

[10] ATLAS Collaboration, G. Aad et al., *Observation of a new particle in the search for the Standard Model Higgs boson with the ATLAS detector at the LHC*, Phys. Rev. Lett. B **716** (2012) 1–29.

[11] CMS Collaboration, S. Chatrchyan et al., *Observation of a new boson at a mass of 125 GeV with the CMS experiment at the LHC*, Phys. Rev. Lett. B **716** (2012) 30.

[12] N. Cabibbo, *Unitary Symmetry and Leptonic Decays*, Phys. Lett. **10** (1963) 531.

[13] M. Kobayashi and T. Maskawa, *CP-Violation in the Renormalizable Theory of Weak Interaction*, Prog. Theor. Phys. **49** (1973) 652.

[14] Z. Maki, M. Nakagawa, and S. Sakata, *Remarks on the United Model of Elementary Particles*, Prog. Theor. Phys. **28** (1962) 870.

[15] B. Pontecorvo, *Inverse beta processes and nonconservation of lepton charge*, Sov. Phys. JETP **7** (1958) 172.

[16] M. Baak et al., *The global electroweak fit at NNLO and prospects for the LHC and ILC*, Eur. Phys. J. C **74** (2014) 3046.

[17] S. Drell and T.-M. Yan, *Massive Lepton-Pair Production in Hadron-Hadron Collisions at High Energies*, Phys. Rev. Lett. **25** (1970) 316.

[18] J. Collins, D. Soper, and G. Sterman, *Transverse Momentum Distribution in Drell-Yan Pair and W and Z Boson Production*, Nucl. Phys. B **250** (1985) 199.

[19] S. Dulat et al., *New parton distribution functions from a global analysis of quantum chromodynamics*, Phys. Rev. D **93** (2016) 033006.

[20] NNPDF Collaboration, R. D. Ball et al., *Parton distributions for the LHC Run II*, JHEP **04** (2015) 040.

[21] G. Altarelli and G. Parisi, *Asymptotic Freedom in Parton Language*, Nucl. Phys. B **126** (1977) 298.

[22] Y. L. Dokshitzer, *Calculation of structure functions of deep-inelastic scattering and e+e- annihilation by perturbation theory in quantum chromodynamics*, Sov. Phys. JETP **46** (1977) 641.

[23] V. N. Gribov and L. N. Lipatov, *Deep inelastic ep scattering in perturbation theory*, Sov. J. Nucl. Phys. **15** (1972) 438.

[24] M. Guzzi, P. Nadolsky, and B. Wang, *Nonperturbative contributions to a resummed leptonic angular distribution in inclusive neutral vector boson production*, Phys. Rev. D **90** (2014) 014030.

[25] D0 Collaboration, V. M. Abazov et al., *Precise study of the Z/γ^* boson transverse momentum distribution in ppbar collisions using a novel technique*, Phys. Rev. Lett. **106** (2011) 122001.

[26] F. Landry, R. Brock, P. Nadolsky, and C.-P. Yuan, *Tevatron Run-1 Z Boson Data and Collins-Soper-Sterman Resummation Formalism*, Phys. Rev. D **67** (2003) 073016.

[27] M. Seymour, *Matrix-Element Corrections to Parton Shower Algorithms*, Comp. Phys. Commun. **90** (1995) 95.

[28] V. V. Sudakov, *Vertex parts at very high-energies in quantum electrodynamics*, Sov. Phys. JETP **3** (1956) 65.

[29] T. Sjostrand, S. Mrenna, and P. Z. Skands, *A Brief Introduction to PYTHIA 8.1*, Comput. Phys. Commun. **178** (2008) 852.

[30] Geant4 Collaboration, S. Agostinelli et al., *Geant4: A Simulation toolkit*, Nucl. Instrum. Meth. A **506** (2003) 250–303.

[31] C. Balazs, J.-W. Qiu, and C.-P. Yuan, *Effects of QCD resummation on distributions of leptons from the decay of electroweak vector bosons*, Phys. Lett. B **355** (1995) 548.

[32] T.Binoth, J. Guillet, and M. Werlen, *A full Next to Leading Order study of direct photon pair production in hadronic collisions*, Eur. Phys. J. C **16** (2000) 311–330.

[33] A. Banfi, S. Redford, M. Vesterinen, P. Waller, and T. Wyatt, *Optimisation of variables for studying dilepton transverse momentum distributions at hadron colliders*, Eur. Phys. J. C **71** (2010) 1600.

[34] A. Banfi, M. Dasgupta, and S. Marzani, *QCD predictions for new variables to study dilepton transverse momenta at hadron colliders*, Phys. Lett. B **701** (2011) 75.

[35] A. Banfi, M. Dasgupta, S. Marzani, and L. Tomlinson, *Probing the low transverse momentum domain of Z production with novel variables*, JHEP **01** (2012) 044.

[36] J. M. Campbell and R. K. Ellis Phys. Rev. D **65** (2002) 113007.

[37] ATLAS Collaboration, G. Aad et al., *Measurement of angular correlations in Drell-Yan lepton pairs to probe Z/γ^* boson transverse momentum at $\sqrt{s}$=8 TeV with the ATLAS detector*, Phys. Lett. B **720** (2013) 32.

[38] ATLAS Collaboration, G. Aad et al., *Example ATLAS tunes of Pythia8, Pythia6 and Powheg to an observable sensitive to Z boson transverse momentum*, Tech. Rep. ATL-PHYS-PUB-2013-017, CERN, Geneva, 2013.

[39] LHCb Collaboration, R. Aaij et al., *Measurement of the cross-section for $Z \to e^+e^-$ production in pp collisions at $\sqrt{s}$=7 TeV*, JHEP **02** (2013) 106.

[40] D0 Collaboration, V. M. Abazov et al., *Measurement of the ϕ^*_η distribution of muon pairs with masses between 30 and 500 GeV in 10.4 fb^{-1} of $p\bar{p}$ collisions*, Phys. Rev. D **91** (2015) 072002.

[41] T. Binoth, J. Guillet, E. Pilon, and M. Werlen, *A Full next-to-leading order study of direct photon pair production in hadronic collisions*, Eur. Phys. J. C **16** (2000) 311.

[42] J. C. Collins and D. E. Soper, *Angular Distribution of Dileptons in High-Energy Hadron Collisions*, Phys. Rev. D **16** (1977) 2219.

[43] D0 Collaboration, V. M. Abazov et al., *Measurement of the differential cross sections for isolated direct photon pair production in $p\bar{p}$ collisions at $\sqrt{s} = 1.96$ TeV*, Phys. Lett. B **725** (2013) 6.

[44] CDF Collaboration, T. Aaltonen et al., *Measurement of the cross section for prompt isolated diphoton production using the full CDF Run II data sample*, Phys. Rev. Lett. **110** (2013) 101801.

[45] ATLAS Collaboration, G. Aad et al., *Measurement of the isolated di-photon cross-section in pp collisions at $\sqrt{s} = 7$ TeV with the ATLAS detector*, Phys. Rev. D **85** (2012) 012003.

[46] ATLAS Collaboration, G. Aad et al., *Measurement of isolated photon pair production in pp collisions at $\sqrt{s} = 7$ TeV with the ATLAS detector*, JHEP **1301** (2012) 086.

[47] CMS Collaboration, S. Chatrchyan et al., *Measurement of differential cross sections for the production of a pair of isolated photons in pp collisions at $\sqrt{s} = 7$ TeV*, Eur. Phys. J. C **74** no. 11, (2014) 3129.

[48] CMS Collaboration, S. Chatrchyan et al., *Production of pairs of isolated photons in association with jets in pp collisions at sqrt(s) = 7 TeV*, Tech. Rep. CMS-PAS-SMP-14-021, CERN, Geneva, 2015.

[49] T. Gleisberg et al., *Event generation with SHERPA 1.1*, JHEP **0902** (2009) 007.

[50] Z. Bern, L. Dixon, and C. Schmidt, *Isolating a light Higgs boson from the diphoton background at the LHC*, Phys. Rev. D **66** (2002) 074018.

[51] C. Balaza, E. Berger, P. Nadolsky, and C.-P. Yuan, *All-orders resummation for diphoton production at hadron colliders*, Phys. Lett. B **637** (2006) 235.

[52] C. Balaza, E. Berger, P. Nadolsky, and C.-P. Yuan, *Calculation of prompt diphoton production cross sections at Tevatron and LHC energies*, Phys. Rev. D **76** (2007) 013009.

[53] P. Nadolsky, C. Balaza, E. Berger, and C.-P. Yuan, *Gluon-gluon contributions to the production of continuum diphoton pairs at hadron colliders*, Phys. Rev. D **76** (2007) 013008.

[54] S. Catani, L. Cieri, D. de Florian, G. Ferrera, and M. Grazzini, *Diphoton production at hadron colliders: a fully-differential QCD calculation at NNLO*, Phys. Rev. Lett. **108** (2012) 072001.

[55] J. Marriner Nucl. Instr. and Meth. in Phys. Res. A **532** (2004) 11.

[56] http://www.fnal.gov/pub/tevatron/tevatron-accelerator.html.

[57] http://bigscience.web.cern.ch/bigscience/Objects/LHC/accelerator.jpg.

[58] D0 Collaboration, V. M. Abazov et al., *The Upgraded D0 Detector*, Nucl. Instr. and Meth. in Phys. Res. A **565** (2006) 463.

[59] ATLAS Collaboration, G. Aad et al., *The ATLAS Experiment at the CERN Large Hadron Collider*, Journal of Instrumentation **3** (2008) S08003.

[60] ATLAS Collaboration, G. Aad et al., *ATLAS Insertable B-Layer Technical Design Report*, CERN-LHCC-2010-013/ATLAS-TDR-019 (2010).

[61] ATLAS Collaboration, G. Aad et al., *Electron and photon energy calibration with the ATLAS detector using LHC Run 1 data*, Eur. Phys. J. C **74** (2014) 3071.

[62] B. Lenzi and R. Turra, *Monte Carlo calibration update for electrons and photons using multivariate techniques*, Tech. Rep. ATL-COM-PHYS-2013-1426, CERN, Geneva, Oct, 2013.

[63] M. Boonekamp, B. Lenzi, N. Lorenzo Martinez, P. Schwemling, F. Teischinger, G. Unal, and L. Yao, *Electromagnetic calorimeter layers energy scales determination*, Tech. Rep. ATL-COM-PHYS-2013-1423, CERN, Geneva, Oct, 2013.

[64] S. Laplace and J. de Vivie, *Calorimeter isolation and pile-up*, Tech. Rep. ATL-COM-PHYS-2012-467, CERN, Geneva, May, 2012.

[65] W. Lampl, S. Laplace, D. Lelas, P. Loch, H. Ma, S. Menke, S. Rajagopalan, D. Rousseau, S. Snyder, and G. Unal, *Calorimeter Clustering Algorithms: Description and Performance*, Tech. Rep. ATL-LARG-PUB-2008-002. ATL-COM-LARG-2008-003, CERN, Geneva, Apr, 2008.

[66] M. Cacciari and G. P. Salam, *Pileup subtraction using jet areas*, Phys. Lett. B **659** (2008) 119–126.

[67] M. Cacciari, G. P. Salam, and S. Sapeta, *On the characterisation of the underlying event*, JHEP **1004** (2010) 065.

[68] E. Barberio and Z. Was, *PHOTOS – a universal Monte Carlo for QED radiative corrections: version 2.0*, Comput. Phy. Commun. **79** (1994) 291.

[69] T. S. et al., *High-Energy-Physics Event Generation with PYTHIA 6.1*, Comput. Phy. Commun. **135** (2001) 238.

[70] M. Mangano, M. Moretti, F. Piccinini, R. Pittau, and A. Polosa, *ALPGEN, a generator for hard multiparton processes in hadronic collisions*, JHEP **0307** (2003) 001.

[71] M. Vesterinen and T. R. Wyatt, *Precise study of the Z/γ^* boson transverse momentum distribution in $p\bar{p}$ collisions using a novel technique*, Tech. Rep. D0-6088, Fermilab, Chicago, Oct, 2010.

[72] H.-L. Lai et al., *New parton distributions for collider physics*, Phys. Rev. D **82** (2010) 074024.

[73] J. Pumplin et al., *New Generation of Parton Distributions with Uncertainties from Global QCD Analysis*, JHEP.

[74] Y. Qin, X. Li, M. Vesterinen, and T. R. Wyatt, *Precise study of the Z/γ^* boson transverse momentum distribution in $p\bar{p}$ collisions using a novel technique*, Tech. Rep. D0-XXXX, Fermilab, Chicago, Mar, 2014.

[75] ATLAS Collaboration, G. Aad et al., *Measurement of the transverse momentum and ϕ^*_η distributions of Drell-Yan lepton pairs in proton-proton collisions at $\sqrt{s}$=7 TeV with the ATLAS detector*, arXiv:1512.02192 [hep-ex].

[76] ATLAS Collaboration, G. Aad et al., *The ATLAS Diamond Beam monitor*, ATL-INDET-PROC-2013-021 (2013).

[77] C. C. Chau, *Status of the DBM geometry and alignment*,. https://indico.cern.ch/event/304225/session/1/contribution/7/material/slides/0.pdf.

[78] ATLAS Collaboration, G. Aad et al., *The ATLAS Simulation Infrastructure*, Eur. Phys. J. C **70** (2010) 823.

[79] S. Van der Meer, *Calibration of the effective beam height in the ISR*, Tech. Rep. CERN-ISR-PO-68-31, CERN, Geneva, 1968.

[80] V. M. Abazov et al., *Luminosity determination in pp collisions at $\sqrt{s} = 8$ TeV using the ATLAS detector at the LHC*, Tech. Rep. ATL-COM-DAPR-2015-014, CERN, Geneva, Aug, 2015.

[81] S. Alioli, P. Nason, C. Oleari, and E. Re, *A general framework for implementing NLO calculations in shower Monte Carlo programs: the POWHEG BOX*, JHEP **06** (2010) 043.

[82] M. Escalier, L. Fayard, and J.-F. Marchand, *Reconstruction of the z vertex and direction of the photon*, Tech. Rep. ATL-PHYS-INT-2010-013, CERN, Geneva, Jan, 2010.

[83] ATLAS Collaboration, G. Aad et al., *Meausrement of the photon identification efficiencies with the ATLAS detector using LHC Run-1 data*, arXiv:1606.01813.

[84] B. Lenzi, C. Royon, and M. Saimpert, *Data-driven corrections for the calorimeter isolation energy of photons computed from topological clusters*, Tech. Rep. ATL-COM-PHYS-2015-258, CERN, Geneva, Apr, 2015.

[85] ATLAS Collaboration, G. Aad et al., *Measurement of the Higgs boson mass from $H \to \gamma\gamma$ and $H \to ZZ^* \to 4l$ channels with the ATLAS detector using 25fb^{-1} of pp collision data*, Phys. Rev. D **90** (2014) 052004.

[86] G. Bohm, *Introduction to statistics and data analysis for physicists*. Hamburg: Verl. Dt. Elektronen-Synchrotron, 2010.

[87] ATLAS Collaboration, G. Aad et al., *Electron efficiency measurements with the ATLAS detector using 2012 LHC proton-proton collision data*, Tech. Rep. ATLAS-CONF-2014-032, CERN, Geneva, 2014.

[88] S. Frixione, P. Nason, and C. Oleari, *Matching NLO QCD computations with Parton Shower simulations: the POWHEG method*, JHEP **11** (2007) 070.

[89] ATLAS Collaboration, G. Aad et al., *Measurements of fiducial and differential cross sections for Higgs boson production in the diphoton decay channel at $\sqrt{s} = 8$ TeV with ATLAS*, JHEP **1409** (2014) 112.

[90] G. D'Agostini, *Improved iterative Bayesian unfolding*, arXiv:1010.0632 [hep-ex].

[91] D. Damazio, T. Kono, F. Monticelli, and G. Pasztor, *Performance of the ATLAS Electron and Photon Triggers in pp Collisions at $\sqrt{s} = 8$ TeV in 2012*, Tech. Rep. ATL-COM-DAQ-2013-121, CERN, Geneva, Oct, 2013.

[92] ATLAS Collaboration, G. Aad et al., *Measurements of Higgs boson production and couplings in diboson final states with the ATLAS detector at the LHC*, Phys. Lett. B **726** (2013) 88.

[93] T. Gleisberg, and S. Hoche, *Comix, a new matrix element generator*, JHEP **12** (2008) 039.

[94] F. Cascioli, and P. Maierhofer, and S. Pozzorini, *Scattering Amplitudes with Open Loops*, Phys. Rev. Lett. **108** (2012) 111601.

[95] A. Bocci, L. Shi, and Z. Liang, *Measurements of the $e \to \gamma$ fake rate*, Tech. Rep. ATL-COM-PHYS-2014-026, CERN, Geneva, Jan, 2014.

Appendices

Appendix A

A brief review of the 2D fit method

The 2D fit method uses a maximum likelihood fit to the two-dimensional distributions of $E_{\mathrm{T}}^{\mathrm{iso}}$ of the two photon candidates. The fit is performed in the **TITI** regions only with the isolation range of $E_{\mathrm{T}}^{\mathrm{iso}}$ between -5.2 GeV and 6 GeV. The 2D fit method subtracts the $Z \to ee$ contribution at the same time as the hadronic background using a Gaussian constraint from the number of the predicted fake photons from the $Z \to ee$ MC.

The total 2D isolation distributions consist of one signal ($\gamma\gamma$) and four background (γj, jγ, jj and ee) categories, each of which corresponds to a template called the probability density function (pdf) and is weighted by its corresponding yield:

$$W_{tot}^{\mathrm{TITI}} F_{tot}^{\mathrm{TITI}} = W_{\gamma\gamma}^{\mathrm{TITI}} F_{\gamma\gamma}^{\mathrm{TITI}} + W_{\gamma j}^{\mathrm{TITI}} F_{\gamma,1}^{\mathrm{TITI}} F_{j,2}^{\mathrm{TITI}} + W_{j\gamma}^{\mathrm{TITI}} F_{j,1}^{\mathrm{TITI}} F_{\gamma,2}^{\mathrm{TITI}} + W_{jj}^{\mathrm{TITI}} F_{jj}^{\mathrm{TITI}} + W_{ee}^{\mathrm{TITI}} F_{e,1}^{\mathrm{TITI}} F_{e,2}^{\mathrm{TITI}}. \tag{A.1}$$

F_{tot}^{TITI} represents the total 2D pdf of the two isolation energies for all the events passing the **TITI** criteria. $F_{\gamma\gamma}^{\mathrm{TITI}}$, $F_{\gamma,1}^{\mathrm{TITI}}$ and $F_{\gamma,2}^{\mathrm{TITI}}$ are the two and one-dimensional pdfs for the diphoton, leading and subleading photons respectively taken from $\gamma\gamma$ MC. The background pdfs $F_{j,1}^{\mathrm{TITI}}$ and $F_{j,2}^{\mathrm{TITI}}$ are estimated from the $\tilde{\mathbf{T}}$**ITI** and **TI**$\tilde{\mathbf{T}}$**I** regions in the data respectively. The di-jet pdf F_{jj}^{TITI} is two-dimensional and evaluated in the $\tilde{\mathbf{T}}\mathbf{I}\tilde{\mathbf{T}}\mathbf{I}$ region in the data sample. The electron background pdfs $F_{e,1}^{\mathrm{TITI}}$ and $F_{e,2}^{\mathrm{TITI}}$ are one-dimensional and are taken from $e\gamma$ and γe data around the Z-mass peak region ($80 < M_{\ell\ell} < 100$ GeV) as described in Section 7.9. The isolation correlations for $\gamma\gamma$ and jj components are kept in the 2D fit method.

The difference between the photon isolation pdf and the electron isolation pdf is not sufficient enough to disentangle their respective yields in the likelihood fit. Hence we use a Gaussian constraint with a central value from $Z \to ee$ MC predictions and a Gaussian width equal to the quadrature sum of the $Z \to ee$ MC statistical uncertainty and the systematic uncertainty arising from the $e \to \gamma$ fake scale factors [95] . These $e \to \gamma$ fake scale factors are derived using $Z \to ee$ data and are applied to the $Z \to ee$ MC to improve the description of fake photons.